Institut für Theoretische Physik
Fakultät Mathematik und Naturwissenschaften
Technische Universität Dresden

Event generation at hadron colliders

Dissertation
zur Erlangung des akademischen Grades
Doctor rerum naturalium
(Dr.rer.nat.)

vorgelegt von
Andreas Schälicke

Dresden 2005

Dedicated to the memory of Prof. Gerhard Soff, 1949 - 2004.

Eingereicht am 31. März 2005

1. Gutachter: Prof. Dr. R. Ketzmerick
2. Gutachter: Prof. Dr. B. R. Webber
3. Gutachter: Prof. Dr. M. L. Mangano

Verteidigt am 15. Juli 2005

Kurzfassung

Diese Arbeit befasst sich mit der Simulation von hochenergetischen Hadron-Kollisionsexperimenten, wie sie im Moment am Tevatron (Fermilab) durchgeführt werden und in naher Zukunft am Large Hadron Collider (LHC) am CERN zu erwarten sind. Für die Beschreibung dieser Experimente wird ein Algorithmus untersucht, der es ermöglicht, exakte Multijet-Matrixelemente auf Baumgraphenniveau in die Simulation einzubeziehen und so die Qualität der Vorhersage deutlich zu verbessern. Die Implementierung dieses Algorithmus in den Eventgenerator "SHERPA" [1] und die Erweiterung des Parton Showers in diesem Programm ist das Hauptthema dieser Arbeit. Die Ergebnisse werden mit experimentellen Daten und mit anderen Simulationen verglichen.

Abstract

This work deals with the accurate simulation of high energy hadron–hadron–collision experiments, as they are currently performed at Fermilab Tevatron or as they are expected at the Large Hadron Collider at CERN. For a precise description of these experiments an algorithm is investigated, which enables the inclusion of exact multi-jet matrix elements in the simulation. The implementation of this algorithm in the event generator "SHERPA" [1] and the extension of its parton shower is the main topic of this work. The results are compared with those of other simulation programs and with experimental data.

Contents

1 Introduction

To a large amount, modern particle physics centres around accelerator experiments, where high-energetic particles are brought to collision. Examples of such collider experiments are: the Large Electron Positron collider (LEP) at CERN, where until November 2000 e^+e^-–collisions at centre-of-mass energies up to 207 GeV took place, or the Tevatron at Fermilab, where proton–anti-proton–collisions at 1960 GeV centre-of-mass energy are currently investigated. To confront the resulting experimental data with theoretical models, a systematic understanding of such multi-particle production processes is of paramount importance. A full, quantum-mechanically correct, treatment is, at the moment, out of reach. There are two reasons for this: First of all, there only is a limited understanding of the non-perturbative phase of QCD, or, in other words, of how colourless hadrons are built from the coloured quarks and gluons. This is especially true for phenomena such as hadronisation or for questions related to the impact of the partonic substructure of the colliding hadrons on the pattern of multiple interactions. In all such cases, phenomenological models for the transition from hadrons to partons or vice versa have to be applied with parameters to be fitted. This clearly puts a constraint on a conceptual understanding of high-energy particle production processes. On the other hand, even considering the, in principle, well-understood perturbative phase of scattering processes alone, there are limits on present technical abilities to calculate all amplitudes that contribute to a given process. This is due to the fact that even at the tree-level the number of Feynman diagrams grows factorially with the number of particles involved. Moreover, at higher orders of the perturbative evolution new difficulties arise, which are connected for instance with the evaluation of multi-leg loop integrals.

This failure necessitates other, approximate solutions, such as simulation programs, usually called event generators. These event generators decompose the full scattering process into a sequence of different stages, which are usually characterised by different energy scales. The past and current success of event generators, like `PYTHIA` [2] or `HERWIG` [3], in describing a full wealth of various data justifies this decomposition intrinsic to all such programs. As a by-product, the decomposition of events into distinguishable, more or less independent phases opens a path to test the underlying assumptions on the dynamics of particle interactions at the corresponding scales. These assumptions, in turn, can be modified and new models can be included on all scales. This property turns event generators into the perfect tool to bridge the gap between experimental data and theoretical predictions. It renders them indispensable for the analyses and planning of current and future experiments. Especially in view of the largest particle physics experiment ever, the Large Hadron Collider (LHC), these Monte Carlo tools move into the centre of interest.

Beam energy	7 TeV
Number of particles per bunch	$1.15 \cdot 10^{11}$
Number of bunches	2808
DC beam current	0.582 A
Luminosity	$1.0 \cdot 10^{34}$ cm^{-1}s^{-1}
Expected events per crossing	19

Table 1.1: Selected LHC parameters according to the "Nominal Proton Performance Version 4.0".

1.1 The Large Hadron Collider

In the near future the Large Hadron Collider (LHC) will start providing proton-proton collisions at centre-of-mass energies of 14000 GeV. It is currently under construction in the same tunnel that had been used by LEP. Some of its key parameters are summarised in Tab. 1.1. The huge c.m. energy and the unprecedented luminosity of the LHC, provides a new challenge for experimentalists and theorists alike. The physics programme includes the precision measurement of Standard Model parameters, like the mass of the W boson, or the gauge boson self-couplings, the investigation of phenomena of the electroweak symmetry breaking (EWSB), the study of heavy flavour physics and CP violation. It also allows the search for new physics which is expected to become apparent at the TeV scale, Supersymmetry being a favourite example.

Five experiments with over 5000 participating physicists from all over the world are under current construction to tackle these tasks. Two general purpose detectors, ATLAS and CMS, are designed for optimal coverage of any signal which may hint new physics. If the Higgs boson exists, it will be discovered there. However, with a bunch crossing rate of 40 MHz, and approximately 20 inelastic proton-proton scatterings per bunch crossing, the amount of generated data will be huge (data acquisition: rate O(100 Hz), size O(100 MB/s)). Thus, the search for new physics will resemble the search for the needle in a hay stack. A collection of processes and their expected event rates are listed in Tab. 1.2.

Final State	**Events per Second**	**Events per Year**
Jet, $E_T > 100\,\text{GeV}$	10^3	10^{10}
Jet, $E_T > 1\,\text{TeV}$	$1.5 \cdot 10^{-2}$	$1.5 \cdot 10^5$
$W \rightarrow l\bar{\nu}_l$	20	$2 \cdot 10^8$
$b\bar{b}$	$5 \cdot 10^5$	$5 \cdot 10^{12}$
$t\bar{t}$	1	$1 \cdot 10^7$
$WW \rightarrow l\bar{\nu}_l l\bar{\nu}_l$	$6 \cdot 10^{-3}$	$6 \cdot 10^4$

Table 1.2: Expected event rates at LHC, evaluated for a lower luminosity of $\mathcal{L} = 10^{33}/\text{cm}^2\text{s}$. The process $p\bar{p} \rightarrow W \rightarrow l\bar{\nu}_l$ is to be used as a luminosity monitor [4].

1.2 New tools for high energy physics

To meet these new challenges posed by the new experiments, the traditional event generators PYTHIA and HERWIG, so far programmed in Fortran, are currently being re-written in the modern, object-oriented programming language C++. Their new versions will be called Pythia7 [5] and Herwig++ [6], respectively. The decision to re-write them from scratch is based on two reasons: First, new features and models concerning the simulation of particle physics at the shifting energy frontier need to be included. In fact this still is an on-going issue also for the Fortran versions (see for instance [7, 8]). Furthermore, and maybe more importantly, there is a wide-spread belief that the old Fortran codes cannot easily be maintained or extended. On top of that, the software paradigm of the new experiments has already shifted to object-orientation, more specifically, to C++ as programming language. On the other hand, by the virtue of being decomposed into nearly independent phases, the simulation of high-energy particle reactions lends itself to modularisation and, thus, to an object-oriented programming style. In this respect it is also natural to further disentangle management and physics issues in event generation. In fact, both Pythia7 and Herwig++ were intended to fully rely on the same management structure, called ThePEG [9, 10]. It includes items such as the event record, mathematical functions, management functionalities, etc.. Using this common event-generation framework, Pythia7 and Herwig++ were thought to just provide their respective, different modules for physics simulation, for instance the implementations of their hadronisation models. In addition to these two re-writes of their older, Fortran-based counterparts, in the past few years a new event generator, called SHERPA, acronym for Simulation for High-Energy Reactions of PArticles, has been developed independently [1]. From the beginning, it entirely has been written in C++. In its current form, it is able to completely simulate electron–positron, unresolved photon–photon and fully hadronic collisions.

But apart from the need for larger transparency and modularity of the codes, the LHC also necessitates the development of new techniques. For instance, in order to meet increasing precision goals for multi-purpose event generators, recently two approaches have been developed that incorporate higher-order corrections into their framework. The first one, called MC@NLO, provides a method to consistently match NLO calculations for specific processes with the parton shower [11, 12], and it is perfectly suited for the accurate description of inclusive cross sections etc.. The idea of this approach is to organise the counter-terms necessary to technically cancel real and virtual infrared divergencies in such a way that the first emission of the parton shower is recovered. Of course, this method depends to some extent on the details of the parton shower, and it has some residual dependence on the process in question. So far, MC@NLO has been implemented in conjunction with HERWIG [13] for the following processes: production of W and Z bosons, or pairs of these bosons [11], production of the Higgs boson, production of heavy quarks [12].

An alternative approach, aiming at a better description of multi-particle topologies is to combine tree-level matrix elements for different multiplicities of additional jets and to merge them with the parton shower. This approach has been presented for the first time for the case of e^+e^- annihilations into jets [14]; later it has been extended to hadronic collisions [15] and it has been reformulated to a merging procedure with a dipole shower in [16]. The idea underlying this method is to separate the kinematical range of parton emission by a $k_\perp$ algorithm [17–19] into a regime of jet production, covered by the appropriate matrix elements, and to a regime of jet evolution, covered by the respective shower. Then, the

matrix elements are reweighted through Sudakov form factors and hard emissions in the parton shower leading to a jet are vetoed such that there is only a residual dependence on the jet resolution cut. This method is one of the cornerstones of the new event generator SHERPA [1]; it has been validated for the cases of e^+e^- annihilations into jets [20] and for the production of single vector bosons at the Fermilab Tevatron [21] and the CERN LHC [22]. The implementation, extension and validation of this procedure has been one of the central topics of this thesis. Of course, this has been done in the framework of SHERPA, which will therefore be briefly described.

1.3 The Monte Carlo Event generator SHERPA

As already stated above, SHERPA has been developed independently from the other new codes. From the beginning, it was constructed in a modular way, with different physics aspects implemented in different, nearly independent parts. This modularity is realised such that SHERPA only provides the framework for event generation. The physics issues related to the various phases of event generation are handled by specific, physics-oriented modules, which rely on a common structure (basic organisational, mathematical or physics tools, or information concerning the physics environment) provided through SHERPA. To further facilitate this, physics interfaces and their specific implementation have been separated. In SHERPA, specific physics modules are interfaced through corresponding (handler) classes, which are sufficiently abstract to support an easy inclusion of other modules with similar tasks. Before the interfaces (abstract handlers) are implemented, the corresponding physics module has been programmed and tested. This is especially true for modules like AMEGIC++ [23–25], providing a full matrix-element generator for the evaluation of multi-particle production cross sections, or APACIC++ [20,26], hosting a parton shower module. In general, these modules can be used as stand-alone codes. They could also be implemented into other event-generation frameworks with minor modifications only, as long as some of the underlying mathematical and physics tools are supplemented as well. In fact, the authors of Herwig++ intend to use AMEGIC++ as their prefered matrix element generator.
So far, the following physics modules have been implemented and tested:

- ATOOLS-2.0

  The toolbox for all other modules. Since the SHERPA framework does not rely on CLHEP etc., the ATOOLS contain classes with mathematical tools like vectors and matrices, organisation tools such as read-in- or write-out devices, and physics tools like particle data or classes for the event record. All of them have been written from scratch.

- BEAM-1.0

  This module manages the treatment of the initial beam spectra for different colliders. At the moment two options are implemented for the beams: They can either be monochromatic, and therefore require no extra treatment, or, for the case of an electron collider laser-backscattering off the electrons is supported in two versions, leading to photonic initial states[1].

[1] It should be stressed, however, that the parameterisation [27] which has been implemented is valid

- PDF-1.0

  In this module the handling of initial state radiation (ISR) is located. It contains interfaces to various proton [28, 29] and photon [30] parton density functions (PDFs), and to the LHAPDF (version 3) interface [31] making available a full wealth of proton PDFs. In addition, an (analytical) electron structure function is made available there as well.

- MODEL-1.0,

  This module comprises the basic physics parameters (like, e.g., masses, mixing angles, etc.) of the simulation run and thus specifies the corresponding physics model. At the moment three different physics models are supported: the Standard Model (SM), its Minimal Supersymmetric extension (MSSM) [32] and the ADD model of large extra-dimensions [33]. For the SM and the ADD model most of the required parameters are directly read in.

- EXTRA_XS-1.0

  In this module a (limited) collection of analytic expressions for simple $2 \to 2$ processes within the SM and classes to embed them into the SHERPA framework are provided. This includes methods used for the definition of the parton shower evolution, such as colour connections and the hard scale of the process. Classes for phase space integration are common with AMEGIC++ and they are located in PHASIC.

- AMEGIC++-2.0

  AMEGIC++ [23] is SHERPAs preferred matrix element generator, which employs the method of helicity amplitudes [34, 35]. It works as a highly automated generator-generator: During the initialisation run, the matrix elements for a set of given processes within the SM, the MSSM, or the ADD model as well as their specific phase space mappings are generated by AMEGIC++ and stored in library files. In the initialisation of the production run, these libraries are linked to the program and used to calculate cross sections and to generate single events based on them. The abilities to calculate total cross sections and to provide parton level predictions has been widely tested [36–38].

- PHASIC++-1.0

  Here all classes concerning the Monte Carlo phase space integration are located. As default the adaptive multi-channel method of [39, 40] is used for the evaluation of the initial (laser-backscattering, initial state radiation) and final state integrals. In addition final state integration through RAMBO [41] and SARGE [42] is supported.

- APACIC++-2.0

  APACIC++ [20, 26] contains classes for the simulation of both the initial and the final state shower, cf. Sec. 3.1. All features for a consistent merging with matrix elements

for the proposed TESLA photon collider only. This is because various assumptions concerning the laser parameters and especially the initial energy of the electrons have been made.

are included, however the main part of the merging procedure is situated in the SHERPA module itself.

- AMISIC++-1.0

  AMISIC [43] contains classes for the simulation of multiple parton interactions according to a formalism similar to [44].

- SHERPA-1.0

  Finally, SHERPA is the steering program that initialises, controls and evaluates the different phases in the entire process of event generation. Furthermore, all necessary routines for the merging of parton showers with matrix elements which are independent of the specific parton shower are found in this module. In addition, the package provides an interface to the Lund String Fragmentation of PYTHIA 6.214 including its hadron decay routines. In the near future, however, the Lund string fragmentation will be replaced with a new version of an independent fragmentation model [45, 46].

1.4 Outline of this thesis

In the framework of this thesis, the event generator SHERPA has been significantly extended. First of all, the matrix element generator AMEGIC++ has been improved in terms of efficiency such that it is now capable of dealing with final states with up to six particles. A short description of the respective improvements and a discussion of how AMEGIC++ has been validated can be found in Chapter 2. In addition, the parton shower module APACIC++ has completely been rewritten in order to facilitate not only multiple QCD bremsstrahlung in the final state, but also in the initial state. Therefore, Chapter 3, includes a general presentation of the parton shower formalism, some details concerning its specific implementation in APACIC++ and a presentation of results indicating its correctness. A more detailed presentation of the classes in APACIC++ can be found in appendix D. In Chapter 4, the merging algorithm of multi-particle matrix elements and the parton shower will be presented. In this thesis, the original ideas have been implemented, considerably extended and validated in a number of different processes. Details of the implementation on the level of classes can again be found in appendix D. Parts of this validation which serve to highlight different aspects of the merging procedure are presented in Chapter 4; a number of complete analyses including comparisons with experimental data can be found in Chapter 5. These complete case studies include e^+e^-–annihilations into hadrons at LEP1 and LEP2 energies, the production of W and Z bosons at the Tevatron and the LHC, and the production of W–pairs at the Tevatron. This thesis closes with a summary in Chapter 6.

2 Calculation of cross sections

The central part of any generated event is the signal process, described by a corresponding matrix element. Traditionally, this signal process has been modelled through an appropriate tree-level expression, usually of the form of a $2 \to 2$ process, eventually supplemented with the decay of heavy particles, taking into account spin correlations according to [47]. However, on the path towards higher precision, new techniques have been developed, some of them involve the calculation of matrix elements for the production of multi-particle final states.

This, however, is a formidable calculational task that cannot be handled without dedicated computer programs. Three major difficulties make these necessary:

1. The number of Feynman diagrams, i.e. quantum mechanical transition amplitudes, grows roughly factorially with the number of external particles. For instance, in the full Standard Model, the calculation of the process $e^+e^- \to e^+e^-e^+e^-e^+e^-$ results in considering 13896 Feynman diagrams. Obviously, in such cases, the common textbook method of squaring the diagrams by employing completeness relations for the external particles and evaluating the traces fails.

2. Apart from the treatment of an enormous number of diagrams, the integration over the phase space of the outgoing particles becomes a tedious task. Its high dimensionality, $3n-4$, for n final-state particles necessitates the use of Monte Carlo methods. To achieve convergence of the Monte Carlo procedure process- and cut-dependent phase-space mappings are required. They are confronted with the need to tame wildly fluctuating integrands, which are due to nearly on-shell propagators. A benefit of Monte Carlo methods, if carefully implemented, is that not only total cross sections but also distributions including all possible types of kinematical cuts can be calculated on an equal footing.

3. An additional complication appears at hadron colliders. There, the partonic initial state is no longer fixed to a specific flavour pair, but can be any combination of two quarks, anti-quarks, or gluons. As a result, the number of subprocesses that has to be considered increases dramatically with the number of final state jets. For instance the process $pp \to 4jets$ contains 486 contributing subprocesses, while the same final state in e^+e^- collisions is generated by 20 individual subprocesses only.

In the past years, therefore different types of programs, also known as parton level generators, have been constructed that deal with the problems outlined above. They can be crudely characterised as being either specialised or multi-purpose generators.

Usually, the former ones contain explicit matrix elements and phase-space mappings for specific classes of processes with specific assumptions. These matrix elements were

constructed before outside the respective program, and this feature also allows, for instance, to implement non-universal higher-order corrections in a controlled way. Often, the phase space mappings have been optimised before as well.

Examples for such programs dealing with some of the processes discussed in Sec. 2.2.1 are LUSIFER [48] and eett6f [49]. Both are constrained to fermions in the final state; in the case of LUSIFER these fermions are bound to be massless, whereas eett6f specialises in top quark pair production channels where the outgoing fermions might be massive, but electrons are disallowed in the final state. Both programs use versions of the adaptive multichannel method [39, 40] for phase space integration. A further dedicated program using the multichannel importance sampling is SIXFAP [50–52]. It provides the electroweak contributions for a large set of six-fermion final states, taking into account possible non-zero fermion masses.

In contrast to specialised programs, multipurpose codes generate both the matrix elements and the phase space mappings with or without some intervention by the user. Examples of these types of programs are AcerMC [53], ALPGEN [54], CompHEP [55], GRACE/GR@PPA [56,57], HELAC/PHEGAS/JetI [58], O'Mega/Whizard [59,60] and MadGraph/MadEvent [61,62], some of which are used in the comparisons in Secs. 2.2.1 and 2.2.2.

The AcerMC [53] Monte-Carlo event generator is specialised for generation of the Standard Model background processes in proton proton collisions at the LHC. The matrix elements have been coded by the MadGraph/HELAS [61, 63] package. The phase-space generation is based on a multi-channel self-optimising approach using the modified Kajantie-Byckling [64] formalism for phase space construction in combination with a modified ac-Vegas [65] algorithm. AcerMC also provides interfaces to the parton shower and hadronisation phases of PYTHIA and HERWIG.

The ALPGEN Monte Carlo [54] relies on the alpha algorithm [66, 67]. This formalism is based on the Schwinger-Dyson method to recursively define one-particle off-shell Green's functions, which are then numerically evaluated through a specific representation of their ingredients. This approach significantly reduces the factorial growth of the number of terms to be calculated with the number of final state particles, and can efficiently deal with a large number of partons in the final state. In ALPGEN a huge number of processes at hadron colliders is implemented ready to use, the amplitudes are supplemented with suitable, predefined phase space mappings. An interface to HERWIG provides the possibility to evolve the parton level final state though parton shower and hadronisation phase. In this combination it is often used in experimental analyses.

A different approach is followed by CompHEP [55]. It relies on the traditional method of constructing and summing Feynman diagrams, where completeness relations are used to square the total amplitude. The integration is achieved through one phase space mapping selected by the user in combination with a Vegas algorithm. This algorithm clearly constrains the range of applicability of this code. However, a nice feature of CompHEP is a graphical interface, which provides complete control over each step of the cross section evaluation.

The program GRACE [56] is another system for the automatic evaluation of Feynman amplitudes. In its extension GR@PPA [57] it can also be used for the calculation of cross sections in hadron-hadron collisions.

On the other hand, HELAC/PHEGAS [58] again employs a Dyson-Schwinger approach, very similar to the alpha algorithm [68], together with a specific colour treatment [69]. For efficient phase space integration all possible kinematical mappings are constructed, dictated

by the amplitude under consideration. The new program JetI adds an improved flavour handling mechanism to the HELAC/PHEGAS package, extending the scope of application to hadron-hadron collisions.

In the package O'Mega/Whizard, O'Mega [59] provides the matrix elements. It also relies on a version of the alpha algorithm. However, in its present version, full QCD has not yet been implemented. The integration of the resulting matrix elements is achieved through Whizard [60], which automatically constructs phase-space mappings and integrates them with the VAMP-algorithm [70] based on Vegas. In fact, Whizard can also be interfaced with other matrix element generators and it can be used to generate unweighted, single events.

MadGraph/MadEvent generates all Feynman diagrams for a process under consideration and employs the method of helicity amplitudes through the HELAS library [63] for their evaluation. The phase space integration is achieved through a single-diagram enhanced mapping [62], which is a new, improved version of the adaptive multichannel method. In this new method, each diagram gives rise to one parametrisation of the phase space, decoupled from all others (in contrast to the original version of the method); their interplay is steered dynamically in order to minimise the overall variance.

In the SHERPA framework the program AMEGIC++ is responsible for the evaluation of matrix elements. It is the topic of the subsequent section.

2.1 The matrix element generator AMEGIC++

AMEGIC++, acronym for A Matrix Element Generator In C++, is a multi-purpose parton-level generator written in C++. It provides a convenient tool for the calculation of cross sections for scattering processes at the tree level in the framework of the SM and the MSSM. Recently the code was extended to cover processes in the ADD model of large extra dimensions as well [25]. The program can also be used to generate single events and it is one of the modules for the new complete event simulation framework SHERPA [1]. As such, the single events of AMEGIC++ can be handed over to the parton shower module APACIC++ [20,26] with the help of a new method that is correct at the next-to-leading logarithmic accuracy [14]. This translates into single parton-level events generated by AMEGIC++ to be correctly linked to fragmentation.

In AMEGIC++, full sets of Feynman diagrams are constructed automatically and are translated by the program into helicity amplitudes in a formalism similar to the one in [34]. A number of refinements of the helicity method has been implemented within the code as well. First of all, the algorithm presented in [71] fixes the relative signs of amplitudes when Majorana fermions are present. Furthermore, the algorithm has be extended to the treatment of spin-2 particles [25]. In addition explicit polarisations for massive or massless external spin-1 bosons are enabled, allowing the consideration of polarised cross sections. Similar considerations help to replace numerators of spin-1 propagators by summing over suitably defined polarisations for off-shell particles disentangling nested Lorentz structures emerging for amplitudes with many internal spin-1 bosons. As a result, AMEGIC++ needs only quite a limited set of building blocks to construct all helicity amplitudes. Internally, they are represented as word strings, which after some manipulation are stored in C++ library files. For QCD processes the algorithm becomes more complex, since a matrix of colour factors has to be evaluated. Therefore, the colour structure of each diagram, represented as a word string, has to be combined with the complex conjugated colour structure of all other dia-

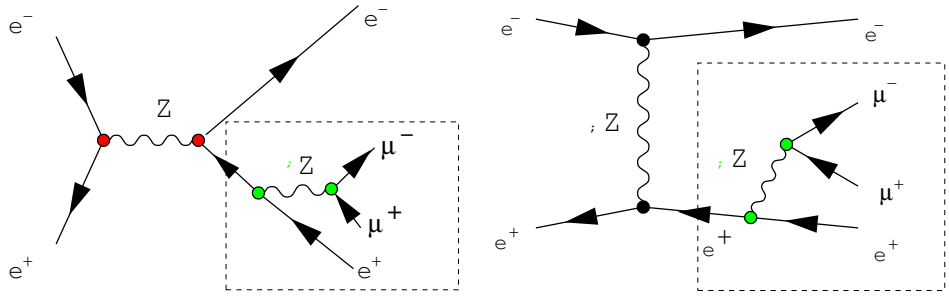

Figure 2.1: Factoring out common pieces of amplitudes with identical colour structure. In the example above, the parts within the boxes are identical, hence the two amplitudes can be added and the terms inside the box can be factored out.

grams and evaluated using the ordinary $SU(3)$ algebra. In order to minimise the size of the colour matrix, i.e. to reduce the number of complex multiplications in the cross section calculation, all diagrams are grouped into sets of amplitudes with identical, common colour structure. An additional speed-up is gained by means of some technical tricks. Firstly, a lookup table with all basic building blocks ensures that each building block is evaluated only once for each call of the full matrix element. Secondly, a number of routines performs algebraic manipulations on the word strings representing the helicity amplitudes, in order to simplify the expressions further. The general idea is to minimise the number of complex multiplications, an illustrative example is shown in Fig. 2.1. Details of these manipulations go beyond the scope of this thesis, however, the achieved increase of performance is substantial; as a result `AMEGIC++` is enabled to calculate processes with up to six-particles in the final state, as demonstrated in following sections.

There are a number of prescriptions to treat unstable particles. At the moment, `AMEGIC++` supports the *fixed-width scheme* (FWS) and the *complex-mass scheme* (CMS).
In the *fixed-width scheme*, the electroweak mixing angle is defined according to

$$\sin^2\theta_W = 1 - \frac{m_W^2}{m_Z^2}\,, \tag{2.1}$$

and it is kept real.
Defining the *complex-mass parameters* of the electroweak gauge bosons, the Higgs boson and the top quark in terms of the real masses and the constant (physical) widths through

$$\begin{aligned} M_V^2 &= m_V^2 - i\Gamma_V\, m_V\,, \quad V = W, Z \\ M_H^2 &= m_H^2 - i\Gamma_H\, m_H\,, \quad M_t = m_t - i\Gamma_t/2\,, \end{aligned} \tag{2.2}$$

the corresponding propagators can be written as

$$\begin{aligned} D_F^{\mu\nu}(q) &= \frac{-g^{\mu\nu} + q^\mu q^\nu / M_V^2}{q^2 - M_V^2}\,, \quad D_F(q) = \frac{1}{q^2 - M_H^2}\,, \\ S_F(q) &= \frac{\not{q} + M_t}{q^2 - M_t^2}\,. \end{aligned} \tag{2.3}$$

This time, in

$$\sin^2\theta_W = 1 - \frac{M_W^2}{M_Z^2}\,, \tag{2.4}$$

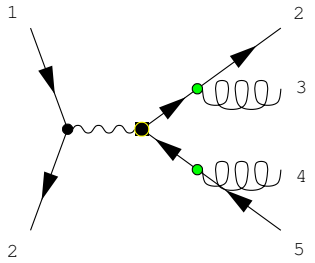

$$D_s(23,45) \times D_a(2,3) \times D_a(5,4) \times P_0(23) \times P_0(45)$$

Figure 2.2: Translation of a Feynman diagram into a phase-space parametrisation. The $D_{s,a}$ denote symmetric or asymmetric decays; the latter ones reproduce the typical feature of collinear emission which is typical for gauge theories with massless spin-1 bosons. The propagator terms for massless particles P_0 peak at the minimal allowed invariant mass.

the real gauge-boson masses are replaced by their complex counterparts yielding therefore a complex $\sin^2\theta_W$.

Within AMEGIC++ the Yukawa couplings of fermions to the Higgs boson and their kinematical masses are decoupled, which is an allowed choice when leading order accuracy is aimed at. This decoupling, however, allows to study, for example, the production of Higgs bosons and their decay into b-quarks, even in those cases where the user prefers to neglect the influence of the b-mass on both the phase space and the helicity structure.

For the integration over the phase space of the outgoing particles, AMEGIC++ employs an adaptive multichannel method [40]. Similar to the implementation of helicity amplitudes building blocks, generic elements for phase-space mappings such as propagator-like structures are provided. The individual Feynman diagrams are analysed individually and one or more suitable phase-space parametrisations for each diagram are automatically created and stored in library files. As an example, consider Fig. 2.2, which exhibits a diagram and its translation into propagator- and decay-parametrisations. These files, both for the amplitudes and the phase-space parametrisations, are compiled and linked to the code before the actual integration starts.

For users of AMEGIC++ only very little intervention is needed. Having specified the process(es), the model framework and its parameters, a first "initialisation" run of the code results in the creation of library files. After their compilation, a second, "production" run will generate the results without any further manipulation.

2.2 Results

In the following two sections, parton level cross sections as determined with the matrix calculator AMEGIC++ are compared with those of other Monte Carlo tools: First, a number of processes in e^+e^- collisions at a future linear collider (NLC) are considered, all of which are characterised by six final state particles. This illustrates the performance of the final state integration. In the subsequent section the focus will shift to the LHC. There, the results for a vast number of multi-jet cross sections, obtained in a comparison of six parton level Monte Carlo programs, are presented.

2.2.1 Cross sections for the NLC

In this section total cross sections for signals and backgrounds of top- and Higgs-production channels in e^+e^- collisions at a future linear collider are presented. In all channels under consideration, six-particle final states emerge. The calculation takes into account the full set of tree-level amplitudes in each process. Two multi-purpose parton level generators, `HELAC/PHEGAS` [58, 68] and `AMEGIC++` [23] are used. Similar to the comparison of four-fermion generators at the LEP2 Monte Carlo Workshop [72], a detailed study and mutual benchmarking of tools for six- and eight-particle final states at a future linear collider has been initiated in the framework of the extended ECFA/DESY study [73]. A first step into this direction has been reported in [36], the major results will be repeated here.

For the case of only massless final state particles, a similar comparison between the programs `LUSIFER` and `MadGraph`, the latter using `Whizard` for the phase-space integration has been presented in [48]. In addition, results achieved by different generators for selected top quark pair production channels in the massless fermion approximation can be found in [74].

Six-particle final states constitute the signature for many processes that will be studied at the precision level at a future e^+e^- linear collider. Important channels include the production and decay of top quark pairs and – if existent – of one or more Higgs bosons, the latter process allowing a test of the structure of the Higgs potential. Furthermore, if no evidence for a Higgs boson was found at the LHC, the study of quartic gauge boson couplings is mandatory in order to understand alternative scenarios of electroweak symmetry breaking. Leaving the framework of the Standard Model (SM) the production of, say, chargino pairs in the Minimal Supersymmetric Standard Model (MSSM) will lead to six-particle final states as well. This process has been studied recently in [75], using `AMEGIC++`. To understand these processes at the precision level, i.e. at the per cent level, it is mandatory to supplement typical approaches such as the narrow-width approximation, with corresponding calculations through full amplitudes, and to quantify the effect of non-resonant contributions. Obviously, for hadronic final states, a full QCD calculation is unavoidable.

Input parameters and phase-space cuts

The SM parameters are given in the G_μ scheme:

$$\begin{aligned}
&m_W = 80.419\ \text{GeV}\,, \quad \Gamma_W = 2.12\ \text{GeV},\\
&m_Z = 91.1882\ \text{GeV}\,, \quad \Gamma_Z = 2.4952\ \text{GeV},\\
&G_\mu = 1.16639 \times 10^{-5}\ \text{GeV}^{-2},\\
&\sin^2\theta_W = 1 - m_W^2/m_Z^2,\\
&\alpha_s = 0.0925(0.0891)\ \text{ at } 360(500)\ \text{GeV}.
\end{aligned} \tag{2.5}$$

The electromagnetic coupling is derived from the Fermi constant G_μ through

$$\alpha_{\text{em}} = \frac{\sqrt{2}\, G_\mu\, M_W^2\, \sin^2\theta_W}{\pi}. \tag{2.6}$$

The mass of the Higgs boson is assumed to be $m_H = 130$ GeV and its associated SM tree-level width is $\Gamma_H = 0.00429$ GeV. For this Higgs boson mass its branching ratios $H \to b\,\bar{b}$ and $H \to W^+\,W^- \to 4f$ are of the same order and therefore both decay channels signify

the occurrence of the Higgs boson as an intermediate state. For the massive fermions, the following masses have been used:

$$\begin{aligned}
&m_\mu = 105.6583 \text{ MeV}, \quad m_\tau = 1.777 \text{ GeV}, \\
&m_u = 5 \text{ MeV}, \quad m_d = 10 \text{ MeV}, \\
&m_s = 200 \text{ MeV}, \quad m_c = 1.3 \text{ GeV}, \\
&m_b = 4.8 \text{ GeV}, \\
&m_t = 174.3 \text{ GeV}, \quad \Gamma_t = 1.6 \text{ GeV}.
\end{aligned} \tag{2.7}$$

The constant widths of the electroweak gauge bosons, the Higgs boson and the top quark are treated through the *fixed-width scheme* (FWS) as defined in Sect. 2.1. CKM mixing of the quark generations and the coupling of the Higgs boson to the very light fermion flavours (e, u, d) is neglected, otherwise the Yukawa couplings are assumed to be given by the actual masses of the fermion in question.
Concerning the phase-space integration, the following cuts on the external particles are applied:

$$\begin{aligned}
&\theta(l, \text{beam}) > 5^\circ \,, \quad \theta(l, l') > 5^\circ \,, \quad E_l > 10 \text{ GeV}, \\
&\theta(q, \text{beam}) > 5^\circ \,, \quad \theta(l, q) > 5^\circ \,, \quad E_q > 10 \text{ GeV}, \\
&m(q, q') > 10 \text{ GeV} \,,
\end{aligned} \tag{2.8}$$

where $\theta(i, j)$ specifies the angle between the particles i and j in the centre-of-mass frame, and l, q and beam denote charged leptons, quarks or gluons and the beam electrons or positrons, respectively. The invariant mass of a jet pair qq' is denoted by $m(q, q')$.
All results presented here are obtained using 10^6 points (before cuts); statistical errors of the Monte Carlo integrations, i.e. one standard deviation, are given in parentheses.

Numerical results

First of all, processes have been considered that serve as signals or backgrounds for the production and decay of top pairs, Table 2.1. Since the branching ratio for the decay of top quarks into bottom quarks and a W ($t \to bW^+$, $\bar{t} \to \bar{b}W^-$) is practically 100% , all modes considered include a pair of bottom quarks. In cases involving a mixture of top production and decay and pure QCD diagrams, the relative importance of the different contributions to the total cross section has been estimated by switching on and off the QCD coupling constant. In both cases (the fully hadronic mode $b\bar{b}u\bar{u}d\bar{d}$ and the semi-leptonic mode $b\bar{b}u\bar{d}e^-\bar{\nu}_e$) the top contribution is by far the dominating channel; the difference of taking into account the QCD contributions or neglecting them is of the order of 2-3%. Also, the total cross section of the fully hadronic channel is substantially larger than the cross section of any other individual $b\bar{b}$+4 jets mode.

For the QCD contributions, a similar pattern arises also in the vector-boson fusion channels, cf. Tables 2.2 and 2.3. These channels are characterised by either an electron-positron (e^-e^+) or an electron-neutrino anti-neutrino ($\nu_e\bar{\nu}_e$) pair in the final state, corresponding to either Z boson or to W boson fusion processes, respectively. Again, switching on and off the QCD coupling constant gives rise to differences on the level of a few per cent. In contrast, taking into account the Higgs boson (Table 2.2) which may be produced in the s-channel through the fusion of two t-channel vector bosons, or neglecting it (Table 2.3) changes the

Top quark channels

Final state	**QCD**	AMEGIC++ [fb]	HELAC [fb]
$b\bar{b}u\bar{d}d\bar{u}$	yes	32.90(15)	33.05(14)
	yes	49.74(21)	50.20(13)
	no	32.22(34)	32.12(19)
	no	49.42(44)	50.55(26)
$b\bar{b}u\bar{u}gg$	–	11.23(10)	11.136(41)
	–	9.11(13)	8.832(43)
$b\bar{b}gggg$	–	18.82(13)	18.79(11)
	–	24.09(18)	23.80(17)
$b\bar{b}u\bar{d}e^-\bar{\nu}_e$	yes	11.460(36)	11.488(15)
	yes	17.486(66)	17.492(41)
	no	11.312(37)	11.394(18)
	no	17.366(68)	17.353(31)
$b\bar{b}e^+\nu_e e^-\bar{\nu}_e$	–	3.902(31)	3.885(7)
	–	5.954(55)	5.963(11)
$b\bar{b}e^+\nu_e\mu^-\bar{\nu}_\mu$	–	3.847(15)	3.848(7)
	–	5.865(24)	5.868(10)
$b\bar{b}\mu^+\nu_\mu\mu^-\bar{\nu}_\mu$	–	3.808(16)	3.861(19)
	–	5.840(30)	5.839(12)

Table 2.1: The cross sections for possible signals and backgrounds of top quark pair production in e^+e^- annihilation. All results in fb for $\sqrt{s} = 360$ GeV (first row) and $\sqrt{s} = 500$ GeV (second row).

total cross sections for all channels considered by a factor of 2 or larger. This is especially pronounced for channels that can be identified as WW-fusion channels with a semi-leptonic or fully hadronic decay of the W-pair produced by the Higgs decay (i.e. $\nu_e\bar{\nu}_e u\bar{d}e^-\bar{\nu}_e$ and $\nu_e\bar{\nu}_e u\bar{d}\mu^-\bar{\nu}_\mu$, or $\nu_e\bar{\nu}_e u\bar{d}d\bar{u}$, respectively), where the cross sections are larger by one order of magnitude.

Another mode for Higgs production at an electron-positron collider is Higgs-strahlung, where the Higgs boson is radiated off a Z-boson in the s-channel. In Table 2.4, total cross sections for such modes are displayed, where the Z boson decays into muons and the Higgs boson goes into four fermions through a pair of W or Z bosons. In Table 2.5, identical total cross sections for the same final states, but neglecting the Higgs contribution, are shown. In both cases, again, the size of the pure QCD contributions is found to be small for most final states, i.e. of the order of few per cent. The only exception is for a pair of muons and four identical quarks; there, the inclusion of QCD changes the results by roughly 20%, when the Higgs boson is taken into account, and by a factor of roughly 2 when its contribution is neglected. It is interesting to note that this relative factor of two compares in size with the effect of including the Higgs boson itself. This, however, is true only for the mode that can be imagined as $e^+e^- \to ZH \to ZZZ \to \mu^+\mu^- u\bar{u}u\bar{u}$. In all other cases, as said before,

Vector fusion with Higgs exchange

Final state	**QCD**	AMEGIC++ [fb]	HELAC [fb]
$e^-e^+u\bar{u}d\bar{d}$	yes	0.6842(85)	0.6858(31)
	yes	1.237(15)	1.265(5)
	no	0.6453(62)	0.6527(35)
	no	1.206(14)	1.2394(75)
$e^-e^+u\bar{u}e^-e^+$	–	6.06(36)e-03	6.113(87)e-03
	–	6.58(23)e-03	6.614(80)e-03
$e^-e^+u\bar{u}\mu^-\mu^+$	–	9.24(12)e-03	9.04(11)e-03
	–	9.25(17)e-03	9.145(74)e-03
$\nu_e\bar{\nu}_e u\bar{d}d\bar{u}$	yes	1.15(3)	1.176(6)
	yes	2.36(7)	2.432(12)
	no	1.14(3)	1.134(5)
	no	2.35(7)	2.429(13)
$\nu_e\bar{\nu}_e u\bar{d}e^-\bar{\nu}_e$	–	0.426(11)	0.4309(48)
	–	0.916(30)	0.9121(48)
$\nu_e\bar{\nu}_e u\bar{d}\mu^-\bar{\nu}_\mu$	–	0.425(12)	0.4221(30)
	–	0.878(27)	0.8888(47)

Table 2.2: The cross sections for different $e^+e^- \to 6f$ final states corresponding to the Higgs production through the vector-boson fusion signal. All results are in fb for $\sqrt{s} = 360$ GeV (first row) and $\sqrt{s} = 500$ GeV (second row).

inclusion of QCD has minor effects only; the Higgs boson in contrast roughly doubles the total cross section in all other channels.

One of the salient research goals at a potential linear collider operating at energies around 500 GeV is the determination of the Higgs potential. For this, the self-couplings of the Higgs bosons have to be checked. In the framework of this thesis, results are provided for the channel where the Higgs bosons emerge in Higgs-strahlungs-like topologies and decay into a pair of bottom quarks. This leads to final states $\mu^+\mu^- + 4b$, where the muons mainly come from the Z bosons. Results for total cross sections for the process $e^+e^- \to \mu^+\mu^- + 4b$, where contributions mediated by Higgs bosons have been included or neglected, are given in Tables 2.6 and 2.7, respectively. From the results displayed one can read off that the inclusion of intermediate Higgs bosons enhances the cross sections by a factor of three to four. Again, also the effect of QCD has been checked. For the process involving the intermediate Higgs bosons, QCD leads to total cross sections that are larger by roughly 30%-40%, without the Higgs bosons, QCD contributes on the level of factors of two to three.

To give a qualitative overview over the obtained results, the deviation $s^{(i)}$ of the two resulting cross sections $\sigma_{\mathrm{H}}^{(i)}$ and $\sigma_{\mathrm{A}}^{(i)}$ for each process i has been calculated through

$$s^{(i)} = \frac{\sigma_{\mathrm{A}}^{(i)} - \sigma_{\mathrm{H}}^{(i)}}{\sqrt{\left(\Delta\sigma_{\mathrm{A}}^{(i)}\right)^2 + \left(\Delta\sigma_{\mathrm{H}}^{(i)}\right)^2}}\,. \tag{2.9}$$

Vector fusion without Higgs exchange

Final state	**QCD**	AMEGIC++ [fb]	HELAC [fb]
$e^-e^+u\bar{u}d\bar{d}$	yes	0.4838(50)	0.4842(25)
	yes	1.0514(97)	1.0445(51)
	no	0.4502(31)	0.4524(23)
	no	1.0239(79)	1.0227(43)
$e^-e^+u\bar{u}e^-e^+$	–	3.757(98)e-03	3.577(43)e-03
	–	4.082(56)e-03	4.214(46)e-03
$e^-e^+u\bar{u}\mu^-\mu^+$	–	5.201(61)e-03	5.119(70)e-03
	–	5.805(67)e-03	5.828(49)e-03
$\nu_e\bar{\nu}_e u\bar{d}d\bar{u}$	yes	0.15007(53)	0.15070(64)
	yes	0.4755(21)	0.4711(24)
	no	0.12828(42)	0.12793(55)
	no	0.4417(19)	0.4398(21)
$\nu_e\bar{\nu}_e u\bar{d}e^-\bar{\nu}_e$	–	0.04546(13)	0.04564(19)
	–	0.16033(63)	0.16011(78)
$\nu_e\bar{\nu}_e u\bar{d}\mu^-\bar{\nu}_\mu$	–	0.04230(12)	0.04180(16)
	–	0.14383(53)	0.14439(65)

Table 2.3: The backgrounds to Higgs production through vector boson fusion. All contributions from intermediate Higgs bosons are neglected. Cross sections are given in fb for $\sqrt{s} = 360$ GeV (first row) and $\sqrt{s} = 500$ GeV (second row).

The distribution of the individual differences is depicted in Fig. 2.3. The average deviation is $\bar{s} = -0.065$, the variance in their distribution is $\sigma_s \approx 1$. The maximal difference between two cross sections is smaller than three standard deviations, $s^{(\text{max.})} \approx 2.6$. The distribution of differences follows roughly a Gaussian distribution. Taken together this translates into both codes being independent (as they should be) and yielding statistically identical results.

Higgs production through Higgs-strahlung

Final state	**QCD**	AMEGIC++ [fb]	HELAC [fb]
$\mu^-\mu^+\mu^-\bar{\nu}_\mu e^-\bar{\nu}_e$	–	0.03244(27)	0.03210(15)
	–	0.03747(29)	0.03749(32)
$\mu^-\mu^+ u\bar{d}e^-\bar{\nu}_e$	–	0.0924(8)	0.09306(46)
	–	0.1106(22)	0.10901(66)
$\mu^-\mu^+\mu^-\mu^+e^-e^+$	–	2.828(67)e-03	2.923(52)e-03
	–	2.731(65)e-03	2.691(42)e-03
$\mu^-\mu^+u\bar{u}d\bar{d}$	yes	0.2534(24)	0.2540(16)
	yes	0.2634(22)	0.2642(15)
	no	0.2441(23)	0.2471(15)
	no	0.2593(22)	0.2589(14)
$\mu^-\mu^+u\bar{u}u\bar{u}$	yes	1.125(8)e-02	1.135(22)e-02
	yes	8.767(65)e-03	8.978(58)e-03
	no	7.929(57)e-03	8.078(92)e-03
	no	6.098(35)e-03	6.013(26)e-03

Table 2.4: The cross sections for different $e^+\,e^- \to 6f$ final states corresponding to the Higgs-strahlung signal. All results are given in fb for $\sqrt{s} = 360$ GeV (first row) and $\sqrt{s} = 500$ GeV (second row).

Backgrounds to Higgs-strahlung

Final state	**QCD**	AMEGIC++ [fb]	HELAC [fb]
$\mu^-\mu^+\mu^-\bar{\nu}_\mu e^-\bar{\nu}_e$	–	0.01845(14)	0.01843(13)
	–	0.03054(23)	0.03092(19)
$\mu^-\mu^+ u\bar{d}e^-\bar{\nu}_e$	–	0.05284(57)	0.05209(33)
	–	0.08911(53)	0.08925(48)
$\mu^-\mu^+\mu^-\mu^+e^-e^+$	–	2.204(52)e-03	2.346(49)e-03
	–	2.280(66)e-03	2.277(62)e-03
$\mu^-\mu^+u\bar{u}d\bar{d}$	yes	0.1412(10)	0.1404(11)
	yes	0.2092(12)	0.2075(13)
	no	0.1358(20)	0.1341(12)
	no	0.2040(12)	0.2015(11)
$\mu^-\mu^+u\bar{u}u\bar{u}$	yes	5.937(24)e-03	5.937(25)e-03
	yes	6.134(29)e-03	6.108(27)e-03
	no	2.722(10)e-03	2.710(11)e-03
	no	3.290(12)e-03	3.303(12)e-03

Table 2.5: Background contributions to the Higgs-strahlungs signal for various $6f$ final states. All diagrams with intermediate Higgs bosons have been neglected. Cross sections are given in fb for $\sqrt{s} = 360$ GeV (first row) and $\sqrt{s} = 500$ GeV (second row).

Triple Higgs coupling

Final state	**QCD**	AMEGIC++ [fb]	HELAC [fb]
$\mu^-\mu^+b\bar{b}b\bar{b}$	yes	2.560(26)e-02	2.583(26)e-02
	yes	3.096(60)e-02	3.019(43)e-02
	no	1.711(55)e-02	1.666(28)e-02
	no	2.34(12)e-02	2.36(10)e-02

Table 2.6: Cross sections for the process $e^+\,e^- \to \mu^-\mu^+b\bar{b}b\bar{b}$. All results are in fb, for $\sqrt{s} = 360$ GeV (first row) and $\sqrt{s} = 500$ GeV (second row).

Backgrounds to triple Higgs coupling

Final state	**QCD**	AMEGIC++ [fb]	HELAC [fb]
$\mu^-\mu^+b\bar{b}b\bar{b}$	yes	7.002(32)e-03	7.044(22)e-03
	yes	6.308(24)e-03	6.364(21)e-03
	no	2.955(11)e-03	2.972(12)e-03
	no	3.704(15)e-03	3.695(13)e-03

Table 2.7: Cross sections for $e^+\,e^- \to \mu^-\mu^+b\bar{b}b\bar{b}$ with all contributions due to intermediate Higgs bosons left out. All results are in fb, taken for $\sqrt{s} = 360$ GeV (first row) and $\sqrt{s} = 500$ GeV (second row).

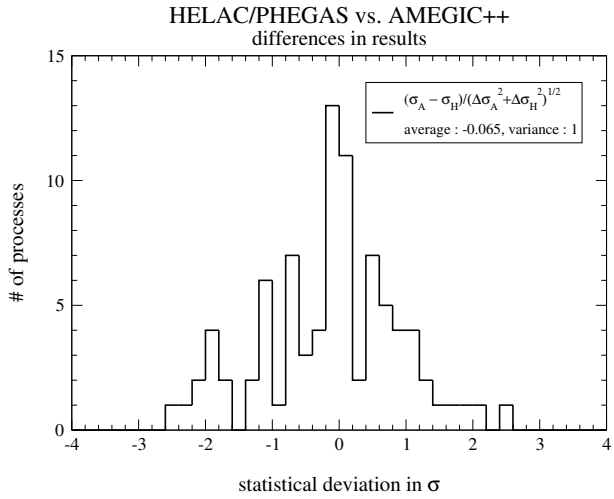

Figure 2.3: The distribution of deviations $s^{(i)}$, given by Eq.2.9, for the eighty-six total cross sections i presented in [36]. The average value is $\bar{s} = -0.065$, their variance is $\sigma_s \approx 1$.

2.2.2 Matrix elements for the LHC

In this section the focus will shift to the LHC. There, new physics phenomena are expected to be observed, many of them will be characterised by the emergence of a vast number of high energy jets. As an example, consider the cascades of decays of heavy squarks or gluinos. The understanding of standard model backgrounds to these multi-jet processes is of special importance, and an accurate description of these multi-jet final states renders exact matrix element calculations, at least at tree-level, unavoidable. In order to validate the reliability of such parton level predictions, a comparison of QCD Monte Carlo tools has been initiated at the MC4LHC workshop 2003. So far six general-purpose programs have participated: `ALPGEN` [54], `CompHEP` [55], `GRACE/GR@PPA` [56, 57], `HELAC/PHEGAS/JetI` [58], `MadGraph/MadEvent` [61, 62], and `AMEGIC++` [23]. All of these programs are capable of calculating matrix elements at the tree-level for a huge number of processes. The processes considered in this study include the production of electroweak gauge bosons, signals and backgrounds to Higgs and top production, and heavy quark production. This enterprise is still an ongoing project, here a brief status report will be given.

Input parameters and phase-space cuts

In the context of the MC4LHC comparison, the following parameters have been used.
The SM parameters are given in the G_μ scheme:

$$\begin{aligned}
&m_W = 80.419\ \text{GeV}\,, \quad \Gamma_W = 2.048\ \text{GeV},\\
&m_Z = 91.1882\ \text{GeV}\,, \quad \Gamma_Z = 2.446\ \text{GeV},\\
&G_\mu = 1.16639 \times 10^{-5}\ \text{GeV}^{-2},\\
&\sin^2\theta_W = 1 - m_W^2/m_Z^2,\\
&\alpha_s = 0.130.
\end{aligned} \tag{2.10}$$

The PDF set used for all calculations is CTEQ6L1, for the factorisation scale a fixed value of $\mu_F = M_Z$. The electromagnetic coupling is derived from the Fermi constant G_μ according to Eq. (2.6). The mass of the Higgs boson is assumed to be $m_H = 120$ GeV and its SM width is fixed to $\Gamma_H = 3.7 \cdot 10^{-3}$ GeV. For the massive fermions, the following masses and widths have been used:

$$\begin{aligned}
&m_\tau = 1.777\ \text{GeV}, \quad \Gamma_\tau = 2.36 \cdot 10^{-12}\ \text{GeV}.\\
&m_b = 4.7\ \text{GeV},\\
&m_t = 174.3\ \text{GeV}, \quad \Gamma_t = 1.508\ \text{GeV}.
\end{aligned} \tag{2.11}$$

The Yukawa couplings are directly calculated from the values above. The couplings of the Higgs boson to the light fermion flavours are neglected.
The constant widths of the electroweak gauge bosons, the Higgs boson and the top quark are treated in the *fixed-width scheme* (FWS). CKM mixing of the first and second quark generation is included with CKM-elements given by

$$\begin{aligned}
&V_{ud} = V_{cs} = 0.975\\
&V_{us} = V_{cd} = \sqrt{1 - V_{ud}^2}\,.
\end{aligned} \tag{2.12}$$

The mixing with the third quark generation is neglected.

In the phase-space integration cuts on transverse momentum p^T, pseudo-rapidity η and the cone distance ΔR have been applied on all final state particles with the exception of massive particles with $m_i > 3$ GeV and neutrinos, whose phase space remains unconstrained. The cuts read, in particular:

$$\begin{aligned} & p_i^T > 20 \text{ GeV}, \\ & |\eta_i| < 2.5 \\ & \Delta R_{ij} = \sqrt{\Delta\phi^2 + \Delta\eta^2} > 0.4 \,, \end{aligned} \tag{2.13}$$

Statistical errors of the Monte Carlo integrations, i.e. one standard deviation, are given in parentheses.

Numerical results

X-sects (pb)	$e^-\bar{\nu}_e + n$ QCD jets						
Number of jets	0	1	2	3	4	5	6
ALPGEN	3904(6)	1013(2)	364(2)	136(1)	53.6(6)	21.6(2)	8.7(1)
AMEGIC++	3908(3)	1011(2)	362.3(9)	137.5(5)	54(1)		
CompHEP	3947.4(3)	1022.4(5)	364.4(4)				
GR@PPA	3905(5)	1013(1)	361.0(7)	133.8(3)	53.8(1)		
JetI	3786(81)	1021(8)	361(4)	157(1)	46(1)		
MadEvent	3902(5)	1012(2)	361(1)	135.5(3)	53.6(2)		

Table 2.8: Cross sections for the process $e^-\bar{\nu}_e + n$ jets at the LHC. All results are in pb.

X-sects (pb)	$e^+\nu_e + n$ QCD jets						
Number of jets	0	1	2	3	4	5	6
ALPGEN	5423(9)	1291(13)	465(2)	182.8(8)	75.7(8)	32.5(2)	13.9(2)
AMEGIC++	5432(5)	1277(2)	466(2)	184(1)	77.3(4)		
CompHEP	5485.8(6)	1287.5(7)	467.3(8)				
GR@PPA	5434(7)	1273 (2)	467.7(9)	181.8(5)	76.6(3)		
JetI	5349(143)	1275(12)	487(3)	212(2)			
MadEvent	5433(8)	1277(2)	464(1)	182(1)	75.9(3)		

Table 2.9: Cross sections for the process $e^+\nu_e + n$ jets at the LHC. All results are in pb.

The first processes considered here are the production of electroweak gauge bosons. In Tables 2.9 and 2.8 the cross sections for the production of positively and negatively charged W bosons accompanied by the production of up to 6 jets are presented[1]. The achieved precision of AMEGIC++ and the other codes is on the sub-per cent level. Note that the cross sections for $pp \to W^+ + X$ are approximately 35% larger than the corresponding cross sections for $pp \to W^- + X$. This is in contrast to the Tevatron, where proton anti-proton collisions are performed, such that the charge does not matter for the production cross

[1] AMEGIC++ is able to calculate the cross section for the production of gauge bosons with up to four extra jets.

X-sects (pb)	$e^-e^+ + n$ QCD jets						
Number of jets	0	1	2	3	4	5	6
ALPGEN	723.4(9)	188.3(3)	69.9(3)	27.2(1)	10.95(5)	4.6(1)	1.85(1)
AMEGIC++	723.1(7)	188.2(3)	69.7(2)	27.3(1)	11.1(1)		
CompHEP	730.9(1)	190.20(7)	70.22(7)				
GR@PPA	724.2(8)	188.4(3)	69.62(8)	26.68(5)	11.02(3)		
JetI	744(7)	187(1)	70.9(4)	28.2(4)			
MadEvent	723(1)	188.6(4)	69.3(1)	27.1(2)	10.6(1)		

Table 2.10: Cross sections for the process $e^-e^+ + n$ jets at the LHC. All results are in pb.

X-sects (pb)	$\nu_e\bar{\nu}_e + n$ QCD jets						
Number of jets	0	1	2	3	4	5	6
ALPGEN	3271(1)	717.4(5)	267.4(4)	105.4(2)	43.7(2)	18.68(8)	7.88(5)
AMEGIC++	3272(3)	716(1)	268.0(6)	105.6(5)	44.3(5)		
CompHEP	3304.7(4)	723.8(4)	268.5(3)				
GR@PPA	3260(1)	715.8(9)	267.1(3)	103.4(3)	43.5(1)		
JetI	3338(42)	710(6)	269(1)	84.6(10)			
MadEvent	3278(4)	715(1)	266.4(4)	105(2)	42.9(3)		

Table 2.11: Cross sections for the process $\nu_e\bar{\nu}_e + n$ jets at the LHC. All results are in pb.

section. At the LHC, because there proton-proton collisions are considered, there is some sensitivity of the cross section on the charge of the W boson. There, each additional jet leads to a decrease of the cross section by a factor of roughly 1/3. The mutual agreement between the different generators is is very good, with the exception of CompHEP and JetI, where the difference is somewhat larger. A similar picture is drawn in Table 2.10, where the cross section for the production of an e^+e^--pair is shown. CompHEP seems to overestimate the cross section for low jet multiplicities, all other results are well within two standard deviations. For the leading order process the achieved precision is on the per mille level (only JetI, missing the final numbers, is slightly worse). Table 2.11, gives the cross section for the production of a neutrino anti-neutrino pair. In contrast to the production of an e^+e^-–pair, the neutrinos do not exhibit a photon coupling, therefore no cuts needs to be applied on them. Again the agreement is fairly good, only CompHEP claims surprisingly low respective errors on the cross section for $n_{\text{jet}} = 0$.

One possible production channel for a Higgs boson at the LHC is Higgs-strahlung. In Tables 2.12 and 2.13 corresponding cross sections have been summarised. It is interesting to note that the cross section for the process $e^-\bar{\nu}_e + b\bar{b}$ actually increases as soon as one additional jet is taken into account, signalling the appearance of a large NLO correction. Within the given error estimates the results are in reasonable agreement.

The jet production cross sections are listed in Table 2.14. They are 8-10 orders of magnitude larger than the cross sections for the other processes considered so far, which nicely underlines the importance of QCD radiation at the LHC. The mutual agreement between the different generators is excellent.

In Tables 2.15 and 2.16 the production of jets accompanied by one or two extra photons is considered. Each appearances of the QED coupling constant reduces the cross section

X-sects (pb)	$e^-\bar{\nu}_e + b\bar{b} + n$ QCD jets				
Number of jets	0	1	2	3	4
ALPGEN	9.34(4)	9.85(6)	6.82(6)	4.18(7)	2.39(5)
AMEGIC++	9.37(1)	9.86(2)	6.87(5)	4.31(6)	
CompHEP	9.415(5)	9.91(2)			
GR@PPA	9.31(1)	9.80(2)			
JetI	9.88(11)	12.68(9)			
MadEvent	9.32(3)	9.74(1)	6.80(2)		

Table 2.12: Cross sections for the process $e^-\bar{\nu}_e + b\bar{b} + n$ jets at the LHC. All results are in pb.

X-sects (pb)	$e^-e^+ + b\bar{b} + n$ QCD jets				
Number of jets	0	1	2	3	4
ALPGEN	18.95(8)	6.80(3)	2.97(2)	1.501(9)	0.78(1)
AMEGIC++	18.86(3)	6.78(2)	3.10(5)		
CompHEP	19.45(2)				
GR@PPA	18.70(2)	6.74(2)			
JetI	19.2(2)	7.0(2)			
MadEvent	18.7(1)	6.72(2)	2.96(1)		

Table 2.13: Cross sections for the process $e^-e^+ + b\bar{b} + n$ jets at the LHC. All results are in pb.

roughly by a factor 1/3000 compared to the pure QCD case above. The process $pp \to \gamma\gamma$ is of special importance, as one of the discovery channels for a light Higgs boson.

Finally, in Tables 2.17 and 2.18 the production of heavy quark pairs is investigated. The cross sections for the process $pp \to t\bar{t} + n$-jet exhibits only very slowly decrease with increasing numbers of jets. On the other hand, the bottom pair production cross section is already at leading order approximately 9 orders of magnitude larger than the top pair production cross section, signalling the dramatically different phase space in addition to the comparably low PDFs at large-x. Here the emission of one extra jet leads to a decrease in cross section of a factor of 1/50. The trend seen in other comparisons also continues here: for processes with at least one extra jet, all Monte Carlos agree perfectly. For the LO process, however, the CompHEP result is slightly larger.

2.3 Summary

The matrix element generator AMEGIC++ has been confronted with other Monte Carlo tools. In the comparison for e^+e^- collisions at a potential NLC, both packages, HELAC/PHEGAS as well as AMEGIC++, lead, with quite different methods, to consistent results for total cross sections for a large number of different processes with six particles in the final state. This provides an independent check of the correctness and the accuracy of the two codes, which can be considered as being successfully tested. For nearly all cross sections the resulting statistical error was significantly smaller than one per cent, roughly five per mille. There

X-sects (μb)	QCD jets				
Number of jets	2	3	4	5	6
ALPGEN	331.7(3)	22.49(7)	4.81(1)	1.176(9)	0.330(1)
AMEGIC++	330.9(3)	22.7(2)	5.0(1)		
CompHEP	338.8(1)	22.79(7)			
JetI	331(3)	22.6(3)	4.7(1)	0.9(1)	
MadEvent	329(1)	22.3(1)	4.86(2)		

Table 2.14: Cross sections for the n-jet production at the LHC. All results are in μb.

X-sects (nb)	$\gamma + n$ QCD jets			
Number of jets	1	2	3	4
AMEGIC++	89.1(2)	19.4(1)	7.55(8)	2.66(2)
CompHEP	90.33(9)	19.78(4)	7.44(3)	
JetI	91.0(6)	19.6(2)	7.5(1)	2.76(9)
MadEvent	89.0(1)	19.55(6)	7.43(2)	2.63(2)

Table 2.15: Cross sections for the process $\gamma + n$ jets at the LHC. All results are in nb.

have been no significant differences between the two codes.

In the framework of the MC4LHC setup, results for large number of important processes at the LHC, provided by six different matrix element calculators, have been investigated. The achieved precision generally lies on the per cent to per mille level. In particular, the mutual agreement between ALPGEN, AMEGIC++ and MadEvent is excellent. Only the CompHEP generator seems to yield a slightly too optimistic error estimate, which is due to the different error handling in Vegas; it also states the largest leading order cross section in most comparisons. The reasons for these deviations remain to be resolved. JetI, being the very recent extension of the existing package HELAC/PHEGAS to hadron-hadron collisions also performs reasonably well.

Summarising, AMEGIC++ successfully managed to calculate reliable predictions for some of the most interesting signal and background channels at a NLC as well as for the LHC.

X-sects (pb)	$\gamma\gamma + n$ QCD jets			
Number of jets	0	1	2	3
AMEGIC++	45.6(1)	25.3(1)	18.5(2)	9.7(1)
CompHEP	46.03(3)	25.76(5)	18.4(2)	
JetI	45.6(4)	25.2(3)	19.3(3)	9.43
MadEvent	45.5(1)	25.2(5)	18.40(4)	9.45(3)

Table 2.16: Cross sections for the process $\gamma\gamma + n$ jets at the LHC. All results are in pb.

X-sects (pb)	$t\bar{t} + n$ QCD jets						
Number of jets	0	1	2	3	4	5	6
ALPGEN	755.4(8)	748(2)	518(2)	310.9(8)	170.9(5)	87.6(3)	45.1(8)
AMEGIC++	754.0(8)	748.7(7)	519(1)	305(3)			
CompHEP	757.8(8)	752(1)	519(1)				
JetI	745(5)	711(7)	515(5)	24.2(5)			
MadEvent	754(2)	749(2)	516(1)	306(1)			

Table 2.17: Cross sections for the process $t\bar{t} + n$ jets at the LHC. All results are in pb.

X-sects (μb)	$b\bar{b} + n$ QCD jets						
Number of jets	0	1	2	3	4	5	6
ALPGEN	470.6(6)	8.83(1)	1.822(9)	0.459(2)	0.150(2)	0.053(1)	0.0215(8)
AMEGIC++	470.7(5)	8.84(2)	1.817(6)	0.460(3)			
CompHEP	476.0(5)	8.89(3)	1.829(6)				
JetI	465(5)	8.7(2)	1.85(4)	0.130(2)			
MadEvent	472(9)	8.81(2)	1.80(5)	0.441(2)			

Table 2.18: Cross sections for the process $b\bar{b} + n$ jets at the LHC. All results are in μb.

3 Parton Shower

In the framework of Monte Carlo event generators the parton shower provides the link between perturbatively calculable differential cross sections at the parton level and models for their transition to observable hadrons with phenomenological parameters, which need to be tuned to data. The inclusion of the parton shower does not only create more realistic high-multiplicity parton final states from low parton multiplicities available through corresponding exact matrix elements, it also reduces the average distance of the partons in momentum space down to a fixed size and thus ensures that the hadronisation parameter tunes are rather independent of the hard process in question. It is this aspect of the parton shower that renders it indispensable for a meaningful simulation with any predictive power. This can then be used in order to calculate hadronisation corrections or to judge detector effects in certain processes. In most cases, results from parton shower Monte Carlos have been in astonishing agreement with data, giving rise to the confidence that simulation tools can also be used to predict signals and backgrounds for the current and the next round of collider experiments.

Although, for more than two decades, parton showers have been widely used in multi-purpose event generators, details of their specific implementation traditionally depend on certain choices and, due to recent developments, on the specific form the hard matrix elements generate the initial parton configurations. Traditional multi-purpose event generators, like `PYTHIA` [2,76] or `HERWIG` [3,77] usually have a $2 \to 2$ process at leading order (LO) as the signal process. There, after defining the corresponding, process-dependent starting conditions for the shower, the latter is allowed to evolve freely. Only recently, this treatment has been consistently extended to next-to-leading order (NLO) precision for $2 \to 2$ processes in the `MC@NLO` framework [11, 12], which uses the machinery of `HERWIG`. There, the NLO calculation is modified in order to match the requirements imposed by the specific form of the parton shower. Another approach, going beyond $2 \to 2$ processes, has been taken in `SHERPA` [1]; there, a fully automated consistent merging of $2 \to n$ processes at the tree-level with the parton shower according to the formalism of [14, 15] has been implemented and tested [21][1]. For the merging with such multi-leg tree-level matrix elements, the parton shower has to be supplemented with the determination of more involved starting conditions and with additional constraints on the phase space of the emitted particles.

In this chapter the specific realisation and implementation of the parton shower in `SHERPA` will be presented. A first version of this module, `APACIC++`, `version 1.0`, has been published some time ago in [26]; it covered the parton shower in the final state only, including some algorithms for the merging with the matrix elements provided by `AMEGIC++` [23–25]. In

[1] A similar approach for the merging of matrix elements with the dipole cascade [78] has been taken in [79]; for some specific processes the formalism has been used to merge multi-jet matrix elements with `PYTHIA` and `HERWIG` [80]. A slightly different method [81] has been advocated by the authors of `ALPGEN` [54], who merge their matrix elements with the parton shower of `HERWIG`.

this first version, many of the steering and service classes were still located within APACIC++; in the mean time, APACIC++ transformed from a stand-alone code to a mere module of the full framework SHERPA. In its present state, version 2.0, which is discussed in the following, APACIC++ thus includes the parton shower in the initial and final state and an improved handling of algorithms necessary for the parton shower aspects of the merging procedure[2]. The outline of this chapter is as follows: After briefly reviewing the parton shower formalism in Sec. 3.1.1, the ideas underlying its particular implementation in APACIC++ will be discussed in Sec. 3.1.2. After a short discussion of the colour treatment, in Sec. 3.1.3, the focus will shift to those aspects, which are specific for the merging procedure with matrix elements, viz Sec. 3.1.4 and Sec. 3.1.5. In Sec. 3.2 exemplary results will be presented, which compare the parton shower results of APACIC++ with analytical approaches and with data. Details of the implementation, including a short description of the class structure of APACIC++ will be given in the appendix D.1.

3.1 APACIC++ – A PArton Cascade In C++

This section comprises a brief overview of the parton shower formalism and the corresponding algorithms implemented in APACIC++. There, the sequence of parton emissions in the shower evolution is organised by virtuality as the ordering parameter. In this respect, the algorithm presented here is closely related to the implementation in PYTHIA [82, 83][3]. However, the APACIC++ version differs in some details like the treatment of massive particles and particular scale choices for the evaluation of coupling constants and parton density functions (PDFs). In addition, it incorporates some unique features that facilitate the merging of matrix elements with the parton shower according to the formalism of [14, 15].

3.1.1 Basics of parton showering

The parton shower evolution relies on the fact that parton emission processes become singular in the soft or collinear limit. When the available phase space is cut accordingly, these singularities translate into large logarithms, which can be resummed according to the DGLAP evolution [86–89]. By taking into account the leading logarithms only, the parton shower picture reduces complex radiation patterns of multiple parton emissions to chains of individual independent parton splittings. They are organised in a probabilistic manner by an ordering parameter, usually some quantity like the virtual mass of the decaying parton or the transverse momentum of the decay products. Suitable constraints on this ordering parameter avoid singular regions of phase space. The probability for no parton splitting to occur between two scales $t_0 < t_1$ is encoded in the Sudakov form factor. The connection of the Sudakov form factor with the DGLAP equation, giving rise to its probabilistic

[2] However, it should be noted that situations like deep-inelastic scattering are still beyond the reach of APACIC++ and, thus, of SHERPA.

[3] Note that recently, a reformulation of PYTHIAs parton shower has been presented [84], which employs transverse momentum as ordering parameter. It has been implemented into the recent version of PYTHIA [76]. In [85] an alternative evolution variable, also related to transverse momentum, has been discussed. It has already been implemented into HERWIG++ [6].

interpretation can be found in App. B.2. The Sudakov form factor is given by

$$\Delta_a(t_0,t_1)=\exp\left\{-\int\limits_{t_0}^{t_1}\frac{\mathrm{d}t}{t}\int\mathrm{d}z\frac{\alpha_S(p_\perp)}{2\pi}\sum_{b,c}P_{a\to bc}(z)\right\}\,, \tag{3.1}$$

where $p_\perp$ is the transverse momentum. It can be written as a function of the scale t and the energy splitting variable z. $P_{a\to bc}(z)$ denotes the splitting function for the branching $a\to bc$. A complete list of splitting functions implemented in `APACIC++` can be found in App. D.1.7. Because of its interpretation as no-splitting probability between two scales, ratios of two Sudakov form factors like

$$P_{\text{nobranch}}=\frac{\Delta(t_0,t_1)}{\Delta(t_0,t)} \tag{3.2}$$

yield the probability for no emission between t_1 and t, which could be resolved at the scale t_0. Given a hard starting scale t_1, this allows the scale for the actual branching t to be generated by equating a random number R with this ratio and solving for t. With a second random number then the splitting variable z can be selected. It is distributed according to

$$P_{\text{split}}=\frac{\alpha_s(p_\perp)}{2\pi}\,P(z)\,. \tag{3.3}$$

This probabilistic interpretation allows the formulation of the parton shower as a Markov-chain of independent $1\to 2$-branchings, where the scale t_1, at which the former splitting occurs, sets the upper limit for the subsequent branching. Organising the parton shower in such a way results in what is known as "forward evolution". This type of evolution is employed for parton showers in the final state, i.e. for the "time-like parton shower", where the resulting parton ensemble is not subject of any other constraint.

For the initial state, however, i.e. for space-like parton evolution, the situation changes drastically. This is because standard forward evolution of a parton ensemble from some comparably low fixed hadronic scale $Q_0^2<0$, of the order of a few Λ_{QCD}, to the fixed scale of hard interaction, $Q^2\ll Q_0^2$, distributed according to the appropriate matrix elements, would be highly inefficient. Therefore it is more convenient to start with specifying the scale Q^2 of the core process and its momentum fractions x_1 and x_2, and subsequently evolve "backwards" to the partons assumed to be resolved from the incoming hadrons. The correct way to perform this backward evolution has been introduced in [90, 91]; it boils down to modifying the Sudakov form factors by dividing by the appropriate PDF at the given scale and at the relevant Bjorken-x. The resulting no-branching probabilities are then given by[4]

$$P_{\text{nobranch}}=\frac{f(x,\,t)}{f(x,\,t_1)}\cdot\frac{\Delta(t_0,t_1)}{\Delta(t_0,t)}\,. \tag{3.4}$$

Again, equating this probability with a random number and solving for t defines the previous branching scale. This time, however, the corresponding splitting variable z is distributed according to

$$P_{\text{split}}=\frac{\alpha_s(p_\perp)}{2\pi}\frac{P(z)}{z}f\left(\frac{x}{z},\,t\right)\,, \tag{3.5}$$

[4] A more efficient, non-Markovian, evolution algorithm is currently under investigation [92].

where x is the momentum fraction of the decaying parton, and $z = x/x_1$ with x_1 being the momentum fraction of the resulting parton from which the backward step started.

In both time-like and space-like evolution, the notion of soft colour coherence [91, 93–96] plays a crucial role. It results in an angular ordering of subsequent branchings, which can be implemented directly through a corresponding choice of the evolution variable. This has been done in HERWIG [3, 77], where a suitable angular variable has been chosen. Alternatively, colour coherence can be implemented by choosing transverse momentum as ordering parameter; this choice has been made in Ariadne [78] which bases its multiple emission treatment on splitting colour dipoles. Recently, two new formalisms to incorporate ordering according to transverse momentum into the more conventional parton picture have been presented in [84, 85]. In its most trivial version, however, angular ordering can be imposed through a direct veto on increasing opening angles. This is how it has been implemented in PYTHIA, where virtuality is the evolution variable. Of course, such a way of implementing colour coherence is by far not as sophisticated as the methods above; nevertheless this method has also been chosen in the framework of APACIC++.

3.1.2 Variables in APACIC++

As indicated above, the parton shower in APACIC++ is organised in terms of virtuality, i.e. in terms of the virtual mass of the decaying particle, and the splitting variable z is interpreted as the energy fraction of one decay product (daughter) w.r.t. the decaying parton (mother).

1. Time-like evolution:

   For parton branchings $a \to bc$ in the final state, the evolution variable t is given by

   $$t = t_a = p_a^2 = (p_b + p_c)^2 \,. \tag{3.6}$$

   The splitting variable z is defined as energy fraction, i.e.

   $$z = \frac{E_b}{E_a} \,, \tag{3.7}$$

   taken in the rest frame of the complete final state parton shower[5]. For the respective transverse momentum, which serves as an argument in the running coupling constant and as a low-energy cut-off, a definition following [17] has been chosen. There,

   $$k_\perp^2 = 2\,\mathrm{Min}\{E_b^2,\, E_c^2\}(1 - \cos\theta_{bc}) \,, \tag{3.8}$$

   which in terms of t_a and z translates into

   $$k_\perp^2 = \mathrm{Min}\left\{\frac{z}{1-z},\, \frac{1-z}{z}\right\} t_a \,. \tag{3.9}$$

[5] In APACIC++, the time-like evolution of a given parton ensemble is performed in its rest frame. After the shower terminates, the resulting partonic final state is fully reconstructed and boosted into the relevant (lab) frame.

There is, however, some residual freedom in the exact choice of scales, which can be altered by a (logarithmically) small factor. In APACIC++, this freedom is used to *define* the transverse momentum as

$$p_\perp^2 = \frac{1}{4}\,\mathrm{Min}\left\{\frac{z}{1-z},\,\frac{1-z}{z}\right\} t_a\,. \tag{3.10}$$

Demanding that all $p_\perp$ are larger than some minimal cut-off, $p_\perp^{(0)}$, immediately poses a constraint on the allowed $(t_a,\,z)$-range for individual branchings, namely

$$t_a > t_0 = 4{p_\perp^{(0)}}^2 \quad \text{and} \quad z \in \left[\frac{t_0}{t_a+t_0},\,\frac{t_a}{t_a+t_0}\right]. \tag{3.11}$$

In addition, the transverse momentum must be positive. Using the definition of the splitting variable, Eq. (3.7), yields a kinematical condition on z, namely

$$z \in \left[\frac{1}{2}\left(1-\sqrt{\frac{t_a}{E_a^2}}\right),\frac{1}{2}\left(1+\sqrt{\frac{t_a}{E_a^2}}\right)\right]. \tag{3.12}$$

For the explicit angular veto employed to model coherence effects, the following approximation for the angle is used

$$\theta_{bc} \approx \sqrt{\frac{t_a}{z(1-z)E_a^2}}\,. \tag{3.13}$$

It stems from $t_a = 2z(1-z)E_a^2\,(1-\cos\theta_{bc})$. This approximation is valid for small θ_{bc}, but it can conveniently be used for large angle emission too, since the actual value is irrelevant for its role as ordering parameter.

Having split parton a into b and c, the two offsprings are massless first. They gain a virtual mass by continuing the parton shower evolution for another step with starting scale t_a. Of course, the sum of their virtual masses cannot be larger than the virtual mass of a, i.e.

$$\sqrt{t_b}+\sqrt{t_c} < \sqrt{t_a}\,. \tag{3.14}$$

This, together with the angular ordering constraint, sets some additional limits on the splitting variables. However, there is still an issue to be resolved: When z was defined, it was implicitly assumed that both outgoing partons are on their mass-shell; this is not true any longer, which implies that the branching kinematics of $a \to bc$ has to be redefined. In APACIC++, this is achieved through a redefinition of the energy splitting variable z, also quite along the lines of what happens inside PYTHIA. In both codes, the modified splitting variable reads

$$\tilde{z} = \left(z-\frac{1}{2}\right)\frac{\lambda(t_a,\,t_b,\,t_c)}{t_a} + \frac{t_a+t_b-t_c}{2t_a}\,, \tag{3.15}$$

where

$$\lambda(a,b,c) = \sqrt{(a-b-c)^2-4bc}\,. \tag{3.16}$$

This modification constitutes a simple linear transformation from the massless to the massive domain, which is always possible as long as the condition given by Eq. (3.14) is satisfied.

If one or more of the partons a, b, and c are massive, the definitions above change as follows:

- The evolution variable is now defined as $\tilde{t}_a = t_a - m_a^2$. This in addition to the usage of mass terms in the splitting kernels (cf. App. D.1.7), leads to a slightly modified Sudakov form factor.
- The argument of the running coupling is now given by the "complete" $k_\perp$ formula, i.e. it is defined through

$$p_\perp^2 = \frac{\mathrm{Min}\{E_b^2,\, E_c^2\}}{2}(1 - \cos\theta_{bc})\,, \tag{3.17}$$

  which assumes on-shell, but not necessarily massless daughters.

The other conditions introduced above are, in principle, not altered, provided that the kinematical variable t_a is used rather than the evolution variable $\tilde{t}_a$. Consequently, the kinematical z-domain is still given by Eq. (3.12), and z is translated into the massive case by Eq. (3.15). This leads to a reinterpretation of the splitting variable, which is necessary, since the splitting functions are calculated with z being the light-cone momentum fraction.

2. Space-like evolution:

For the parton shower in the initial state, i.e. space-like showers, the evolution proceeds backwards. The ordering parameter here is the virtual mass of the respective initial state parton. Therefore in branchings $b \to ac$ the scale is given by

$$t = t_a = p_a^2 < 0\,, \tag{3.18}$$

and, wherever it is needed, the absolute value is taken. The definition of the splitting variable is a little bit more tricky. In order to ensure four-momentum conservation in the reconstruction of the showering kinematics, the two shower branches of the two incoming partons are coupled. For the two incoming particles, labelled by a and $\tilde{a}$, the Sudakov form factors, cf. Eq. (3.4), are used to choose their virtual mass, t_a and $t_{\tilde{a}}$. The parton with larger off-shellness is selected for the reconstruction of the corresponding backward step. Assume that $t_a < t_{\tilde{a}}$, and, hence, that a is selected. Then z is defined through

$$z = \frac{(p_a + p_{\tilde{a}})^2}{(p_b + p_{\tilde{a}})^2}\,, \tag{3.19}$$

clearly a Lorentz-invariant measure. This implies that, step by step, the c.m. energy squared in the parton system is enhanced by a factor $1/z$. In the same way, the Bjorken-x of partons a and b are related by

$$x_b = x_a/z\,, \tag{3.20}$$

where the first Bjorken-x of the partons entering the hard process are taken directly from the matrix element evaluation. In this respect, at each step of the space-like shower evolution, the current pair of partons is oriented along the beam axis, with Bjorken-x as if they were massless. It is this Bjorken-x and a scale $Q^2 = p_\perp^2$ that constitute the parameters for the calculation of the PDF at the corresponding step. In the c.m. system of partons b and $\tilde{a}$, the transverse momentum of a and c is given by

$$k_\perp^2 = -(1-z)\, t_a \,. \tag{3.21}$$

Following a similar reasoning as in the final state treatment, the transverse momentum entering the running coupling as well as the PDF evaluation is *defined* through

$$p_\perp^2 = -\frac{1-z}{4}\, t_a \,. \tag{3.22}$$

Again demanding that all $p_\perp$ are larger than some minimal cut-off, $p_\perp^{(0)}$, and taking into account that the resulting Bjorken-x of parton b must not exceed 1, results in a constraint on the allowed $(t_a,\, z)$-range for individual initial state branchings, reading

$$t_a < t_0 = -4{p_\perp^{(0)}}^2 \quad \text{and} \quad z \in \left[x_a,\, \frac{t_a - t_0}{t_a}\right] . \tag{3.23}$$

The impact of of shower parameters like a cut $p_\perp^{(0)}$ on the evaluation of Sudakov form factor has been recently investigated in [97].

Having thus constructed the backward step $b \to ac$ leading to the parton b, it is clear that c may experience a final state shower evolution. Its starting scale, by default, is given by t_a. For kinematic reasons, however, the actual scale that is chosen in the shower evolution must also satisfy

$$t_c < t_{c,\max} = \frac{\lambda_{a\tilde{a}}\lambda_{b\tilde{a}} - s_{a\tilde{a}}s_{b\tilde{a}}}{2t_{\tilde{a}}} + t_a + t_{\tilde{a}} \tag{3.24}$$

with

$$s'_{a\tilde{a}} = s_{a\tilde{a}} - t_a - t_{\tilde{a}} \,, \qquad s'_{b\tilde{a}} = s_{b\tilde{a}} - t_b - t_{\tilde{a}} \tag{3.25}$$

$$\lambda_{a\tilde{a}} = \lambda(s'_{a\tilde{a}}, t_a, t_{\tilde{a}}) \qquad \lambda_{b\tilde{a}} = \lambda(s'_{b\tilde{a}}, t_b, t_{\tilde{a}}) \tag{3.26}$$

where $s_{a\tilde{a}} = (p_a + p_{\tilde{a}})^2$ and $s_{b\tilde{a}} = (p_b + p_{\tilde{a}})^2 = s_{a\tilde{a}}/z$. Similar to the approximation of Eq. (3.13), the opening angle of this splitting can be estimated by

$$\theta_{ac} \approx \sqrt{\frac{t_a}{(1-z)\, E_a^2}} \,. \tag{3.27}$$

Knowing t_b and t_c as well as the four-momenta p_a and $p_{\tilde{a}}$, the four-momenta p_b and p_c are constructed explicitely in the c.m. frame of p_a and $p_{\tilde{a}}$. In this system, energies and momenta are fixed according to

$$E_c = \frac{s_{b\tilde{a}} + t_b + t_a - t_c}{2\sqrt{s_{a\tilde{a}}}} \tag{3.28}$$

$$p_{\mathrm{z},c} = \frac{s_{b\tilde{a}} - 2E_{\tilde{a}}E_c}{2p_{\mathrm{z},a}} \tag{3.29}$$

$$p_{\perp c} = \sqrt{E_c^2 - p_{\mathrm{z},c}^2 - t_c} \,, \tag{3.30}$$

where the transverse momentum is distributed uniformly in its azimuthal angle. Furthermore,

$$p_b = p_a + p_c \,. \tag{3.31}$$

Subsequently, the system is boosted into the rest frame of partons b and $\tilde{a}$ and rotated such that their momenta point along the beam axis.

3.1.3 Colour treatment

When the parton shower terminates, the resulting multi-parton ensemble needs to be transformed into hadrons. Due to a lack of quantitative understanding of non-perturbative physics, this is achieved through phenomenological models. These models have some different underlying physics assumptions, highlighted by the examples of the string model [98–103] stressing the role of colour coherence [104], and of cluster fragmentation models [6, 45, 105–107] that are closer to the independent fragmentation approach [108] and the concept of pre-confinement [109]. However, they have in common that they rely on having as input a parton ensemble with a well-defined colour structure in the $N_c \to \infty$ limit. This necessitates that the parton shower must distribute colours in this limit. In most cases, like, e.g. in a splitting $q \to qg$ the colour structure is unambiguously defined, ensuring that a well-defined colour structure at the beginning of the parton shower evolution can be mapped onto a well-defined colour structure at its end. However, there are cases with ambiguities, namely in splittings of the type $g \to gg$. In this case, there are two ways of locally distributing colour. Denoting a colour state by its colour triplet and anti-triplet labels in the $N_c \to \infty$ limit, $(a, \bar{b})$, these two ways in the splitting $g(1) \to g(2)g(3)$ can be visualised as

$$(a, \bar{b}) \to (a, \bar{c}) + (c, \bar{b}) \quad \text{or} \quad (a, \bar{b}) \to (c, \bar{b}) + (a, \bar{c}) \,. \tag{3.32}$$

In APACIC++, the choice is made in the following way: In the shower evolution, the decaying gluon 1 was produced in another parton branching process, where the other decay product is colour-connected to the gluon. For both gluons 2 and 3, the transverse momentum w.r.t. this colour partner is determined according to Eq. (3.9). The choice is then made such that the gluon with the smaller relative $k_\perp$ is colour connected with this partner parton.

3.1.4 Initialisation of the parton shower

Within the SHERPA framework, an algorithm along the lines of [14, 15] for the consistent merging of tree-level matrix elements for multi-particle production with the parton shower of APACIC++ has been implemented [110]. The key idea of this algorithm is to separate the phase space for parton emission into the hard region of jet production accounted for by suitable tree-level matrix elements and the softer region of jet evolution covered by the parton shower. Then, extra weights are applied on the former and vetoes on the latter, such that the overall dependence on the separation cut is minimal. The separation is achieved through a $k_\perp$ measure [17–19]. The weight attached to the matrix elements is constructed employing Sudakov form factors, thereby taking into account those terms that would appear in a corresponding parton shower evolution. Therefore, a "pseudo parton shower history" is reconstructed by clustering the initial and final state particles from the tree-level matrix

element according to the $k_\perp$-algorithm. This procedure provides the scales necessary for the evaluation of the weight, namely the nodal values of the different $k_\perp$, where two jets have been merged into one.

Within APACIC++, the reconstructed "shower history" is utilised for the determination of initial conditions for the shower evolution. Then, starting from the hard $2 \to 2$ core process, all partons obtain as starting scale for their shower evolution the nodal virtuality, where they emerge for the first time. It should be stressed at this point that there is some residual mismatch in the parton shower variables used in APACIC++, namely virtuality $t = p^2$, and the scales ($k_\perp$ measures) used in the Sudakov form factors employed in the reweighting of the matrix elements. This point will be discussed in more detail in the following section.
For the scale of the four partons entering or leaving the $2 \to 2$ process, there are a few options, defining the respective choice of scale t_{start}:

- Processes of the type $e^+e^- \to q\bar{q}$: $t_{\text{start}} = \hat{s} = (p_q + p_{\bar{q}})^2$.
- Drell-Yan type (e.g. $q\bar{q} \to e^+e^-$): $t_{\text{start}} = \hat{s} = (p_q + p_{\bar{q}})^2$.
- "Drell-Yan+jet"-type (e.g. $q\bar{q} \to W^{(*)}g$): For the incoming partons the choice is $t_{\text{start}} = \hat{s} = (p_q + p_{\bar{q}})^2$. For the final state parton, however, the start scale for the shower evolution is different, namely the nodal value where it has been produced, usually $\hat{t}$ or $\hat{u}$.
- QCD processes: In this case, different colour flows are usually competing. The winner is selected according to the respective contribution, which is related to a specific propagator structure ($\hat{s}$-, $\hat{t}$-, or $\hat{u}$-channel). The choice of starting scale follows the selection of the colour structure; in most cases therefore the starting scale t_{start} is the minimum of $\hat{t}$ and $\hat{u}$.

In order to account for colour coherence, a maximal allowed branching angle θ_{crit} has to be determined for each parton. Using the knowledge of the colour connections of the $2 \to 2$ process, θ_{crit} is defined as the angle between the parton in question and the parton colour connected to it. In case of gluons the choice of this angle is, of course, ambiguous; there, the maximum of both possible values is taken.

Having fixed the starting scales of the hardest partons, the starting scales for the evolution of softer partons are easy to obtain. In principle, there are only two ways, in which softer partons may emerge, which lead to a slightly different treatment.

- Branchings in the final state:
  There the harder, i.e. the more energetic, of the two offsprings inherits as starting scale and angle the values of the decaying parton, whereas the parameters of the softer offspring are taken directly from the node. In other words, the initial virtual mass equals the invariant mass of the pair, and the starting angle is given by its opening angle.
- Branchings in the initial state:
  There, in analogy to the treatment of the space-like shower evolution, the virtual mass and the starting angle of the time-like offspring are given by the virtual mass of the initial state parton that branches "backwards" and the respective opening angle w.r.t. the corresponding beam. The "new" initial state parton inherits the starting scale and angle of the line pointing towards the "core" process.

3.1.5 Merging issues

Having fixed the starting scales, the parton shower can be evolved. Due to the merging prescription, emissions inside the parton shower have to be vetoed, if they result in the production of partons with transverse momenta $k_\perp$ larger than a given jet resolution scale, $p_\perp^{\text{cut}}$. Parton showers attached to matrix elements with the highest multiplicity must live up for the production of eventual extra jets. In this case, the veto scale is not the jet resolution scale but rather given by the smallest $k_\perp$ of the partons stemming from the matrix element. However, in the parton evolution of such multi-parton final states, there is a last subtlety. It is connected to the fact that, through showering, the partons may acquire a virtual mass different from their on-shell mass used in the matrix element. This recoil has to be compensated for, if possible in such a way that the other partons stemming from the matrix element are least perturbed. This is solved in the following way: The merging procedure results in the reconstruction of a pseudo parton shower history of the parton ensemble. Thus, to each parton produced in the matrix element a partner can be assigned such that both emerge in a branching of the pseudo parton shower history. If one of them or both acquire a mass, the respective partner takes care of the recoil. The strategy employed for this is very similar to the one used when the initially massless partons in the showering acquire a mass; in both cases the energy splitting variable is shifted through a linear transformation, for the shower case, cf. Eq. (3.15). In the initial branchings of the shower initiators, there are two cases to be considered:

- Both partners experience a parton shower evolution. Then, the reconstructed energy splitting variable of the branching where they have been produced, is shifted according to Eq. (3.15).
- In the branch $a \to bc$, only one partner (b) experiences a parton shower evolution, the mass of its partner is (c) fixed, since it can be thought of as an internal line of the matrix element - it branches according to the pseudo parton shower history. Then z is shifted according to

$$\tilde{z} = \left(z - \frac{t_a + t_b^{(0)} - t_c^{(0)}}{2t_a} \right) \frac{\lambda(t_a, t_b, t_c)}{\lambda(t_a, t_b^{(0)}, t_c^{(0)})} + \frac{t_a + t_b - t_c}{2t_a} \,, \tag{3.33}$$

  where $t_i^{(0)}$ denote the matrix element masses and t_i the new virtualities. This modification results in a change of the opening angle θ_{bc}, leading to a modified momentum even for the particle with the mass unchanged. In order to comply with four-momentum conservation, its offsprings have to be adjusted, too. This transformation can easily be achieved through a rotation followed by a boost along the direction of particle c.

Within `APACIC++`, an additional veto on "losing" a jet produced in the matrix element is introduced. Losing a jet through the shower is possible due to a mismatch of the quantities responsible for jet definition ($k_\perp$) and jet evolution (virtual mass). This leads to recoils imposed by the shower evolution resulting in a change of $k_\perp$, while the virtuality of the internal line in question is preserved. Therefore, a check on the number of jets is performed after the shower evolution is finished. This is done by demanding that the - now off-shell - shower seeds are still separated in $k_\perp$. If this is not the case the event is rejected, and a new event is generated from the beginning, i.e. with a new kinematical situation but the same flavour constellation of the jets.

3.2 Results

In this section some results will be presented that validate the implementation of the parton shower algorithms, discussed in the previous sections.

3.2.1 Comparison with analytic Sudakov form factors

First of all, the parton shower of APACIC++ will be confronted with known analytical results dealing with the resummation of large logarithms emerging in multiple parton emission. Such results are available mainly for e^+e^- annihilation into hadrons. There, analytical calculations describe the relative rates for different jet multiplicities in the $k_\perp$-algorithm. For the massless case, results can be found in [17], massive quarks are dealt with in [111]. All results presented here relate to e^+e^- annihilations at $E_{\text{c.m.}} = 91.2$ GeV, i.e. to the LEP1 energy. The formalism resulting in such resummed expressions for jet rates will be discussed in some detail in Sec. 4.1, since they represent a very nice way to describe the merging procedure on the theoretical level. However, in the following discussion the focus will be on the performance of the parton shower implemented in APACIC++, eventually supplemented with the exact matrix elements for multi-jet production, made available through the merging procedure.

To gain some first idea about the behaviour of the merged cross sections and the effect of the Sudakov form factors, consider Fig. 3.1. There, tree-level cross sections for the production of up to four jets, out of which two may be b-jets (left) are contrasted with the weight applied to them in the merging procedure (right). The jets are defined through a Durham jet measure with resolution parameter y, which represents the minimal relative transverse momentum of two separated jets. Already here, it becomes apparent that the massive b-quarks are suppressed w.r.t. massless ones in the cross section, whereas the weights are nearly identical for massless and massive jets. In Fig. 3.2 the merging has been performed; in the left plot the resulting jet cross sections and their sum are shown for the massless case, the right plot exhibits the corresponding cross sections when two b-quarks are involved. It is surprising how stable the total cross sections are w.r.t. the jet definition cut. In Fig. 3.3 the resulting two- and three-jet rates are displayed. Clearly, due to the "dead cone" effect the b-quarks tend to radiate less, leading to an enhanced two-jet rate compared to light quarks. For three jets, the situation is slightly different; for small value of y it is the four-jet rate that starts dominating. In this region therefore the three-jet rate for massive quarks starts to exceed the massless one, which tends to have a larger fraction of four-jet events.

In Fig. 3.4, the results of the parton shower as implemented in APACIC++ are confronted with these analytical jet rates, which basically represent a resummed tree-level calculation. The agreement over a wide range of phase space, down to small values of $y \leq 0.004$ is very good. Only for very small values of y the three-jet rate as obtained from the parton shower starts to overshoot the analytical result, which is due to the increased importance of four-jet events in this region. Finally, Fig. 3.5, exhibits the ratio of three-jet rates with b-quarks and with light quarks (u, d, and s) only. There, data from the Delphi collaboration [112] are contrasted with a full next-to-leading order calculation [113] with varying b-quark mass, with the pure parton shower result as obtained by APACIC++ and with the result of the combined matrix element plus Sudakov weight. The data clearly prefer a lighter b-quark

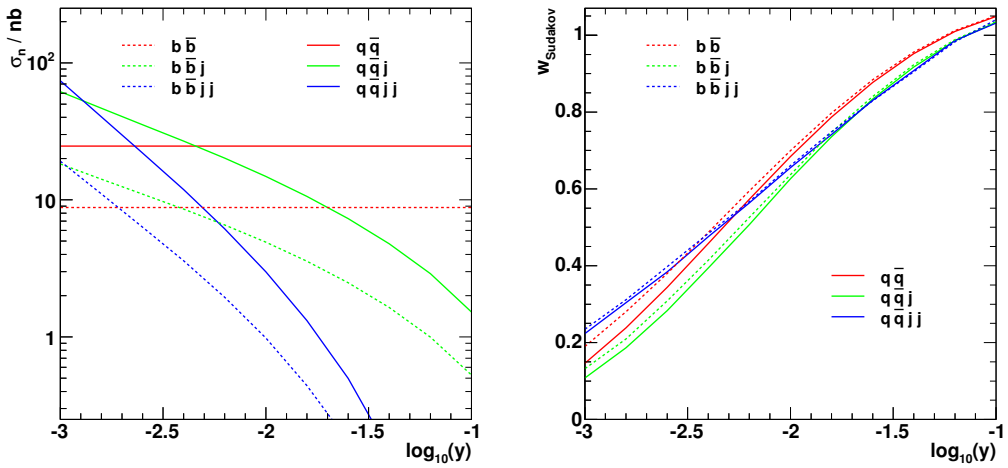

Figure 3.1: Cross section for the production of up to four jets (left) and the corresponding Sudakov weight that will be attached in the merging procedure (right) vs. the jet resolution y. Two/three/four-jet topologies are depicted in red/green/blue, massless jet-configurations are shown with solid lines, jet configurations involving two massive b-quarks with $m_b = 4.5$ GeV are shown with dashed lines.

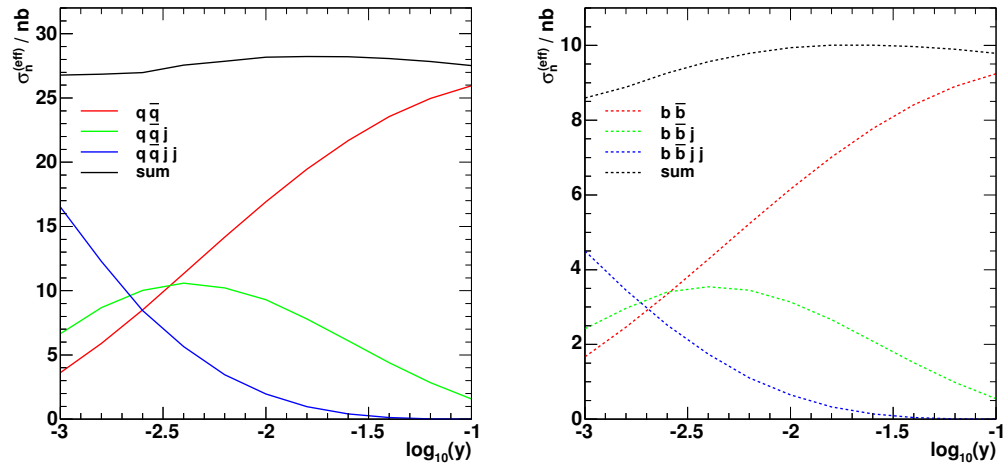

Figure 3.2: Cross section times Sudakov weight vs. the jet resolution y for each jet configuration and the sum of them. The left plot shows massless jets, the right one displays jet configurations with two massive b-quarks.

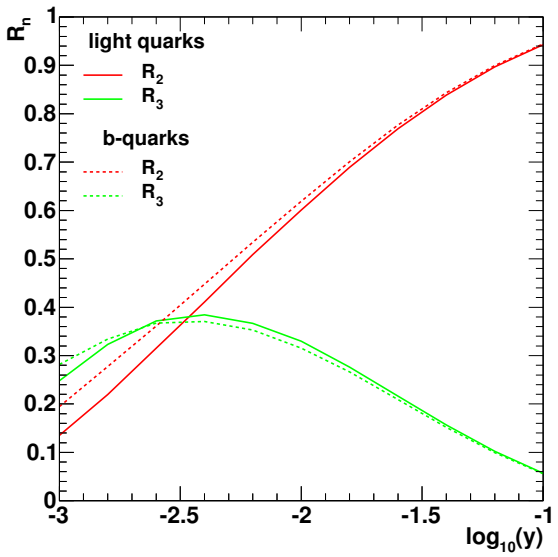

Figure 3.3: Jet rates for two- and three jets from the combined matrix element plus Sudakov weight.

with $m_b \approx 3$ GeV in the NLO calculation [6]. In addition, the parton shower obviously describes the data surprisingly well; for the merged matrix element plus Sudakov weight result, a running b-quark mass seems to be also appropriate.

[6] This result is consistent with the value obtained by evolving the measurement at the Υ resonance up to the Z boson mass, cf. [112].

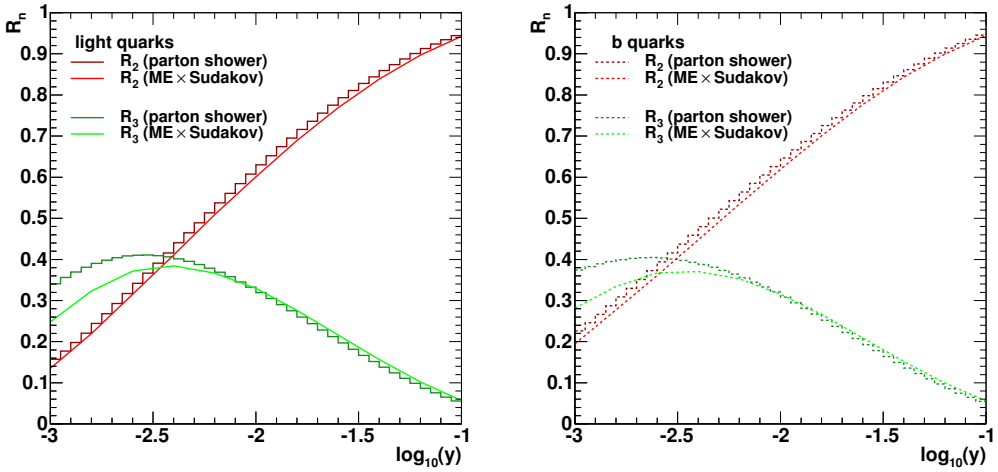

Figure 3.4: Analytical results for the jet rates from Fig. 3.3 vs. the results obtained from the parton shower.

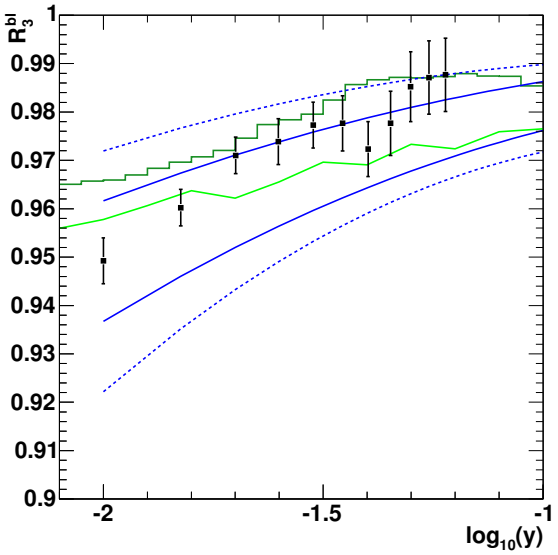

Figure 3.5: Heavy-to-light three-jet rate ratio $R_3^{bl} = R_3^{(b)}/R_3^{(uds)}$ in dependence on the Durham jet resolution y. Data (black points) from a Delphi measurement [112] are shown together with the SHERPA prediction (the dark green histogram corresponds to the shower result and the light green curve is obtained by combining matrix elements with Sudakov weights), and with an analytic calculation [113] (blue lines, dashed=LO, solid=NLO) for two different values of m_b, m_b =3, 5 GeV.

3.2.2 Comparison of shower and hadron level: Hadronisation corrections

Before further comparing results of the parton shower with experimental data, it must be stressed that many of such comparisons are feasible and meaningful on the hadron level only. This implies that the partons emerging from the shower must be hadronised with some phenomenological model. In the case of SHERPA, the choice at the moment is to employ the Lund string model for it. This model has a number of parameters to be tuned to data. The tuning of Monte Carlo event generators to data is an intricate procedure, involving an optimisation in a multi-dimensional phase space of parameters. These parameters may be perturbative (like, for instance, α_s), or non-perturbative (like, for example, the string tension in the Lund model), or they could characterise the transition between the perturbative and the non-perturbative regime (e.g. the parton shower cut-off). For further details on such a tuning procedure, the reader is referred to [114, 115]. The parton shower of APACIC++ in its versions 1.0 and 2.0 together with the Lund string model implemented in PYTHIA has been tuned in [116] and [117], respectively.

Hadronisation and the tuning of phenomenological models, however, induces some source of systematic error in any simulation that needs to be investigated. In Fig. 3.6 the parton shower results for total jet rates in the Durham scheme for 2-5 jets are confronted with results after hadronisation. Evidently, both results coincide on a level of 10% or better down to jet resolutions of $y \approx 0.001$. This corresponds to relative transverse momenta of the order of 3 GeV, a kinematical regime, where decays of b-hadrons start to matter. This also implies that down to such low values parton shower results can be compared directly to data. In Fig. 3.7, two event shape variables, thrust and oblateness, are studied. Again, results before and after hadronisation are compared. In general, event shape observables characterise the global properties of hadronic events. A thrust of 1, for example, describes a perfect, "pencil-like" two-jet event, where both jets are oriented back-to-back and have no transverse spread. Clearly, such a configuration is severely suppressed at the hadron level, since it corresponds to events with few, highly collinear particles only. Thus, in the $T = 1$ bin, hadronisation corrections are large. Over a wide range of thrust values away from such extreme configuration, however, the shapes of the results before and after hadronisation are nearly identical; hadronisation corrections in this region therefore add just a constant that can be taken directly from data. In this region of, say, $0.05 \leq T \leq 0.6$, the parton shower results can be confronted directly with data. Similar reasoning holds true not only for the other exemplary observable, oblateness, but for a plethora of observables.

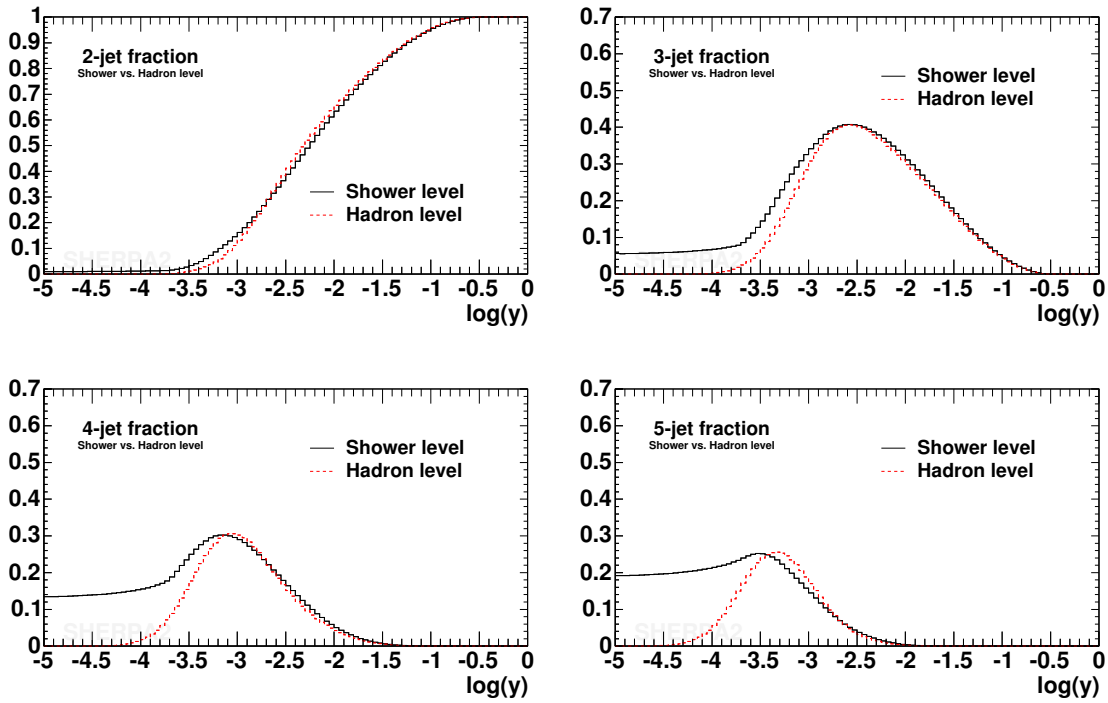

Figure 3.6: Durham jet rates at LEP1. The shower level result (solid lines) of SHERPA is contrasted with its result after hadronisation (dashed lines).

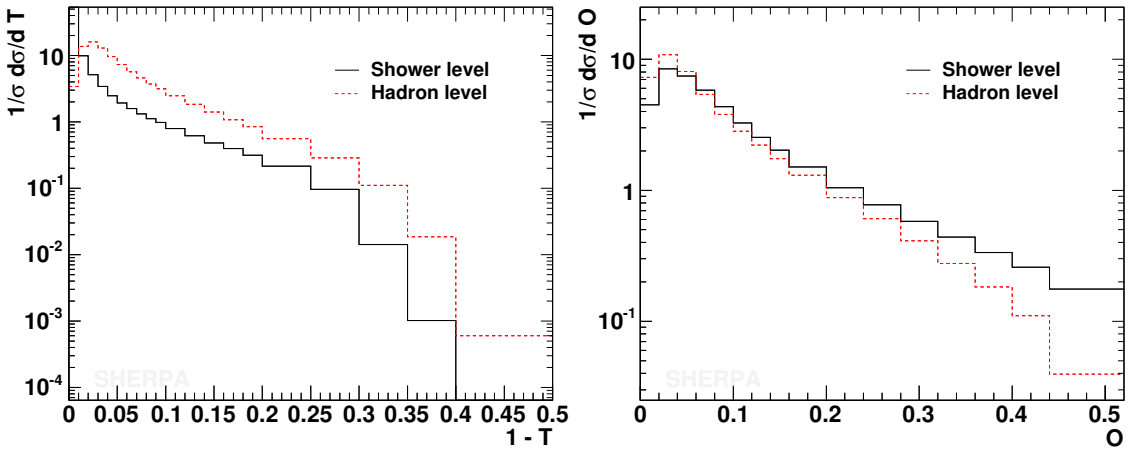

Figure 3.7: Thrust and Oblateness at LEP1. The shower level result (solid lines) of SHERPA is contrasted with its result after hadronisation (dashed lines).

3.2.3 Comparison with experimental data from LEP

Having validated the numerical correctness of the parton shower implementation, the focus shifts from the investigation of the behaviour of the Sudakov form factors to the study of experimental observables. There, experimental data can be confronted with the results obtained with the parton shower, eventually after a merging with multi-jet matrix elements. As mentioned above, in the previous section, the considered data are on the hadron level, consequently a hadronisation model has to be applied. The parameters of the model were tuned, the perturbative input consisted of a sample of multi-jet matrix elements for up to five jets, merged with the parton shower of `APACIC++`. The quality of the tuning can be judged by considering the multiplicity distribution of charged hadrons and of their scaled momentum, cf. Fig. 3.8. In this plot as well as in each of the following ones, data are confronted with the parton shower implemented in `APACIC++` (solid lines) and with the merged multi-jet matrix element plus parton shower (dashed lines), both after hadronisation. For the merged results, contributions from different jet multiplicities are indicated in different colours. Clearly, the merged sample tends to produce a slightly larger fraction of events with harder jets, leading to higher parton and hadron multiplicities; this is visible from the fact that the "parton shower only" sample slightly undershoots the bins with comparably high hadron multiplicity. For the momentum distribution, however, this minor trend washes out. In both cases, the results obtained from the simulation show excellent agreement with data, taking into account the experimental errors indicated by the yellow bands.

The first real test of the parton shower performance is to check whether it is able to reproduce event shape observables, such as thrust, major, the C-parameter, or oblateness [7], cf. Figs. 3.9 and 3.10. In all cases, the agreement of the data with the generated events is excellent. In the "parton shower only" sample the trend mentioned above, namely of being a little bit softer than the merged sample, is continued.

Turning from the event shape observables to jet observables, the small differences between the two samples vanish nearly completely. In Fig. 3.11, the relative fractions of events with different numbers of jets are exhibited in dependence on the jet resolution parameter y. The mutual agreement of the two samples and their agreement with data is excellent: The parton shower is perfectly capable of describing jet multiplicities at LEP1. This finding is repeated for the differential jet rates, cf. Fig. 3.12. In Fig. 3.13, the topological structure of four jet events is investigated. To this end, the Bengtsson-Zerwas angle [118] and the modified Nachtmann-Reiter angle [119] are studied. Apparently, the merged sample is in perfect agreement with the data, whereas the "parton shower only" sample exhibits a slight shift away from them. This, however, is not a big surprise; after all, these observables do depend on interferences between different diagrams. To take these interferences into account clearly is well beyond the abilities of the parton shower. A more in-depth comparison of the merged sample with data from both LEP1 and LEP2 can be found in chapter 5.

[7] For definitions, the reader is referred to appendix A.1.

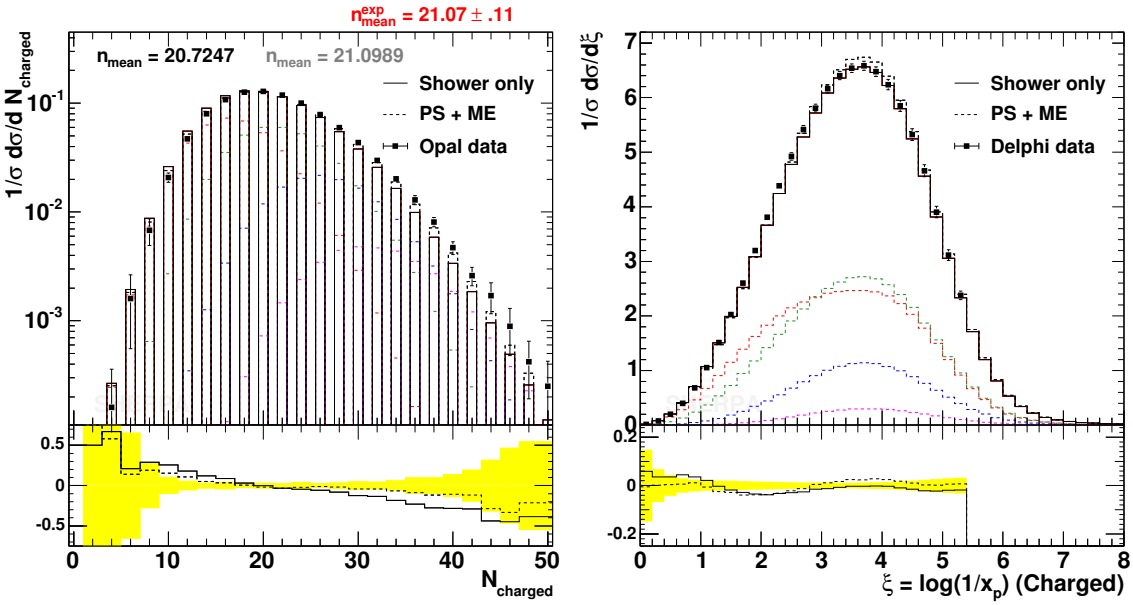

Figure 3.8: Charged multiplicity and scaled momentum at LEP1. The left plot shows the distribution of the number of charged particles together with a measurement by Opal [120]. The mean charge multiplicity is also stated together with its PDG value [121]. On the right hand side, a scaled momentum distribution is plotted against Delphi data [114]. The data are contrasted with results obtained through the parton shower alone (solid lines) with those obtained when the merging of matrix elements for up to five jets and the parton shower has been employed (dashed lines). In the latter case coloured lines indicate the contributions from individual matrix elements.

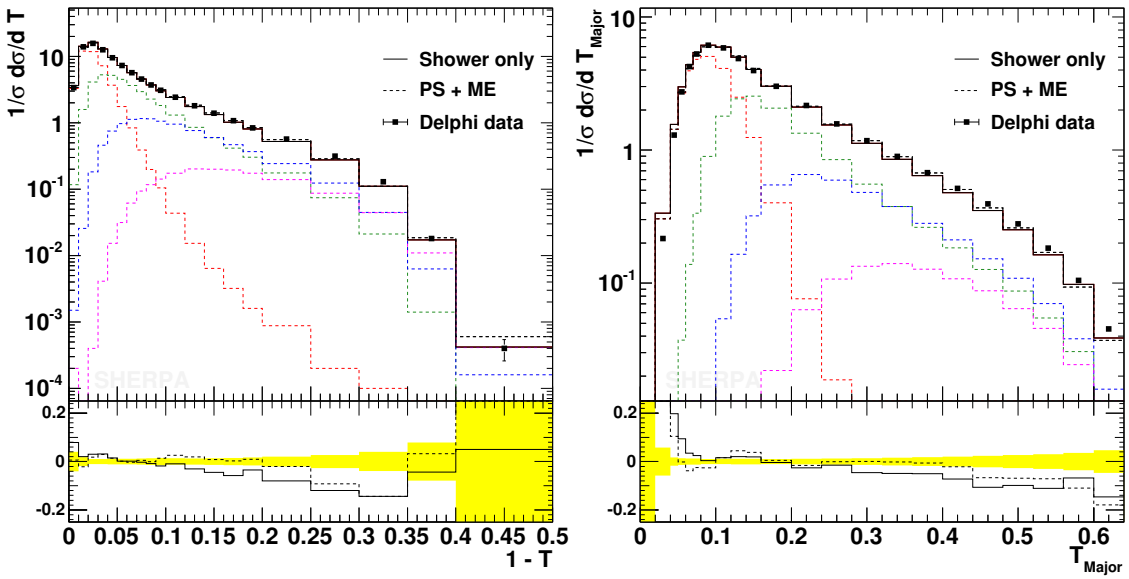

Figure 3.9: Thrust and Major at LEP1. The hadron level result of SHERPA is contrasted with measurement from the Delphi collaboration [114]. Line styles and colours are the same as in Fig. 3.8.

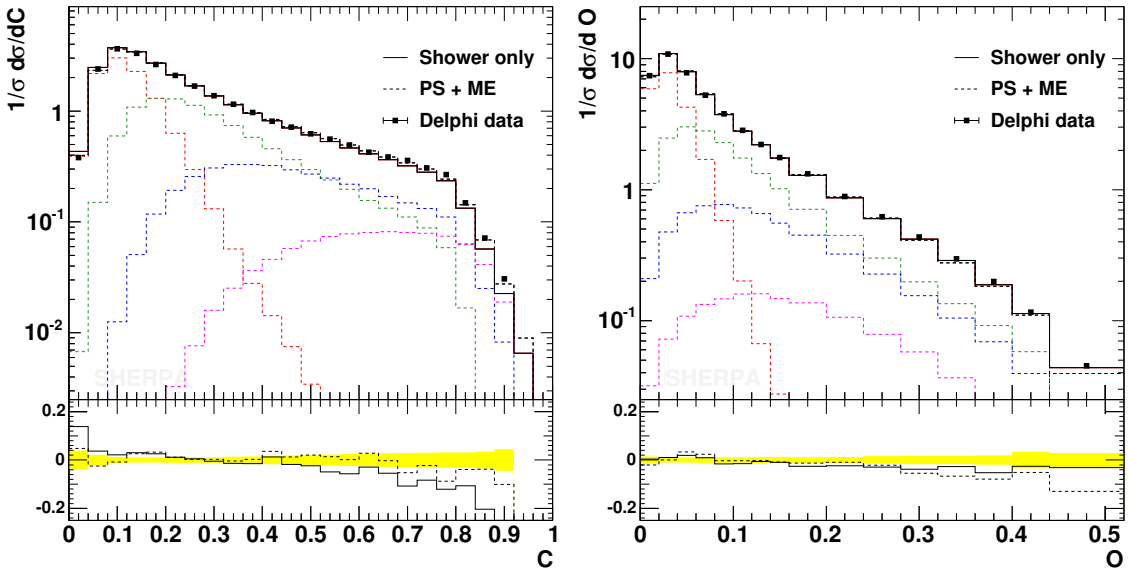

Figure 3.10: C-Parameter and Oblateness at LEP1. This plot shows the event shape variables C-parameter and oblateness, together with Delphi data [114]. Line styles and colours are the same as in Fig. 3.8.

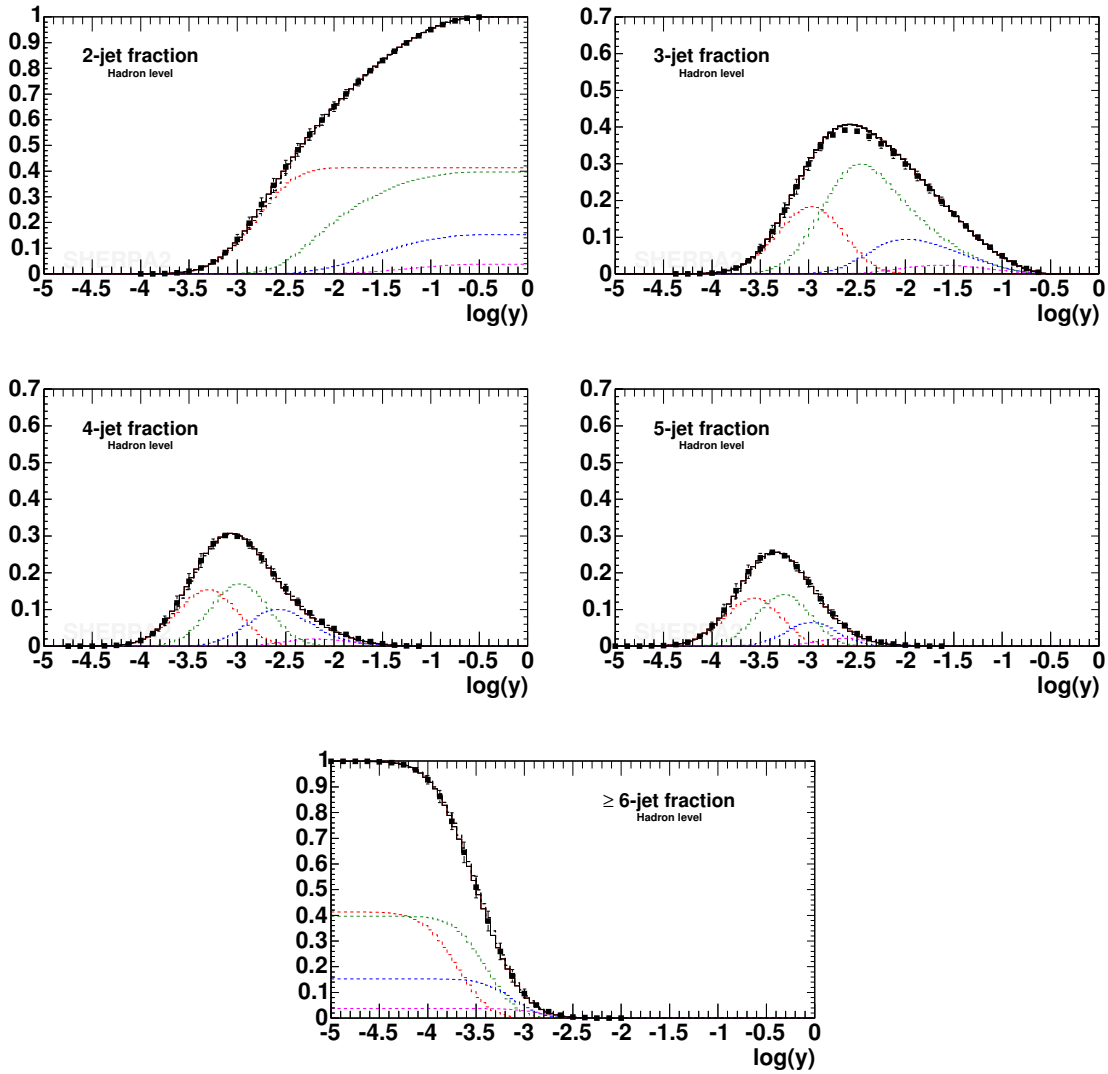

Figure 3.11: Durham jet rates at LEP1, taken from [122]. Line styles and colours are the same as in Fig. 3.8.

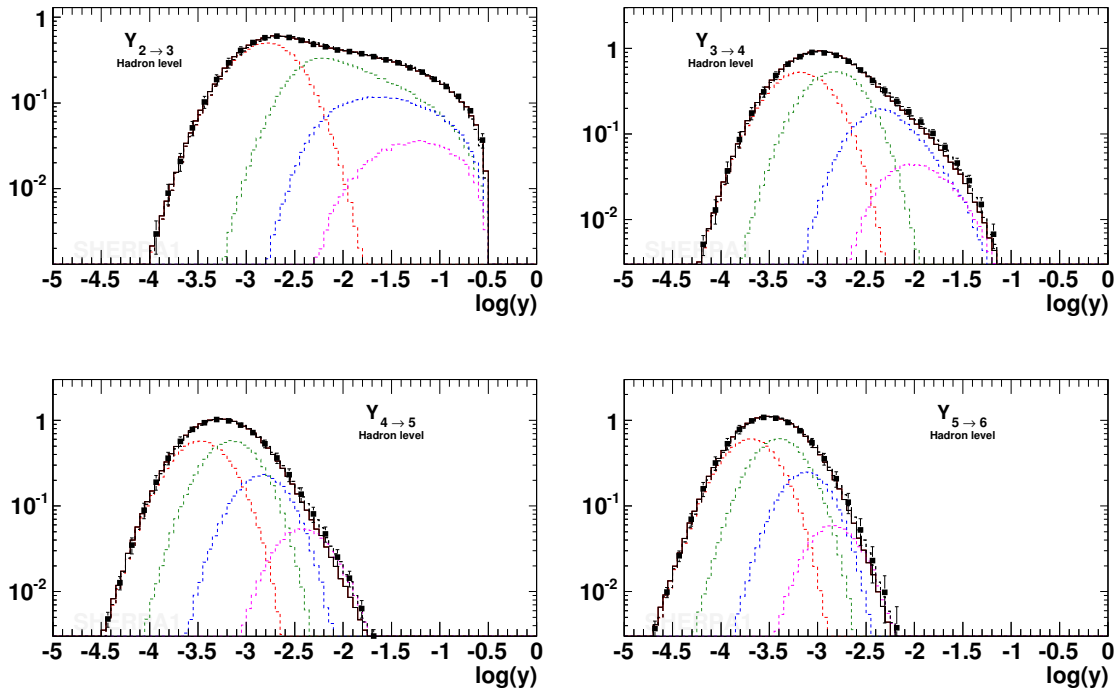

Figure 3.12: Differential jet rates in the Durham scheme at LEP1, taken from [122]. Line styles and colours are the same as in Fig. 3.8.

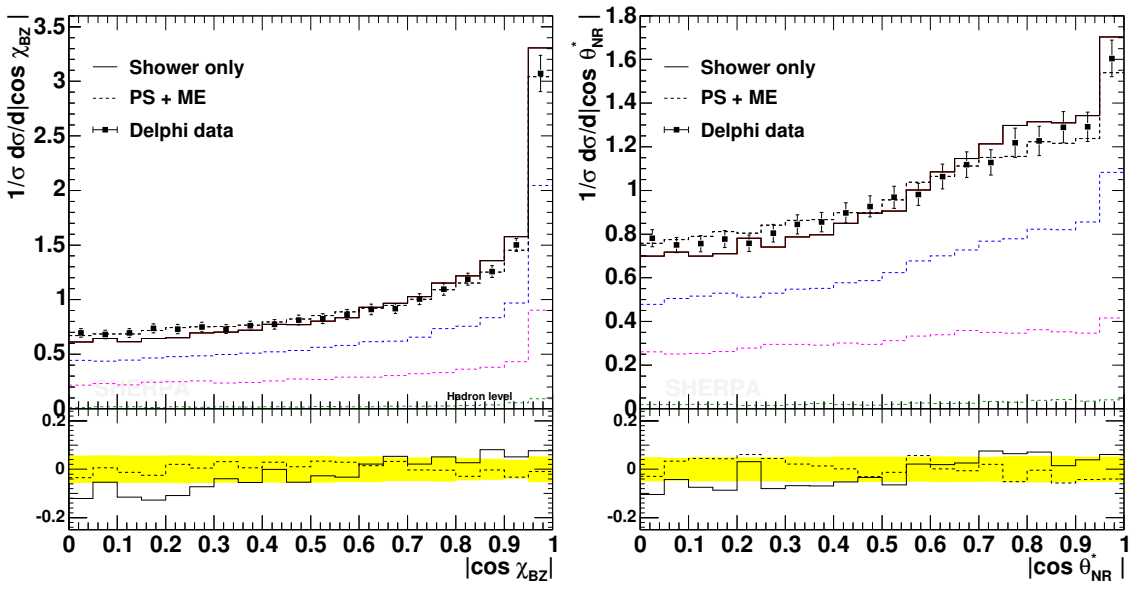

Figure 3.13: Four-jet angle distributions. Shown are the Bengtsson-Zerwas angle (left) and the modified Nachtmann-Reiter angle (right). The data points are from a DELPHI measurement [117].

3.2.4 Comparison with experimental data from Tevatron

Having investigated the final state parton shower, the focus shifts now on a study of the parton shower in the initial state. There, a good observable to judge the performance of the parton shower is the transverse momentum distribution of lepton pairs in Drell-Yan scattering. In Fig. 3.14 the $p_\perp$ distribution of such pairs with masses at the Z-pole (91 ± 15 GeV) is displayed. In order to describe the left side of the distribution, the initial partons have to be supplemented with intrinsic transverse momentum w.r.t. the hadron they stem from. In SHERPA, this intrinsic $k_\perp$ is distributed according to a Gaussian, with expectation value $k_\perp = 0.8$ GeV. In this plot, two different simulations runs are confronted with data, both only use the parton shower for parton radiation. They differ in the choice of the starting scale of the shower evolution; one is starting at $t = M_{ll}^2 \approx M_Z^2$, the other one is starting at the c.m. energy squared of the incoming hadrons. Clearly, this leads to differences in the treatment of hard radiation, and as expected in the former case, parton radiation ceases to exist at scales of the order of the hard scale. The agreement of both simulation runs with data at scales up to 40-50 GeV, however, is excellent. In Fig. 3.15, the same observable is depicted once more, this time, however, the data are confronted with the pure parton shower, starting at the high scale, and with the merged result, including up matrix elements for the production of the Z accompanied with up to three hard jets. The results again are in great agreement with data. This shows that also the implementation of the initial state parton shower in APACIC++ has succeeded.

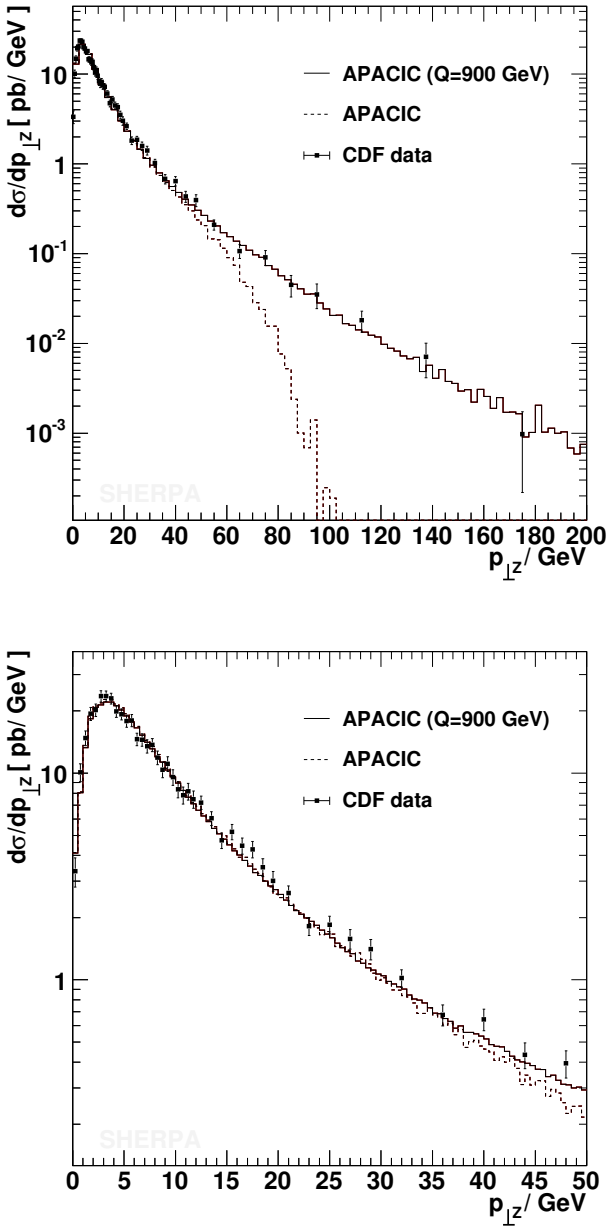

Figure 3.14: The $p_\perp$ distribution of the Z-boson in comparison with data from CDF at the Tevatron, Run I [123]. The bottom plot shows the same distribution as the top one, but with focus on the low momentum region. The solid line indicates the shower result when using a fixed start scale of 1800 GeV, while the the dashed line is obtained when using $s' \approx M_Z^2$ as start scale. The SHERPA results have been multiplied by a constant K-factor of 1.45 to match the data.

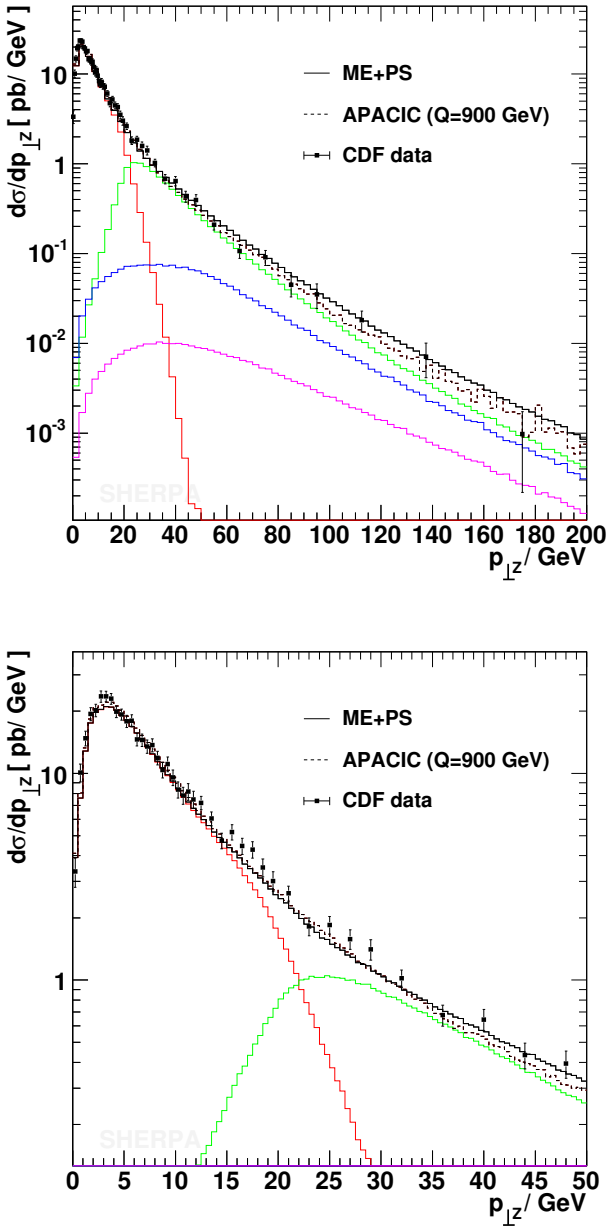

Figure 3.15: The $p_\perp$ distribution of the Z-boson in comparison with data from CDF at the Tevatron, Run I [123]. This plot shows the same distributions as Fig. 3.14, but this time the pure shower performance is compared with the result obtained when merging matrix elements with up to 3 extra jets. The jet scale Q_{cut} was fixed to 20 GeV. The coloured lines give the contributions from individual matrix elements.

3.3 Summary

In this chapter, the new version of the program APACIC++ has been presented. In contrast to its first version, APACIC++ ceased to be a stand-alone program; now, it is just the parton shower module of a larger framework. This transformation resulted in a relocation of many steering and service classes. On the other hand, the scope of APACIC++ widened in such a way that in its present state it is also capable of performing the parton shower in the initial state of hadronic collisions. In addition, the merging procedure with the matrix elements has been refined. On the technical side, some algorithms have been changed, in particular, the look-up tables for the Sudakov form factors have been replaced by an algorithm based on the hit-or-miss method.

Some exemplary results obtained with the new version of APACIC++ have been presented as well. The comparison with known analytical results, that properly resum large logarithms, validates the physical and numerical correctness of the implementation of the Sudakov form factors. This is not too obvious, since the analytical results contains logarithms in terms of transverse momentum scales, whereas the parton shower in APACIC++ has been formulated in terms of virtual mass, supplemented with appropriate scale choices and an explicit angular ordering. Both the parton shower alone and it being merged with matrix elements results in an excellent agreement with a collection of precise data. These results span up to five orders of magnitude and the agreement is, especially for the LEP1 data, on the level of a few percent. This proves the validity and underlines the abilities of the parton shower implemented in APACIC++.

4 Merging matrix elements and parton showers

The analysis of multi-particle final states becomes increasingly important in the search for the production and decay of new, heavy particles. Therefore, in order to guide such analyses, their simulation in Monte Carlo event generators should be as correct as possible. There are two complementary approaches to model the production of multi-particle final states: First, employing fixed-order perturbation theory, exact matrix elements at tree-level or beyond describe particle production in specific processes through Feynman diagrams, taking into account all quantum interferences at the corresponding level of accuracy. Alternatively, the parton shower approach organises the emission of secondary partons in such a way that all leading collinear or soft logarithms of the form $\alpha_S^n \log^{2n}$ are resummed. The former way of modelling particle production has the benefit of being well-defined and exact up to given fixed-order accuracy for large angle or high energy emission of partons, whereas the second approach correctly treats the soft and collinear regions of phase space. Of course, a combination of both approaches allows for a better description of particle production over the full available phase space. A way of merging multi-particle matrix elements at tree-level with the subsequent parton shower consistently at leading logarithmic accuracy and taking into account important parts of the next-to-leading logarithms was formulated first for the process e^+e^- →hadrons in [14]. The principles of its application to hadronic processes have been discussed in [15]. In both cases, the phase space of particle production is divided into two disjoint regimes, one of jet production covered by the corresponding matrix elements, and one of jet evolution modelled through the parton shower. The separation in both cases, e^+e^- →hadrons and hadronic collisions, is achieved through a $k_\perp$ jet measure [17–19]. The implementation of this algorithm is discussed in detail in this chapter; it forms the cornerstone of the new event generator `SHERPA` [1]. The approach has been extended in [79] to cover also the dipole shower formulation of multiple parton emission [78]. A somewhat related approach has been taken in [81]. The algorithm has been tested in a variety of versions, ranging from its prime example e^+e^- →hadrons [26] over the production of gauge bosons in hadronic collisions at the Tevatron [21, 80] or the LHC [22] to W-pair production at the Tevatron [124].

To some extent, however, all existing algorithms so far assume that there is a signal process (like, e.g., $e^+e^- \to q\bar{q}$ or $q\bar{q} \to l\bar{\nu}_l$) with one specific order in the electroweak coupling constant and that all additional jets are emitted through strong interactions. This implies that all matrix elements have the same order in the electroweak coupling constant and that they form a hierarchy of extra orders in α_s, related to extra jets. Despite its apparent success there is one question that remains to be answered. This is the question of how to deal with situations where both electroweak and strong amplitudes contribute significantly to the same final state. For example, at LEP2 both pure QCD amplitudes and W boson pair

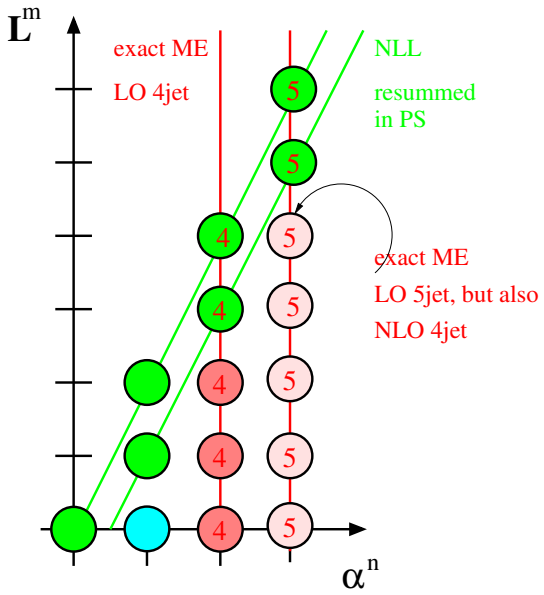

Figure 4.1: Schematic picture of perturbative orders in e^+e^- →jets. Clearly, for every order in α_s one additional gluon can be emitted that can be soft or collinear leading to maximal two more large logarithms.

production amplitudes contribute to the total cross section of 4-jet production processes. Depending on the specific kinematical situation, their relative amount may vary; however, they exhibit different properties. This is exemplified by their colour flows, being responsible for the kinematical domain in which hadrons are formed. It is clear that a consistent merging procedure for such processes is highly desirable. Such a merging algorithm has to take proper care of relevant coupling constants, and it has to reliably predict the corresponding colour structure.

In the next section, Sec. 4.2, the algorithm is discussed for both e^+e^- and hadronic processes. Certain aspects presented here have not been covered before. They include the treatment of jet production beyond the availability of corresponding matrix elements and some ways of using variable jet resolution scales for different jet multiplicities. In addition, some first steps into the direction of treating matrix elements, where electroweak and strong interactions compete with each other are reported. The presentation proceeds with examples highlighting the ideas underlying the algorithm, cf. Sec. 4.3. Finally, a large amount of results indicating its quality are presented in Sec. 4.4. Details on the specific implementation of the algorithm into `SHERPA` are given in the appendix, Sec. D.2.

4.1 NLL jet rates and Sudakov form factors

In the following the basic ideas underlying the merging of matrix elements and parton showers are discussed for the example of e^+e^-–annihilations into jets.

In the Durham scheme two particles i and j belong to different jets if they are separated by

a distance

$$y_{ij} = 2\frac{\min\{E_i^2, E_j^2\}}{Q^2}(1-\cos\theta_{ij}) \geq y_{\rm cut}\,, \tag{4.1}$$

where $y_{\rm cut} = {Q_0}^2/Q^2$ denotes a jet resolution of the clustering scheme, and Q is the overall energy scale, e.g. the c.m. energy in e^+e^-–annihilations. Then the exclusive n-jet rates can be calculated by resuming all terms up to next-to-leading logarithms (NLL) [17]. In particular these include the contributions proportional to the leading logarithms $\alpha_S^n \log^{2n}(y_{\rm cut})$ and $\alpha_S^n \log^{2n-1}(y_{\rm cut})$, viz Fig. 4.1. For $n = 2, 3, 4$ they are given by

$$R_2(Q,Q_0) = \left[\Delta_q(Q,Q_0)\right]^2\,, \tag{4.2}$$

$$R_3(Q,Q_0) = 2\left[\Delta_q(Q,Q_0)\right]^2 \int_{Q_0}^{Q} dq\,\Gamma_q(q,Q)\Delta_g(q,Q_0)\,, \tag{4.3}$$

$$\begin{aligned} R_4(Q,Q_0) = {} & 2\left[\Delta_q(Q,Q_0)\right]^2 \\ & \left\{ \int_{Q_0}^{Q} dq\,\Gamma_q(q,Q)\Delta_g(q,Q_0) \int_{Q_0}^{Q} dq'\,\Gamma_q(q',Q)\Delta_g(q',Q_0) \right. \\ & + \int_{Q_0}^{Q} dq\,\Gamma_q(q,Q)\Delta_g(q,Q_0) \int_{Q_0}^{q} dq'\,\Gamma_g(q',q)\Delta_g(q',Q_0) \\ & \left. + \int_{Q_0}^{Q} dq\,\Gamma_q(q,Q)\Delta_g(q,Q_0) \int_{Q_0}^{q} dq'\,\Gamma_f(q')\Delta_f(q',Q_0) \right\} \end{aligned} \tag{4.4}$$

where $\Gamma_{q,g,f}$ are the branching probabilities, for the branching $q \to qg$, $g \to gg$ and $g \to q\bar{q}$. At NLL accuracy they read

$$\Gamma_q(q,Q) = \frac{2C_F}{\pi}\frac{\alpha_{\rm S}(q)}{q}\left(\ln\frac{Q}{q} - \frac{3}{4}\right)\,, \tag{4.5}$$

$$\Gamma_g(q,Q) = \frac{2C_A}{\pi}\frac{\alpha_{\rm S}(q)}{q}\left(\ln\frac{Q}{q} - \frac{11}{12}\right)\,, \tag{4.6}$$

$$\Gamma_f(q) = \frac{N_f}{3\pi}\frac{\alpha_{\rm S}(q)}{q}\,, \tag{4.7}$$

with $C_F = (N_c^2-1)/2N_c$ and $C_A = N_c$ for N_c colours, N_f is the number of active flavours. The $\Delta_{q,g}$ are the well known quark and gluon Sudakov form factors

$$\Delta_q(Q,Q_0) = \exp\left(-\int_{Q_0}^{Q} dq\,\Gamma_q(q,Q)\right)\,, \tag{4.8}$$

$$\Delta_g(Q,Q_0) = \exp\left(-\int_{Q_0}^{Q} dq\,\left[\Gamma_g(q,Q) + \Gamma_f(q)\right]\right)\,, \tag{4.9}$$

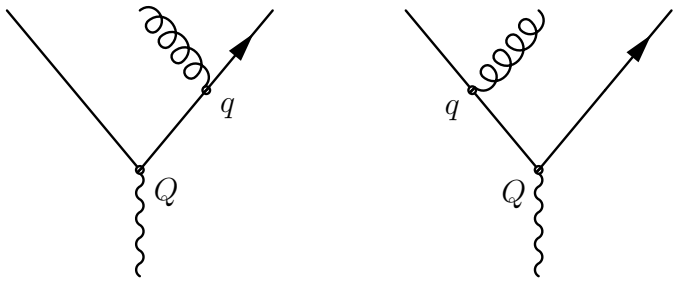

Figure 4.2: Possible topologies for the emergence of a 3 jet event in e^+e-–annihilations.

with

$$\Delta_f(Q, Q_0) = \left[\Delta_q(Q, Q_0)\right]^2 / \Delta_g(Q, Q_0) \; . \tag{4.10}$$

The expression for the two-jet rate R_2 can be understood quite easily. Knowing that a Sudakov form factor $\Delta_i(Q, Q_0)$ has interpretation as no branching probability, the two-jet rate is just the combined probability that neither the quark nor the anti-quark have emitted another parton at scales above the jet resolution scale Q_0.
On the other hand the ratio of two Sudakov form factors

$$P_{\text{nobranch}} = \frac{\Delta(Q, Q_0)}{\Delta(Q_1, Q_0)}. \tag{4.11}$$

are known to yield the probability for a parton i to evolve from a scale Q to a scale Q_1 with out any emission resolvable at Q_0.

Then the three-jet rate, given in Eq. (4.3), can be interpreted as sum of two probabilities: In either case one quark does not emit any parton resolvable at Q_0, and whereas the other quark evolves down to an intermediate scale q without any resolvable branching. Then, at the scale q, a splitting into quark and gluon occurs, and both partons evolve down to the jet resolution scale without branching any further, cf. Fig. 4.2.
Further scrutinising the expression for the three-jet rate given in Eq. (4.3), a differential form can be derived,

$$\begin{aligned} \frac{dR_3(Q, Q_0)}{dq} &= 2\left[\Delta_q(Q, Q_0)\right]^2 \Gamma_q(q, Q)\Delta_g(q, Q_0) \\ &= \Gamma_q(q, Q)\, F_{q\bar{q}g}(Q_0, Q; q) \, . \end{aligned} \tag{4.12}$$

It can be observed that the differential rate can be subdivided into a part for splitting of the quark, which is represented by the integrated splitting kernel $\Gamma_q(q, Q)$ and a product of Sudakov form factors, namely $F_{q\bar{q}g}(Q_0, Q; q)$. The integrated splitting kernel is of order α_S^1, whereas the Sudakov form factor contains the resumation. Similar expressions can be obtained for the four-jet rate. Here, the differential rate for the Abelian part is given by

$$\begin{aligned} \frac{dR_4^A(Q, Q_0)}{dq\, dq'} &= 2\left[\Delta_q(Q, Q_0)\right]^2 \Gamma_q(q, Q)\, \Delta_g(q, Q_0)\, \Gamma_q(q', Q)\Delta_g(q', Q_0) \\ &= \Gamma_q(q, Q)\, \Gamma_q(q', Q)\, F_{q\bar{q}gg}(Q_0, Q; q, q') \, , \end{aligned} \tag{4.13}$$

and differential rate for the Non-Abelian part reads

$$\begin{aligned}\frac{dR_4^{NA}(Q,Q_0)}{dq\,dq'} &= 2\left[\Delta_q(Q,Q_0)\right]^2\,\Gamma_q(q,Q)\,\Delta_g(q,Q_0)\,\Gamma_g(q',q)\,\Delta_g(q',Q_0)\\ &= \Gamma_q(q,Q)\,\Gamma_g(q',q)\,F_{q\bar{q}gg}(Q_0,Q;q,q')\,. \end{aligned} \tag{4.14}$$

It should be noted, that the differential four-jet rates for Abelian and Non-Abelian part differ only in the combination of splitting kernels, while the Sudakov form factor $F_{q\bar{q}gg}(Q_0,Q;q,q')$ are the same. Again, the splitting kernel is found to be of order α_S^2, while the Sudakov form factor contains the resumation starting with order α_S^0. Similar findings hold true for higher jet rates as well. The differential jet rate for the production of four quarks, together with the corresponding expressions for the five-jet rate are summarised in Appendix C.

The idea now is to obtain an improved NLL jet rate by combining fixed order matrix elements and resumed order jet rates, which is achieved by replacing the splitting kernels in Eqs. (4.12) - (4.14) with the corresponding leading order matrix elements. This is possible because splitting kernels are obtain by the small angle approximation of the corresponding matrix element. Consequently the expressions have the same behaviour in the regime of leading logarithms, i.e. small jet measures y_{ij}. On the other hand the combination of Sudakov form factors approaches one in the regime of large angle emission, where the matrix elements are known to yield the correct description. Thus, the inclusion of the matrix elements in the jet rates results in improved NLL jet-rates, which are the starting point for the merging procedure discussed below.

4.2 The algorithm

In this section the merging algorithm together with its extensions, as implemented in `SHERPA`, will be discussed. It can be divided into three parts. First of all, a sample of matrix elements has to be defined, from which processes are selected for the generation of individual events. The four-momenta of the particles are distributed according to the corresponding matrix element. Then, having fixed the number, flavours and four-momenta of the particles, a pseudo parton shower history is constructed through backwards clustering of the particles according to the $k_\perp$-algorithm. Here, care has to be taken in situations, where one particular clustering allows for different colour flows. The nodal values of this clustering serve as input for the construction of a weight applied on the matrix element. This weight resums higher order effects at leading logarithmic accuracy and consists of Sudakov form factors for coloured lines (e.g., quarks or gluons) and of ratios of the strong coupling constant. If the event is accepted, parton showers are attached to the outgoing particles. For this, again the nodes of the clustering serve as input. Inside the parton shower, those emissions are vetoed that lead to additional unwanted jets. At this point there is some subtlety, since it is obviously impossible to calculate matrix elements for an infinite number of additional jets. Hence, there is some maximal number $n_{\max}$ of jets covered by the matrix elements, higher jet multiplicities must be accounted for by the parton shower. This leads to a somewhat modified treatment of the parton shower for those events with $n_{\max}$ jets stemming from the matrix elements.

Apart from this special treatment for configurations with the largest number of jets produced through matrix elements, there are cases where a similar treatment is necessary for configurations with the minimal number of jets. Examples include both electroweak such

as $e^+e^- \to W^+W^- \to jets$ and the QCD production of jets in hadronic collisions. Using the $k_\perp$ measure to separate matrix elements with the minimal number of jets $n_{\min}$ from higher jet multiplicities with $n > n_{\min}$ also restricts the phase space for the minimal number of jets. Since the separation of different jet multiplicities is slightly washed out by the parton shower and hadronisation, the lowest jet multiplicity samples experience a loss of events at the phase space boundary, which is not compensated for by smaller jet multiplicities. To deal with this problem one may try to use generation cuts that are much tighter than the analysis cuts - an option that is clearly not very efficient. Alternatively, a lower jet definition cut may be used for the lowest jet multiplicity. This idea leads to an extension of the algorithm, which enables a merging of processes with different jet multiplicities and different separation cuts. In fact, this algorithm is closely related to the highest multiplicity treatment.

In the following, the algorithm and some of its refinements are discussed in greater detail, dividing the procedure into three steps, namely matrix element generation, parton clustering and Sudakov weight construction and into, finally, running the parton showers.

4.2.1 Combination of matrix elements

1. Composition of the process samples:
   In each run, processes with a fixed identical number of electroweak couplings may be combined, which differ only in the number of extra jets produced through QCD. All strongly interacting particles are subject to phase space cuts according to the $k_\perp$-algorithm [17–19]. This is necessary in order to allow a reweighting of the matrix element with Sudakov form factors. Phase space cuts on other particles are not needed unless for the sake of avoiding potential infrared divergencies. As an example consider the case of a (massless) lepton pair, which have to be cut through, e.g. a cone algorithm or by demanding some minimal invariant masses.

   In the original algorithm, however, it was implicitly assumed that any gauge boson of the electroweak interactions is connected to maximally one strongly interacting line only; in other words, it was implicitly assumed that any photon, W or Z boson would couple to one quark line only. The present proposal aims at widening the scope in such a way that competition between strong and electroweak interactions is possible.

2. Selection of a particular process:
   For all the processes contributing in a single run, labelled with i, total cross sections are evaluated at tree-level through

$$\sigma_i^{(0)} = \int \mathrm{d}\Omega |\mathcal{M}(\mu_R, \mu_F)|^2 \,, \tag{4.15}$$

   where $\mathrm{d}\Omega$ denotes the integral over the available phase space. For convenience, here any eventual integration over the Bjorken-x of incoming partons is subsumed in $\mathrm{d}\Omega$. The matrix element $\mathcal{M}$ eventually is extended by parton distribution functions; it is evaluated at $\mu_R = \mu_F = Q_{\mathrm{cut}}$, the cut parameter of the $k_\perp$-algorithm[1].

[1] A comment is in order here: Often in hadronic collisions, it proves useful to use the $k_\perp$ algorithm with a parameter D, which can be identified as a pseudo cone-size. In such a case, the Q_{cut} value is rescaled by D.

The probability $\mathcal{P}_i$ for a process i to be selected for event generation is then given by

$$\mathcal{P}_i^{(0)} = \frac{\sigma_i^{(0)}}{\sum_j \sigma_j^{(0)}} \,. \tag{4.16}$$

Having selected the process, four-momenta for the incoming and outgoing particles are chosen according to its matrix element.

3. Highest multiplicity treatment:
For those processes that have the highest multiplicity of jets in the matrix element, i.e. where $n = n_{\max}$, already during integration the scale Q_s of the softest jet produced through QCD is determined according to the $k_\perp$-algorithm. Then, the parton distribution functions in the matrix element are taken at the factorisation scale $\mu_F = Q_s$, whereas the renormalisation scale used in the evaluation of the coupling constant remains at $\mu_R = Q_{\text{cut}}$. Of course, this will later on affect the Sudakov weights and the parton showering as well; at that point, however, it implicitly takes into account the possibility of having softer extra jets emitted in the initial state parton shower.

4. Multi-cut treatment:
There is some condition that the multi-cut treatment does not lead to ambiguities, namely that the jet definition becomes tighter with increasing jet multiplicity. In other words, for each jet multiplicity n, a jet separation cut $Q_{\text{cut}}^{(n)}$ is defined such that $Q_{\text{cut}}^{(n-1)} \leq Q_{\text{cut}}^{(n)}$. For the calculation of the corresponding a priori cross sections $\sigma^{(n)}$ the factorisation scale is also set dynamically to

$$\mu_F = Q_{\min} = \min\left\{Q_s, Q_{\text{cut}}^{(n+1)}\right\} \,, \tag{4.17}$$

where Q_s is the scale of the softest jet in the process. Again, the renormalisation scale is fixed at $\mu_R = Q_{\text{cut}}^{(n)}$.

4.2.2 Pseudo parton shower history

1. Clustering of particles:
In the original version of the merging procedure, only QCD clusterings have been considered. There, for each allowed pair of partons a relative transverse momentum has been defined. According to the $k_\perp$-algorithm, its square reads

$$Q_{ij}^2 = 2\min\{E_i^2, E_j^2\}(1 - \cos\theta_{ij}) \tag{4.18}$$

for a pair of partons in e^+e^- collisions. In hadronic collisions it is given by

$$Q_{ij}^2 = 2\min\{p_{\perp,i}^2, p_{\perp,j}^2\}\,\left[\cosh^2(\eta_i - \eta_j) - \cos^2(\phi_i - \phi_j)\right] \tag{4.19}$$

for the clustering of two final state hadrons, and by

$$Q_i^2 = p_{\perp,i}^2 \tag{4.20}$$

when a final state parton is to be clustered with an initial state particle. In the original algorithm, the pair with the lowest $k_\perp$ has been clustered. In order to prohibit "illegal"

clusterings, such as, for instance, the clustering of two quarks instead of a quark-anti-quark pair, only those pairs have been considered that correspond to a Feynman diagram contributing to the process in question.

Going beyond this, some new problems may manifest themselves, which are related to the possibility of having competing colour flows. A good example for this is the possible competition of clustering a quark-anti-quark pair into either a gluon or a Z-boson. To resolve this ambiguity, there are, in principle, two options: One would be to globally select a specific colour configuration according to the relative weight of different colour-ordered amplitudes. This is clearly the preferred choice. The other one, that will be pursued as a proposal here, is to try to decide locally which colour configuration to chose.

For this, relative weights are constructed for each possible clustering, which take into account the coupling and pole structure of the underlying Feynman diagram(s). In each case, the contribution $\mathcal{W}_{ij}$ to the weight for a specific clustering of two particles $ij \to k$ can be written as

$$\mathcal{W}_{ij;k}(q) = \frac{[g_{ij}(\mu_R) g_{kl}(\mu_R)]^2}{(q^2 - m_k^2)^2 + m_k^2 \Gamma_k^2}\,, \tag{4.21}$$

where $g_{ij}(\mu_R)$ is the coupling constant at the vertex and $g_{kl}(\mu_R)$ denotes the coupling constant of the resulting propagator in the potential next clustering $kl \to m$. In addition, the propagator term contains the mass and the (fixed) width of particle k. Clearly, m_k and Γ_k may be zero, for instance for gluons or massless quarks. In the equation above, q^2 is the square of the four-momentum q of the pair ij.

Now, for each allowed clustering of pairs ij, all potential $\mathcal{W}_{ij}(q)$ with different coupling structure are added, and the pair with the largest total weight

$$\mathcal{W}_{ij}^{\text{tot}}(q) = \sum_k \mathcal{W}_{ij;k}(q) \tag{4.22}$$

is selected. The emerging propagator k is then chosen according to the relative probability

$$\mathcal{P}_k = \frac{\mathcal{W}_{ij;k}(q)}{\mathcal{W}_{ij}^{\text{tot}}(q)}\,. \tag{4.23}$$

2. Core $2 \to 2$ process:
In the original as well as in the extended version of the merging algorithm, proposed here, this clustering procedure is repeated recursively, until a core $2 \to 2$ process is recovered. It defines the initial colour flow in the large N_c limit necessary for the fragmentation. In addition, through this choice of an initial colour flow, the hard process scales Q_h for the partons in this process are defined. The following cases must be considered:

   - Two particles with and two particles without colour quantum number, for instance $e^+e^- \to q\bar{q}$, $q\bar{q} \to e^+e^-$, or $gg \to H \to \tau\tau$ in an effective model for the ggH coupling. Then, for the two coloured objects, $Q_h^2 = \hat{s}$.

- Three particles with colour quantum numbers and one without, for instance in $q\bar{q} \to Wg$. Then, for the incoming particles $Q_h^2 = \hat{s}$, and for the outgoing ones Q_h is given by their transverse momentum.
- Four particles with colour. In this case, often different colour structures are competing. The selection is then made according to relative contributions which can usually be connected with the $\hat{s}$, $\hat{t}$ or $\hat{u}$ channel exchange of colour. The hard scale for all four particles is then chosen according to this selection. Hence, usually, the minimum of $\hat{u}$ and $\hat{t}$ is the relevant scale.

3. Construction of the Sudakov weight:
Having fixed the parton shower sequence and the hard scales Q_h, the Sudakov weight can be calculated. To a large extent, the construction prescription for this is the same for the original approach as well as for its proposed extension. In both cases, the Sudakov weights consists of ratios of the strong coupling constant taken at the varying nodal scales and at the fixed renormalisation scale and of Sudakov form factors, which in next-to-leading logarithmic (NLL) approximation are given by

$$\Delta(Q, Q_0) = \exp\left[-\int_{Q_0}^{Q} \mathrm{d}q\, \Gamma(Q, q)\right] . \tag{4.24}$$

Here, $\Gamma(Q, q)$ is the integrated splitting function for the particle in question. For convenience, it incorporates a factor $\alpha_S(q)/q$. Integrated splitting functions for different splittings are listed in appendix D.2. In terms of these constituents the Sudakov weight is constructed as a product of

- factors $\alpha_S(Q)/\alpha_S(\mu_R)$ for each node with $Q = k_\perp$ which involves a strong coupling constant;
- factors $\Delta(Q_1, Q_{\mathrm{cut}})/\Delta(Q_2, Q_{\mathrm{cut}})$ for each internal line (propagator) that carries colour quantum numbers, where the arguments are given by the nodal $k_\perp$ scales Q_1 and Q_2;
- and of factors $\Delta(Q_1, Q_{\mathrm{cut}})$ for colour-charged outgoing lines emerging at a node with $Q_1 = k_\perp$.

At this point it should be noted that in such cases where coloured particles are produced through s-channel electroweak interactions the nodal scale value of the vertex should be the invariant mass $\hat{s}$ of the particles rather than their transverse momentum, which again is beyond the scope of the original algorithm.

4. Highest multiplicity treatment:
In case, a hard process with the maximal number of jets accommodated by the matrix elements has been chosen, the parton shower must be able to produce higher jet configurations. Of course, these additional jets may in principle emerge at transverse momenta larger than the jet definition cut Q_{cut}. On the other hand, it is clear that they should be softer than the softest jet produced by the matrix element in order to ensure that the matrix element is used to cover the hard regions of phase space. Since the Sudakov form factors forming the weight attached to the matrix elements

can be identified as a no-radiation probability between two scales, the soft scales of the Sudakov form factors need to be modified. Because in this situation radiation from the parton shower must be softer than Q_s, the scale of the softest jet in the matrix element, rather than Q_{cut}, this modification amounts to a replacement $Q_{\text{cut}} \to Q_s$ in all Sudakov form factors, i.e. for both internal and external lines.

5. Multi-cut treatment:
Similarly to the highest multiplicity treatment discussed above, in the multi-cut treatment the soft scales of the Sudakov weight are also set dynamically, i.e. in dependence on the actual kinematical configuration. The scale Q_{cut} in the Sudakov form factors for an n-jet process is replaced by Q_{min} defined according to Eq. (4.17). In case the process is purely electroweak, like $e^+e^- \to ZZ \to q\bar{q}q\bar{q}$, this prescription translates into completely switching off all Sudakov form factors if $Q_s \leq Q_{\text{cut}}^{(n+1)}$.

4.2.3 Starting the parton shower

1. Vetoing emissions:
According to the paradigm of the merging procedure, inside the parton shower[2] all emissions leading to extra unwanted jets are vetoed. This is implemented in the following way:

   - The probability for no branching resolvable at a scale t_0, usually the infrared cut-off of the parton shower, between two scales t_1 and t_2 is given by the ratio

   $$\mathcal{P}_{\text{no}}(t_1, t_2) = \frac{\Delta(t_1, t_0)}{\Delta(t_2, t_0)} \tag{4.25}$$

   of Sudakov form factors. Equating this with a random number allows solving for t_2, the scale of the next trial emission[3].

   - Having at hand the transverse momentum related to this trial emission, it can be compared with the jet resolution of the $k_\perp$-algorithm. If this particular emission would give rise to an unwanted jet, the next trial emission is constructed with its upper scale t_1 equal to the actual scale t_2 of the vetoed emission.

   For a single parton line starting at some scale Q the matrix element correction weight reads

   $$W_{\text{ME}} = \Delta(Q, Q_{\text{cut}})\,. \tag{4.26}$$

[2]It should be noted here that SHERPA employs a parton shower ordered by virtualities, supplemented by an explicit veto on rising opening angles in branching processes. This is an apparent mismatch to the transverse momenta taken as scales so far. Thus, in the following it should be understood that all scales Q emerging from the parton shower denote the transverse momentum that can be approximated from the splitting kinematics formulated in terms of t, the respective virtual mass.

[3]It should be noted here that in usual parton shower programs the Sudakov form factors rely on the integral over splitting functions rather than on integrated splitting functions. Therefore, usually a splitting variable z is selected with a second random number. In SHERPAs parton shower module APACIC, only then transverse momenta can be constructed from t and z. This, however, is primarily a technical issue.

The combined weight of all possible rejections due to vetoed emissions in the parton shower for the same parton, starting at scale Q at NLL accuracy reads

$$\begin{aligned} W_{\mathrm{PS}} &= \left[1 + \int_{Q_{\mathrm{cut}}}^{Q} \mathrm{d}q\, \Gamma(Q,q) + \int_{Q_{\mathrm{cut}}}^{Q} \mathrm{d}q\, \Gamma(Q,q) \int_{Q_{\mathrm{cut}}}^{q} \mathrm{d}q'\, \Gamma(Q,q') + \dots\right] \\ &= \Delta^{-1}(Q, Q_{\mathrm{cut}})\,. \end{aligned} \tag{4.27}$$

Combining both thus formally leads to a cancellation of large logarithms of the form $\log Q/Q_{\mathrm{cut}}$ at NLL precision. However, there are remaining dependencies on Q_{cut}, some of which are due to the fact that the actual implementation of the parton shower is at a different level of logarithmic accuracy.

For the highest multiplicities or for the multi-cut treatment, the veto of course is performed w.r.t. Q_s or Q_{min}, respectively. In case the process is purely electroweak no shower veto is applied at all as long as $Q_{\mathrm{min}} \leq Q_{\mathrm{cut}}$.

2. Starting scales:
   The reasoning above immediately implies which starting scales are to be chosen for the parton shower evolution of each parton. In each case it should be the scale where the parton was first produced, in accordance with how the Sudakov weights are constructed and how the vetoing applied in the parton shower cancels the dependence on the jet resolution scale.

   There is one last minor point to be discussed, namely the scale, at which the parton density functions are evaluated in the backward evolution of initial state showers. Remember that there, in order to recover the correct parton distribution functions at each step of the space-like evolution, the ratio of Sudakov form factors describing the no-branching probability between t_1 and t_2 are supplemented with corresponding factors, namely,

$$\mathcal{P}_{\mathrm{no}}(t_1, t_2) = \frac{f(x,\, t_2)}{f(x,\, t_1)} \cdot \frac{\Delta(t_1, t_0)}{\Delta(t_2, t_0)}\,. \tag{4.28}$$

   If this expression is to describe the first emission through the parton shower along an incoming parton line, the hard scale t_1 in the parton distribution function is replaced by either Q_{cut} (or Q_s or Q_{min}, if the process in question has the maximal number of jets in the matrix element, or if the multi-cut treatment is active).

4.3 Examples

In this section, the algorithms discussed above are illustrated through some examples, namely

1. $e^+e^- \to$ jets,
2. $p\bar{p} \to W +$ jets ,
3. $p\bar{p} \to$ jets , and
4. $e^+e^- \to d\bar{d}u\bar{u}(g)$.

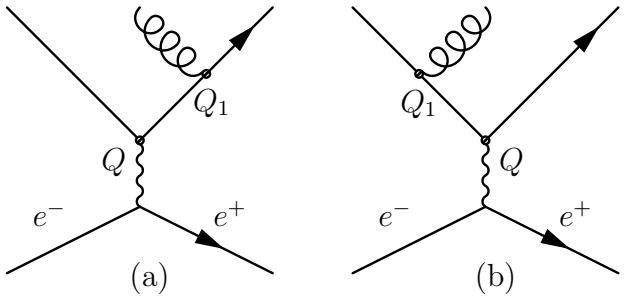

Figure 4.3: The diagrams contributing to $e^+e^- \to 3$jets.

4.3.1 Example I – $e^+e^- \to$ jets

As a first example for the original version of the algorithm, consider the process $e^+e^- \to$ jets at LEP1. Choosing a jet resolution of $Q_{\text{cut}} = 5.77\,\text{GeV}$ ($y_{\text{cut}} = 0.004$ in the Durham scheme), the a-priori cross sections $\sigma_i^{(0)}$ and the resulting effective cross sections $\sigma_i = \sigma_i^{(0)} \cdot W_{\text{ME}}$ for a specific choice of $\alpha_S = 0.127$ are given by

$$
\begin{aligned}
\sigma_2^{(0)} &= 40.46\,\text{nb} & \sigma_2^{\text{nmax}=5} &= 18.80\,\text{nb} & (\mathcal{R}_2 &= 38.8\%)\\
\sigma_3^{(0)} &= 43.38\,\text{nb} & \sigma_3^{\text{nmax}=5} &= 21.10\,\text{nb} & (\mathcal{R}_3 &= 43.5\%)\\
\sigma_4^{(0)} &= 14.05\,\text{nb} & \sigma_4^{\text{nmax}=5} &= 6.90\,\text{nb} & (\mathcal{R}_4 &= 14.2\%)\\
\sigma_5^{(0)} &= 2.80\,\text{nb} & \sigma_5^{\text{nmax}=5} &= 1.69\,\text{nb} & (\mathcal{R}_5 &= 3.5\%)\\
& & \sigma_{\text{tot}}^{\text{nmax}=5} &= \sum_{i=2}^{5} \sigma_i^{\text{nmax}=5} = 48.49\,\text{nb}
\end{aligned}
$$

Assume now that at some point a three-jet event is chosen with a $q\bar{q}g$ final state. The diagrams contributing to this process are depicted in Fig. 4.3. There are two allowed clusterings, namely qg and $\bar{q}g$. If the former leads to a smaller $k_\perp$, i.e. if $Q(qg) < Q(\bar{q}g)$ this clustering is selected, of course with scale $Q_1 = Q(qg)$, and the core $2 \to 2$ process is readily recovered. Its associated hard scale is $Q = \sqrt{s}$. The Sudakov weight is constructed, leading to

$$
\begin{aligned}
\mathcal{W}_{\text{ME}} &= \Delta_{\bar{q}}(Q, Q_{\text{cut}})\, \frac{\Delta_q(Q, Q_{\text{cut}})}{\Delta_q(Q_1, Q_{\text{cut}})}\, \frac{\alpha_S(Q_1)}{\alpha_S(Q_{\text{cut}})}\, \Delta_q(Q_1, Q_{\text{cut}}) \Delta_g(Q_1, Q_{\text{cut}})\\
&= \Delta_{\bar{q}}(Q, Q_{\text{cut}})\, \Delta_q(Q, Q_{\text{cut}})\, \frac{\alpha_S(Q_1)}{\alpha_S(Q_{\text{cut}})}\, \Delta_g(Q_1, Q_{\text{cut}})\,, \qquad (4.29)
\end{aligned}
$$

where the first factor in the first line corresponds to the anti-quark line, the second factor is for the internal quark line, the ratio of the strong coupling constants applies for the vertex, and the two last factors correspond to the two outgoing lines. Emissions in the parton shower for all three lines are vetoed if their transverse momentum is larger than Q_{cut}; the start scales for the parton shower evolution are t for both the quark and the anti-quark line, and t_1 for the gluon.

If, in contrast in the simulation the matrix elements are restricted by $n_{\text{max}} = 3$, the highest multiplicity treatment would apply to the three-jet configuration. Consequently,

the cross sections and rates change according to

$$\begin{aligned}
\sigma_2^{(0)} &= 40.46\,\text{nb} & \sigma_2^{\text{nmax}=3} &= 18.80\,\text{nb} & (\mathcal{R}_2 = 36.3\%) \\
\sigma_3^{(0)} &= 43.38\,\text{nb} & \sigma_3^{\text{nmax}=3} &= 32.94\,\text{nb} & (\mathcal{R}_3 = 63.7\%) \\
& & \sigma_{\text{tot}}^{\text{nmax}=3} &= \sum_{i=2}^{3} \sigma_i^{\text{nmax}=3} = 51.74\,\text{nb}\,,
\end{aligned} \tag{4.30}$$

and the weight for the three-jet configuration would be given by

$$\begin{aligned}
\tilde{\mathcal{W}}_{\text{ME}} &= \Delta_{\bar{q}}(Q, Q_1)\, \frac{\Delta_q(Q, Q_1)}{\Delta_q(Q_1, Q_1)}\, \frac{\alpha_S(Q_1)}{\alpha_S(Q_1)}\, \Delta_q(Q_1, Q_1) \Delta_g(Q_1, Q_1) \\
&= \Delta_{\bar{q}}(Q, Q_1)\, \Delta_q(Q, Q_1)\,.
\end{aligned} \tag{4.31}$$

Emissions in the parton shower for all three lines would then be vetoed if their transverse momentum was larger than Q_1; the start scales for the parton shower evolution again are t for both the quark and the anti-quark line, and t_1 for the gluon.

4.3.2 Example II – $p\bar{p} \to W +$ jets

The next example that will be considered is a case where both initial and final state emissions may occur. Hence, the reconstruction of the pseudo parton shower history and the evaluation of the corresponding weight is more involved.
Again, the starting point will be the calculation of cross sections. For $Q_{\text{cut}} = 20$ GeV, $\alpha_S = 0.118$, and by using the CTEQ6L parton distribution functions, they read

$$\begin{aligned}
\sigma_0^{(0)} &= 953.03\text{pb} & \sigma_0^{\text{nmax}=3} &= 825.77\text{pb} \\
\sigma_1^{(0)} &= 155.76\text{pb} & \sigma_1^{\text{nmax}=3} &= 108.35\text{pb} \\
\sigma_2^{(0)} &= 36.75\text{pb} & \sigma_2^{\text{nmax}=3} &= 20.10\text{pb} \\
\sigma_3^{(0)} &= 7.22\text{pb} & \sigma_3^{\text{nmax}=3} &= 3.32\text{pb} \\
& & \sigma_{\text{tot}}^{\text{nmax}=3} &= \sum_{i=0}^{3} \sigma_i^{\text{nmax}=3} = 957.54\text{pb}\,.
\end{aligned} \tag{4.32}$$

In the following, the construction of the weights for different multiplicities and the starting conditions for the subsequent parton shower will be briefly discussed.

1. $n = 0$:
   Starting with the lowest multiplicity of jets produced in the matrix element, $n = 0$, the leading order contributions to W^- production are recovered. They are of the Drell–Yan type, i.e. processes of the form

   $$q\,\bar{q}' \to e\bar{\nu}_e\,.$$

   Obviously, this is already a $2 \to 2$ process, therefore clustering does not take place. Due to the absence of any strong interaction, the rejection weight is merely given by two quark Sudakov form factors:

   $$\mathcal{W}_{\text{ME}} = \Delta_q(Q, Q_{\text{cut}})\, \Delta_{\bar{q}'}(Q, Q_{\text{cut}})\,, \tag{4.33}$$

   where the hard scale Q is fixed by the invariant mass of the fermion pair, $Q^2 = M^2_{e\bar{\nu}_e}$.

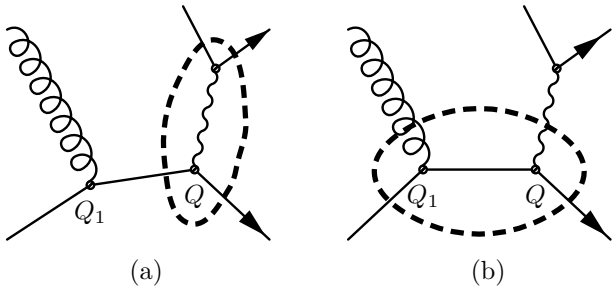

Figure 4.4: Two possible cluster configurations of $W+1$jet events. The dashed line highlights the hard $2 \to 2$ process.

The parton shower for both the quark and the anti-quark in the initial state starts with scale t, for the first emission. However, the parton distribution weight is taken at $\mu_F = Q_{\text{cut}}$, i.e. it is given by $\mathcal{W}_{\text{PDF}} = f(x,q)/f(x,\mu_F)$ rather than by $\mathcal{W}_{\text{PDF}} = f(x,q)/f(x,Q)$. Also, the jet veto inside the parton shower is performed w.r.t. Q_{cut}.

2. $n = 1$:
For $n = 1$ jets, different cluster configurations are possible, two of which are exhibited in Fig. 4.4. The hard $2 \to 2$ process either is again of the Drell–Yan type (Fig. 4.4a) or, for example, of the type $q\bar{q}' \to gW$ (Fig. 4.4b). The respective weights in both cases read:

$$\mathcal{W}_{\text{ME}}^{(a)} = \mathcal{W}_{\text{ME}}^{(b)} = \Delta_q(Q, Q_{\text{cut}})\, \Delta_{\bar{q}'}(Q, Q_{\text{cut}})\, \Delta_g(Q_1, Q_{\text{cut}}) \frac{\alpha_s(Q_1)}{\alpha_s(Q_{\text{cut}})} \,. \tag{4.34}$$

where Q is the scale of the core $2 \to 2$ process and the nodal value Q_1 is given by the transverse momentum of the extra jet. For the first configuration, $Q^2 = p_W^2 = M_{e\nu}^2$, and the gluon jet tends to be soft, i.e. Q_1 preferentially is close to Q_{cut}. The second configuration differs from the first only by the result of the clustering and in the scale of the core process, now given by

$$Q^2 = p_{\perp,g}^2 + M_{e\bar{\nu}_e}^2 = M_{\perp,W}^2 \,. \tag{4.35}$$

The transverse momentum of the gluon jet $p_{\perp,g}^2$ now is of the order of the W-boson mass. In the first case, $Q_1 = p_{\perp,g}$ emerges as a part of the clustering procedure, whereas in the second case, it is read off directly from the core process. It is important, however, that the scale in both cases is defined in the same way in order to guarantee a smooth transition between the regime where clustering (a) and the regime where clustering (b) is chosen.

In both cases considered here, the parton shower for both the quark and the anti-quark in the initial state again starts with the respective scale t, and the parton distribution weights are treated in the same manner as before. The parton shower for the final state jet in contrast starts at t_1, all emissions in the three parton showers are vetoed if their transverse momentum exceeds Q_{cut}.

3. $n = 2$:
Many processes contribute to the production of two extra jets, some illustrative examples are displayed in Fig. 4.5. The cases a) and b) displayed there are very similar

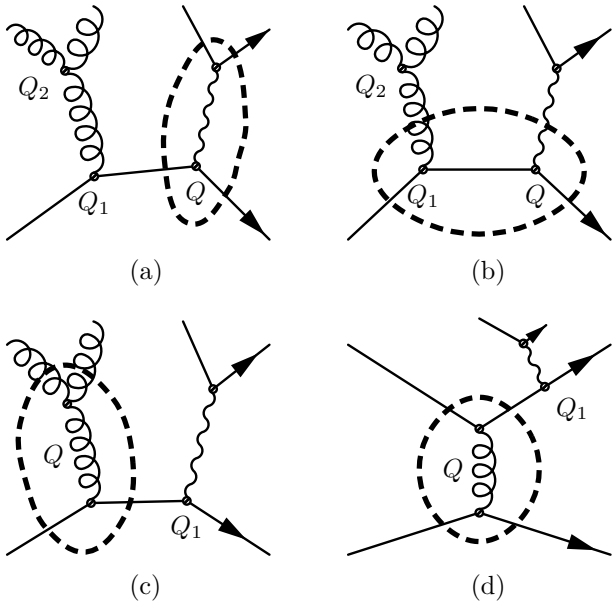

Figure 4.5: Four possible cluster configurations of a $W + 2$jet event. The dashed line highlights the hard $2 \to 2$ process, being either of Drell–Yan type (a), a vector boson production (b) or a pure QCD process (c,d).

to the example with one extra jet only. The corresponding weights read:

$$\mathcal{W}^{(a)}_{\mathrm{ME}} = \mathcal{W}^{(b)}_{\mathrm{ME}} = \Delta_q(Q, Q_{\mathrm{cut}})\, \Delta_{\bar{q}'}(Q, Q_{\mathrm{cut}}) \times \Delta_g(Q_1, Q_{\mathrm{cut}})\, \Delta_g(Q_2, Q_{\mathrm{cut}}) \frac{\alpha_s(Q_1)}{\alpha_s(Q_{\mathrm{cut}})}\, \frac{\alpha_s(Q_2)}{\alpha_s(Q_{\mathrm{cut}})} \,. \quad (4.36)$$

The nodal value Q_2 is given by the $k_\perp$-algorithm, again it is the transverse momentum of the gluon. The scales Q_1 and Q are chosen in full analogy to the one-jet case discussed above.

In contrast a new situation arises when a pure QCD process has been chosen as the "core" $2 \to 2$ process, see for instance Fig. 4.5c). Since the "core" process is not resolved, there is only one scale available, $Q^2 = p_\perp^2$, the transverse momentum of the outgoing jets. The correction weight in this case thus reads:

$$\mathcal{W}^{(c)}_{\mathrm{ME}} = \Delta_q(Q, Q_{\mathrm{cut}})\, \frac{\Delta_q(Q, Q_{\mathrm{cut}})}{\Delta_q(Q_1, Q_{\mathrm{cut}})}\, \Delta_{\bar{q}'}(Q_1, Q_{\mathrm{cut}})\, [\Delta_g(Q, Q_{\mathrm{cut}})]^2 \left[\frac{\alpha_s(Q)}{\alpha_s(Q_{\mathrm{cut}})}\right]^2 . \quad (4.37)$$

In this case, the Sudakov form factors in the denominator corresponding to the internal quark line and its external continuation cancel only, if both quarks have the same mass, which is not necessarily the case[4].

In contrast to the case exhibited in diagram 4.5c), where the boson was clustered with an initial state parton, Fig. 4.5d) pictures an example configuration, where the boson

[4]This example shows that the prescription implicitly deals with flavour changing currents as well.

is clustered with a final state parton. In this case, the corresponding correction weight is given by

$$\mathcal{W}_{\mathrm{ME}}^{(d)} = [\Delta_q(Q, Q_{\mathrm{cut}})]^2 \, \frac{\Delta_{q'}(Q, Q_{\mathrm{cut}})}{\Delta_{q'}(Q_1, Q_{\mathrm{cut}})} \, \Delta_{q''}(Q_1, Q_{\mathrm{cut}}) \Delta_{\bar{q}'}(Q, Q_{\mathrm{cut}}) \left[\frac{\alpha_s(Q)}{\alpha_s(Q_{\mathrm{cut}})}\right]^2 . \tag{4.38}$$

The starting conditions for the parton showers for the first two cases, Fig. 4.5c) and 4.5b), are very similar to the $n = 1$ case: The initial state partons start their evolution at t, the two extra jets start their evolution at t_1 and t_2, respectively, and all are subject to a jet veto inside the parton shower with transverse momentum Q_{cut}. For the last two cases, the situation changes. There, the electroweak boson does not play any significant role for the parton shower; all four parton showers start at their common QCD core process scale, t. Of course, again, emissions with transverse momentum larger than Q_{cut} from any of the four shower seeds are vetoed. It should be noted here that there is a potential mismatch of logarithms of correction weight and veto weight in the quark line that changes its flavour. This happens if the two quarks adjacent to the electroweak boson have different mass; mass effects, however, usually can be safely neglected as long as no top quarks are present.

The extension to higher multiplicities is straightforward. However, assume again for illustrative reasons that $n_{\max} = 2$, leading to the application of the highest multiplicity treatment for the two-jet configuration. Then, during cross section evaluation the factorisation scale is set dynamically to $\mu_F = Q_s$, i.e. to the nodal value of the softest emission. This leads to the following cross sections

$$\begin{aligned}
\sigma_0^{(0)} &= 953.03\mathrm{pb} & \sigma_0^{\mathrm{nmax}=2} &= 825.77\mathrm{pb} \\
\sigma_1^{(0)} &= 155.76\mathrm{pb} & \sigma_1^{\mathrm{nmax}=2} &= 108.35\mathrm{pb} \\
\sigma_2^{(0)} &= 34.29\mathrm{pb} & \sigma_2^{\mathrm{nmax}=2} &= 22.01\mathrm{pb} \\
& & \sigma_{\mathrm{tot}}^{\mathrm{nmax}=2} &= \sum_{i=0}^{2} \sigma_i^{\mathrm{nmax}=2} = 956.13\mathrm{pb}\,.
\end{aligned} \tag{4.39}$$

Assuming that $Q_2 < Q_1$, the correction weight for the diagram a) in Fig. 4.5 would read

$$\begin{aligned}
\tilde{\mathcal{W}}_{\mathrm{ME}}^{(a)} &= \Delta_q(Q, Q_2) \, \Delta_{\bar{q}'}(Q, Q_2) \, \Delta_g(Q_1, Q_2) \, \Delta_g(Q_2, Q_2) \frac{\alpha_s(Q_1)}{\alpha_s(Q_2)} \, \frac{\alpha_s(Q_2)}{\alpha_s(Q_2)} \\
&= \Delta_q(Q, Q_2) \, \Delta_{\bar{q}'}(Q, Q_2) \, \Delta_g(Q_1, Q_2) \, \frac{\alpha_s(Q_1)}{\alpha_s(Q_2)} \, .
\end{aligned} \tag{4.40}$$

The parton showers for the four legs would start at t for the two quark lines, and at t_1 and t_2 for the two gluon lines, respectively. Vetos would be applied for emissions with a $k_\perp$ larger than Q_2, which implies that there would be no jet veto in the parton shower evolution of the second gluon line. Of course, the scales in the parton distribution weights of the first initial state radiation inside the shower would also be adjusted.

The situation is even more extreme when considering diagram d). There, the softest QCD radiation actually is at the core process. Thus, no correction weight whatsoever

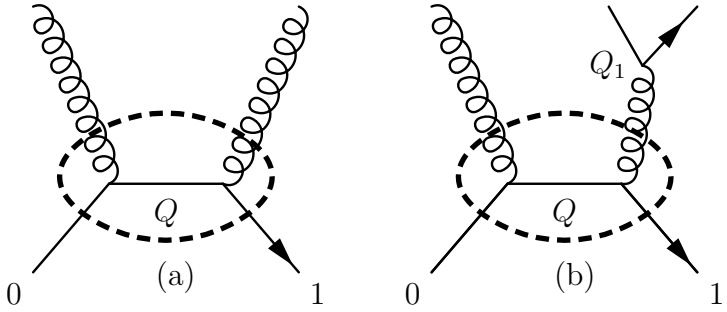

Figure 4.6: Examples for the production two and three jets.

would be applied, cf. Eq. 4.38, if the masses of q' and q'' are identical,

$$\tilde{\mathcal{W}}^{(d)}_{\mathrm{ME}} = [\Delta_q(Q,Q)]^2 \frac{\Delta_{q'}(Q,Q)}{\Delta_{q'}(Q_1,Q)} \Delta_{q''}(Q_1,Q)\Delta_{\bar{q}'}(Q,Q) \left[\frac{\alpha_s(Q)}{\alpha_s(Q)}\right]^2 = \frac{\Delta_{q''}(Q_1,Q)}{\Delta_{q'}(Q_1,Q)} \,. \tag{4.41}$$

All parton showers for all four legs would start at t, and the veto would be applied for emissions larger than Q, but this phase space region is kinematically excluded anyway.

4.3.3 Example III – $p\bar{p} \to$ jets

In this example the operation of the multi-cut treatment is illustrated through the case of $p\bar{p} \to \leq$ 3jets. The two-jet sample here is generated with a jet resolution cut of $Q^{(2)}_{\mathrm{cut}} =$ 20 GeV, and the three-jet sample is produced with $Q^{(3)}_{\mathrm{cut}} = 30$ GeV. The corresponding a-priori cross sections read

$$\begin{aligned} \sigma_2^{(0)} &= 30.423\mathrm{mb} & \sigma_2^{\mathrm{nmax}=3} &= 13.903\mathrm{mb} \\ \sigma_3^{(0)} &= 0.133\mathrm{mb} & \sigma_3^{\mathrm{nmax}=3} &= 0.092\mathrm{mb} \\ & & \sigma_{\mathrm{tot}}^{\mathrm{nmax}=3} &= \sum_{i=2}^{3} \sigma_i^{\mathrm{nmax}=3} = 13.995\,\mathrm{mb} \;. \end{aligned} \tag{4.42}$$

In their calculation, the factorisation scale of the two-jet events has consistently been set to Q_{min} defined as

$$Q_{\mathrm{min}} = \min\left\{p_\perp, Q^{(3)}_{\mathrm{cut}}\right\} \,, \tag{4.43}$$

where $p_\perp$ is the transverse momentum of the outgoing jets. In contrast, in the evaluation of the cross section of the three-jet events, the factorisation scale has consistently been set to Q_s, the scale of the softest jet.

In Fig. 4.6, exemplary diagrams for the two processes, the production of two and three jets, are depicted. For a typical two-jet event, such as the one in diagram a), the weight

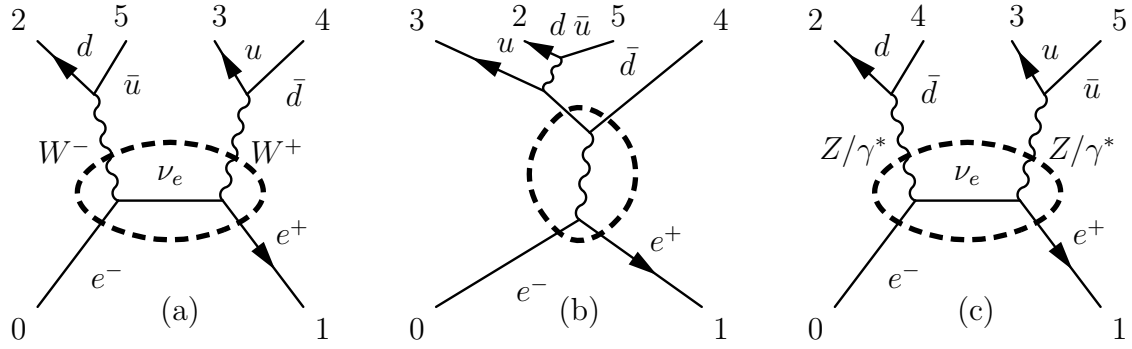

Figure 4.7: Possible cluster configurations in $e^+e^- \to d\bar{d}u\bar{u}(g)$. The dashed line indicates the core $2 \to 2$ process.

reads

$$\mathcal{W}_{\mathrm{ME}}^{(a)} = [\Delta_q(Q, Q_{\min})]^2 \, [\Delta_g(Q, Q_{\min})]^2 \, \left[\frac{\alpha_s(Q_{\min})}{\alpha_s(Q_{\mathrm{cut}}^{(2)})}\right]^2 . \tag{4.44}$$

The shower for all four legs starts at t, with a veto on emissions harder than $Q_{\min}$, and again the parton distribution weight in the first emission of each of the initial state shower evolutions is adjusted.
For the three-jet event depicted in diagram b), the weight reads

$$\mathcal{W}_{\mathrm{ME}}^{(b)} = [\Delta_q(Q, Q_s)]^2 \, \Delta_g(Q, Q_s) \frac{\Delta_g(Q, Q_s)}{\Delta_g(Q_1, Q_s)} [\Delta_q(Q_1, Q_s)]^2 \left[\frac{\alpha_s(Q)}{\alpha_s(Q_{\mathrm{cut}}^{(3)})}\right]^2 \frac{\alpha_s(Q_1)}{\alpha_s(Q_{\mathrm{cut}}^{(3)})} . \tag{4.45}$$

The parton shower for the two incoming quarks, for the outgoing gluon and for the harder of the two outgoing quarks starts at t, the parton shower of the softer of the two quarks emerging from the gluon line starts at t_1. The veto is performed w.r.t. the scale Q_1.

4.3.4 Example IV – $e^+e^- \to d\bar{d}u\bar{u}(g)$

In the process $e^+e^- \to d\bar{d}u\bar{u}$, there are basically three classes of subprocesses that can emerge as the core $2 \to 2$ process, namely

- $e^+e^- \to W^+W^-$,
- $e^+e^- \to Z^0/\gamma \, Z^0/\gamma$, and
- $e^+e^- \to d\bar{d}$ or $e^+e^- \to u\bar{u}$,

all of which are depicted in Fig. 4.7. The first two are electroweak processes, with W-pair production usually largely dominating, whereas the latter can either lead to a QCD or to an electroweak topology. Interferences between QCD and electroweak diagrams are negligible, therefore it is convenient to consider both contributions as independent.

$i\&j$	Probability
2&4	$P_{24} = p_{24}^Z + p_{24}^\gamma$
	$p_{24}^Z = \left[\frac{\alpha_{\text{QED}}(\mu)}{\sin^2\theta_w}\right]^2 \frac{(g_{1,d}^2+g_{2,d}^2)(g_{1,e}^2+g_{2,e}^2)}{(q^2-M_Z^2)^2+M_Z^2\Gamma_Z^2}$
	$p_{24}^\gamma = [\alpha_{\text{QED}}(\mu)]^2 \frac{Q_d^2 Q_e^2}{(q^2)^2}$
2&5	$P_{25} = p_{25}^W$
	$p_{25}^W = \left[\frac{\alpha_{\text{QED}}(\mu)}{2\sin^2\theta_w}\right]^2 \frac{(M_{ud}^{\text{CKM}})^2}{(q^2-M_W^2)^2+M_W^2\Gamma_W^2}$
3&4	$P_{34} = p_{34}^W$
	$p_{34}^W = \left[\frac{\alpha_{\text{QED}}(\mu)}{2\sin^2\theta_w}\right]^2 \frac{(M_{ud}^{\text{CKM}})^2}{(q^2-M_W^2)^2+M_W^2\Gamma_W^2}$
3&5	$P_{35} = p_{35}^Z + p_{35}^\gamma$
	$p_{35}^Z = \left[\frac{\alpha_{\text{QED}}(\mu)}{\sin^2\theta_w}\right]^2 \frac{(g_{1,u}^2+g_{2,u}^2)(g_{1,e}^2+g_{2,e}^2)}{(q^2-M_Z^2)^2+M_Z^2\Gamma_Z^2}$
	$p_{35}^\gamma = [\alpha_{\text{QED}}(\mu)]^2 \frac{Q_u^2 Q_e^2}{(q^2)^2}$

Table 4.1: All possibilities for the (electroweak) first clustering of $e^+e^- \to d\bar{d}u\bar{u}$. For brevity of the example only one Feynman diagram is taken into account for each possible propagator flavour. The particle are numbered according to Fig. 4.7.

In the following, the focus will be mainly on the electroweak contributions. There exist 4 different possibilities for the first clustering, listed in Tab. 4.1. After, for instance, choosing 2&5 (the $d\bar{u}$-pair) to be clustered first and to become a W^- boson, a second clustering leads to the $2 \to 2$ core process. Of course, the first step restricts the possibilities for any subsequent clustering - in this example three options remain. Their probabilities are listed Tab. 4.2.

One possible outcome of the clustering procedure is a W pair production process as depicted in Fig. 4.7a. The evaluation of the Sudakov weight in this case yields

$$\mathcal{W}_{\text{ME}}^{(a)} = \Delta_d(Q_1, Q_{\text{cut}})\Delta_{\bar{u}}(Q_1, Q_{\text{cut}})\Delta_u(Q_2, Q_{\text{cut}})\Delta_{\bar{d}}(Q_2, Q_{\text{cut}}) \tag{4.46}$$

in the WW case; when the $q\bar{q}$ production process is chosen instead, cf. Fig. 4.7b, the correction weight is given by

$$\mathcal{W}_{\text{ME}}^{(b)} = \Delta_d(Q_1, Q_{\text{cut}})\Delta_{\bar{u}}(Q_1, Q_{\text{cut}})\Delta_u(Q, Q_{\text{cut}})\Delta_{\bar{d}}(Q, Q_{\text{cut}}) \tag{4.47}$$

Both weights look very similar, and indeed for massless quarks this holds true for all Sudakov weights that can be obtained. However, while in the first example both scales Q_1 and Q_2 are of the order M_W, the relevant scales in the second case are more likely to be $Q_1 \approx M_W$ and $Q \approx 2M_W$, of course depending on the exact kinematical configuration. Of course, these different clusterings result in different starting conditions for the shower.

$i\&j$	Probability
2&3	$P_{23} = p_{23}^d$
	$p_{23}^d = \frac{1}{2}\left[\frac{\alpha_{\mathrm{QED}}(\mu)}{\sin^2\theta_w}\right]^2 \frac{(M_{ud}^{\mathrm{CKM}})^2}{(q^2)^2}(g_{1,u}^2 + g_{2,u}^2)$
2&4	$P_{24} = p_{24}^{\bar{u}}$
	$p_{24}^{\bar{u}} = \frac{1}{2}\left[\frac{\alpha_{\mathrm{QED}}(\mu)}{\sin^2\theta_w}\right]^2 \frac{(M_{ud}^{\mathrm{CKM}})^2}{(q^2)^2}(g_{1,d}^2 + g_{2,d}^2)$
3&4	$P_{34} = p_{34}^W$
	$p_{34}^W = \left[\frac{\alpha_{\mathrm{QED}}(\mu)}{2\sin^2\theta_w}\right]^2 \frac{(M_{ud}^{\mathrm{CKM}})^4}{(q^2 - M_W^2)^2 + M_W^2\Gamma_W^2}$

Table 4.2: All possibilities for the clustering of $e^+e^- \to W^-\bar{d}u$. For brevity of the example only one Feynman diagram is taken into account for each possible propagator flavour.

4.4 Results

The detailed presentation of examples in the previous section, Sec. 4.3 will be supplemented with results in this section. To validate the consistency of the approach, clearly a careful examination is mandatory, checking whether the exclusive samples prepared through the re-weighted matrix elements and further evolved through the parton shower combine into a consistent, inclusive sample. Any larger discontinuity that becomes visible, in particular on scales comparable to the merging scale Q_{cut}, may serve as an indication for a mismatch of leading logarithms. Obviously, a good way of scrutinising the radiation pattern in the interaction of matrix elements and parton shower is to investigate differential jet rates, especially in a $k_\perp$-scheme. These rates are defined through the jet resolution in the corresponding scheme, where an $n+1$-jet event turns into an n-jet event.

4.4.1 Results for $e^+e^- \to$ jets at LEP1

To start with, differential jet rates in $e^+e^- \to$ jets are compared. In e^+e^-–annihilations, it is often convenient to define a variable y_{cut} rather than Q_{cut}; in the Durham scheme employed here, it is defined through

$$y_{\mathrm{cut}} = \frac{Q_{\mathrm{cut}}^2}{E_{\mathrm{c.m.}}^2} \tag{4.48}$$

implying that two particles i and j belong to different jets if they are separated by a distance

$$y_{ij} \geq 2\frac{\min\{E_i^2, E_j^2\}}{E_{\mathrm{c.m.}}^2}(1 - \cos\theta_{ij})\,. \tag{4.49}$$

In Fig. 4.8, results for differential jet rates are shown ranging over four orders of magnitude in y_{cut}. The dependence on the actual value of Q_{cut} in the generation of two different samples is barely visible. Also, the distributions seem to be perfectly smooth around the generation

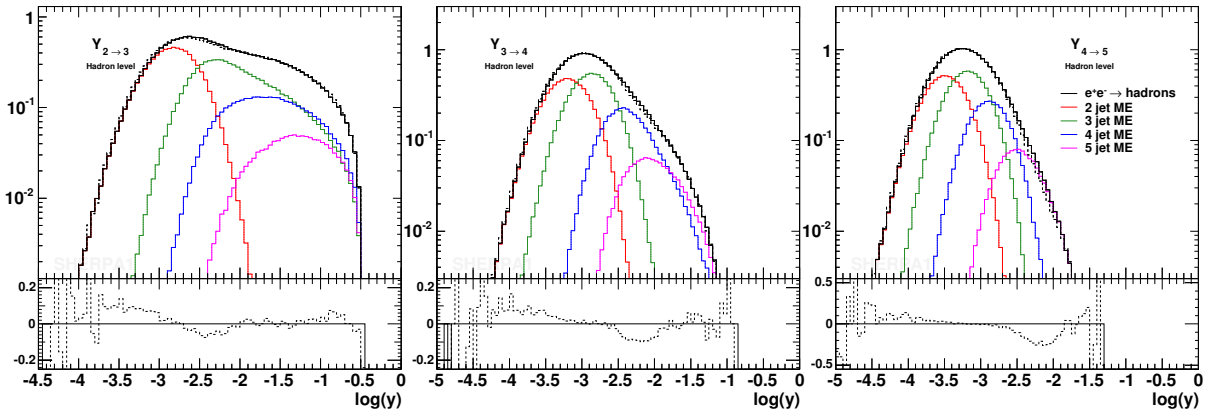

Figure 4.8: Differential jet rates in the Durham scheme at LEP1. The shown results are obtained through the merging of matrix elements for up to five jets with the parton shower, with two different separation cuts. The solid lines correspond to a cut at $y_{\text{cut}} = 10^{-2.5}$, and the dashed curve illustrates the result using $y_{\text{cut}} = 10^{-2}$. In the former case coloured lines indicate the contributions from individual matrix elements: two jets (red), three jets (green), four jets (blue), and five jets (purple).

cut. Therefore, one may conclude that the merging in this case has been accomplished with very high quality.

The samples generated by SHERPA also reproduce event shape observables such as thrust, thrust-major, thrust-minor or oblateness, cf. Fig. 4.9. Again, the dependence on the generation cut is rather small, deviations are well below 20%.

Going to more exclusive observables that are sensitive to the full interference structure of matrix elements, various four-jet correlations may be tested. Examples for such correlations are the Bengtsson-Zerwas and the Nachtmann-Reiter angle, see the appendix A.2 for their definition. In Fig. 4.10, data taken at LEP1 [117] are compared with results of the merged samples of SHERPA and with a "shower"-only result. Of course, the latter lacks the exact treatment of quantum interferences, which is possible only through full matrix elements. Correspondingly, there is a visible shape difference between data and the merged sample on the one hand and the shower-only sample on the other hand. This beautifully underlines the power of the merging approach.

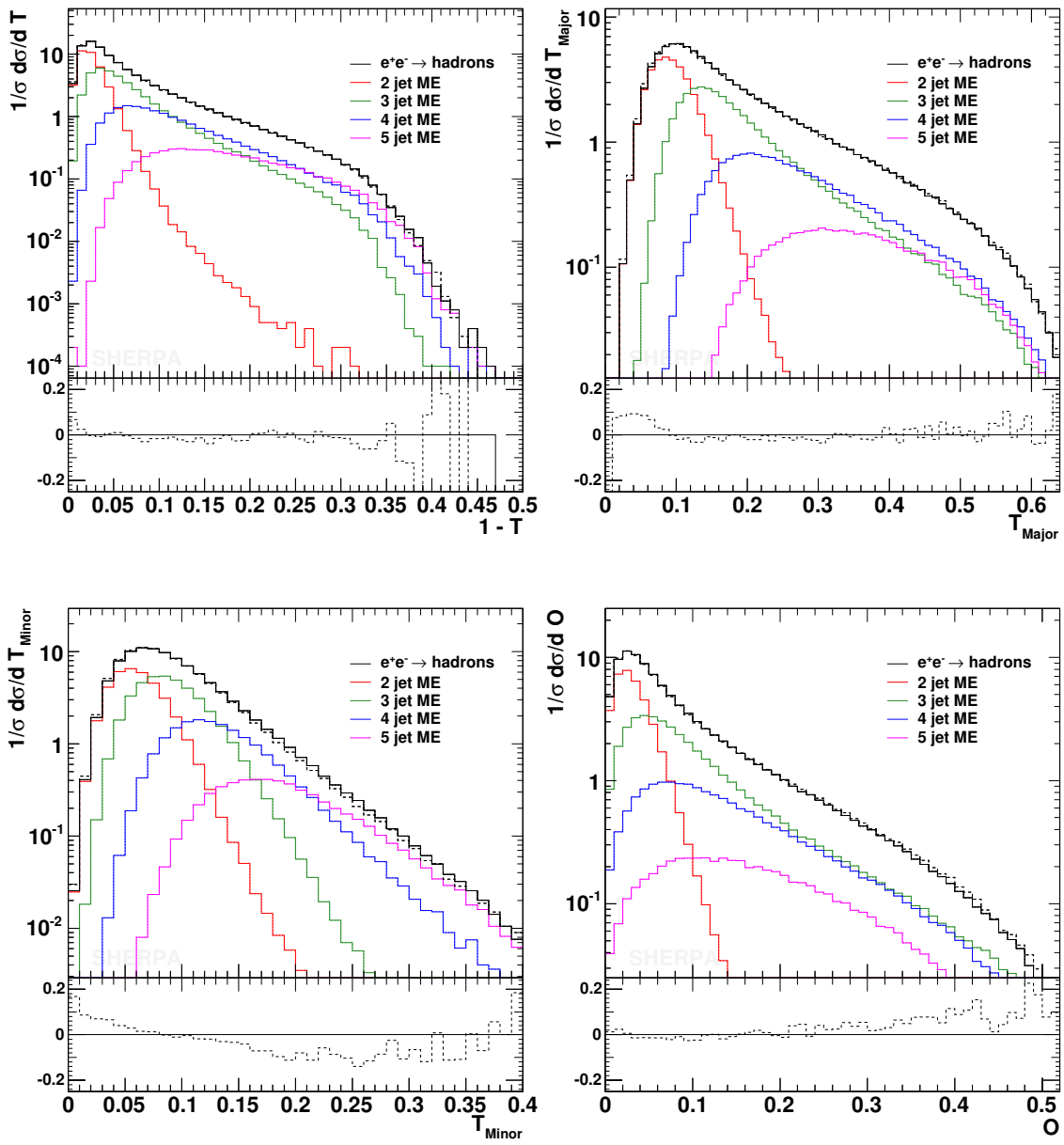

Figure 4.9: Thrust (top left), thrust-major (top right), thrust minor (bottom left), and oblateness (bottom right) at LEP1. For definitions of these observables, cf. appendix A. The hadron level result of SHERPA is pictured for two different separation cuts $y = 10^{-2.5}$ and $y = 10^{-2}$. Line styles and colours are the same as in Fig. 4.8.

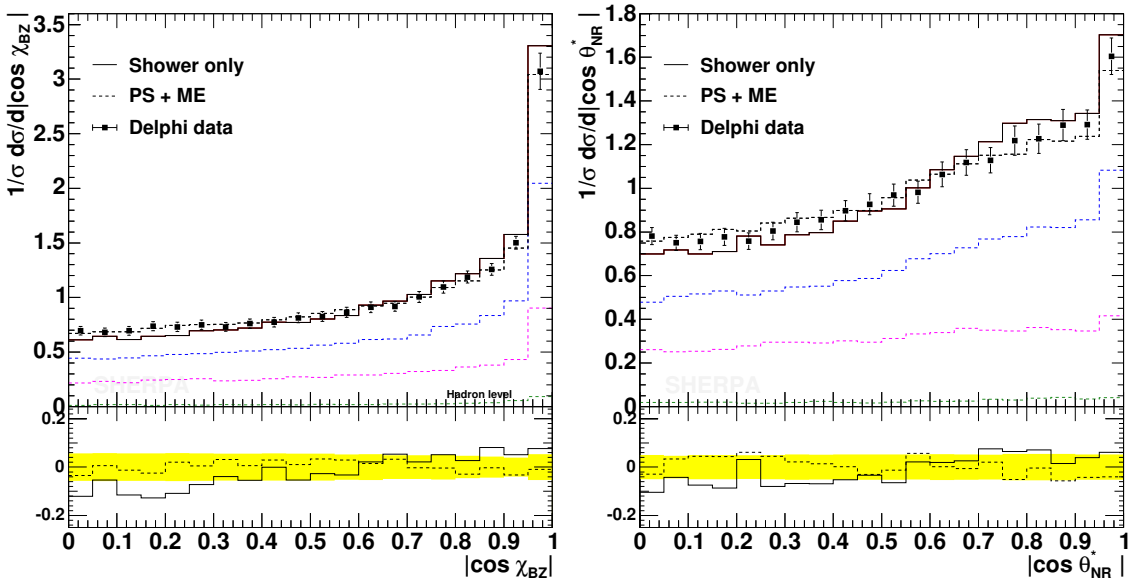

Figure 4.10: Four-jet angle distributions for the Bengtsson-Zerwas angle (left) and the modified Nachtmann-Reiter angle (right). The data points are from a DELPHI measurement [117].

4.4.2 Results for $p\bar{p} \to W +$ jets at Tevatron, Run I

The investigations for the case of $p\bar{p} \to W+$jets start with an analysis of differential jet rates in the $k_\perp$-algorithm for this process at Tevatron, Run I. Results of SHERPA with different jet resolution cuts during the generation of the respective sample are exhibited in Fig. 4.11. The results are not quite as good as those obtained for the previous case of e^+e^-–annihilations into jets, on the other hand, the example presented here is much more complicated. This extra complication is due to a more intricate radiation pattern with emissions in both the initial and the final state. Still the relative differences are marginal, ranging up to 20%. Only in the sample with the highest jet resolution cut it becomes apparent that the parton shower is not able to fill the phase space properly. This is the reason for the visible hole in the differential jet rates around the cut.

In analogy to the event shapes above, the transverse momentum distribution of the W boson and of the electron produced in its decay may be considered as inclusive observable. The dependence of these observables on the jet resolution cut in the generation of the samples and on the maximal number of jets covered by the matrix elements is displayed in Figs. 4.12 and 4.13, respectively. In both cases it becomes apparent that the dependences are negligible - results of different samples produced under different conditions are in very good agreement with each other.

Finally, measured total cross sections for different jet multiplicities in $W +$ jet [125] are compared with those obtained from SHERPA after reweighting the matrix elements with up to 4 jets with the Sudakov weights and after applying a constant K-factor of 1.44 to all samples, that has been calculated to match the SHERPA result with a NNLO prediction [126, 127]. Taking into account the errors, the results are in great agreement with each other, cf. Fig. 4.14. Correspondingly, the $p_\perp$ spectra of the jets are depicted in Fig. 4.15. There, the

measurement of transverse energy distributions of jets for different multiplicities [125] are compared with results from SHERPA. Again, the results agree very well after applying a global K-factor on the latter. In both cases, jets were defined through a cone algorithm with cone size of $R = 0.4$ and a transverse energy of the jets of at least $E_T = 15$ GeV.

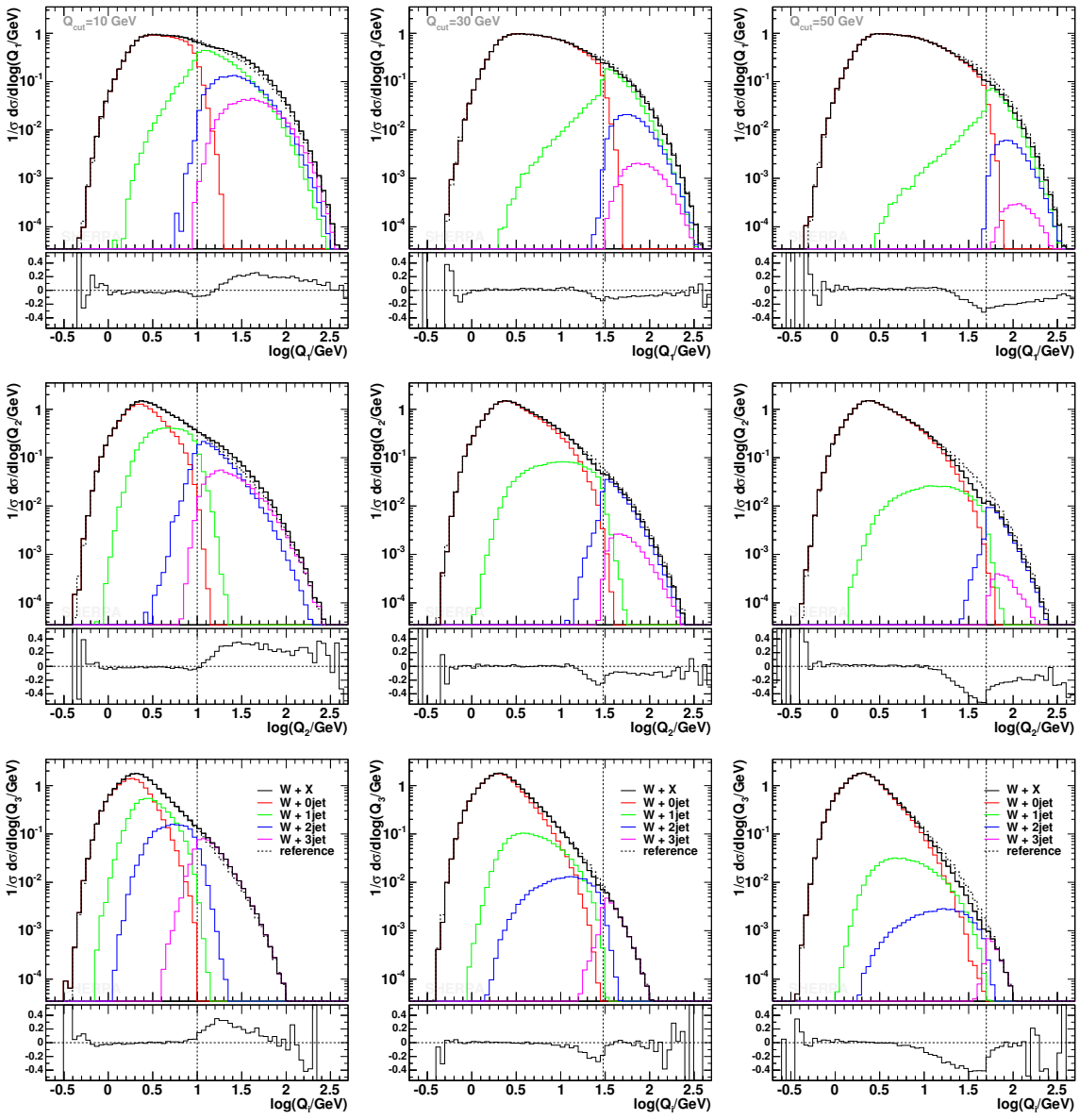

Figure 4.11: Differential jet rates for the $1 \to 0$, $2 \to 1$ and $3 \to 2$ transition (top to bottom), for $Q_{\text{cut}} = 10$ GeV, 30 GeV, and 50 GeV (from left to right). In each plot, the results are compared with those for $Q_{\text{cut}} = 20$ GeV.

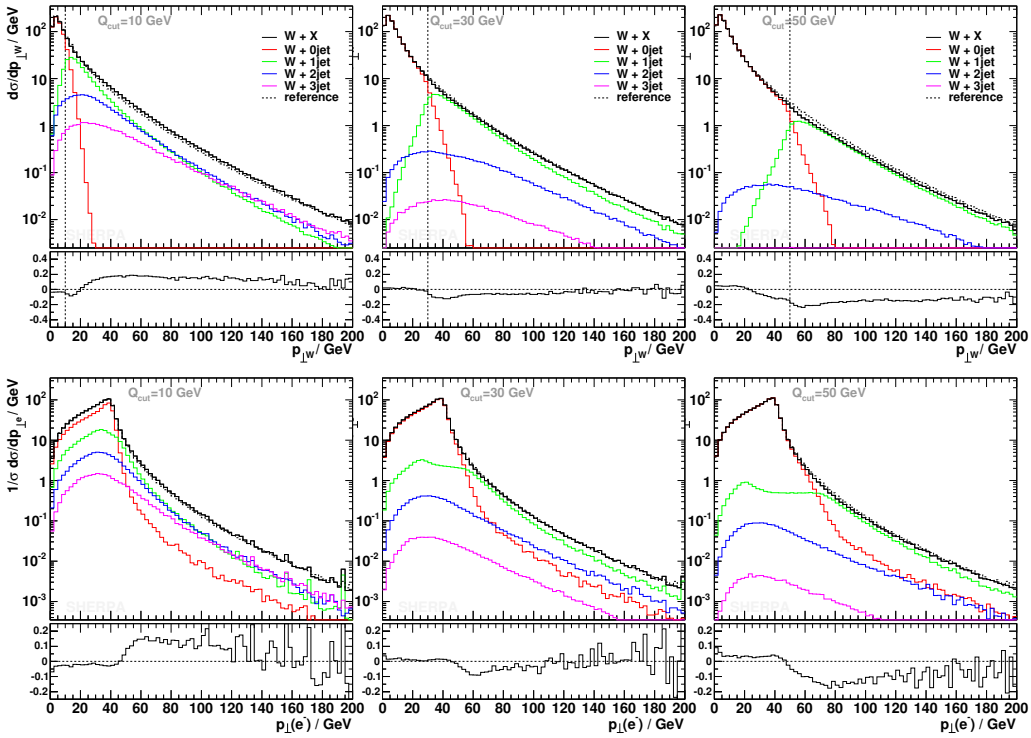

Figure 4.12: $p_\perp(W^-)$ and $p_\perp(e^-)$ for $Q_{\text{cut}} = 10$ GeV, 30 GeV and 50 GeV in comparison with $Q_{\text{cut}} = 20$ GeV.

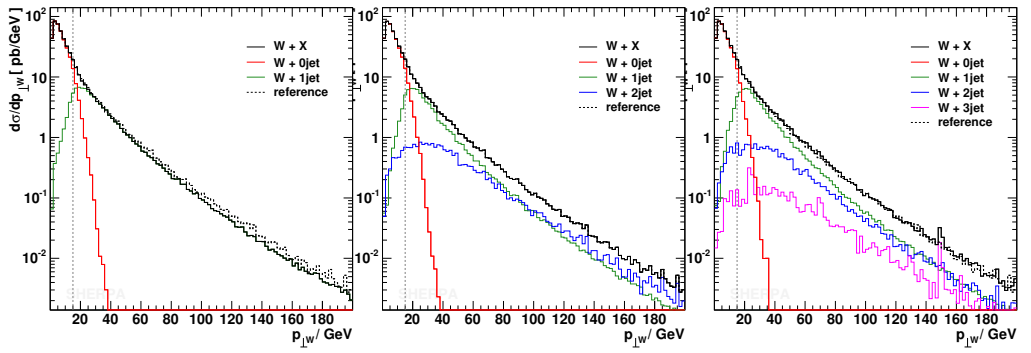

Figure 4.13: $p_\perp(W^-)$ for $Q_{\text{cut}} = 15$ GeV and different maximal numbers of ME jets included. The dashed line corresponds to a maximal number of ME jets $n_{\max} = 2$.

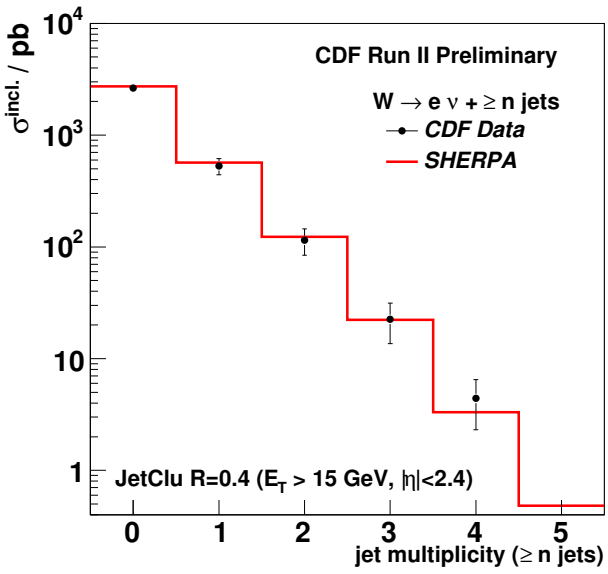

Figure 4.14: Inclusive cross sections for the process $p\bar{p} \to W + n\text{jets}$. The SHERPA prediction is contrasted with the measurement by CDF [125]

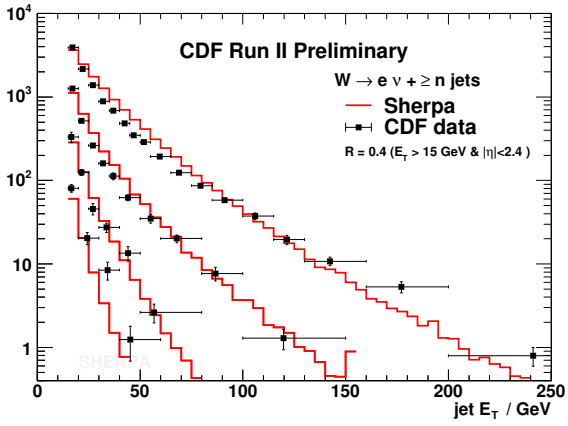

Figure 4.15: Jet transverse energy distribution for the process $p\bar{p} \to W + n\text{jets}$ from a CDF [125] measurement. From top to bottom, the lines correspond to the highest E_T jet distribution in inclusive $W + 1\text{jet}$ events, the second highest E_T jet distribution in inclusive $W + 2\text{jet}$ events, the third highest E_T jet distribution in inclusive $W + 3jet$ events, and the fourth highest E_T jet distribution in inclusive $W + 4\text{jet}$ events. The SHERPA result includes matrix elements with up to 4 jets.

4.4.3 Results for $p\bar{p} \to$ jets at Tevatron, Run I

Before investigating in greater detail the consistency of the merging prescription for jet production at hadron colliders, in particular at the Tevatron, Run I, consider Fig. 4.16. There, the differential $3 \to 2$ jet rates for samples with $n_{\max} = 3$ for $Q_{\text{cut}} = 20$, 30, and 40 GeV are compared with a the result for a sample, where two different jet resolution cuts have been applied for the different multiplicities, namely $Q_{\text{cut}}^{(2)} = 30$ GeV and $Q_{\text{cut}}^{(2)} = 40$ GeV. Obviously, for $Q \geq 40$ GeV the four results are in fair agreement with each other, as expected. Below 40 GeV, the sample generated with $Q_{\text{cut}} = 40$ GeV starts to undershoot the other three curves significantly, as expected. In principle, there should be no contribution left at all, since there are no matrix elements for any jet configurations populating this regime. However, due to the parton shower, some of the jets produced at higher $p_\perp$ values spread out, leading to some non-negligible fraction of events migrating into that region. The same pattern repeats itself at Q-values below 30 GeV. This region is not filled by the $Q_{\text{cut}} = 30$ GeV and the mixed sample any longer. This implies that in order to describe jet observables at jet resolutions above, say, 30 GeV, a $Q_{\text{cut}} \leq 30$ GeV should be applied. Due to the steep descend of cross sections this may not be very efficient, rendering a multi-scale treatment the method of choice.

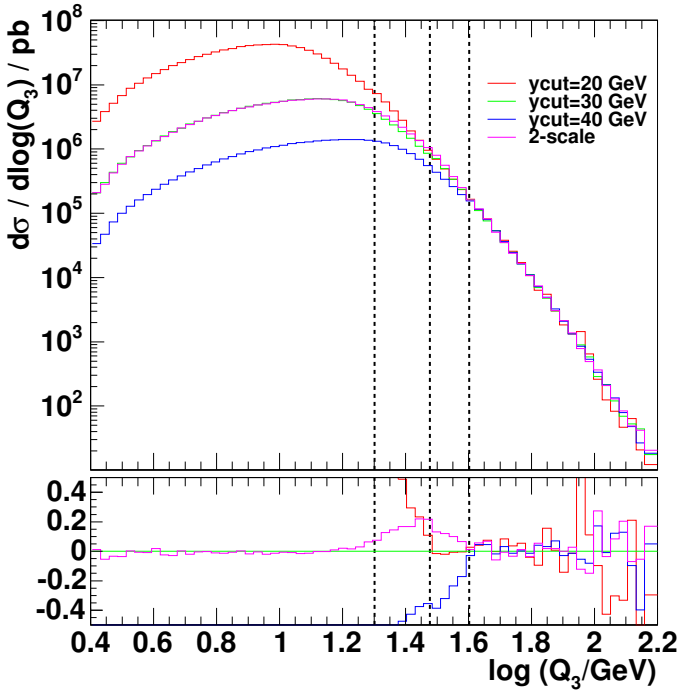

Figure 4.16: Differential $3 \to 2$ jet rate at the Tevatron, Run I. Different samples with different values of Q_{cut} are displayed in different colours, the respective Q_{cut} values are indicated with dashed vertical lines. Clearly, above 40 GeV, all samples coincide, then successively, different samples die off. Apparently the sample with mixed cuts ($Q_{\text{cut}}^{(2)} = 30$ GeV and $Q_{\text{cut}}^{(3)} = 40$ GeV), depicted in purple, agrees very well with the sample produced with the lower of the two cuts.

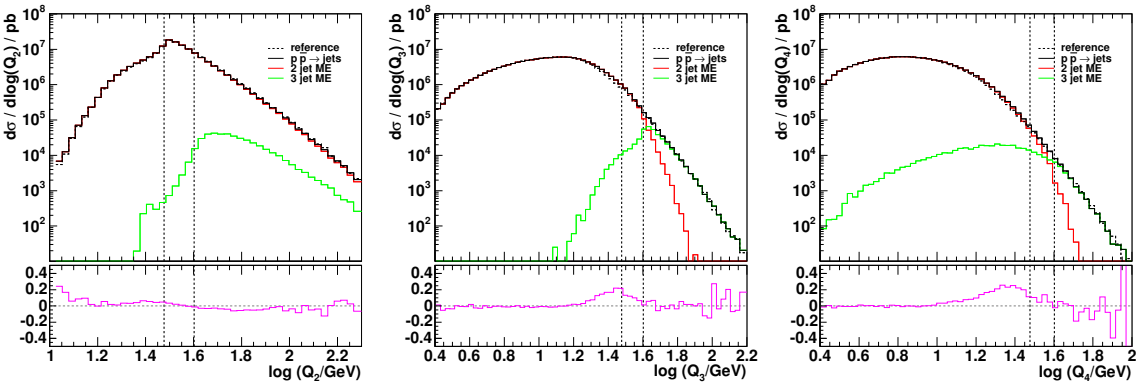

Figure 4.17: Differential $2 \to 1$, $3 \to 2$, $4 \to 3$ jet rate at the Tevatron, Run I. The mixed sample with two cuts ($Q^{(2)}_{\text{cut}} = 30$ GeV and $Q^{(3)}_{\text{cut}} = 40$ GeV, as above), depicted with the solid black line is compared with a reference sample with one, common cut only ($Q^{(3)}_{\text{cut}} = 30$ GeV), displayed with the dashed black line. Deviations are maximally of the order of 20%, indicating the success of the multi-cut treatment. Note also that in the $3 \to 2$ jet rate, around 40 GeV the effect of merging the 2 with the three jet configuration becomes visible.

In Fig. 4.17, the mixed sample from above is further investigated. There, in addition to the summed result, also the contributions from different jet multiplicities are displayed. Clearly, the two samples fill quite separate regions of phase space, i.e. above and below the jet resolution cut. Of course, as before, there is some residual migration of the samples over the respective jet resolution cut. The sum, however, is remarkably smooth over the cut. This allows to efficiently generate an inclusive QCD sample with jets resolved at 40 GeV, for example, where higher jet configurations are accounted for by corresponding matrix elements and the phase space below the matrix element cuts for them is properly filled by the lowest multiplicity contribution. The quality of this approach is further highlighted in Figs. 4.18 and 4.19. There, again, differential jet rates are depicted, this time the cuts have been chosen as $Q^{(2)}_{\text{cut}} = 2.5$ GeV and $Q^{(\geq 3)}_{\text{cut}} = 10$ GeV. The plots cover up to ten orders of magnitude with an extremely smooth prediction.

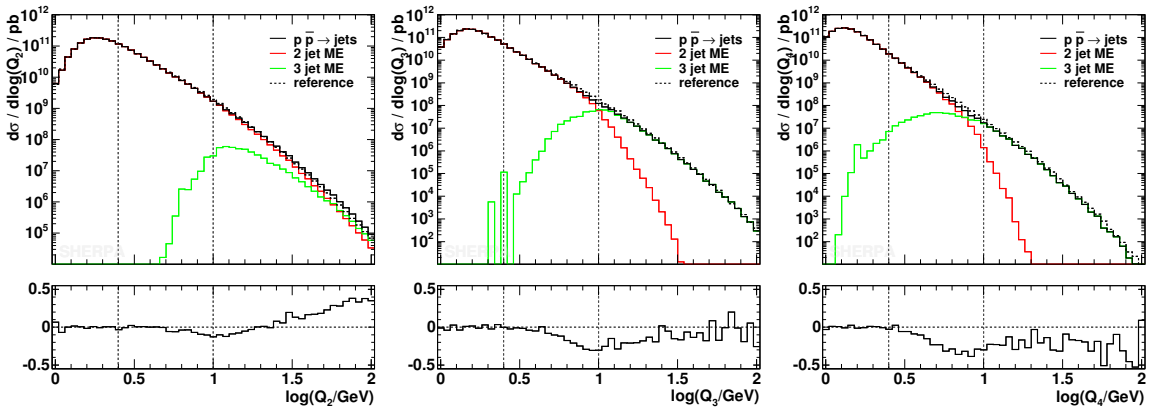

Figure 4.18: Differential jet rates at the Tevatron, Run I. From left to right, the rates for $2 \to 1$, $3 \to 2$, and for $4 \to 3$ transitions at the hadron level are exhibited; the samples are produced with $n_{\max} = 3$ and $Q_{\text{cut}}^{(2)} = 2.5$ GeV & $Q_{\text{cut}}^{(3)} = 10$ GeV. A reference curve is shown in black-dashed lines, contributions from different multiplicities are displayed in different colours.

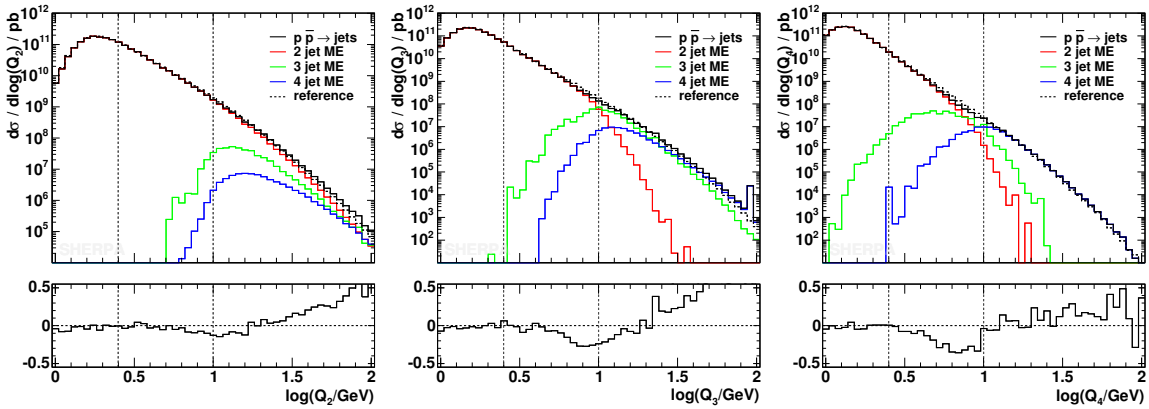

Figure 4.19: Differential jet rates at the Tevatron, Run I. From left to right, the rates for $2 \to 1$, $3 \to 2$, and for $4 \to 3$ transitions at the hadron level are exhibited; the samples are produced with $n_{\max} = 4$ and $Q_{\text{cut}}^{(2)} = 2.5$ GeV & $Q_{\text{cut}}^{(3,4)} = 10$ GeV. A reference curve is shown in black-dashed lines, contributions from different multiplicities are displayed in different colours.

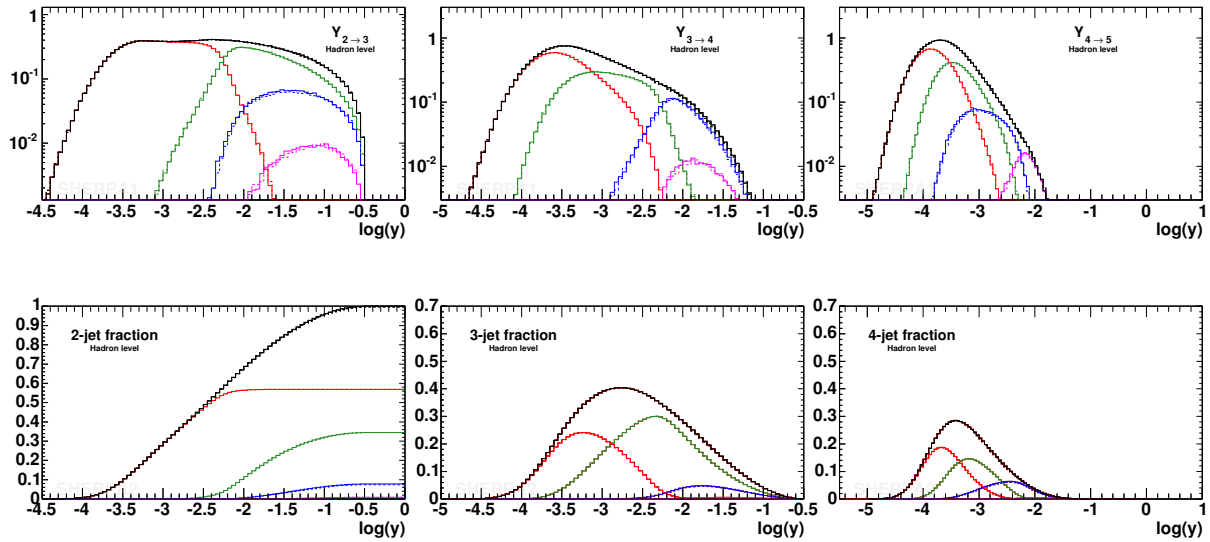

Figure 4.20: Differential (upper row) and total (lower row) jet rates in the Durham scheme at LEP2 for QCD events. The result of the original and the alternative merging procedure are compared, (original=solid black, alternative=dashed red), differences are hardly visible.

4.4.4 Results for $e^+e^- \to d\bar{d}u\bar{u}(g)$ at LEP2

In this section, the quality of the alternative algorithm will be validated. To this end, e^+e^- →jets at LEP2 are chosen as the reference process.

Strong interactions

Concentrating first on the case where QCD alone contributes to the production of extra jets, in Fig. 4.20 differential and total jet rates in the Durham scheme at LEP2 as described with the original and with the alternative approach are compared. Clearly, the results are nearly indistinguishable. This implies that in this case the ordering of the hardness of emissions according to the $k_\perp$ measure is nearly identical with an ordering according to the virtual masses occurring in the propagator terms. The same holds also true for event shape observables, depicted in Fig. 4.21. There, measurements of thrust, thrust-major and the C-parameter [128] are exhibited and compared to the simulation of `SHERPA`. Again, the alternative and the original algorithm perform equally well and both reproduce the data nicely.

Electroweak interactions

It is expected that differences in the two prescriptions to reconstruct the pseudo parton shower history appear when the electroweak production of four quarks is investigated. Both for event shape observables displayed in Fig. 4.22 and for total or differential jet rates depicted in Fig. 4.23 the differences are sizable, reaching up to 50%. This can be easily understood. In Fig. 4.24 the cross sections for three typical core $2 \to 2$ processes are considered, namely W pair production, Z/γ pair production, and the QED/electroweak analogue to the QCD processes. Apparently, the alternative algorithm correctly reproduces

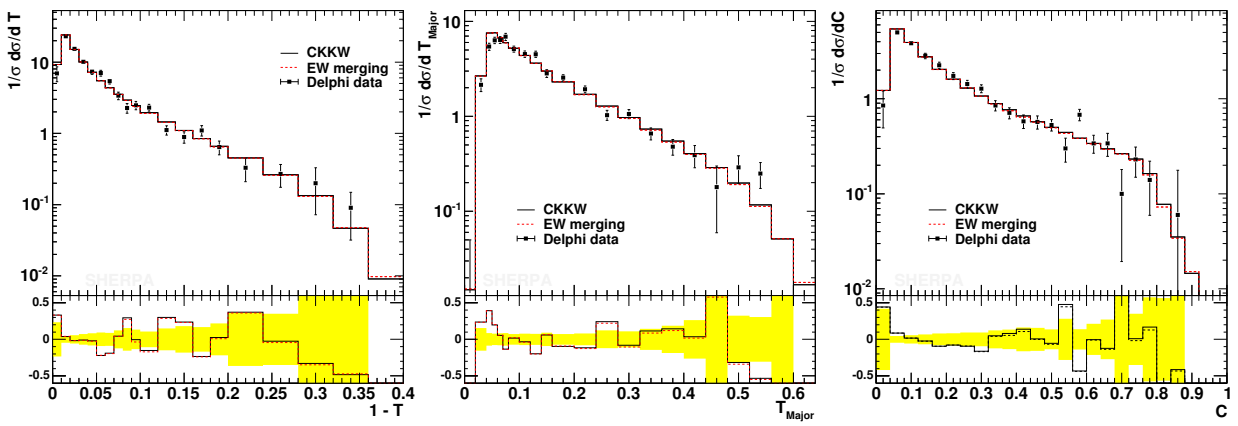

Figure 4.21: Thrust, thrust major and C-parameter. Delphi data [128] taken at LEP2 events ($E_{\mathrm{cms}} = 189$ GeV) are compared to simulation using the original and the alternative way of constructing the pseudo parton shower history (original=solid black, alternative=dashed red).

the expected cross sections for the WW and ZZ channel (2 pb and 0.02 pb). Hence, the relative contributions of the three considered processes are consistent with the matrix element. In contrast, the original algorithm fails to reproduce the correct rate for the WW channel, because it triggers an unphysical migration into the QCD-like configurations. Consequently, both samples differ in their colour structure, in their Sudakov weights and, ultimately, in the starting scales for their parton shower.

This finding gives a clear hint that the pole structure of propagators has to be taken into proper account when merging such matrix elements with the parton shower. Thus, in the following, the focus will be on the self-consistency of such an approach. To investigate this, again differential and total jet rates are considered. In Fig. 4.26 corresponding results for a 4 jet and for a combined $(4 + 5)$-jet sample produced according to the alternative algorithm are contrasted with each other. They are in nice agreement, hinting that the combination of exclusive samples into an inclusive one was successfully achieved. In Fig. 4.25 the corresponding event shape observables are shown. There, the differences between both samples are marginal; they differ only in the low-statistics bins. Note that in all Figs. 4.22-4.26 the multi-cut treatment has been employed. The 4-jet matrix element cut has been chosen to $y_{\mathrm{cut}}^{(4)} = 10^{-4}$, while the 5-jet matrix element was separated by $y_{\mathrm{cut}}^{(5)} = 10^{-2.2}$. This is important, since there exists no 3-jet matrix element, which could compensate for the phase space cut in the 4-jet matrix element.

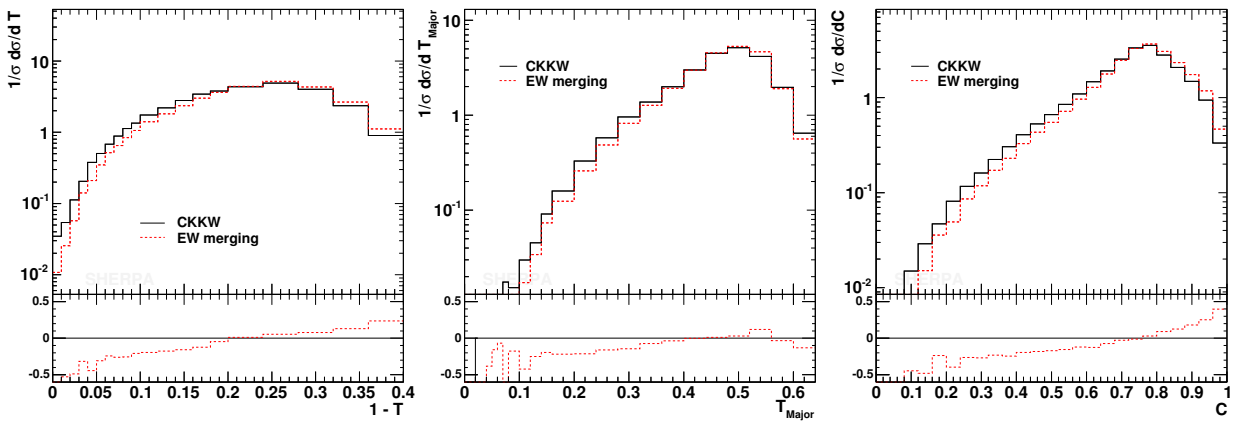

Figure 4.22: Thrust, thrust-major and C-parameter in electroweak four jet events at LEP2. This time, the results of the two merging prescriptions (original=solid black, alternative=dashed red) differ significantly, by up to 50%.

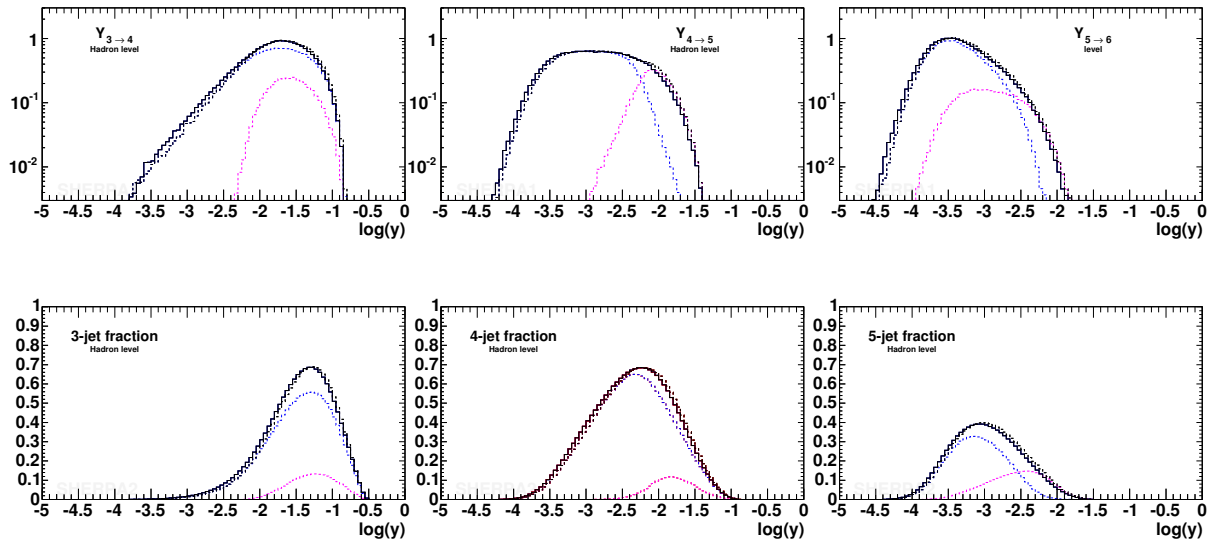

Figure 4.23: Differential (upper row) and total (lower row) jet rates in electroweak four jet events at LEP2. The results of the two merging prescriptions (original=solid black, alternative=dashed red) are compared with each other, differences are visible.

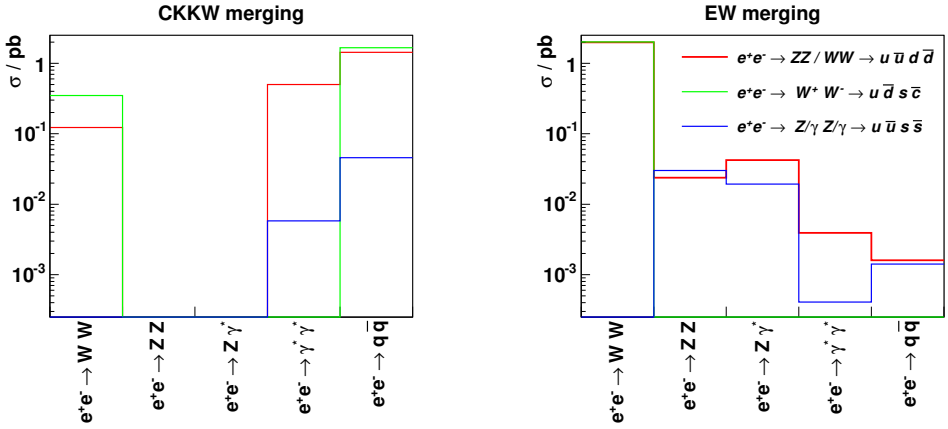

Figure 4.24: Statistics of selected "core" processes for different electroweak 4-jet channels. The result of the original (left plot) with the alternative algorithm (right plot) is compared.

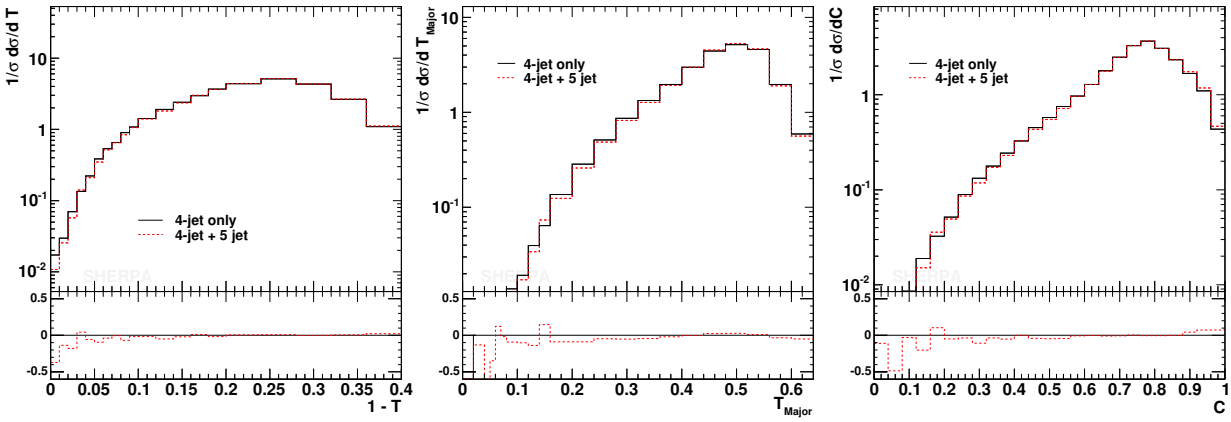

Figure 4.25: Thrust, thrust-major and C-parameter in electroweak four jet events at LEP2. Results of SHERPA for a merged (4+5)-jet sample ($y_{\text{cut}} = 10^{-2.2}$) are contrasted with those of a pure 4-jet sample where the parton shower was running freely.

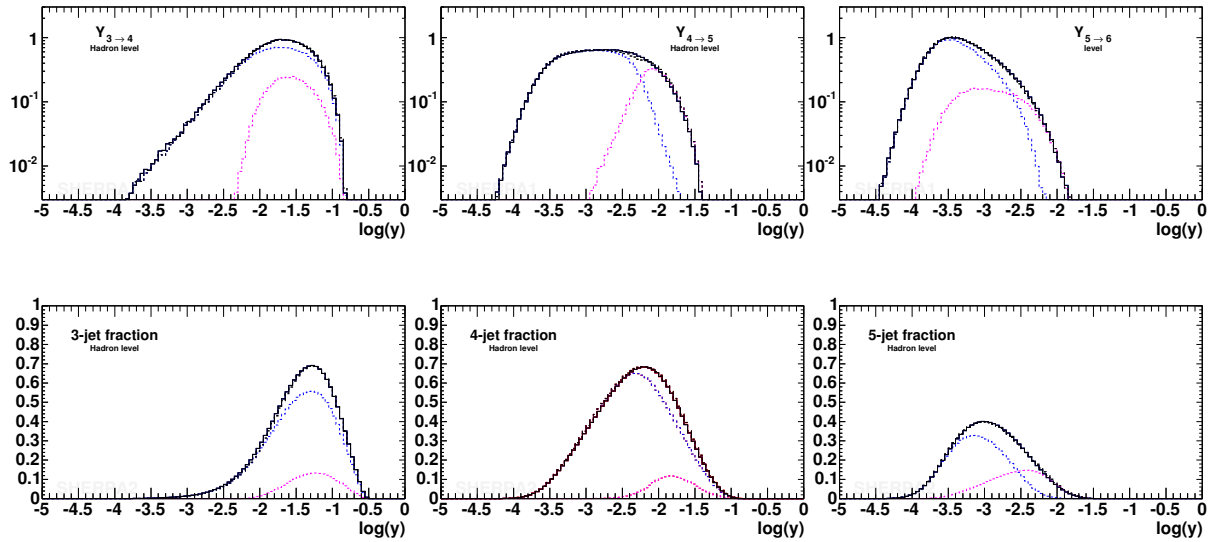

Figure 4.26: Differential (upper row) and total (lower row) jet-rates in electroweak four jet events at LEP2. Results of a merged (4+5)-jet sample ($y_{\mathrm{cut}} = 10^{-2.2}$) are contrasted with those of a pure 4-jet sample.

4.5 Summary

In this chapter, the procedure for a consistent merging of matrix elements for the production of multi-particle final states at tree-level and the parton shower has been discussed in great detail, going beyond the scope of previous publications on that subject. In particular, some improvements of the method have been presented which consistently treat situations, where the parton shower must fill the phase space for the production of jets which is not covered by corresponding matrix elements. In addition, some ideas of how to extent the original algorithm to cases were electroweak and strong interactions compete have been set forth. A large number of examples has demonstrated how the algorithm works in various cases. An extended comparison with data and other Monte Carlo tools, both in e^+e^-–annihilations and in hadronic collisions, is the topic of the next chapter 5.

The implementation of the algorithms presented here, into the new event generator `SHERPA` is discussed in appendix D.2.

5 Applications – Results

The quality of any event generator can ultimately be judged only through direct comparison with experimental data. Therefore, the performance of the SHERPA Monte Carlo is finally investigated in different experimental scenarios. First, in Sec. 5.1, SHERPA results are confronted once again with LEP1 data. The high precision of these data offers an unrivalled challenge to the treatment of final state parton showering and hadronisation of any Monte Carlo program. Then, in Sec. 5.2, the discussion is continued with a study of the energy extrapolation behaviour of SHERPA, using data taken at the second phase of the LEP collider. After this, the focus again shifts to the topic of this thesis, namely the simulation of hadron collision experiments. Unfortunately, data on the hadron level at the highest accessible energies, i.e. at the Tevatron, are still rare, therefore the discussion of data is supplemented with internal consistency checks, and with comparisons with other Monte Carlo codes. Two important physics channels are considered. First the production of a singe electroweak boson, both at the Tevatron (in Sec. 5.3) and the LHC (in Sec. 5.4), is investigated. Then the collection of applications is concluded with an analysis of W-pair production, in Sec. 5.5.

5.1 Hadron production at LEP1

Throughout this thesis, LEP1 measurements have been used to investigate different aspects of shower evolution, and the merging of matrix elements and parton showers. The high quality and precision of LEP1 data has proven to be of special value for the determination of the performance of any Monte Carlo program. About 4 million Z events have been collected by each LEP experiment representing an unique and unrivalled challenge to any event generator. These data also allow the tuning of Monte Carlo event generators, especially of the fragmentation parameters that are model dependent. Further details on such a tuning procedure can be found in [114–116].

In this section an extended comparison of the merging procedure with experimental data is pursued. All predictions have been obtained by using matrix elements with up to 5 jets. The separation cut has been set to $y_{\text{cut}} = 10^{-2.4}$. Contributions from the different jet multiplicities are indicated by different colours: two jets (red), three jets (green), four jets (blue), and five jets (purple).

The first observables to be studied are charged multiplicity and charged scaled momentum, see Fig. 5.1. The experimental error on these observables is particularly small, indicated by the yellow band in the lower part of the plots. However, after tuning, the agreement with data is excellent. In fact, these two distributions have the largest impact on the tuning of the (soft) hadronisation parameters.

The data survey is continued by looking at event shapes. In Fig. 5.2 Thrust, thrust major, thrust minor, and oblateness are depicted. Again, the description of the data is very

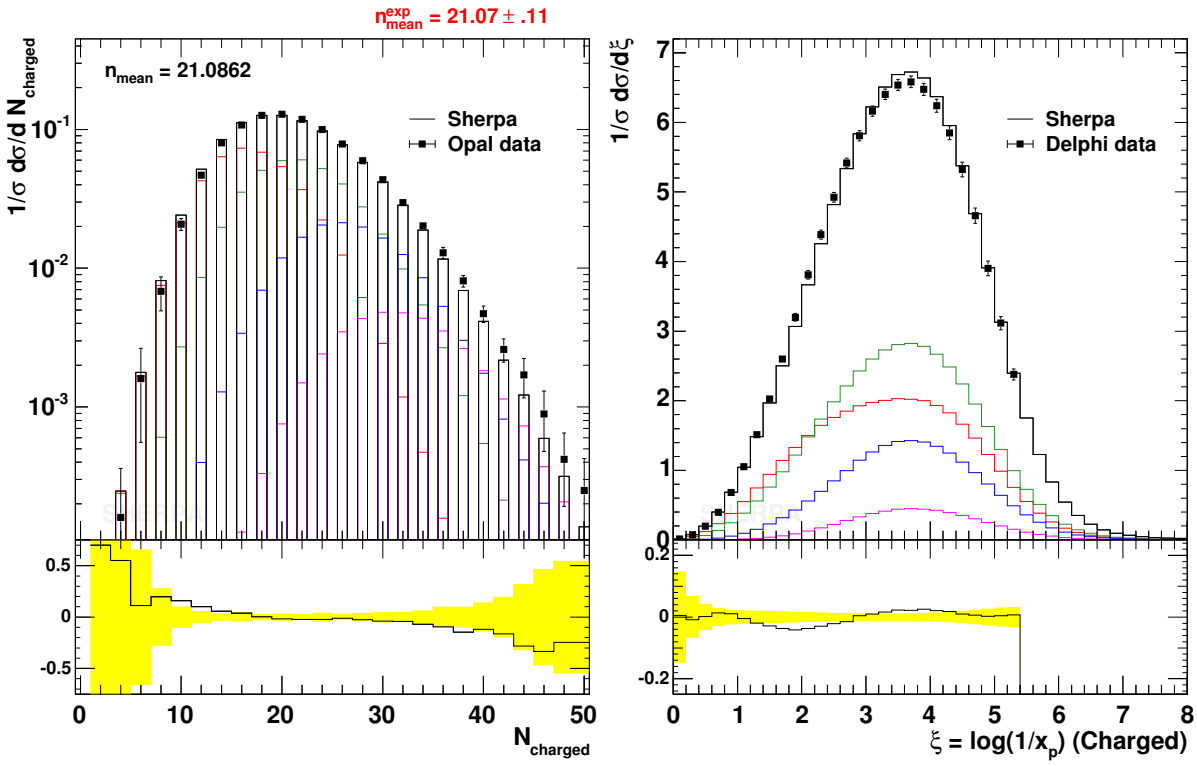

Figure 5.1: Charged multiplicity and scaled momentum at LEP1. The left plot shows the distribution of the number of charged particles together with a measurement by Opal [120]. The mean charge multiplicity is also stated together with its PDG value [121]. On the right hand side, the scaled momentum distribution is plotted against Delphi data [114]. The data are contrasted with results obtained through the merging of matrix elements for up to five jets and the parton shower. The separation cut has been set to $y_{\text{cut}} = 10^{-2.4}$. Coloured lines indicate the contributions from individual matrix elements: two jets (red), three jets (green), four jets (blue), and five jets (purple)

good, with the data covering five orders of magnitude. Note the different influence of multi-jet matrix elements. For instance the low-statistics bins in minor are largely dominated by the 5-jet matrix elements, whereas oblateness is mainly generated by the 2- and 3-jet contributions. Another class of event shapes is shown in Fig. 5.3, namely C-parameter, D-parameter, sphericity, and aplanarity. The SHERPA result lies well within the experimental error band, only sphericity shows a small shift, due to a slight excess in the high statistics bins. A similar picture is drawn in Fig. 5.4 where wide jet broadening, narrow jet broadening, total jet broadening, and jet broadening difference are presented.

For the analysis of the merging procedure, differential jet-rates have proven to be very useful. Already, in Sec. 3.2.3, they have been discussed in a comparison with the pure parton shower result, see Fig. 3.12. In both cases very good agreement with data was observed.

Finally, the topological structure of four-jet events is investigated using 4-jet angles, cf. Fig. 5.5. There, the Bengtsson–Zerwas angle [118], the Körner–Schierholz–Willrodt angle [129], the modified Nachtmann-Reiter angle [119], and the angle α_{34} [130] are shown. These observables are very sensitive to inter-jet correlations and quantum interferences between different diagrams, which should be described by the appropriate matrix elements. Indeed, all plots are dominated by 4- and 5-jet contributions. The agreement with data is overwhelming, especially for the Bengtsson–Zerwas and for the modified Nachtmann-Reiter angle.

Summarising, the SHERPA Monte Carlo event generator is very well suited for the description of experimental data at LEP1.

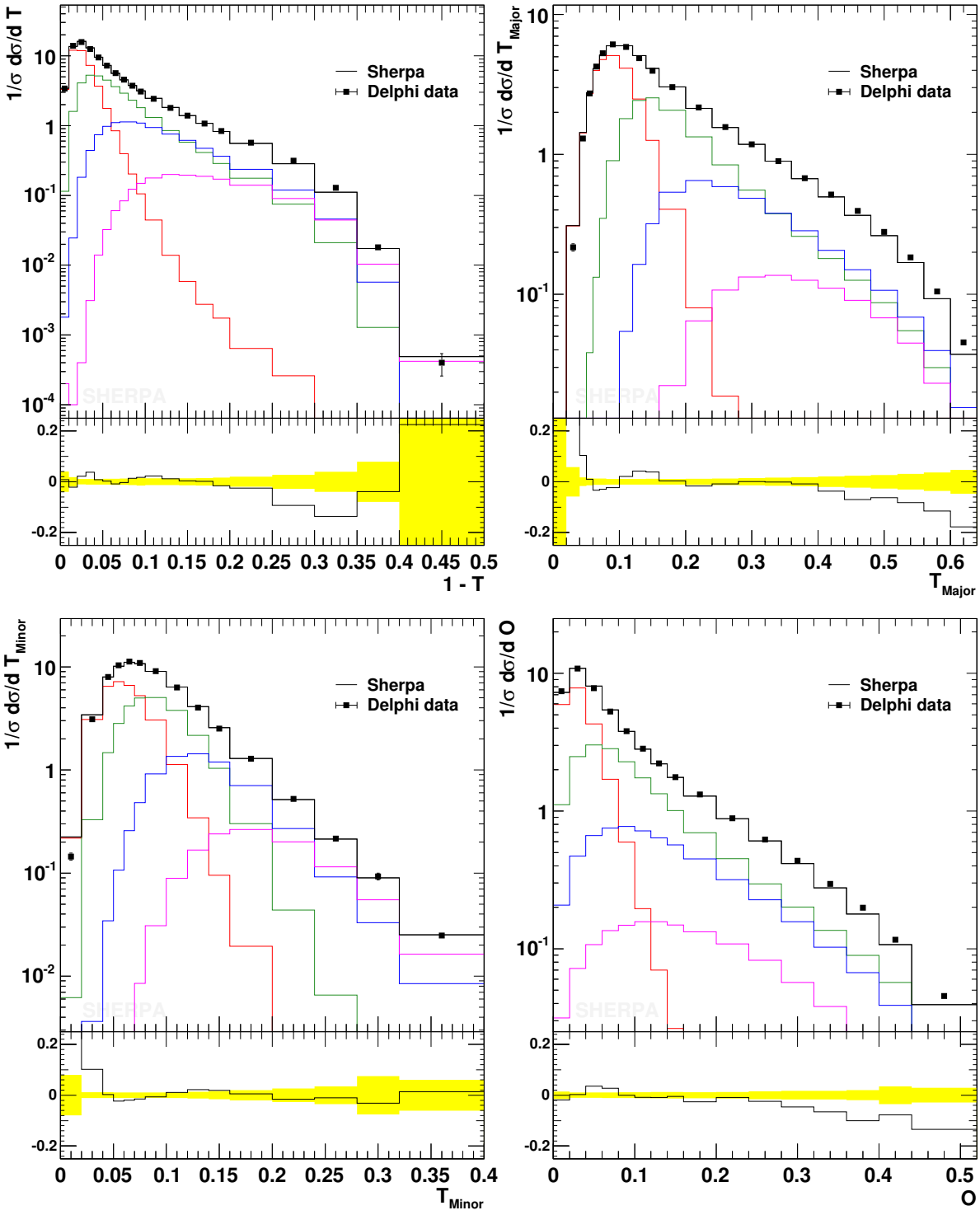

Figure 5.2: Thrust (top left), thrust-major (top right), thrust minor (bottom left), and oblateness (bottom right) at LEP1. For definitions of these observables, cf. appendix A. The hadron level result of SHERPA is pictured for a separation cut of $y_{\text{cut}} = 10^{-2.4}$. Line colours are the same as in Fig. 5.1.

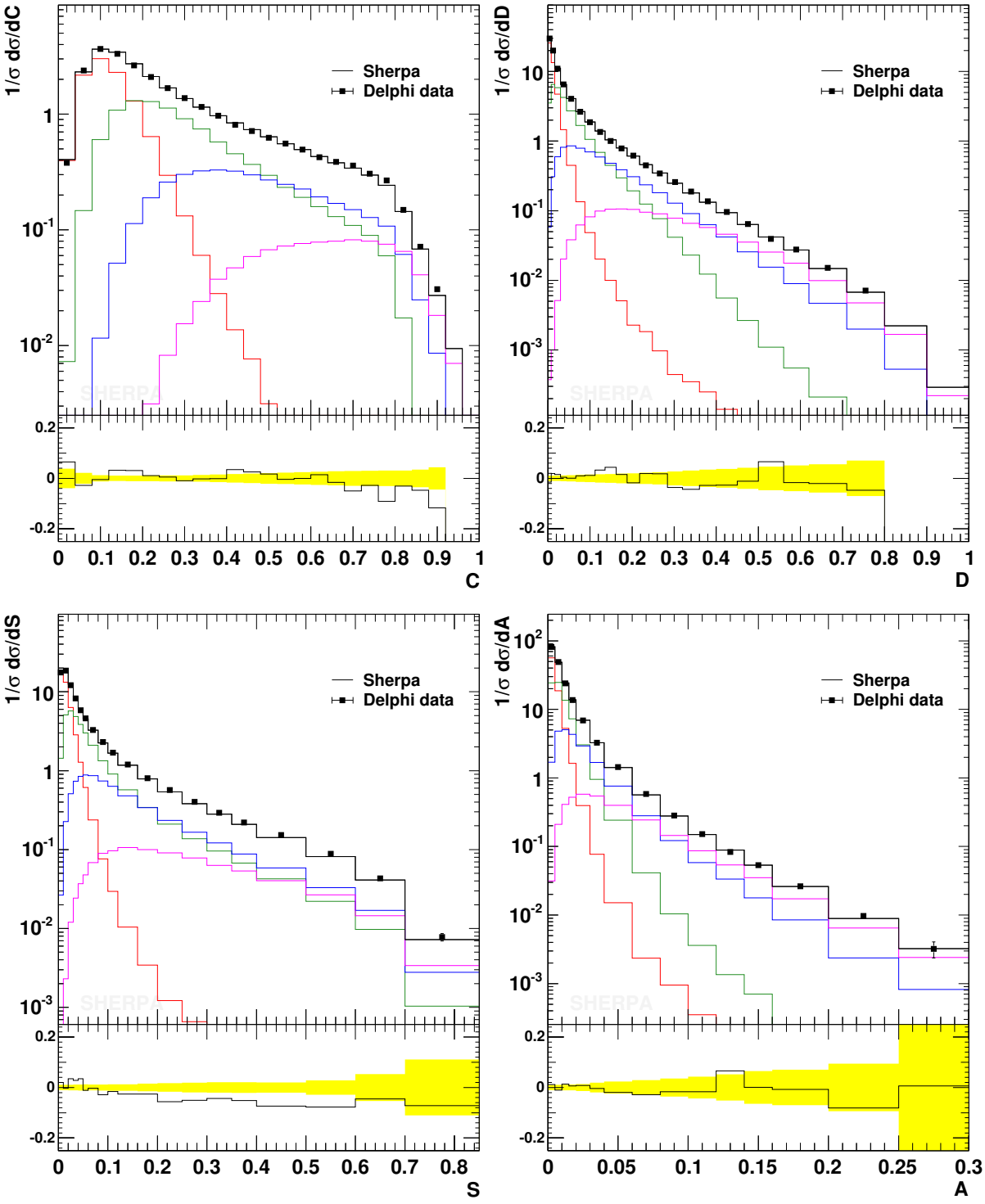

Figure 5.3: C-parameter (top left), D-parameter (top right), sphericity (bottom left), and aplanarity (bottom right) at LEP1. For definitions of these observables, cf. appendix A. The hadron level result of SHERPA is pictured for a separation cut of $y_{\text{cut}} = 10^{-2.4}$. Line colours are the same as in Fig. 5.1.

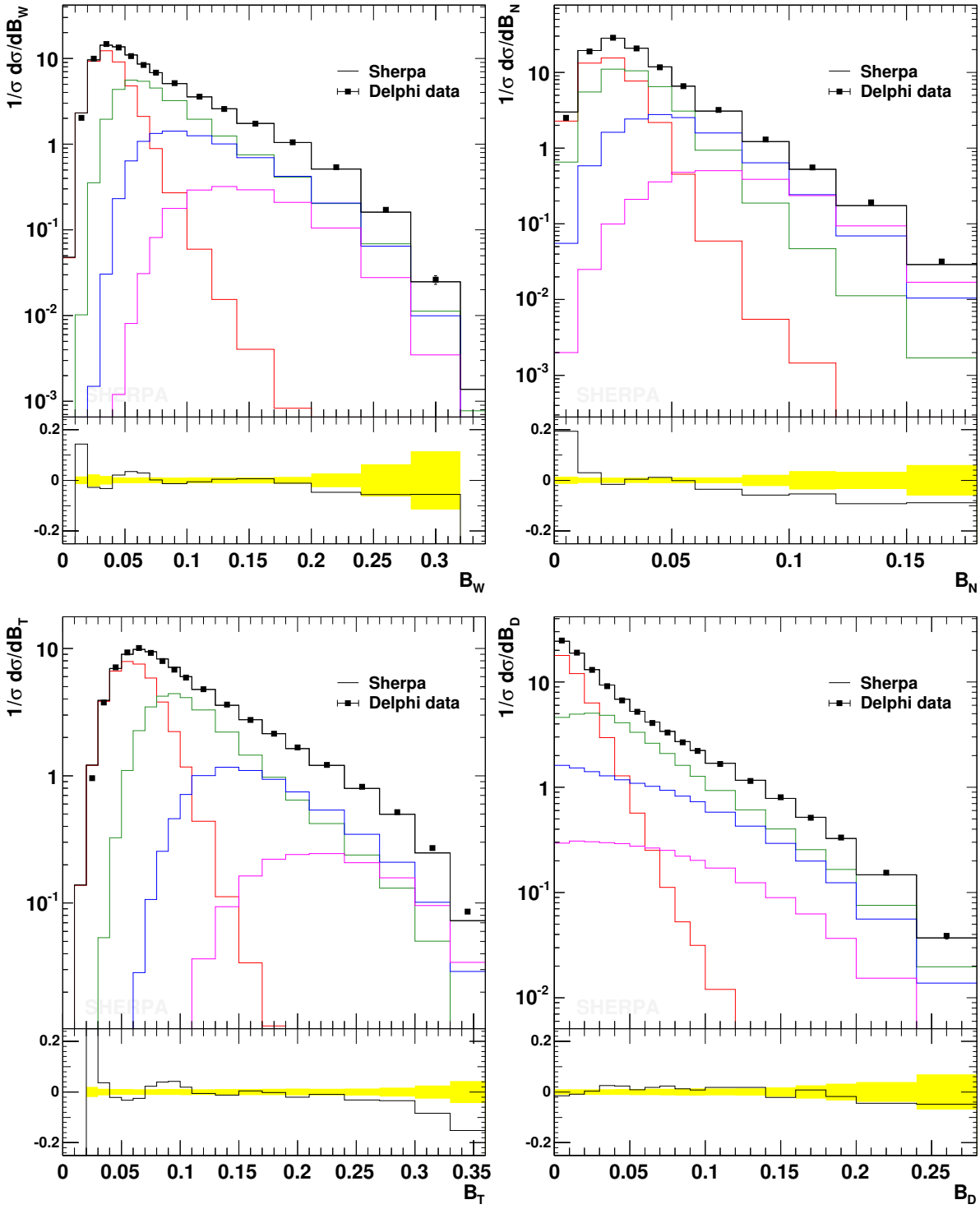

Figure 5.4: Wide jet broadening (top left), narrow jet broadening (top right), total jet broadening (bottom left), and jet broadening difference (bottom right) at LEP1. For definitions of these observables, cf. appendix A. The hadron level result of SHERPA is pictured for a separation cut of $y_{\text{cut}} = 10^{-2.4}$. Line colours are the same as in Fig. 5.1.

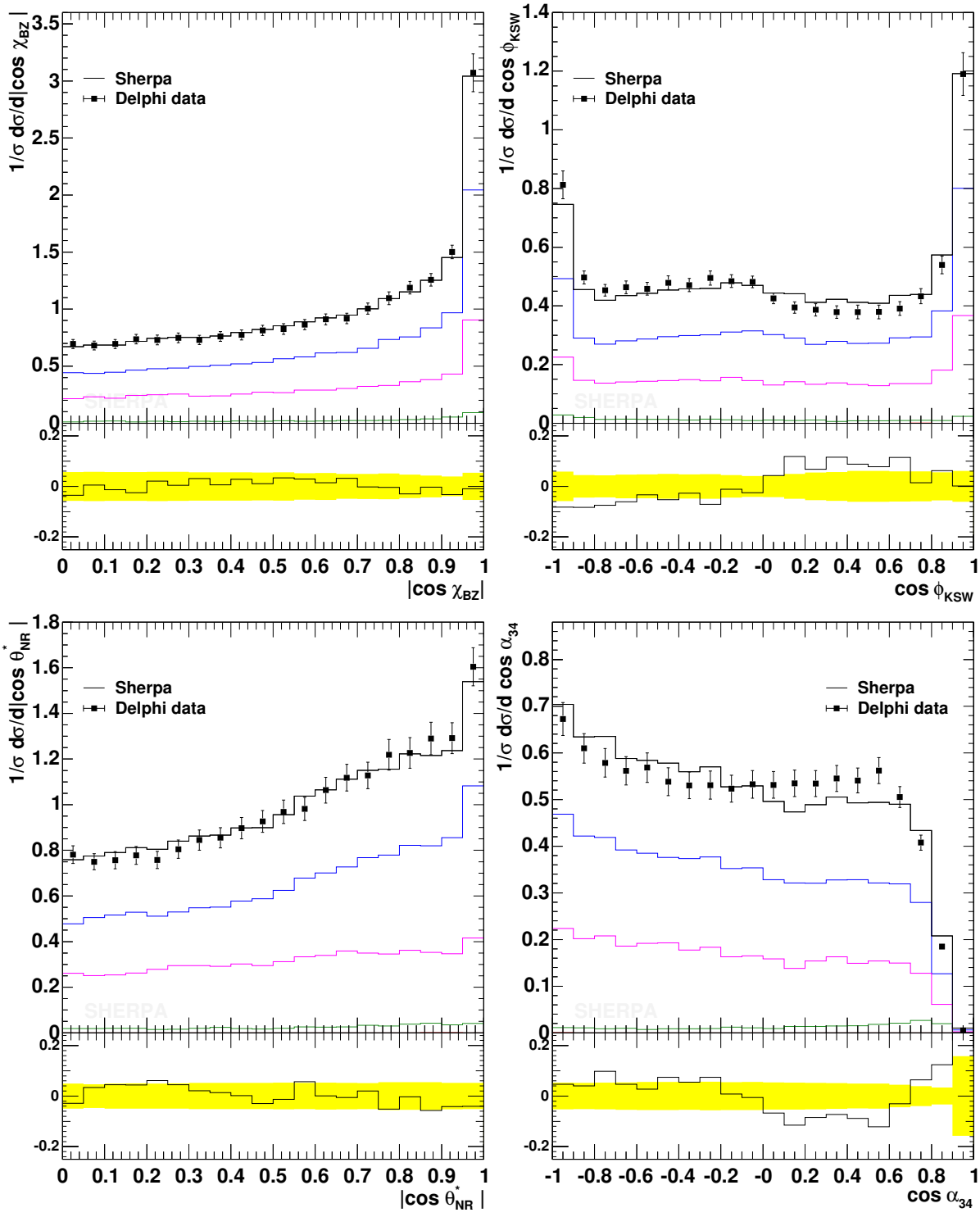

Figure 5.5: Four-jet angle distributions. The hadron level result of SHERPA is pictured for a separation cut of $y_{\text{cut}} = 10^{-2.4}$. Shown are the Bengtsson-Zerwas angle (top left), the Körner–Schierholz–Willrodt angle (top right), the modified Nachtmann-Reiter angle (bottom left), and the angle α_{34} (bottom right). The definitions of these observables can be found in appendix A. The data points are from a DELPHI measurement [117].

5.2 Hadron production at LEP2

In this section the comparison with LEP data is continued. This time, however, LEP2 data serve as benchmark. Having seen in the previous section that the agreement with data at the Z-pole is excellent, the question now to be tackled is, whether the same parameter set, obtained from a tuning on LEP1 data, can also be used at higher energies. Then the Monte Carlo, SHERPA, needs to be tuned only once, with data where the statistics is best, i.e. Z-pole data, and can then be used for the simulation of data at any c.m. energy.

The energy chosen is 189 GeV, which is the LEP measurement with the largest integrated luminosity above the Z boson resonance. At these high energies any QCD analysis is confronted with two problems. First, the high cross section of the Z resonance peak raises the possibility of hard initial state photon radiation (ISR), allowing the creation of a nearly on-shell Z boson. These radiative return events constitute a large fraction of all hadronic events, and have to be discarded. The second problem is caused by the large cross section for W-pair production. Since hadronic WW events populate the same phase space as QCD four-jet events, they are difficult to separate. Each LEP experiment has developed an independent strategy to reduce this WW background. Usually a sophisticated combination of cuts on the final state particles enables to reduce the background to approximately 10%. The remaining contribution, as well as the implication of these cuts on QCD events has to be estimated by Monte Carlo, and needs to be corrected[1]. This adds a significant bias on the data.

In the following comparison, the results obtained with SHERPA by merging matrix elements and parton showers is presented. Matrix elements with up to 5 jets have been employed. All parameters are the same as in the LEP1 analysis in the previous section.

The first observables considered are event shapes obtained by a DELPHI measurement [128]. In Fig. 5.6 thrust, major, minor and oblateness are pictured. The experimental errors, as indicated by the yellow band in the lower part of each plot, are significantly larger than the statistical error in the simulation. In all distributions SHERPA lies well within two standard deviations. Note that the prediction is very smooth and, in fact, nicely interpolates between the data points. Coloured lines indicate the contributions from individual matrix elements: two jets (red), three jets (green), four jets (blue), and five jets (purple). However, the overall distribution (black) does not posses any bumps or holes. A similar picture is drawn in Fig. 5.7, where C-parameter, D-parameter, sphericity and aplanarity are shown. Again the agreement with data is very good. The uncertainties caused by the experimental subtraction of the WW background are well visible, resulting in the case of D-parameter even in negative experimental data points. SHERPA is also able to describe wide jet broadening, jet broadening difference, heavy jet mass and jet mass difference, as shown in Fig. 5.8.

In Fig. 5.9 the focus shifts from event shapes to differential jet-rates. There, the SHERPA prediction is confronted with data from an OPAL measurement [122]. Differential jet-rates are naturally very sensitive to the details of the merging procedure. However, apparently the merging of the different matrix elements leaves no visible distortion. The agreement with the data is very satisfying.

[1] An accurate Monte Carlo description of both the QCD and the EW contribution is therefore essential for the experimental analysis. In Sec. 4.2 an extension of the merging algorithm was proposed, that allows for competing electroweak propagators.

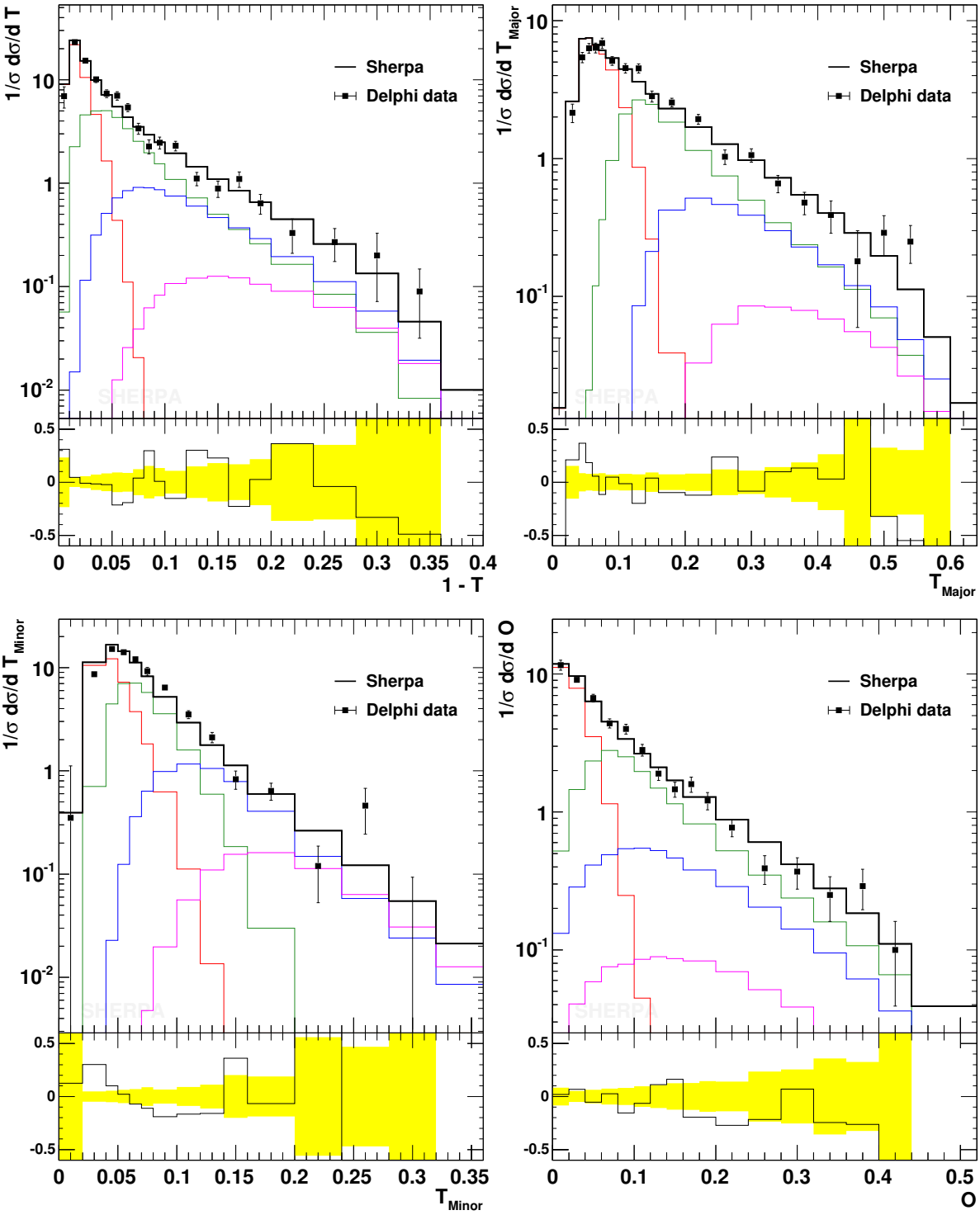

Figure 5.6: Thrust (top left), thrust-major (top right), thrust minor (bottom left), and oblateness (bottom right) at LEP2. For definitions of these observables, cf. appendix A. The data are obtained by the DELPHI collaboration [128] at a c.m. energy of 189 GeV. Shown is the results obtained through the merging of matrix elements for up to five jets with the parton shower. The separation cut is $y_{\text{cut}} = 10^{-2.4}$. Coloured lines indicate the contributions from individual matrix elements: two jets (red), three jets (green), four jets (blue), and five jets (purple).

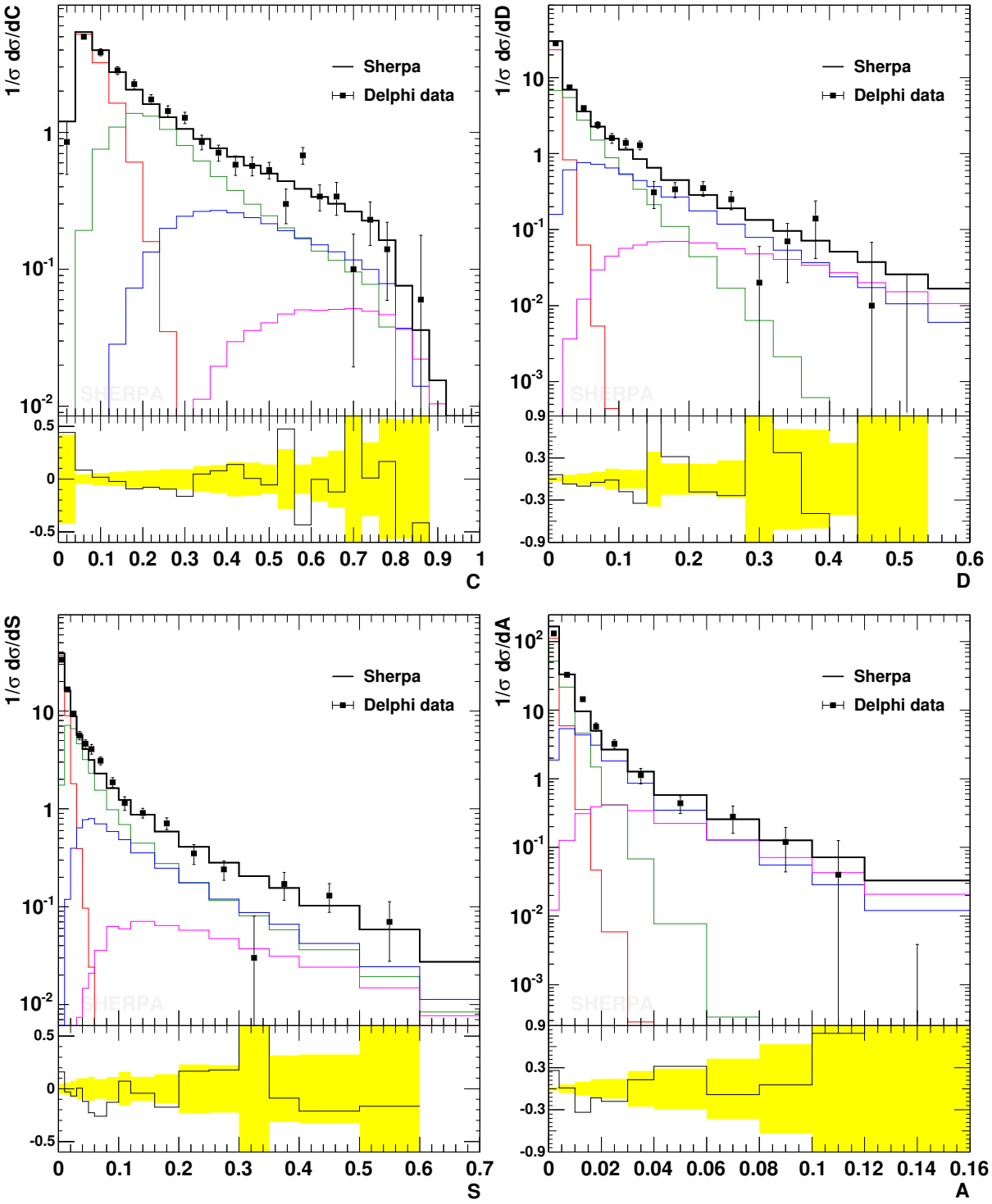

Figure 5.7: C-parameter (top left), D-parameter (top right), sphericity (bottom left), and aplanarity (bottom right) at LEP2. For definitions of these observables, cf. appendix A. The data are obtained by the DELPHI collaboration [128] at a c.m. energy of 189 GeV. The hadron level result of SHERPA is pictured for a separation cut of $y_{\text{cut}} = 10^{-2.4}$. The line colours are the same as in Fig. 5.6.

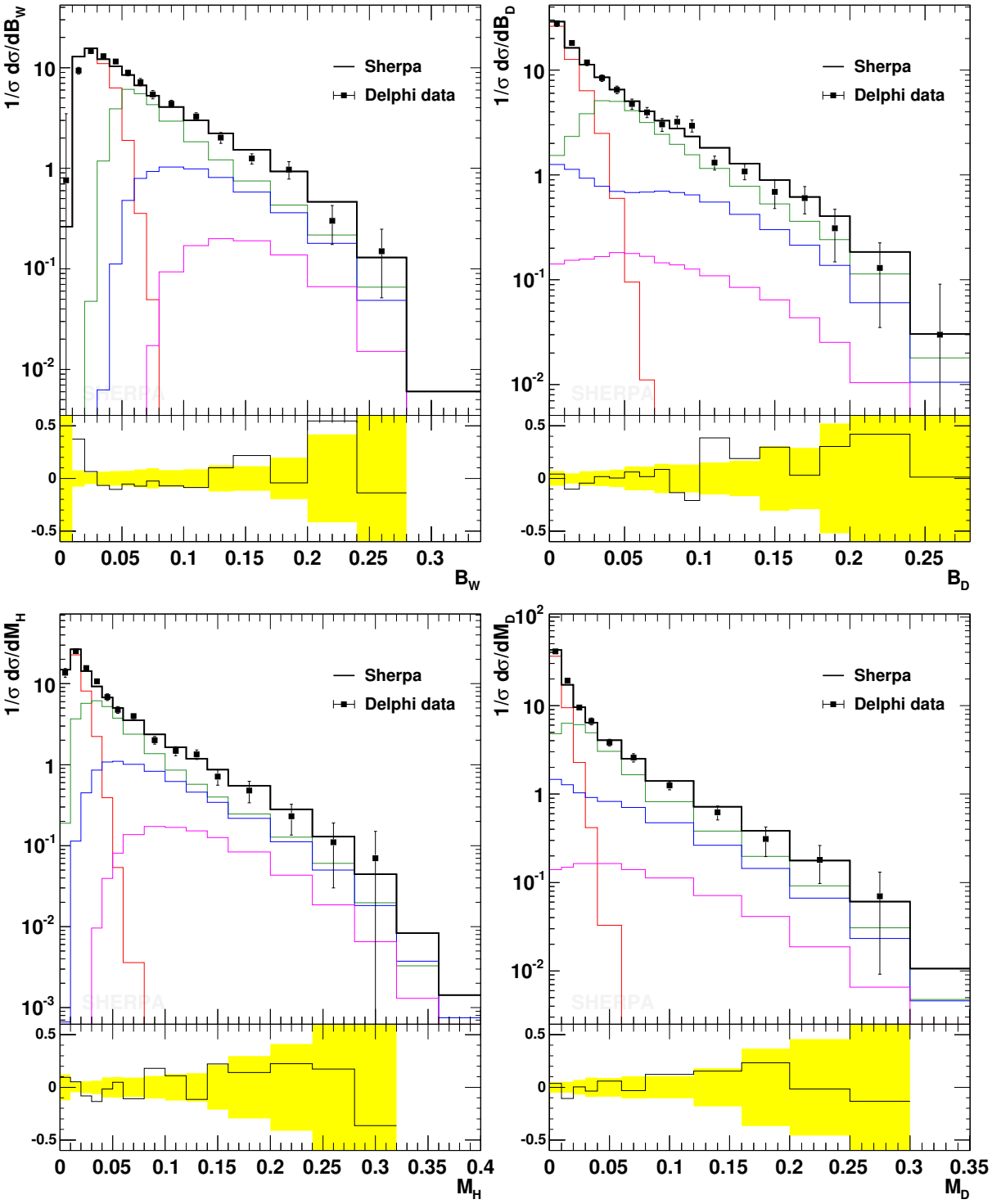

Figure 5.8: Wide jet broadening (top left), jet broadening difference (top right), heavy jet mass (bottom left) and jet mass difference (bottom right). The data are obtained by the DELPHI collaboration [128] at a c.m. energy of 189 GeV. LEP2. For definitions of these observables, cf. appendix A. The hadron level result of SHERPA is pictured for a separation cut of $y_{\text{cut}} = 10^{-2.4}$. Line colours are the same as in Fig. 5.6.

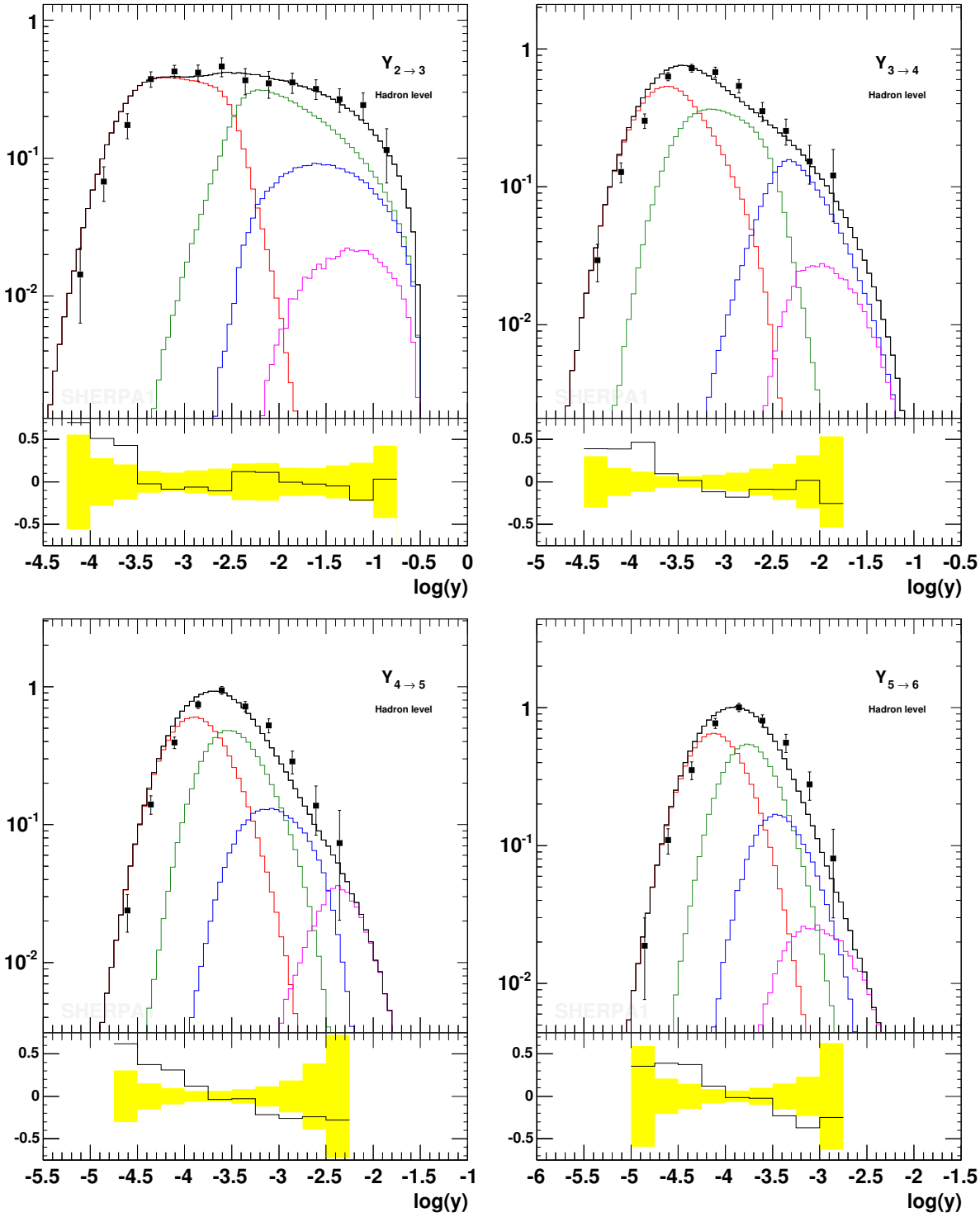

Figure 5.9: Differential jet-rates in the Durham scheme at LEP2 ($E_{\text{cms}} = 189$ GeV). The data points indicate a OPAL measurement [122]. Line colours are the same as in Fig. 5.6.

5.3 W/Z + jets production at the Fermilab Tevatron

Having discussed the performance of SHERPA in e^+e^- annihilations, the focus now shifts on hadronic collisions. The starting point for this is the discussion of results obtained for the Fermilab Tevatron, operating at 1.8 TeV (Run I) and 1.96 TeV (Run II) centre-of mass energy in proton-antiproton reactions. In particular, results obtained from SHERPA for the case of single electroweak gauge bosons are discussed.

The production of such electroweak gauge bosons, e.g. $W^\pm$ and Z bosons, is one of the most prominent processes at hadron colliders. Especially through their leptonic decays they leave a clean signature, namely either one charged lepton accompanied by missing energy for W bosons or two oppositely charged leptons for the Z bosons. The combination of clear signatures and copious production rates allows a measurement of some of their parameters, e.g. the W mass and width, at the Tevatron with a precision comparable with that reached at LEP2 [131–140]. Furthermore, especially in combination with additional jets, the production of gauge bosons represents a serious background to many other interesting processes, leading to multi-particle final state topologies. The production and decay of pairs of top quarks or of SUSY particles may serve as illustrative examples for such signal processes. The special interest in this classic production process is reflected by the fact that it was one of the first to be calculated at next-to-leading order (NLO) [141–145] and next-to-next-to-leading order (NNLO) [126, 127] in QCD. Recently, the first distribution related to these processes, namely the boson rapidity, has been calculated at NNLO [146]. In addition to such fixed-order calculations, programs such as RESBOS [147] have been made available, which resum soft gluon effects. Cross sections and distributions for W or Z bosons being produced together with jets can be evaluated at the parton level through a number of different computer codes: specialised ones such as VECBOS [148], and multi-purpose parton-level generators such as CompHEP [55], GRACE/GR@PPA [56, 57], MadGraph/MadEvent [61, 62], ALPGEN [54], and AMEGIC++ [23]. All of them operate at the tree level, at NLO, the program MCFM [149, 150] provides cross sections and distributions for W/Z+jets for up to 2 jets.

Apart from such techniques, based on analytical methods, event generators play a major role in the experimental analysis of collider experiments. In the past years, programs such as PYTHIA [76,82] or HERWIG [3,77] proved to be successful in describing global features of boson production processes, such as the bosons transverse momentum or rapidity distribution. Apart from the parton shower, which takes proper care and resums the leading and some of the sub-leading Sudakov logarithms, these programs include the first-order matrix element for the emission of an extra parton, implemented through a correction weight on the parton shower. Because of the different approximations made for their parton shower, this is realized in different manners inside the two programs, cf. [151] and [152, 153].

In view of the need for more precise simulations, both in terms of total rates and in the description of exclusive final states, two quite orthogonal approaches have been developed recently, which aim at a systematic combination of higher-order matrix elements with the parton shower. The first one, called MC@NLO, provides a method to consistently match NLO calculations for specific processes with the parton shower. It has been implemented for the production of colour-singlet final states, such as W and Z bosons, or pairs of these bosons [11], or the Higgs boson, and for the production of heavy quarks [12]. The implementations are available as a code called MC@NLO [13] residing on top of HERWIG. The idea of this approach is to organise the counter-terms necessary to technically cancel real and virtual infrared divergencies in such a way that the first emission of the parton shower is recovered.

This allows the generation of hard kinematics configurations, which can eventually be fed into a parton shower Monte Carlo. As discussed at length in Sec. 4.2, an alternative approach is implemented in SHERPA. It employs matrix elements at the tree level for different jet multiplicities and merges them with the parton shower. In the following sections this merging procedure, as implemented in SHERPA is validated for the example of single-boson production. Results will be compared with those of other approaches, and with data. The observables, that will be studied, are inclusive, like the transverse momentum and rapidity distribution of the bosons, and more exclusive, like the transverse momentum distribution of additional jets. In a first step, the self-consistency of the method will be checked by analysing the dependence of different observables on the separation cut and on the maximal number of extra jets provided by the matrix elements, see Sec. 5.3.2. Following this, the results of the merging method will be contrasted with those of other approaches: on the matrix element level, the jet transverse momentum distributions of SHERPAs reweighted matrix elements will be compared with those of a full-fledged NLO calculation provided by MCFM; see Sec. 5.3.3. Then, the results after parton showering and hadronisation will be compared with those of other event generators in Sec. 5.3.3, specifically with those obtained from PYTHIA and MC@NLO. Finally, the ability of the method to describe inclusive observables that have been measured, such as the bosons transverse momentum, will be exhibited in Sec. 5.3.3. A successor of this study, dealing with the production of electroweak gauge bosons at the CERN LHC, is presented in Sec. 5.4.

5.3.1 Input parameters and phase-space cuts

The PDF set used for all analyses is CTEQ6L [29]. The value of α_s is chosen according to the value taken for the PDF, namely 0.118. For the running of the strong coupling the corresponding two-loop equation is used. Jets or initial partons are restricted to the light flavour sector, namely g, u, d, s, c. In fact these flavours are taken to be massless and the Yukawa couplings of the quarks are neglected throughout the entire analysis.

SM input parameters

The SM parameters are given in the G_μ scheme:

$$\begin{aligned}
&m_W = 80.419\ \text{GeV}\,, \quad \Gamma_W = 2.06\ \text{GeV},\\
&m_Z = 91.188\ \text{GeV}\,, \quad \Gamma_Z = 2.49\ \text{GeV},\\
&G_\mu = 1.16639 \times 10^{-5}\ \text{GeV}^{-2},\\
&\sin^2\theta_W = 1 - m_W^2/m_Z^2,\\
&\alpha_s = 0.118\,.
\end{aligned} \tag{5.1}$$

The electromagnetic coupling is derived from the Fermi constant G_μ according to

$$\alpha_{\text{em}} = \frac{\sqrt{2}\, G_\mu\, M_W^2\, \sin^2\theta_W}{\pi}. \tag{5.2}$$

The constant widths of the electroweak gauge bosons are introduced via the fixed-width scheme. CKM mixing of the quark generations is neglected.

Cuts and jet criteria

For all jet analyses the Run II $k_\perp$-clustering algorithm defined in [154] is used. The parameter of this jet algorithm is a pseudo-cone of size D given below for the Tevatron analysis. For the charged leptons the following cuts are applied:

$$p_\perp^{\text{lepton}} > 20 \text{ GeV}, \quad |\eta^{\text{lepton}}| < 1, \quad m_{ll} > 15 \text{ GeV}. \tag{5.3}$$

For the case of W production an additional cut on missing transverse momentum according to the neutrino has been required, namely

$$p_\perp^{\text{miss}} > 20 \text{ GeV}. \tag{5.4}$$

For the jet definition a pseudo-cone size of $D = 0.7$ has been used in addition to cuts on pseudo-rapidity and transverse momentum:

$$p_\perp^{\text{jet}} > 15 \text{ GeV}, \quad |\eta^{\text{jet}}| < 2. \tag{5.5}$$

5.3.2 Consistency checks

In this section the self-consistency of the results obtained with SHERPA is checked by analysing the dependence of different observables on the key parameters of the merging procedure, namely the separation scale Q_{cut} and the highest multiplicity of included matrix elements $n_{\max}$. All plots in this section correspond to W^- boson production at the Tevatron, Run II. If not stated otherwise, the distributions shown are inclusive hadron level results, i.e. no cuts have been applied.

Variation of the separation cut Q_{cut}

In all figures, the black, solid line represents the total inclusive result as obtained by SHERPA. A vertical dashed line indicates the respective separation cut Q_{cut}, which has been varied between 10 GeV and 50 GeV. To guide the eye, all plots also show the same observable as obtained with a separation cut $Q_{\text{cut}} = 20$ GeV, shown as a dashed black curve. The coloured lines give the contributions of different multiplicity processes. Note that the separation cut always marks the transition between n-jet and $n+1$-jet matrix elements.

Figs. 5.10 and 5.11 show the transverse momentum and the rapidity distribution of the W^- boson and the corresponding electron. For the transverse momentum of the W below the cut, the distribution is dominated by the LO matrix element with no extra jet, i.e. the transverse momentum is generated by the initial state parton shower only. Around the cut, a small dip is visible in Fig. 5.10. The $p_\perp$ distribution of the electron, in contrast, is hardly altered. The rapidity distributions in Fig. 5.11 exhibit the asymmetry, which has been anticipated when considering merely the negatively charged W boson. The shape of these distributions is very stable under a variation of the separation cut. In all observables a small increase of the total cross section of a few percent when changing Q_{cut} from 10 GeV to 50 GeV is visible. This underlines the fact that the dependence on the separation cut is weak.

Differential jet-rates with respect to the $k_\perp$-algorithm are interesting observables, since they basically exhibit the distributions of nodal values using the cluster algorithm. For simplicity, the Run II $k_\perp$-algorithm has been used with $D = 1$ for the analysis. Any

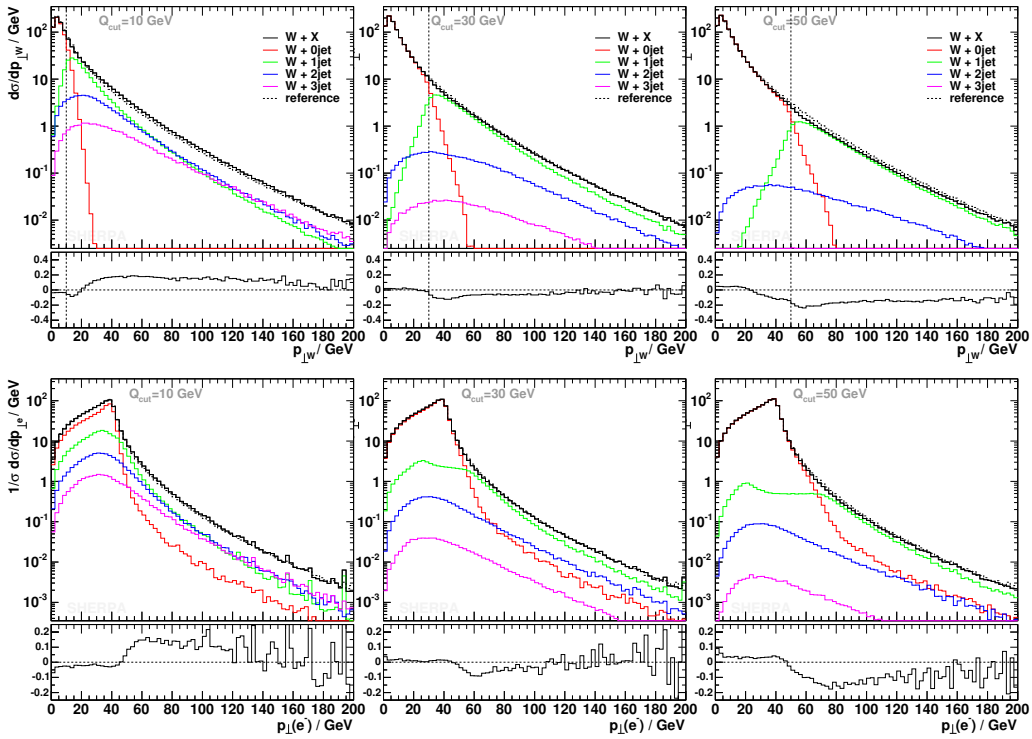

Figure 5.10: $p_\perp(W^-)$ and $p_\perp(e^-)$ for $Q_{\text{cut}} = 10$ GeV, 30 GeV and 50 GeV in comparison with $Q_{\text{cut}} = 20$ GeV.

problem of QCD radiation with respect to the separation should immediately manifest itself in these distributions. In Fig. 5.12 the $1 \to 0$, $2 \to 1$ and $3 \to 2$ differential jet-rates are shown. Within the given approximation the independence is satisfactory.

Variation of the maximal jet multiplicity $n_{\max}$

For very inclusive observables such as transverse momentum and rapidity of the W boson, it is usually sufficient to include the matrix element with only one extra jet in order to obtain a reliable prediction. Consequently, the inclusion of matrix elements with more than one extra jet in the simulation should not significantly change the result. This can be used as another consistency check. Figs. 5.13 and 5.14 impressively picture the dependence on the maximal jet number in the matrix elements included. They show that the treatment of the highest multiplicity (cf. Sec. 4.2) completely compensates for the missing matrix elements, whereas the contribution of the lowest multiplicity is not altered.

Matrix element, parton shower and hadronisation

In addition to the self-consistency of the algorithm tested so far at the hadron level, it is worth checking that the parton shower and hadronisation do not induce significant changes with respect to the initial reweighted matrix element in high-$p_\perp$ regions. Fig. 5.15 proves that the predictions of SHERPA, e.g. the $p_\perp$ distribution of the hardest jet in W production, are remarkably stable in the region of matrix element dominance.

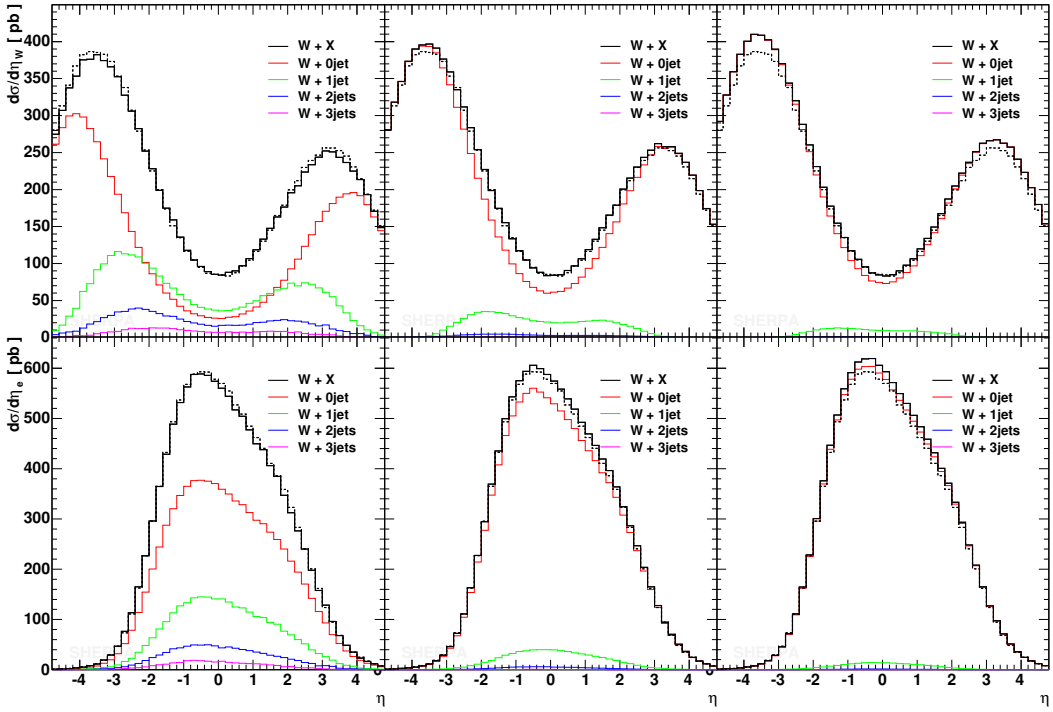

Figure 5.11: $\eta(W^-)$ and $\eta(e^-)$ for $Q_{\text{cut}} = 10$ GeV, 30 GeV and 50 GeV in comparison with $Q_{\text{cut}} = 20$ GeV.

Variation of factorisation and renormalisation scale

Finally, the sensitivity of the previous results with respect to changes in the renormalisation and factorisation scale are examined. In the following, all scales occurring in the event generation, both at the matrix element and at the parton shower level, are multiplied by constant factors, ranging from 0.5 up to 5. It is clear that the total cross section changes with changing scales: starting with 930 pb for the default scale choice, 887 pb (959 pb) are obtained when using a scale factor of 0.5 (2). The shapes of the $p_\perp$ distributions of the jets, however, experience only mild changes. This is greatly exemplified by the left panel of Fig. 5.16, where the $p_\perp$ spectrum of the hardest jet is displayed. In the right panel of Fig. 5.16 the result of the left panel is broken down for two different scale prefactors, 1 and 5, to the different contributions. Clearly, at the individual level different jet multiplicities differ also in their shapes; in their interplay, however, these effects cancel in terms of the overall shape.

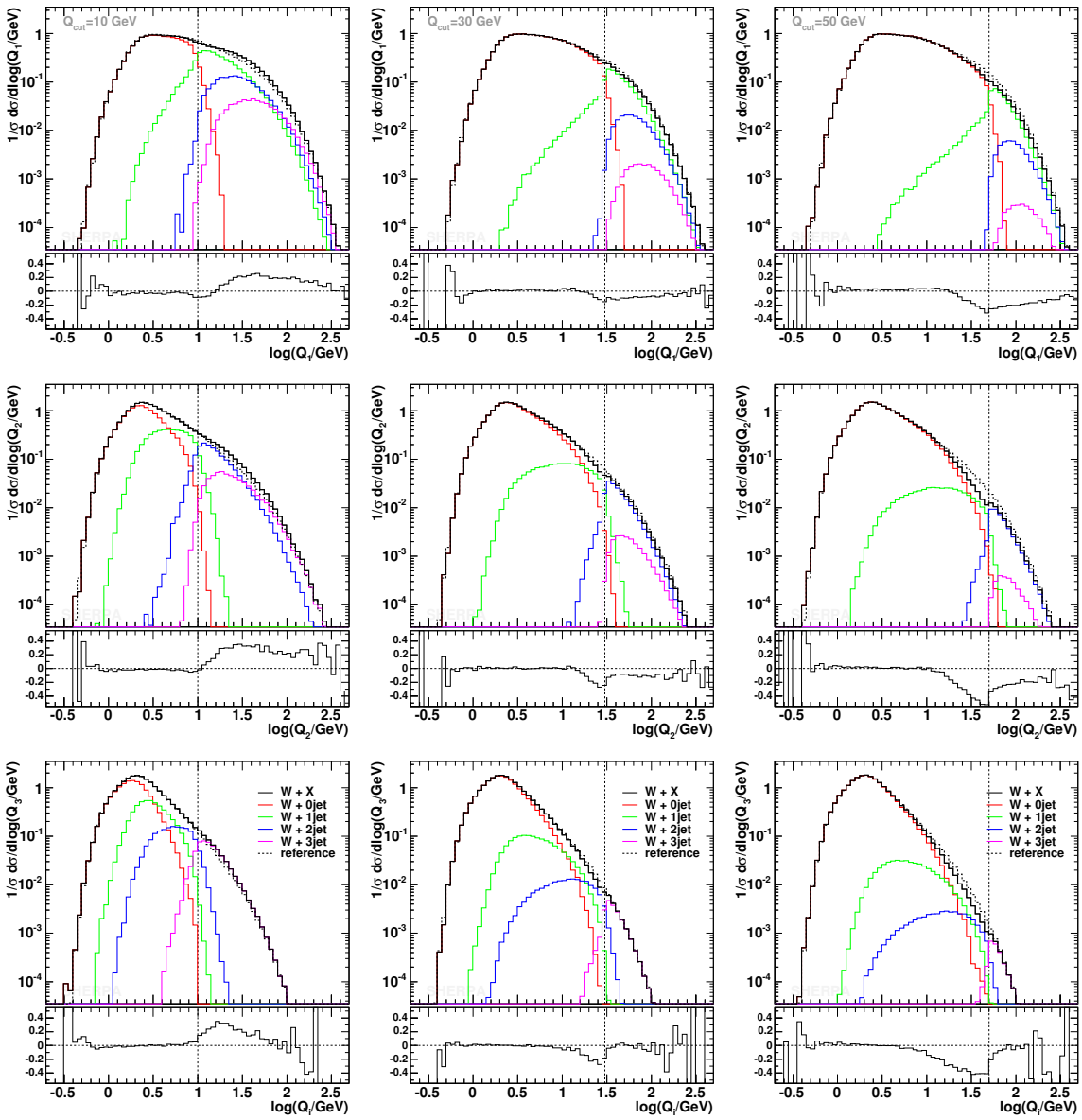

Figure 5.12: Differential jet-rates for the $1 \to 0$, $2 \to 1$ and $3 \to 2$ transition (top to bottom), for $Q_{\text{cut}} = 10$ GeV, 30 GeV, and 50 GeV (from left to right). In each plot, the results are compared with those for $Q_{\text{cut}} = 20$ GeV.

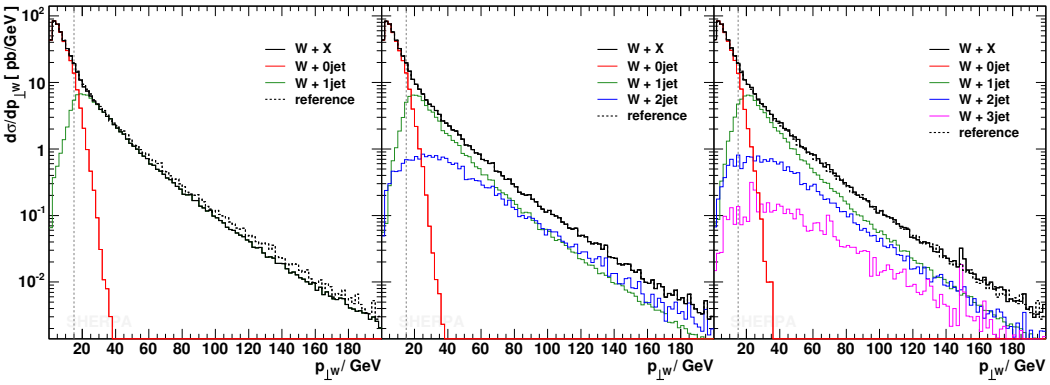

Figure 5.13: $p_\perp(W^-)$ for $Q_{\text{cut}} = 15$ GeV and different maximal numbers of ME jets included. The dashed line corresponds to a maximal numbers of ME jets $n_{\text{max}} = 2$.

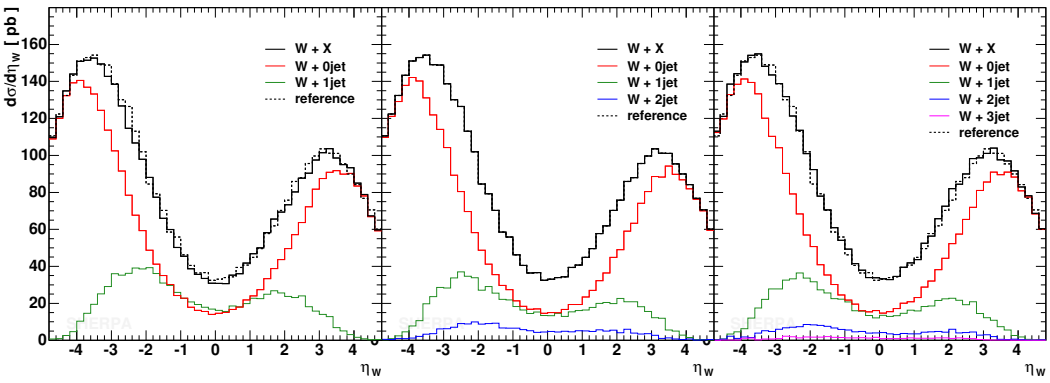

Figure 5.14: $\eta(W^-)$ for $Q_{\text{cut}} = 15$ GeV and different maximal numbers of ME jets included. The dashed line corresponds to a maximal numbers of ME jets $n_{\text{max}} = 2$.

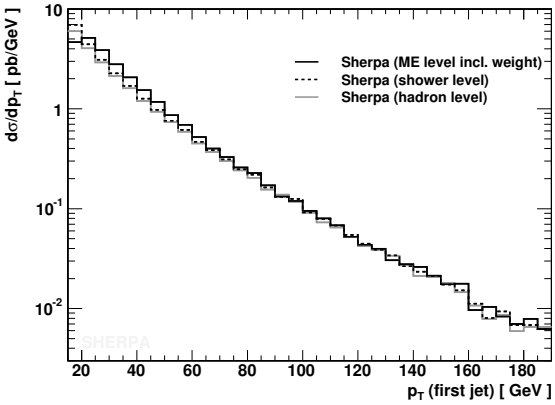

Figure 5.15: The $p_\perp$ of the hardest jet in inclusive W production at the Tevatron, Run II. The solid line indicates the distribution as delivered by the matrix elements (including the Sudakov and coupling weight); the dashed line is obtained after parton shower evolution; and the dotted line gives the final result after hadronisation. Here $Q_{\text{cut}} = 15$ GeV.

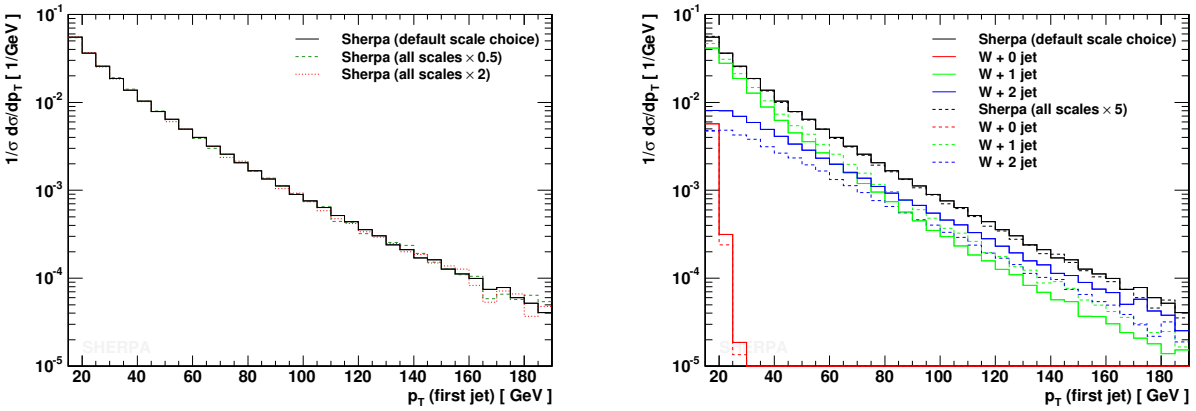

Figure 5.16: The $p_\perp$ of the hardest jet in inclusive W production at the Tevatron, Run II, and its dependence on different choices in the renormalisation and factorisation scale. In the left plot, the solid line indicates the default hadron level result; the green dashed and the red dotted line are obtained by multiplying all scales in the coupling constants and the PDFs in both the matrix elements and the parton shower by a factor of 0.5 or 2, respectively. In the right plot, the same observable is investigated in more detail with the default scales (solid lines) and with all scales multiplied by a factor of 5. In addition the different contributions of different jet multiplicities are shown.

5.3.3 SHERPA vs. data and other MCs

In order to study the impact of the merging prescription, the predictions obtained with SHERPA may also be compared with other approaches. In a first step, in Sec. 5.3.3 the transverse momentum distribution of the first and second hardest jets in exclusive and inclusive boson-plus-jet production from SHERPA are confronted with the NLO QCD predictions of the parton level generator MCFM [149,150]. In Sec. 5.3.3 the full event generators MC@NLO [13] and PYTHIA [76] are used to investigate the capabilities of SHERPA when studying W/Z+jet production at the hadron level. Finally Sec. 5.3.3 contains a comparison of the predictions made for the bosons transverse momentum distribution with those measured by the D0 and CDF collaborations at the Tevatron, Run I.

SHERPA vs. MCFM

In order to compare the SHERPA predictions for W/Z+1jet and W/Z+2jet production, a two-step procedure is chosen. In a first step the Sudakov and α_s reweighted matrix elements are compared with exclusive NLO results obtained with MCFM. In the case of the next-to-leading order calculation, the exclusiveness of the final states boils down to a constraint on the phase space for the real parton emission. The exclusive SHERPA results consist of appropriate leading order matrix elements with scales set according to the $k_\perp$-clustering algorithm and made exclusive by suitable Sudakov form factors, cf. Sec. 4.2. In a second step, the jet spectra for inclusive production processes are compared. For the next-to-leading order calculation, this time the phase space for real parton emission is not restricted and the SHERPA predictions are obtained from a fully inclusive sample, using matrix elements with up to two extra jets and the parton showers attached. If not stated otherwise, all results have been obtained using the input parameters and phase-space cuts summarised before. Jets are found using the Run II $k_\perp$-clustering algorithm defined in [154] with a pseudo-cone size of $D = 0.7$ and a minimal $p_\perp$ of 15 GeV.

Exclusive jet $p_\perp$ spectra

In Fig. 5.17 the jet $p_\perp$ distribution for the exclusive production of W+1jet and Z+1jet are shown. In both figures, the SHERPA prediction is compared with the exclusive NLO result obtained with MCFM and with the naive LO prediction, which is the same for the two programs. For the fixed-order NLO and LO result, the renormalisation and factorisation scales have been set to $\mu_R = \mu_F = 80.419\ \text{GeV} = M_W$. All distributions have been normalised to the corresponding total cross section. This allows for a direct comparison of the distributions shape. As stated above, the SHERPA results stem from Sudakov and α_s reweighted W+1jet or Z+1jet LO matrix elements (without highest multiplicity treatment). The change between the naive leading order and the next-to-leading order distribution is significant. At next-to-leading order the distributions become much softer. For a high-$p_\perp$ jet it is much more likely to emit a parton that fulfils the jet criteria and therefore removes the event from the exclusive sample. The SHERPA predictions show the same feature. The inclusion of Sudakov form factors and the scale setting according to the merging prescription improves the LO prediction, resulting in a rather good agreement with the next-to-leading order result.

In the high-$p_\perp$ tail, however, the NLO calculations from MCFM tend to be a bit below the SHERPA results. The reason is simply connected to the fact that relevant scales in the high-$p_\perp$

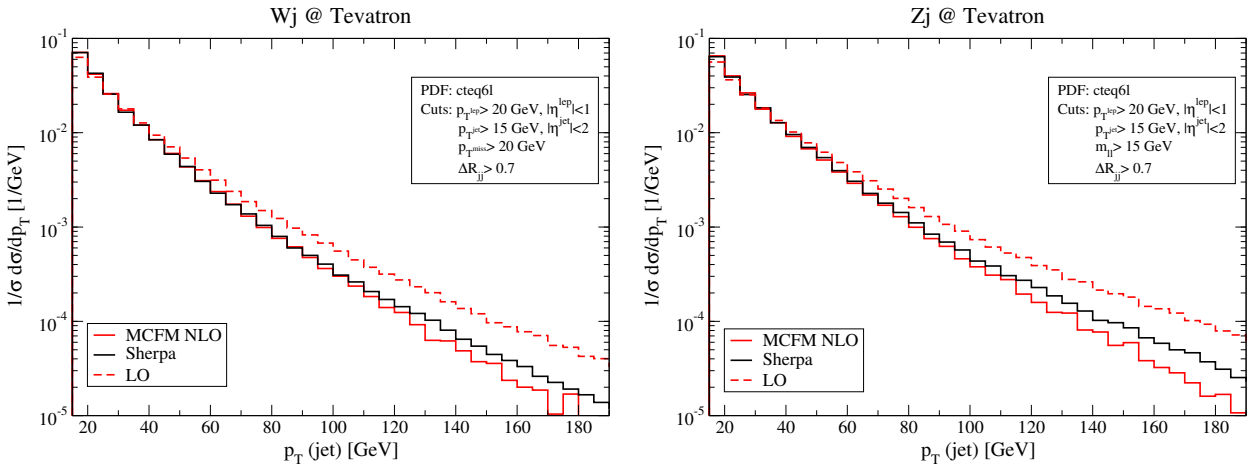

Figure 5.17: Jet $p_\perp$ distribution of exclusive $W+1$jet (left) or $Z+1$jet (right) events at the Tevatron, Run II.

tail are much larger than the default choice of $\mu_R = \mu_F = 80.419$ GeV. A more appropriate and often used scale choice is $\mu = \sqrt{M_W^2 + p_\perp^2}$. In order to highlight the scale dependence, Fig. 5.18 contains the jet $p_\perp$ distribution in Z+1jet events. In this plot, the renormalisation and factorisation scales have been chosen to be $\mu_R = \mu_F = 160.838$ GeV $= 2M_W$. Changing the scale in this manner indeed has quite a small impact on the total cross section at NLO, but the tail of the distribution is considerably enhanced. With the above choice of μ_R and μ_F the agreement of NLO and the SHERPA result is impressive.

The $p_\perp$ distributions of the first and second jets in W+2jet and Z+2jet production are presented in Fig. 5.19. Again, the next-to-leading order distributions are softer than the leading order ones, for the same reason as for the 1-jet case. In addition, at low-$p_\perp$ the leading order result is smaller than the next-to-leading order one. Taken together, the curves have a significantly different shape over the whole interval, hence a constant K-factor multiplying the LO prediction won't lead to correct results. Nevertheless, as before, the SHERPA prediction reproduces very well the shape of the NLO result delivered by MCFM, only by using LO 2-jet matrix elements with appropriate α_S and Sudakov weights. Fig. 5.20 shows that, similar to the Z+1jet case, for W+2jet in the high-$p_\perp$ tail, the situation is even better using higher renormalisation and factorisation scales (e.g. $\mu_R = \mu_F = 160.838$ GeV) in the NLO calculation.

Inclusive jet $p_\perp$ spectra

NLO results for inclusive boson plus jet(s) production obtained with MCFM are compared with fully inclusive samples generated with SHERPA. There, the matrix elements for W/Z+0,1,2jet production have been used including the highest multiplicity treatment for the W/Z+2jet case. The Sudakov and α_s reweighted matrix elements have now been combined with the initial and final state parton showers. The hadronisation phase for the SHERPA events has been discarded. As for the exclusive case the naive leading order prediction is given by the corresponding leading order matrix element that is identical to the one in Figs. 5.17 and

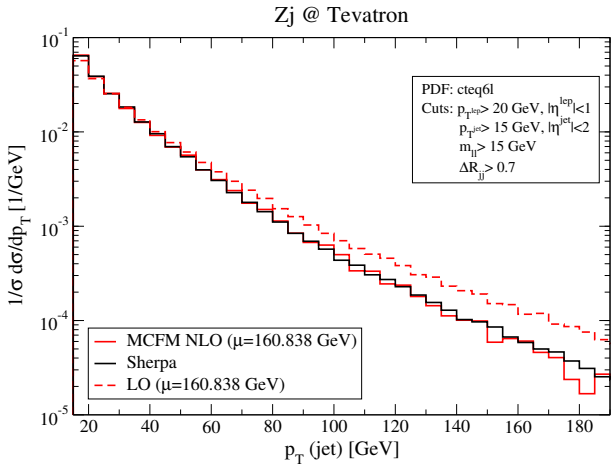

Figure 5.18: Jet $p_\perp$ distribution of $Z + 1$jet events at the Tevatron where for the NLO and LO calculation the renormalisation and factorisation scales have been chosen to be $\mu_R = \mu_F = 160.838$ GeV.

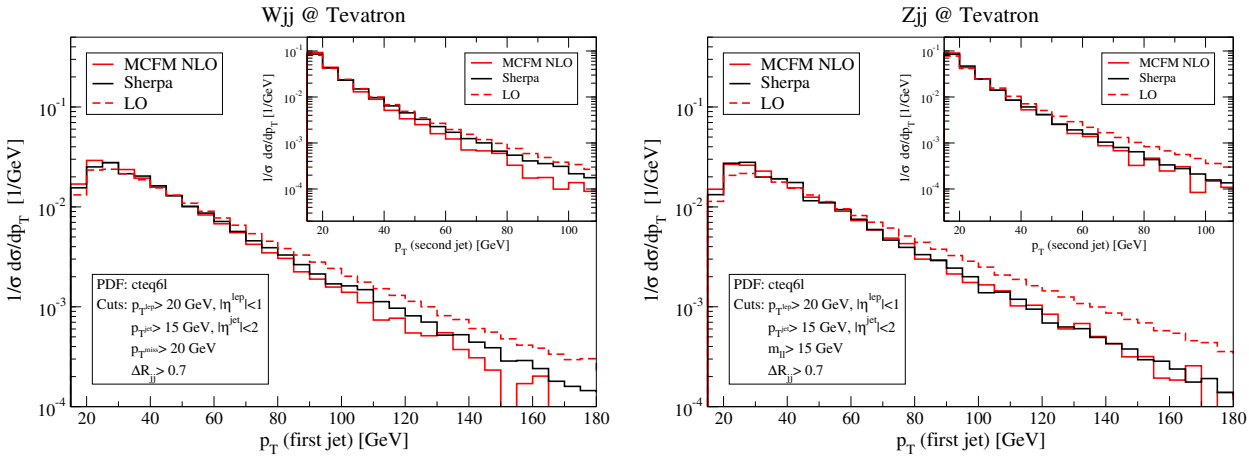

Figure 5.19: The $p_\perp$ distribution of the first and second jets in exclusive $W + 2$jet (left) and in exclusive $Z + 2$jet (right) events at the Tevatron, Run II.

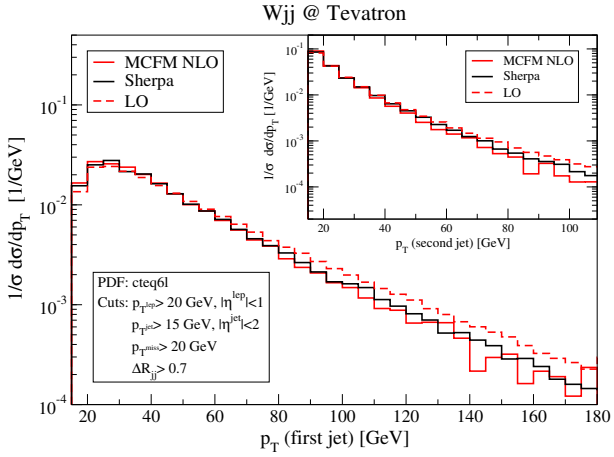

Figure 5.20: The $p_\perp$ distribution of the first and second jets in exclusive W + 2jet events at the Tevatron where for the NLO and LO calculation the renormalisation and factorisation scales have been chosen to $\mu_R = \mu_F = 160.838$ GeV.

5.19. For the NLO prediction again the renormalisation and factorisation scales have been chosen to coincide, namely $\mu_R = \mu_F = 80.419$ GeV.

In Fig. 5.21, the $p_\perp$ spectra for the hardest jet in inclusive W/Z+1jet production are shown. Compared with the exclusive predictions, the high-$p_\perp$ tail is filled again and, hence, the differences between the NLO calculations and the LO ones appear to be smaller. For both cases, the SHERPA result and the NLO calculation are in good agreement.

In Fig. 5.22 the $p_\perp$ spectra for the first and second hardest jets in inclusive W/Z+2jet production are presented. Considering the scale dependence of the next-to-leading order result in the high-$p_\perp$ region, as already studied in Fig. 5.20 for the exclusive result, the curves are in good agreement.

Altogether, the merging procedure in SHERPA, including the scale-setting prescription of the approach and the Sudakov reweighting of the LO matrix elements, proves to lead to a significantly improved leading order prediction. Seemingly, it takes proper care of the most relevant contributions of higher order corrections. Although it should be stressed that the rate predicted by SHERPA is still a leading order value only, a constant K-factor is sufficient to recover excellent agreement with a full next-to-leading order calculation for the distributions considered. Furthermore, by looking at the inclusive spectra it is obvious that this statement still holds true after the inclusion of parton showers and the merging of exclusive matrix elements of different jet multiplicities.

SHERPA vs. MC@NLO and PYTHIA

In a next step, results obtained with SHERPA (with $n_{\max} = 3$) are compared with those obtained from two other event generators, namely MC@NLO and PYTHIA. The former program incorporates a consistent matching of a full next-to-leading order calculation with the parton shower provided by HERWIG [3, 77]. It thus employs an angular-ordered shower, taking full account of coherence effects. In contrast, PYTHIA uses tree-level matrix elements, in this case

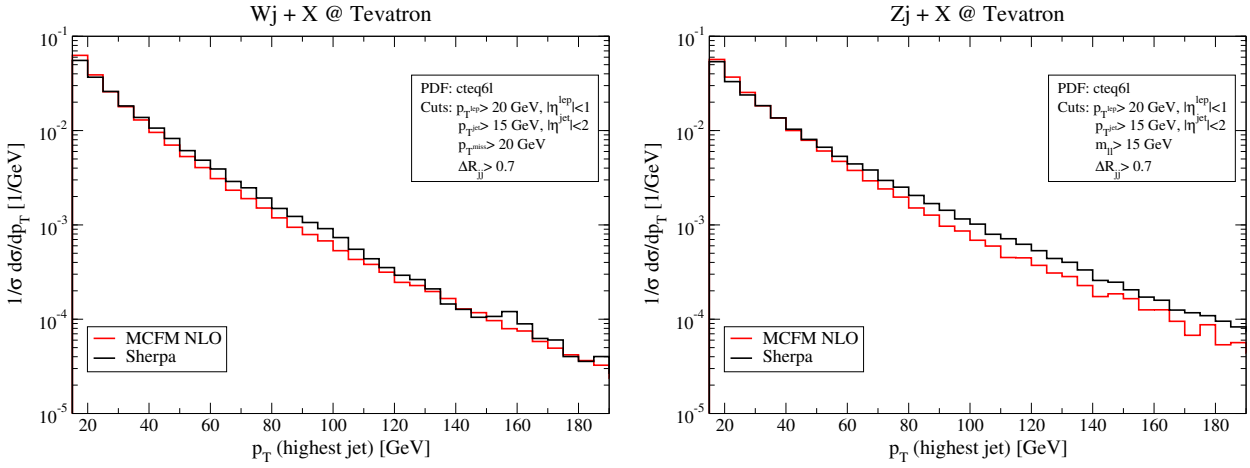

Figure 5.21: The $p_\perp$ distribution of the hardest jet for inclusive W + 1jet (left) and for inclusive Z + 1jet (right) production at the Tevatron, Run II. The scales in `MCFM` were chosen as $\mu_F = \mu_R = M_W$.

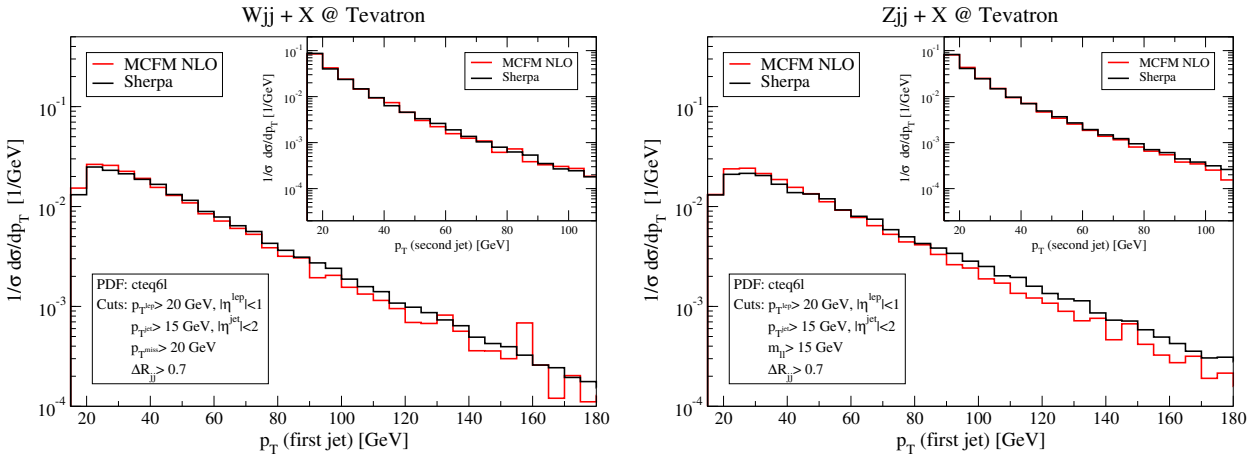

Figure 5.22: The $p_\perp$ distribution of the hardest two jets for inclusive W + 2jet (left) and for inclusive Z + 2jet (right) production at the Tevatron, Run II. The scales in `MCFM` were chosen as $\mu_F = \mu_R = M_W$.

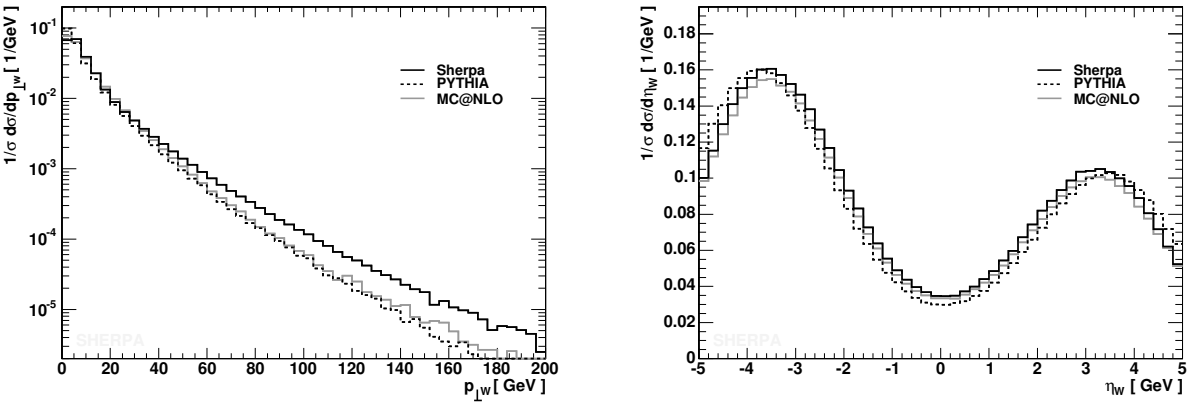

Figure 5.23: The $p_\perp$ (left) and η (right) distribution of the W^- boson for inclusive production at the Tevatron, Run II. Plotted are the results as obtained with the generators `PYTHIA` (green), `MC@NLO` (red) and `SHERPA` (black).

for $q\bar{q} \to e^+e^-$ and it employs a virtuality-ordered parton shower to model further emissions. In this framework, coherence effects are approximated through an explicit veto on rising opening angles in the splitting. Hence, the parton shower implementations of `PYTHIA` and `SHERPA` are quite similar. However, in order to account in `PYTHIA` for jets with a $p_\perp$ larger than the "natural" starting scale of the parton shower equal to the invariant mass of the lepton pair, the starting scale has been increased to the centre-of mass energy of the proton-proton system, i.e. to 1.96 TeV. This choice is supplemented with a matrix element correction procedure implemented through reweighting meant to reproduce the exact matrix element for the emission of an additional jet. Apart from this scale choice in `PYTHIA`, standard settings have been used for both codes suitable for inclusive W production at the Tevatron and the underlying event has been switched off. The corresponding process number in `PYTHIA` is `MSEL=12`, the relevant `MC@NLO` process is `IPROC=-1471`. Inclusive quantities like, for instance, the $p_\perp$ and η distributions of the W are in good agreement, see Fig. 5.23, and only in the high-$p_\perp$ tail of the distribution some deviations become visible. However, more exclusive quantities such as the $p_\perp$-distributions of the first three jets show differences which increase with the increasing order of the jet. This can clearly be seen from Fig. 5.24. The predictions for the hardest jet start to disagree with a factor of roughly 2 at jet-$p_\perp$s of the order of 100 GeV, reaching up to nearly an order of magnitude at $p_\perp$ around 200 GeV. This trend is greatly enhanced for the second and third jets, where discrepancies are of the order of one magnitude for the second jet at $p_\perp \approx 100$ GeV or even higher for the third jet.

These discrepancies, however, were to be expected since the other two programs do not include any higher order correction beyond first order in the strong coupling constant. In the case of `MC@NLO`, predictions have been compared with those obtained from `MCFM`; after a careful calibration of input parameters such as CKM elements etc., inside the code both programs coincided in all observables tested [155]. Therefore, differences in the $p_\perp$ distribution of the hardest jet have to be attributed to a combination of distinct parameter settings and of differences in parton showering and hadronisation. The latter type of difference should

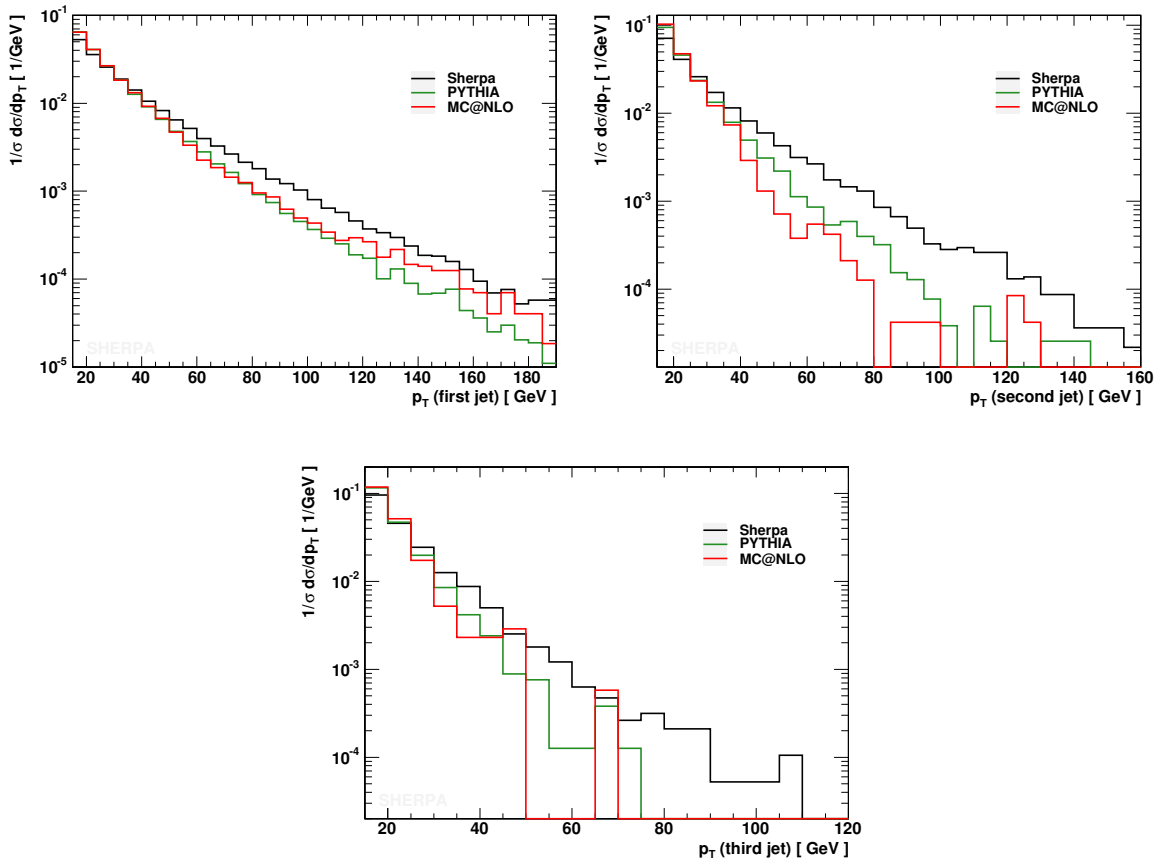

Figure 5.24: Jet $p_\perp$ distribution of the three hardest jets in inclusive W production at the Tevatron, Run II. Compared are the hadron level results of SHERPA (black), PYTHIA (green) and MC@NLO (red) after 2.5 million events.

be taken as some kind of theoretical uncertainty. For higher jet configurations, however, the remaining discrepancies are due to different physics input.

SHERPA vs. data

Having compared the SHERPA predictions for the case of the jet transverse momentum distributions in exclusive and inclusive W/Z+1jet and W/Z+2jet production against other Monte Carlo programs, a comparison with experimental data provides an ultimate test of SHERPA's ability to describe such processes. Unfortunately, so far only the inclusive W- and Z-boson transverse momentum distribution measured in Tevatron, Run I, have been published, which allows for an overall check only. In both cases, matrix elements with up to four (W) or three (Z) extra jets have been taken into account – as indicated by the different colours - to generate the SHERPA sample. The black line represents the sum of all contributions. For this sample the required separation cut has been chosen to $Q_{\text{cut}} = 20$ GeV.

In Fig. 5.25, the (inclusive) $p_\perp$ distribution of the W is compared with data from D0, taken at Run I of the Tevatron [156]. The agreement with data is excellent. It can be recognised that approaching the merging scale from below, the W+0jet contribution steeply falls

and the distribution for larger momenta is mainly covered by the W+1jet part, as expected. In order to match the measured distribution, the SHERPA result has been multiplied by a constant K-factor of 1.25.

Similarly, in Fig. 5.26, the (inclusive) $p_\perp$ distribution of the Z is compared with data, this time taken by CDF at Run I of Tevatron [123]. Again the overall agreement is excellent. This time the result has been multiplied by a constant K-factor of 1.6 to match the data. The result is perfectly smooth around the merging scale of $Q_{\text{cut}} = 20$ GeV. This is especially highlighted in the right plot of Fig. 5.26, which concentrates on the low momentum region. It is interesting to note that the description of the data for momenta smaller than the merging scale is almost only covered by the Z+0jet contribution and is therefore very sensitive to the details of the parton showers and the treatment of beam remnants. A parameter of specific impact on the very low momentum region therefore is the primordial (or intrinsic) $k_\perp$ used for the interacting partons. This is modelled through a Gaussian distribution with a central value of 0.8 GeV. Nevertheless, the shower performance of SHERPA has not been especially tuned; the low momentum behaviour may therefore still be improved once a detailed parameter tune is available.

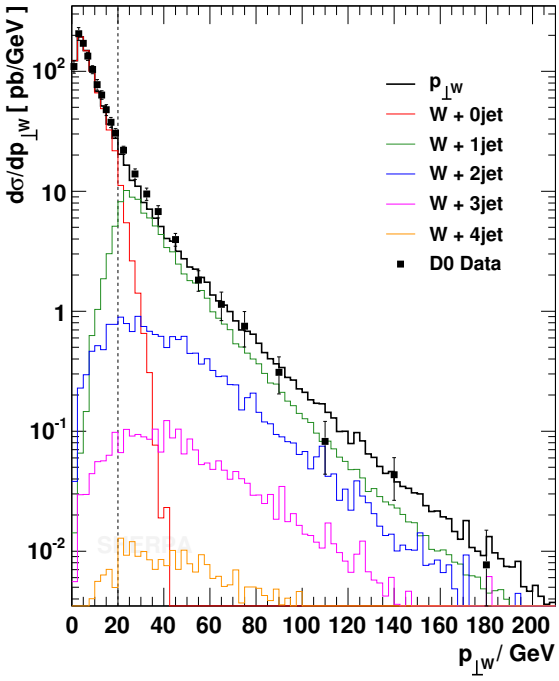

Figure 5.25: The $p_\perp$ distribution of the W-boson in comparison with data from D0 at the Tevatron, Run I [156]. The total result is indicated by the black line. The coloured lines show the contributions of the different multiplicity processes. Here matrix elements with up to four extra jets have been considered. The applied separation cut is $Q_{\text{cut}} = 20$ GeV.

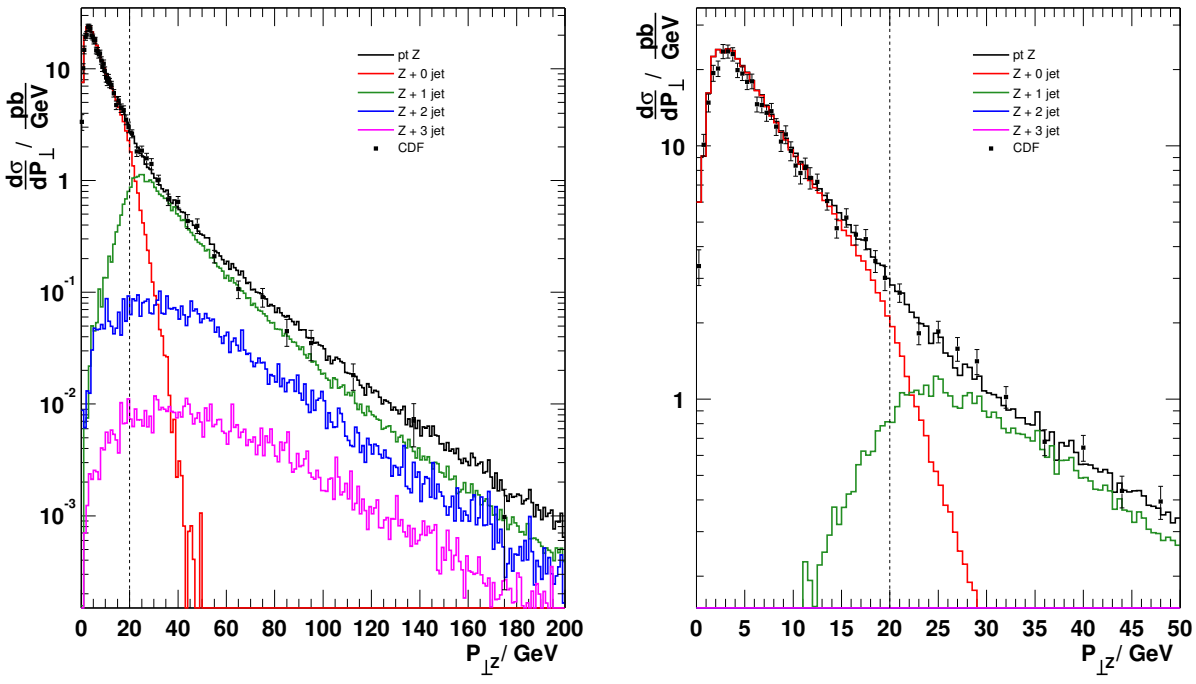

Figure 5.26: The $p_\perp$ distribution of the Z-boson in comparison with data from CDF at the Tevatron, Run I [123]. The total result is indicated by the black line. The coloured lines show the contributions of the different multiplicity processes. The applied separation cut is $Q_{\text{cut}} = 20$ GeV. The right plot focuses on the low momentum region of the left one.

5.4 W/Z + jets production at the CERN LHC

In this section, the analysis of electroweak boson production is continued for the Large Hadron Collider (LHC) at CERN, which will start to deliver proton-proton collision at a centre-of-mass energy of 14 TeV, in spring 2008. Apart from the enormous energy available, the LHC is characterised by an unprecedented luminosity, resulting also in a large production rate for electroweak bosons. For instance of a single W boson will occur with a frequency of order 10 Hz, that should enable a precise determination of the W mass [157,158]. It also renders this process a prime candidate for luminosity monitoring [28,159–161]. Further, the production of W and Z bosons together with jets constitute an important background to all kinds of searches for new physics, such as, e.g. super-symmetry. An example for this is the production and decay of gluinos, where the production of jets plus a Z boson decaying into neutrinos constitutes a major background.

In Sec. 5.3 it has been shown that at the Tevatron, some results for this type of process obtained from other multi-purpose event generators such as `PYTHIA` [82, 83], `HERWIG` [3, 77] or even `MC@NLO` [11–13] differ significantly from the results obtained by `SHERPA` [1]. In particular, it has been shown that `SHERPA` predicts additional jets to be produced at significantly larger rates with significantly larger transverse momenta. The reason for this apparent difference lies in the way the different codes implement the knowledge of exact matrix elements for the production of multi-particle final states.

In the following sections, the previous analysis will be extended to the case of the CERN LHC. The procedure is kept very similar to the one in Sec. 5.3. First, in Sec. 5.4.2, a number of consistency checks will focus on the independence of the results on variations of the internal jet definition and of the number of matrix elements involved. Also, the effect of scale variations in both the matrix elements and in the parton shower is investigated there. Then, in Sec. 5.4.3, results obtained with `SHERPA` will be contrasted to those obtained from fixed order (LO and NLO) calculations provided by `MCFM`. Finally, different multi-purpose event generators, namely `PYTHIA`, `MC@NLO` and `SHERPA`, will be compared in Sec. 5.4.4.

5.4.1 Input parameters and phase-space cuts

For all analyses, the PDF set CTEQ6L has been used, and α_S has been chosen according to the corresponding value of this PDF, namely $\alpha_S = 0.118$. For the running of the strong coupling constant, the corresponding two-loop equation has been employed. Jets or initial partons are restricted to the light flavour sector, namely g, u, d, s, and c. All flavours are taken to be massless.

SM input parameters

The SM parameters are given in the G_μ scheme:

$$\begin{aligned}
&m_W = 80.419\ \text{GeV}\,, \quad \Gamma_W = 2.06\ \text{GeV},\\
&m_Z = 91.188\ \text{GeV}\,, \quad \Gamma_Z = 2.49\ \text{GeV},\\
&G_\mu = 1.16639 \times 10^{-5}\ \text{GeV}^{-2},\\
&\sin^2\theta_W = 1 - m_W^2/m_Z^2,\\
&\alpha_s = 0.118.
\end{aligned} \tag{5.6}$$

The electromagnetic coupling is derived from the Fermi constant G_μ according to

$$\alpha_{\rm em} = \frac{\sqrt{2}\, G_\mu\, M_W^2\, \sin^2\theta_W}{\pi}\,. \tag{5.7}$$

The constant widths of the electroweak gauge bosons are introduced through the fixed-width scheme. CKM mixing of the quark generations is neglected.

Cuts and jet criteria

For all jet analysis the Run II $k_\perp$-clustering algorithm defined in [154] has been used. The additional parameter of this jet algorithm is a pseudo-cone size D, whose value has been chosen to $D = 0.4$. In addition jets have to fulfil the following cuts on pseudo-rapidity and transverse momentum,

$$p_T^{\rm jet} > 20\ {\rm GeV}, \quad |\eta^{\rm jet}| < 4.5. \tag{5.8}$$

For charged leptons the cuts applied are:

$$p_T^{\rm lepton} > 15\ {\rm GeV}, \quad |\eta^{\rm lepton}| < 2.4, \quad m_{ll} > 15\ {\rm GeV}. \tag{5.9}$$

No cut on missing transverse momentum has been applied.
Note that the cut on the invariant mass of the lepton pair is just $m_{ee} > 15\,{\rm GeV}$ which is rather small. The description of such low mass lepton pairs constitutes a real challenge for the description through the merging prescription. The reason is that at large $Q_{\rm cut} = \mathcal{O}(100\,{\rm GeV})$, lepton pairs with such low invariant mass clearly are softer than any jet produced through the matrix element,rendering a consistent merging a complicated task. The final selection criteria correspond to the separation of the leptons amongst each other and with respect to jets,

$$\Delta R_{lj} > 0.4, \quad \Delta R_{ll} > 0.2. \tag{5.10}$$

5.4.2 Consistency checks

Before comparing the results of SHERPA with those of other programs, again some consistency checks will be performed. To do so, the dependence of some observables in reactions of the type $pp \to e^+e^- + X$ on internal parameters intrinsic for the merging procedure will be investigated. After evaluating the sensitivity of the results on the principal parameters defining the merging procedure, $Q_{\rm cut}$ and $n_{\rm max}$, the effect of scale variations will be investigated. This, together with the dependence on $Q_{\rm cut}$ and $n_{\rm max}$ yields an estimate for the uncertainty related to predictions of SHERPA.

The results presented in this section were generated with the following setup: When varying $Q_{\rm cut}$, $n_{\rm max} = 3$. When studying the impact of $n_{\rm max}$, $Q_{\rm cut} = 15$ GeV; this clearly maximises the impact of the higher order matrix elements. When scale variations are under consideration, the choices $Q_{\rm cut} = 20$ GeV and $n_{\rm max} = 2$ have been made.

In the following, Z-boson production will be investigated in more detail. Nevertheless, the process under consideration is $pp \to Z/\gamma^* \to e^+e^- + X$, where the full γ-Z interference is taken into account and full spin correlations are respected. Note that the cut on the invariant mass of the lepton pair is just $m_{ee} > 15\,{\rm GeV}$ which is rather small. The description of such low mass lepton pairs constitutes a real challenge for the description through the

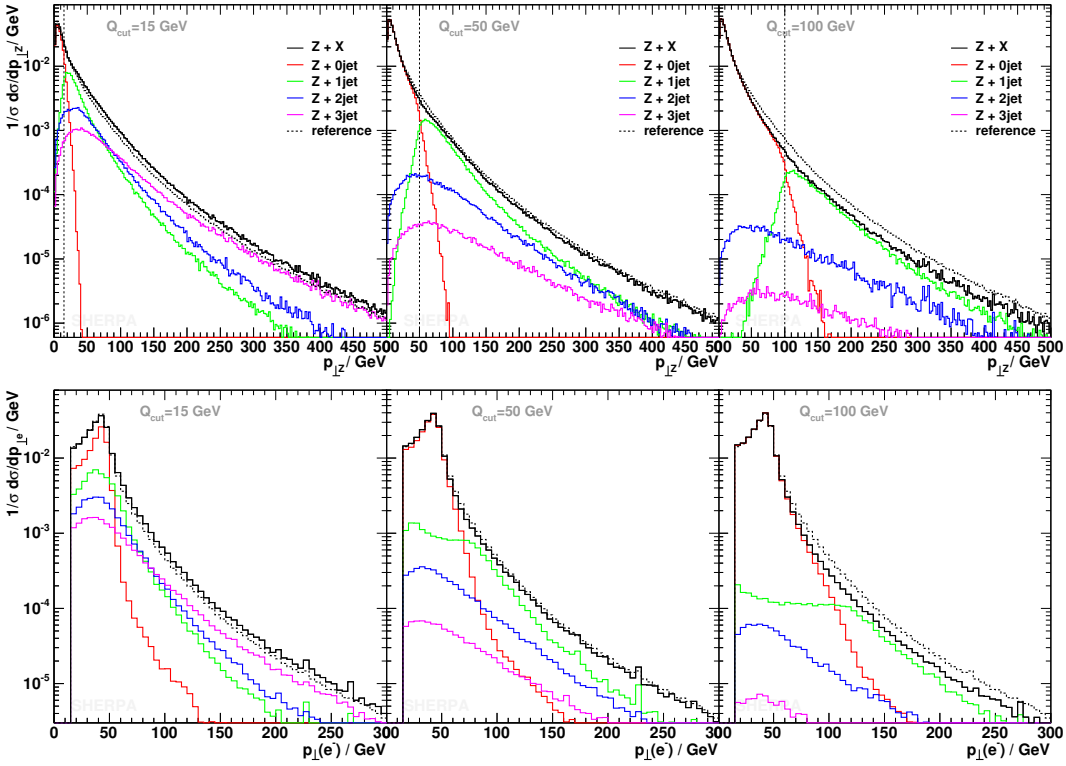

Figure 5.27: $p_\perp(Z)$ (upper row) and $p_\perp(e^-)$ (lower row) for $Q_{\text{cut}} = 15$ GeV, 50 GeV and 100 GeV (from left to right). The dashed reference spectrum has been obtained after averaging the results for $Q_{\text{cut}} = 15$, 20, 30, 50, 100 GeV.

merging prescription. The reason is that at large $Q_{\text{cut}} = \mathcal{O}(100\,\text{GeV})$, lepton pairs with such low invariant mass clearly are softer than any jet produced through the matrix element, rendering a consistent merging a complicated task.

Observables related to the leptons

Starting from more inclusive observables, first of all the effect of parameter variation on the leptons will be considered. In Fig. 5.27, the $p_\perp$ spectra of both the lepton pair (upper row) and of the electron alone (lower row) are shown for three different values of Q_{cut}: From left to right, in the columns $Q_{\text{cut}} = 15$, 50, 100 GeV, as indicated by the thin vertical lines. In each plot, the resulting spectrum is compared to a reference obtained when averaging the results for $Q_{\text{cut}} = 15$, 20, 30, 50, 100 GeV; In this and all other plots, contributions stemming from the different matrix element multiplicities are indicated through coloured lines.

Considering $Q_{\text{cut}} = 15$ GeV obviously produces the hardest boson/lepton spectrum. It is the smallest cut considered here and therefore the distributions are dominated by matrix elements that in contrast to the parton shower favour rather hard parton kinematics. For very high $p_\perp$ the distributions are almost completely covered by the matrix element with the highest multiplicity considered (here, $n_{\text{max}} = 3$). This shows that the LHC provides enough

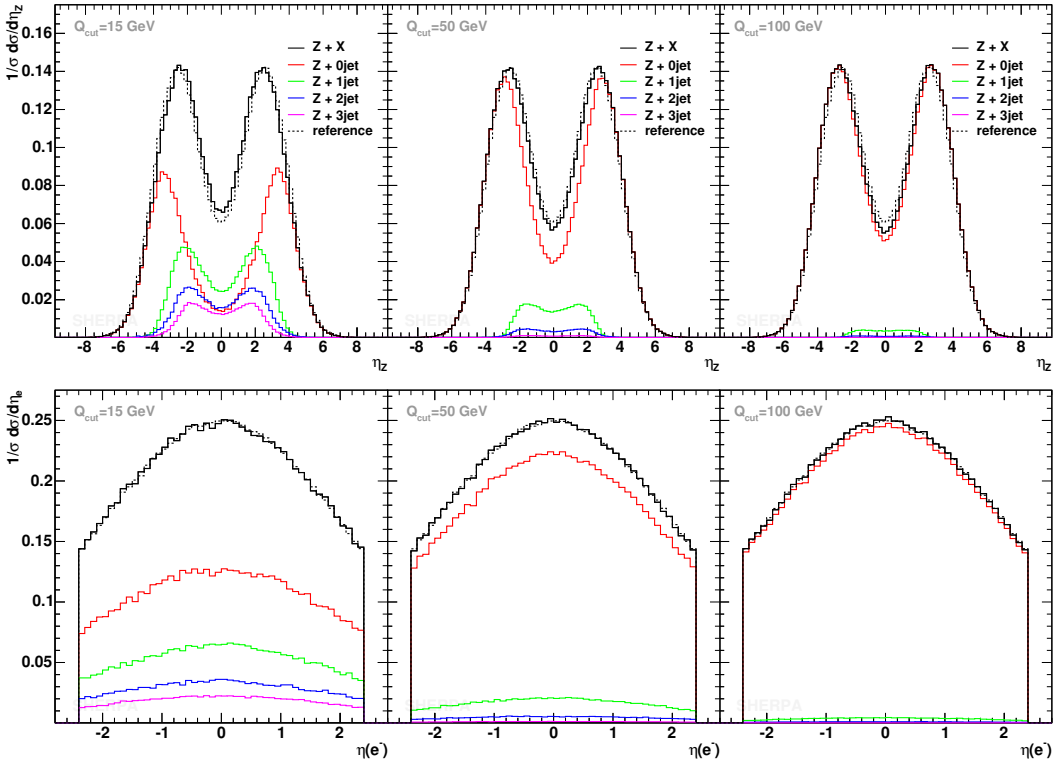

Figure 5.28: $\eta(Z)$ (upper row) and $\eta(e^-)$ (lower row) for $Q_{\text{cut}} = 15$ GeV, 50 GeV and 100 GeV (from left to right). The dashed reference spectrum has been obtained after averaging the results for $Q_{\text{cut}} = 15$, 20, 30, 50, 100 GeV.

phase space to produce a sufficient amount of events with three and more jets of $p_\perp > Q_{\text{cut}}$. For the case of $Q_{\text{cut}} = 50$ GeV the situation is slightly different. The high-$p_\perp$ tail is filled to an equal amount by the different multiplicities, the total sum being slightly below the reference curve. This reference curve contains three results with jet resolutions smaller than 50 GeV somehow dominating the averaged result. The spectrum for $Q_{\text{cut}} = 100$ GeV starts to underestimate (w.r.t. the reference) the boson transverse momentum at $p_\perp(Z) \approx 35$ GeV and the lepton $p_\perp$ for values larger than 60 GeV. To understand this, one has to remember that the boson transverse momentum for values below the resolution cut is almost completely covered by the parton shower. The shower, however, is known to suffer from a lack of hard QCD radiation. This leaves not enough hard partons, the boson can recoil against. Beyond this influence of the Q_{cut} variation on the intermediate and high boson transverse momenta, it has to be noted that all curves are very smooth around the jet resolution cut. Although the cut defines a rather sharp transition from the parton shower to the matrix element domain no significant holes in the boson and lepton $p_\perp$ spectra can be observed.

In Fig. 5.28 the pseudo-rapidity spectra of the lepton pair and the single electron are displayed; again for $Q_{\text{cut}} = 15$, 50, 100 GeV with the same way of generating the reference. While the electron observable is nearly unaltered, the differences in the η distribution of the lepton pair can be understood easily: The smaller the chosen cut, the larger the influence of the matrix elements with extra external legs. These matrix elements however prefer

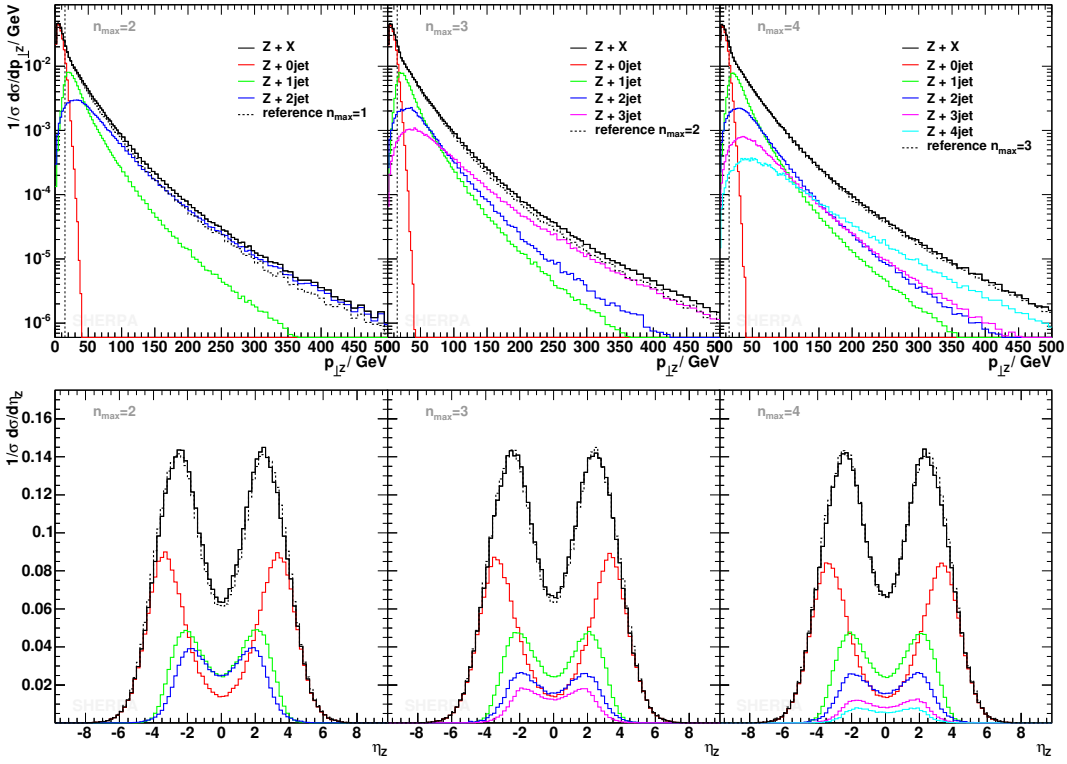

Figure 5.29: $p_\perp(Z)$ (upper row) and $\eta(Z)$ (lower row) for $Q_{\text{cut}} = 15$ GeV and different maximal numbers (2-4, from left to right) of ME jets included. The dashed line corresponds to the maximal number of ME jets reduced by one.

to produce the boson much more central than the parton shower does. This effect yields slightly tighter spectra with the central rapidities being pronounced for smaller resolution cuts.

The effect of varying $n_{\max}$ on the transverse momentum and pseudo-rapidity spectrum of the lepton pair is exhibited in Fig. 5.29. In this figure, results are compared for $n_{\max} = 2, 3, 4$. In each plot, a reference result is given with the corresponding $n_{\max}^{\text{ref}} = n_{\max} - 1$. For the case of the $p_\perp$ distribution it has already been observed that the high-$p_\perp$ region is described through higher multiplicity matrix elements. As a consequence, it is the high-$p_\perp$ region that is affected by the variation of $n_{\max}$. However, while the effect is clearly noticeable when going from one to two extra partons the change becomes smaller the more matrix elements are included. From the very right plot one can conclude that considering $Z + 3$ extra parton matrix elements is a reasonable choice to simulate inclusive Z production. The change in the η distribution for different $n_{\max}$ is as expected, considering what has already been seen for varying the jet resolution. The higher multiplicity matrix elements favour the region of small $|\eta|$ yielding slightly tighter pseudo-rapidity distributions. Again, the more matrix elements have been taken into account the smaller the influence when adding an even higher multiplicity.

In comparison to what has been observed when studying gauge boson production at the Fermilab Tevatron [21] and Sec. 5.3, the LHC provides much more phase space for additional

hard QCD radiation, enhancing the influence of higher order matrix elements. Therefore a modest value of the jet resolution parameter and the inclusion of a sufficient large number of matrix element legs is advisable for LHC analyses.

Jet observables

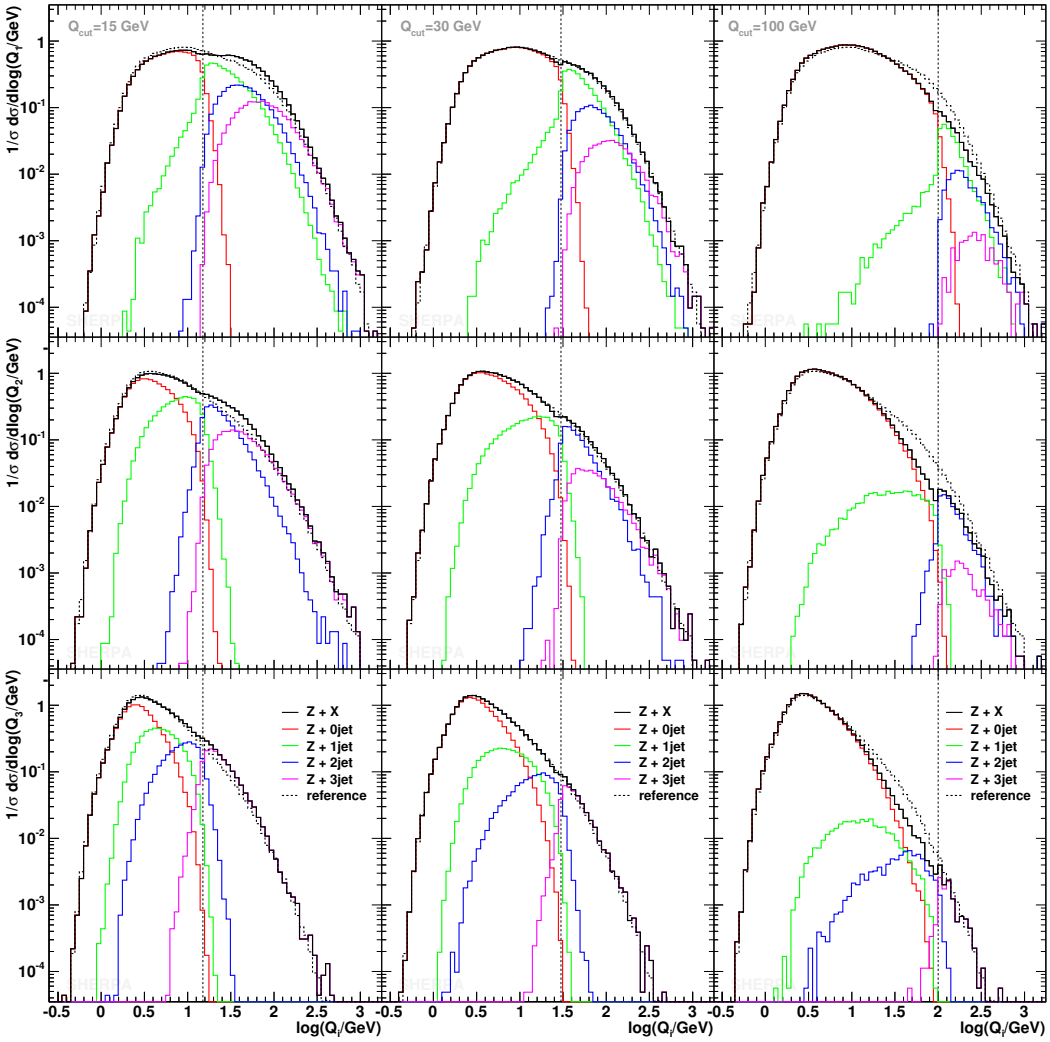

Figure 5.30: Differential jet rates for the $1 \to 0$, $2 \to 1$ and $3 \to 2$ transition (top to bottom), for $Q_{\text{cut}} = 15$ GeV, 30 GeV, and 100 GeV (from left to right). The dashed reference curve in each plot is obtained after averaging the corresponding results for $Q_{\text{cut}} = 15$, 20, 30, 50, 100 GeV.

As has already been seen in the previous discussion, in Sec. 5.3, a very sensitive test of the merging procedure is provided by observables based on jets. In particular, differential jet rates have turned out to be very useful. In Fig. 5.30, differential jet rates using the Run II $k_\perp$-clustering algorithm with $D = 1$ are depicted. Again, the results for three different values of Q_{cut} are depicted: From left to right, in the columns $Q_{\text{cut}} = 15$, 30, 100 GeV, as

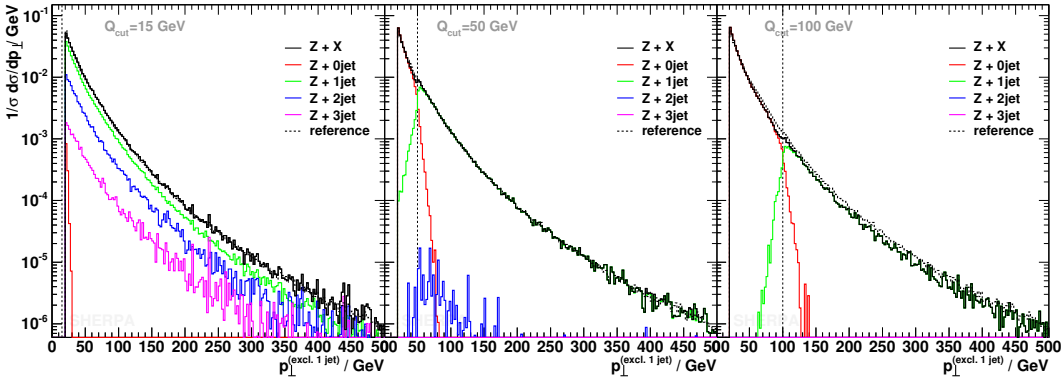

Figure 5.31: $p_\perp$ of the jet in exclusive $Z + 1$ jet production. For the jet definition, the Run II $k_\perp$-algorithm with $D = 0.4$ and $p_\perp^{\text{jet}} > 20$ GeV is used. From left to right, results for $Q_{\text{cut}} = 15, 50, 100$ GeV are contrasted with a reference: the average of the results for $Q_{\text{cut}} = 15, 20, 30, 50, 100$ GeV. The thin horizontal line indicates the jet resolution scale used.

indicated by the thin vertical lines. In each plot, the resulting spectrum is compared to the average of the results for $Q_{\text{cut}} = 15, 20, 30, 50, 100$ GeV. In the three rows, the differential jet rates for the $1 \to 0$, the $2 \to 1$, and for the $3 \to 2$ transition (from top to bottom) are shown. Starting the discussion with the results for $Q_{\text{cut}} = 30$ GeV, very good agreement with the reference curves can be observed. While the $3 \to 2$ transition is perfectly smooth around the cut the results for $1 \to 0$ and $2 \to 1$ exhibit small dips at the cut scale, again due to mismatches of matrix element and parton shower kinematics. Similar structures can be observed for the case of $Q_{\text{cut}} = 100$ GeV. However, more obvious here is that the parton shower fails to fill the phase space for hard emissions up to this very large cut. For $Q_{\text{cut}} = 15$ GeV no visible dips at the cut scale are observed. Instead, this sample seems to slightly overestimate the contributions from higher order matrix elements. A small kink at Q_{cut} can be observed for the $1 \to 0$ and $2 \to 1$ transition. This residual dependence of the results on Q_{cut} may be used to tune the perturbative part of the Monte Carlo event generator.

In Fig. 5.31 the $p_\perp$ spectrum of the jet in exclusive $Z + 1$ jet production is shown for three choices of the jet resolution scale, $Q_{\text{cut}} = 15, 50, 100$ GeV, indicated by the thin vertical line. The results are contrasted with a reference curve, again the average of results for $Q_{\text{cut}} = 15, 20, 30, 50, 100$ GeV. The jet has been defined using the Run II $k_\perp$-algorithm with a minimal jet-$p_\perp$ of 20 GeV and $D = 0.4$. The smallest value of Q_{cut} presented here, namely 15 GeV, is smaller than the actual jet cut used in the analysis. Accordingly, matrix elements with more than one extra leg have a non-vanishing influence on the jet-$p_\perp$ distribution. This changes as soon as Q_{cut} becomes larger than 20 GeV. For $Q_{\text{cut}} = 50$ GeV and even more for $Q_{\text{cut}} = 100$ GeV the contributions from matrix elements with $n_{\max} > 1$ are almost negligible. There, only a small dip in the $p_\perp$ distribution around the resolution scale can be observed. As has been seen in the transverse momentum distribution of the lepton pair, cf. Fig. 5.27, for $Q_{\text{cut}} = 100$ GeV, the shower is not able to fill the full phase space below the cut properly. However, the overall agreement of the three results is satisfactory, keeping in mind the large parameter range used for Q_{cut}.

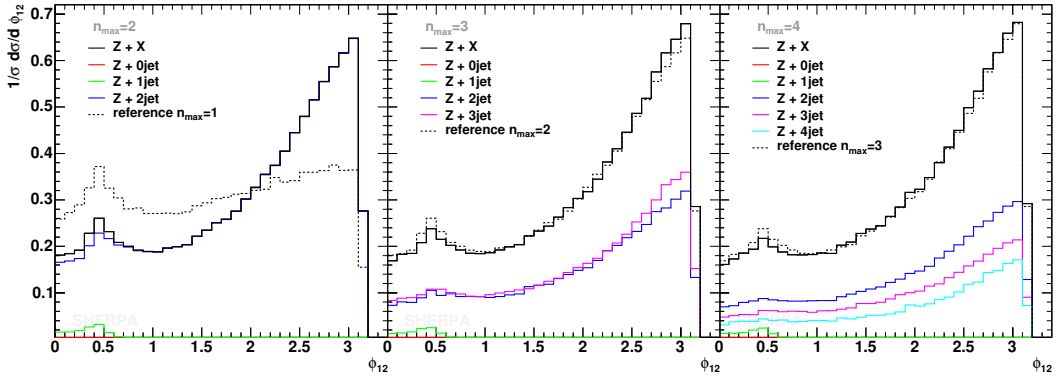

Figure 5.32: $\Delta\phi_{12}$ for $Q_{\text{cut}} = 15$ GeV and different maximal numbers of ME jets included. The dashed line corresponds to the reference result obtained with $n_{\text{max}}^{\text{ref}} = n_{\text{max}} - 1$.

To highlight the effect of taking into account different maximal numbers of final state partons through matrix elements, a two-jet correlation is exhibited in Fig. 5.32. There, the relative transverse angle $\Delta\phi$ between the two hardest jets in inclusive $Z + 2$jet production is displayed; from left to right, n_{max} has been chosen to $n_{\text{max}} = 2, 3, 4$. Each result is contrasted with a reference that has been obtained with $n_{\text{max}}^{\text{ref}} = n_{\text{max}} - 1$. From the very left plot it is clear, that the one-jet matrix element is incapable of describing the $\Delta\phi$ distribution correctly since the parton shower does not treat interferences properly. On the other hand, as soon as $n_{\text{max}} \geq 2$, the two-jet correlations are consistently described and changes due to the inclusion of higher order matrix elements are rather modest.

Variation of renormalisation and factorisation scale

To check how sensitive the results of SHERPA with respect to changes in the renormalisation and factorisation scale are, in Fig. 5.33 and Fig. 5.34 results obtained with the default scale choices are confronted with results obtained when all scales appearing in the coupling constants and PDFs are multiplied by common factors of 0.5 and 2. For this comparison, samples have been generated using $Q_{\text{cut}} = 20$ GeV and $n_{\text{max}} = 2$.

In Fig. 5.33 the transverse momentum and pseudo-rapidity distribution of the Z/γ^* boson are depicted. For the case of the $p_\perp$ spectrum, except for the very first bins the spectrum obtained with a factor of 0.5 (2) is always above (below) the default result. The differences are rather constant and of the order of $10 - 15\%$. As has been seen before, cf. Fig. 5.27 and 5.29, for transverse momenta above the cut scale the distribution is predominantly described by higher order matrix elements, whose scale dependence is known to be tamed with respect to the lowest order process [150]. This lowest order process, however, dominates the region of very low boson momenta. There the $2 \to 2$ cross section exhibits a strong decline when the scales become smaller. This effect potentially leads to the reversal of the discrepancies. The situation in the case of the pseudo-rapidity distribution is very similar. From Fig. 5.28 and Fig. 5.29 one can read off that the region of large values of $|\eta|$ is described by the parton shower attached to the $2 \to 2$ matrix element. For $|\eta| > 5$ the spectrum, where all scales have been multiplied by a factor of two, is enhanced up to 20%. A factor of 0.5 on the

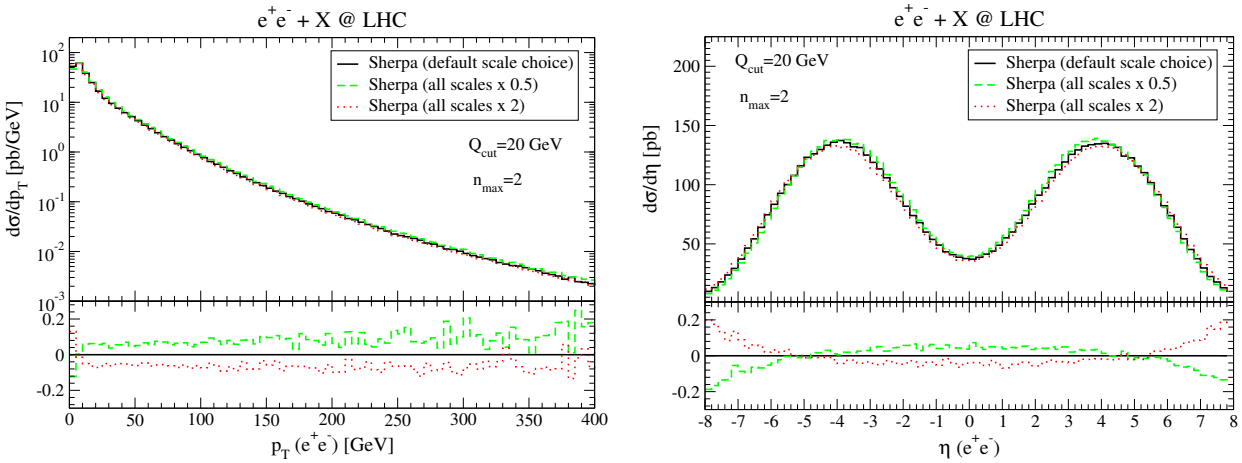

Figure 5.33: The transverse momentum (left) and pseudo-rapidity (right) distribution of the boson in inclusive Z/γ^* production at the LHC and their dependence on different choices for the factorisation and renormalisation scale. Results have been obtained using $Q_{\text{cut}} = 20$ GeV and $n_{\max} = 2$. The black solid lines indicate the default hadron level result. To obtain the green dashed (red dotted) line, all scales appearing in the coupling constants and the PDFs in both the matrix elements and the parton showers are multiplied by a factor of 0.5 (2). In the lower parts of the plots the variations of the results with respect to the default scale choice are presented.

other hand depopulates this phase space region by up to 20%. In the intermediate range of pseudo-rapidity the deviations of the two spectra from the default scale choice are well below 10%.

In Fig. 5.34 the transverse momentum distribution of the hardest jet in inclusive Z/γ^* production is depicted. In contrast to the two distributions above, this result has no significant contribution from the leading order $2 \to 2$ process. Therefore, the two results obtained after scale manipulation do not cross each other. Over the whole range of jet transverse momentum the deviations of the two curves from the default result are very moderate.

It can be concluded that the predictions of SHERPA show rather mild variations over a wide range of the phase space when multiplying all scales appearing in the coupling constants and PDFs by common factors of 0.5 and 2. The largest deviations from the default choice of scales are observed in those phase space regions that are predominantly covered by the $2 \to 2$ matrix element with the parton shower attached.

5.4.3 SHERPA vs. NLO results

Having investigated the self-consistency of the merging procedure as implemented in SHERPA its parton level results are again compared with those from MCFM, v. 4.0, [149, 150]. For all calculations with MCFM the CTEQ6L PDF has been used, and $\alpha_S(m_Z) = 0.118$ in accordance with the value of the PDF evolution. The renormalisation and factorisation scales have been chosen to be identical with the bosons mass, i.e. $\mu_R = \mu_F = \mathrm{m_Z}$ or $\mu_R = \mu_F = \mathrm{m_W}$, respectively. Phase space cuts are listed above. In contrast to the Tevatron study, this time

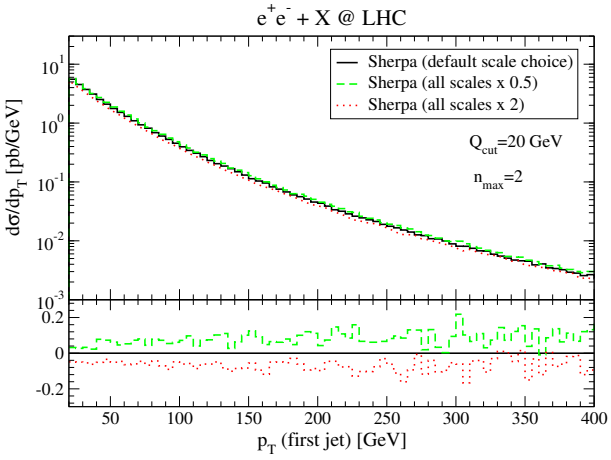

Figure 5.34: The $p_\perp$ spectrum of the hardest jet in inclusive Z/γ^* production at the LHC and its dependence on different choices for the factorisation and renormalisation scale. Results have been obtained using $Q_{\rm cut} = 20$ GeV and $n_{\rm max} = 2$. Jets are defined through the Run II $k_\perp$-algorithm with $D = 0.4$ and $p_\perp^{\rm jet} > 20$ GeV. The black solid line corresponds to the default hadron level result. To obtain the green dashed (red dotted) line, all scales appearing in the coupling constants and the PDFs in both the matrix elements and the parton showers are multiplied by a factor of 0.5 (2). In the lower part of the plot the variations of the results with respect to the default scale choice are presented.

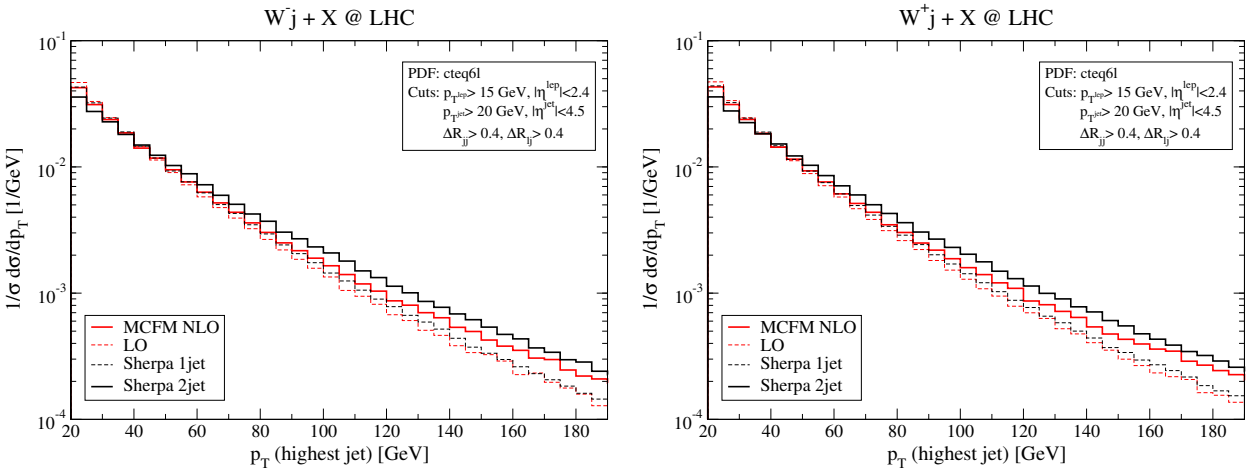

Figure 5.35: The p_T distribution of the hardest jet for inclusive W^- (left) and W^+ (right) plus one jet events at the LHC.

only "inclusive" quantities are compared. The SHERPA results were obtained after the parton shower evolution. For the sake of a better comparison, all curves have been normalised to one, eliminating the enhancement of the cross section due to the NLO corrections.

First of all, in Figs. 5.35 and 5.36 the $p_\perp$ spectra of the hardest jet in inclusive $W^+ + 1$

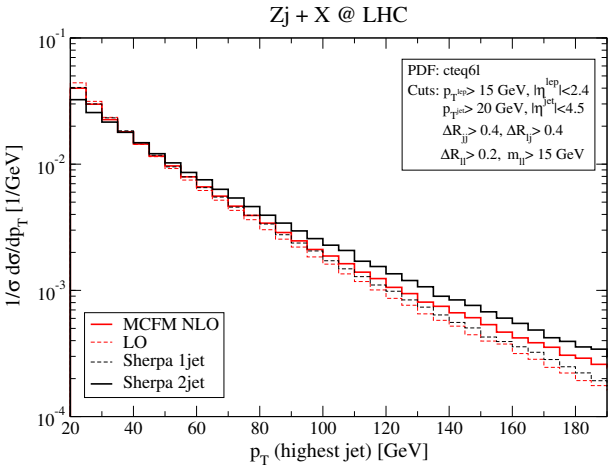

Figure 5.36: The p_T distribution of the hardest jet for inclusive Z plus one jet events at the LHC.

jet, $W^- + 1$ jet, and $Z/\gamma^* + 1$ jet production are exhibited. For all cases, results at leading and at next-to-leading order were contrasted with results from SHERPA that were obtained with $n_{\max} = 1$ and with $n_{\max} = 2$, respectively. In all plots the high-$p_\perp$ tail is significantly enhanced when going from LO to NLO. The SHERPA samples with $n_{\max} = 2$ show the same behaviour but tend to pronounce the high-$p_\perp$ region even more. This is in striking contrast to the $n_{\max} = 1$ samples. They are incapable of recovering the shape of the distribution at NLO, and tend to look like the LO result. This is not surprising. The NLO calculation takes into account LO matrix elements with two final state partons as the real contribution to the NLO result. Due to the large phase space available at the LHC this real contribution tends to produce an extra jet that alters the kinematics of the first jet. Obviously this significant change in the kinematics can not be appropriately recovered by the parton shower. The $n_{\max} = 2$ SHERPA samples also include the parton shower, resulting in increased parton emission thus enhancing the high-$p_\perp$ tail even more. It would for sure be instructive to check this behaviour with a resummed NLO computation for these processes.

In Figs. 5.37 and 5.38 the $p_\perp$ spectra of the two hardest jets in inclusive $W^+ + 2$ jet, $W^- + 2$ jet, and $Z/\gamma^* + 2$ jet production are displayed. This time next-to-leading order results from MCFM are compared with the corresponding SHERPA samples with $n_{\max} = 2$. It has been shown in [150] that the shapes of the distributions when going from LO to NLO are quite stable. The shapes of the next-to-leading order and the SHERPA result are in good agreement, the latter having the tendency to produce the first jet slightly harder. In Fig. 5.39 the $p_\perp$ spectra of the two hardest jets in inclusive $W^- + 2$jet production are displayed once more. This time, however, the renormalisation and factorisation scale in the NLO calculations has been chosen as $\mu_R = \mu_F = 2\,m_W$. For this choice of the scales the agreement of MCFM and SHERPA is even better. This highlights the effect of scale variations, a good way to estimate residual uncertainties due to higher order corrections and shows that the results of SHERPA are well within theoretical uncertainties[2].

[2]It should be noted that the effect of this scale variation on the total cross section merely is of the order of 1%, although the shape of the distribution in the high-$p_\perp$ tail changes considerably.

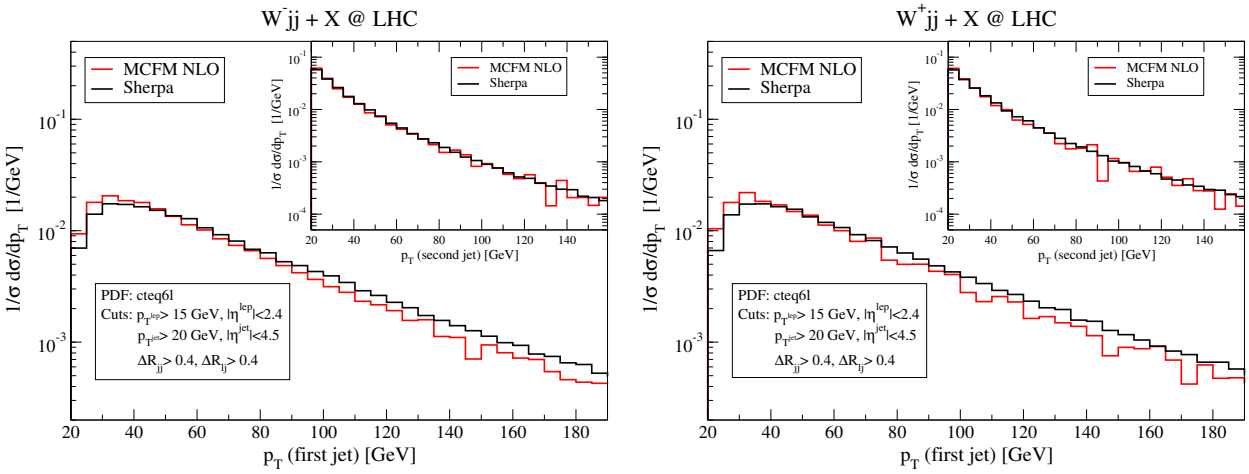

Figure 5.37: The p_T distribution of the two hardest jets in inclusive W^- (left) and W^+ (right) plus two jet production at the LHC.

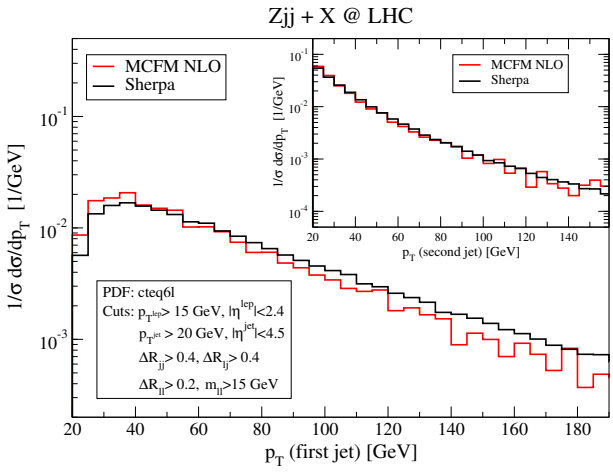

Figure 5.38: The p_T distribution of the two hardest jets in inclusive Z plus two jet production at the LHC.

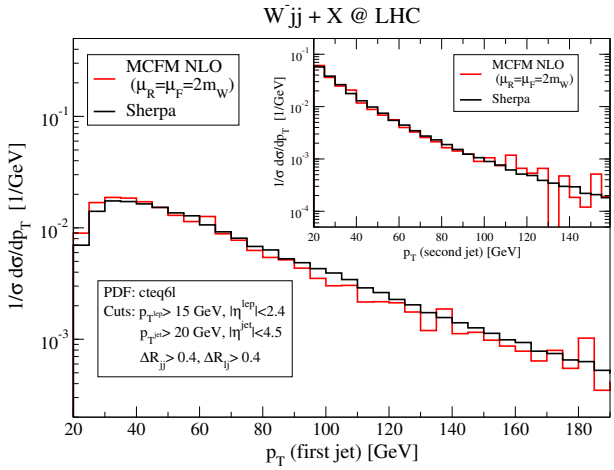

Figure 5.39: The p_T distribution of the first and second hardest jet in inclusive W^- plus two jet production at the LHC. For the NLO calculation the renormalisation and factorisation scale have been chosen to $\mu_R = \mu_F = 2\,\mathrm{m_W}$.

5.4.4 SHERPA vs. MC@NLO and PYTHIA

In this section, hadron-level results of SHERPA will be compared with those of two other event generators, namely MC@NLO [11–13] and PYTHIA [82, 83]. The particular settings are the same standard settings as in the study before, however, this time the standard value of the shower starting scale in PYTHIA is $\sqrt{s} = 14$ TeV.

First of all, the results of the three programs for some rather inclusive quantities are compared. The transverse momentum and pseudo-rapidity distributions of the produced bosons are presented in Fig. 5.40 and Fig. 5.41. The SHERPA predictions depicted have been obtained with $n_{\max} = 1$ and $Q_{\mathrm{cut}} = 20$ GeV, in order to match the abilities of the other codes. To compare the different samples, they all have been subject to a cut on the boson invariant mass of the form

$$m_V - 30 \cdot \Gamma_V \leq m_V^* \leq m_V + 30 \cdot \Gamma_V \,, \tag{5.11}$$

where no additional phase space cuts have been applied. All distributions have been normalised to their respective cross section.

The results for both processes look very similar. The boson transverse momentum distributions of MC@NLO and SHERPA agree fairly well. In the case of Z/γ^* production they match nearly perfectly for values of $p_\perp > 100$ GeV. In the intermediate range of $10\,\mathrm{GeV} < p_\perp < 100\,\mathrm{GeV}$ SHERPA apparently is below MC@NLO. This discrepancy may have its origin in the different shower approaches used within the two programs. This statement is also hinted at by the fact that the PYTHIA result follows the SHERPA distribution for $p_\perp < 35$ GeV. For larger values of $p_\perp$, however, the PYTHIA distribution is far below MC@NLO and SHERPA predicting much less bosons with large transverse momentum. For the case of W^+ production the MC@NLO and SHERPA prediction cross at $p_\perp \approx 60$ GeV. SHERPA produces slightly less events with smaller boson $p_\perp$ and tends to pronounce the high $p_\perp$ region a bit. Again PYTHIA produces fewer bosons with intermediate and large boson transverse

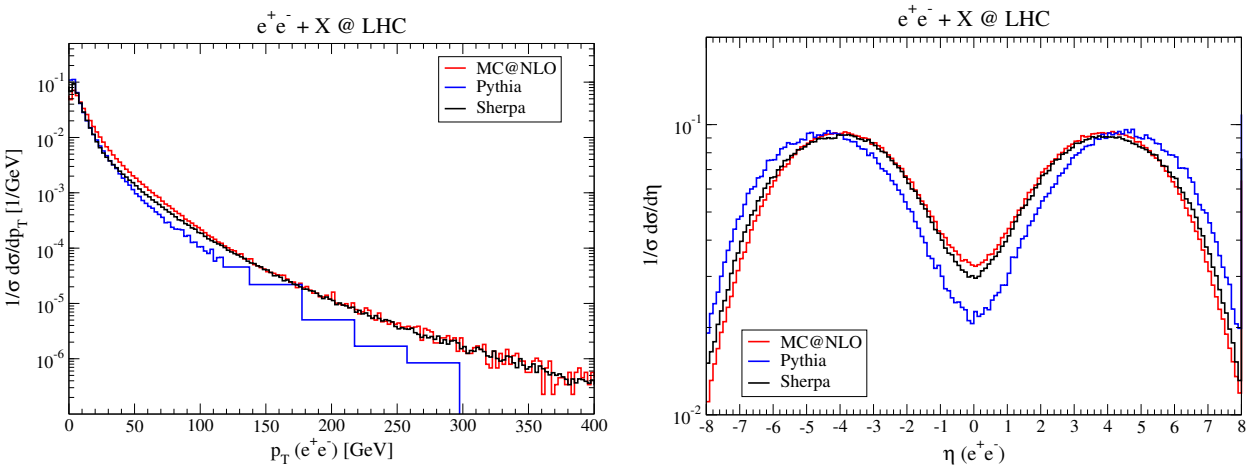

Figure 5.40: The $p_\perp$ (left) and η (right) distribution of the lepton pair in inclusive production of a Z/γ^* boson decaying into e^+e^- at the LHC. The results of the generators `MC@NLO` (red), `PYTHIA` (blue), and `SHERPA` (black) are compared.

momenta. Looking at the pseudo-rapidity distributions, it can be recognised, that `MC@NLO` and `SHERPA` both tend to produce the bosons much more central than `PYTHIA`. Especially the region of $|\eta| < 4$ is filled significantly with respect to `PYTHIA`, which, in contrast, features a much broader shape. This effect is of course directly correlated to the larger amount of hard QCD radiation the other two programs produce, since this enhanced QCD radiation allows for larger boson recoils. Finally, from Fig. 5.29 it can be anticipated how the `SHERPA` results change under the inclusion of matrix elements with extra QCD legs: the boson transverse momentum distribution develops a more pronounced large $p_\perp$ tail and the very cental region of η is filled even more, thus reducing the amount of events with large values of $|\eta|$. So while the $p_\perp$ spectra would be slightly harder than those of `MC@NLO` the η distributions would fit even better than they do for the case of including $V + 0$ and $V + 1$parton matrix elements only.

For the comparison of jet observables, only the case of Z/γ^* production is studied. The qualitative statements implied by it, however, will hold true as well in the case of W production. To judge the abilities of the three programs to produce extra hard QCD radiation associated to the electro-weak gauge bosons, the transverse momentum distributions of the three hardest jets accompanying the produced boson are depicted in Fig. 5.42 and Fig. 5.43. For `SHERPA` the jet resolution parameter has been chosen to $Q_{\text{cut}} = 20$ GeV. The standard sample used for the comparison has been generated using again only matrix elements with up to one additional parton. To test the predictions of `SHERPA` as well samples with $n_{\max} = 2(3)$ have been considered, the corresponding results are shown as dashed (dotted) lines in the plots. Since it is actually the production rate that is important here, this time the curves have not been normalised. Instead the corresponding differential cross sections are presented.

For the hardest jet produced the predictions of `MC@NLO` and `SHERPA` agree rather well. The total rate of `SHERPA` is 12% smaller than that predicted by `MC@NLO` but with a slightly harder tail. This difference in rate can be traced back to the different inclusive production cross sections. However, for $n_{\max} = 2$, the two total cross sections of $Z + 1$jet nearly coincide (cf.

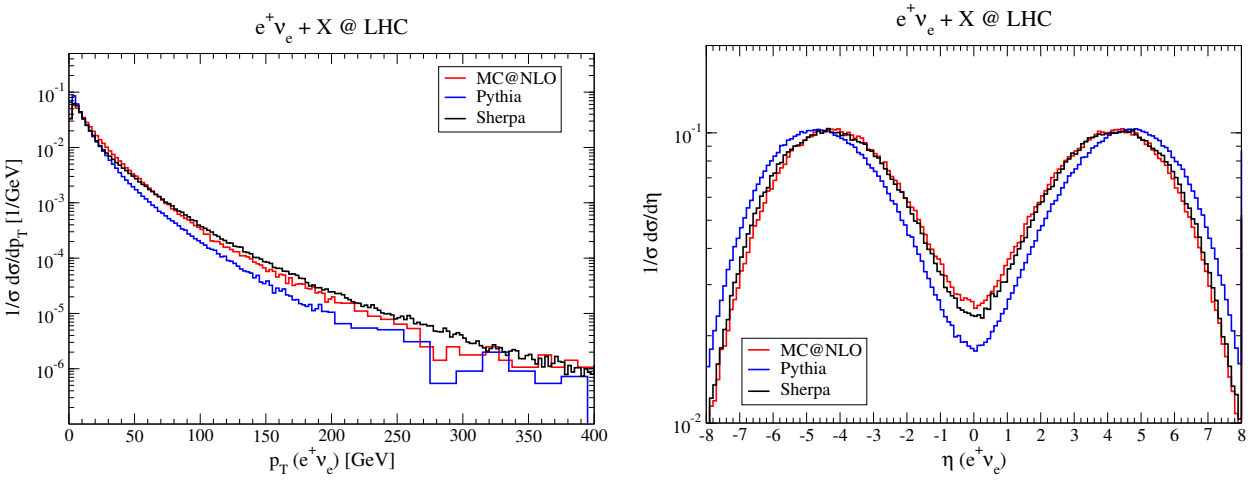

Figure 5.41: The W^+ $p_\perp$ (left) and η (right) distribution in inclusive production at the LHC. The results of the generators `MC@NLO` (red), `PYTHIA` (blue), and `SHERPA` (black) are compared.

the dashed black curve in Fig. 5.42). In terms of shape, `SHERPA` apparently favours jets with larger transverse momentum. As has been seen in the closely related boson $p_\perp$ distribution in Fig. (5.40) `PYTHIA` predicts a much smaller rate (60% w.r.t. the rate predicted by `MC@NLO`) for the production of extra hard QCD radiation with a seemingly softer distribution.

For the second jet the situation changes significantly. Here, even in the case of including only matrix elements with up to one extra parton the two jet rate predicted by `SHERPA` is 17% larger than that of `MC@NLO`. Including matrix elements with two extra partons the difference becomes nearly 90%. As for the case of the first jet, `PYTHIA` predicts the radiation of a second jet with a much smaller rate. Similar statements hold true when looking at the third jet but this time the differences are even larger. Note, that a reliable prediction of the three jet rate requires the inclusion of matrix elements with at least three extra partons. While the sample with matrix elements up to one extra parton predicts a three jet rate of 9.6 pb, the samples with two(three) extra partons predict 16.3(21.1) pb. However, this is not surprising keeping in mind that the LHC provides enough phase space to produce massive bosons in association with a multitude of high energetic jets that are best described by the corresponding matrix elements and that can not be appropriately described by parton shower emissions.

To summarise: the predictions of `MC@NLO` and `SHERPA` agree fairly well for the shape of the boson transverse momentum and pseudo-rapidity distribution. Here, `MC@NLO` is of course superior in predicting the rate of inclusive Z/γ^* and W production since it considers the corresponding production process at NLO in the coupling constant. This situation changes when studying the jets that potentially accompany the boson. As soon as more than one extra jet is considered `SHERPA` predicts significantly larger jet production rates and jet transverse momentum distributions that feature an enhanced population of the high-$p_\perp$ region. Concerning `PYTHIA` it has to be stated that the shape of the boson transverse momentum and the boson pseudo-rapidity distribution differ significantly from the two other programs. This is directly related to the smaller amount of hard radiation produced by `PYTHIA`, clearly observed in the jet $p_\perp$ spectra.

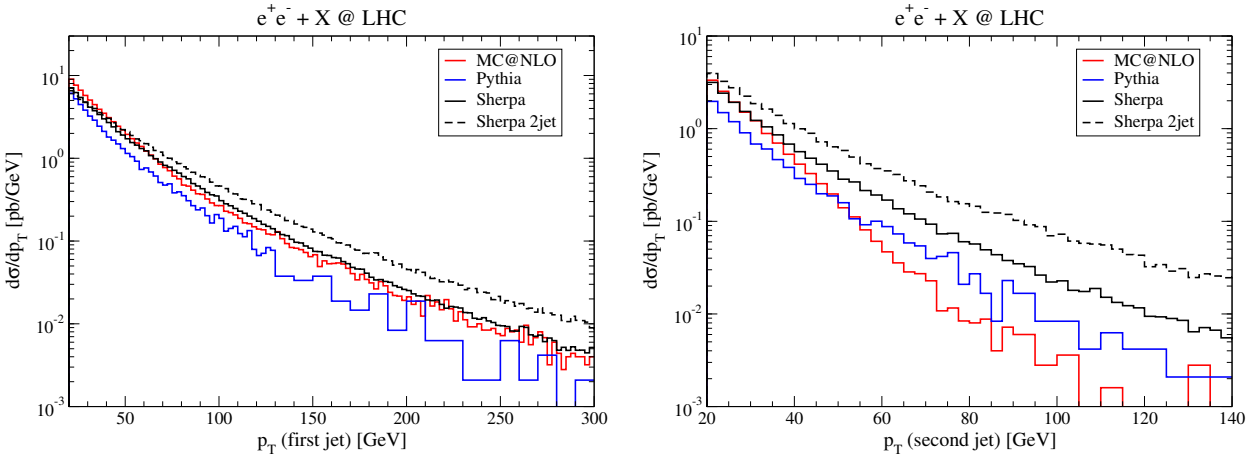

Figure 5.42: The $p_\perp$ distribution of the first (left) and second (right) hardest jet in inclusive Z/γ^* production at the LHC as obtained by `MC@NLO` (red), `PYTHIA` (blue) and `SHERPA` (black). In the right plot, the dashed curve corresponds to the prediction of `SHERPA` when matrix elements for up to two additional partons are used.

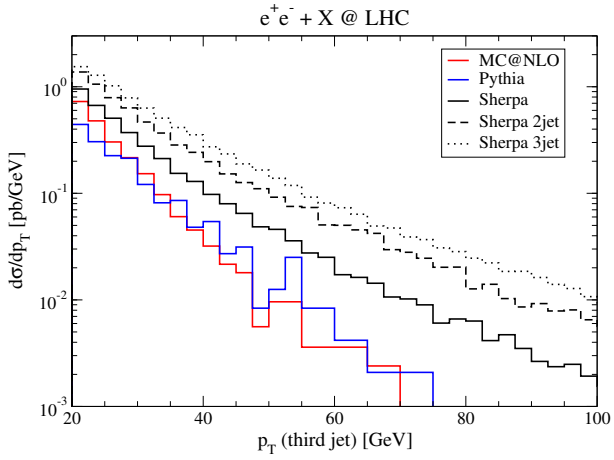

Figure 5.43: The $p_\perp$ distribution of the third hardest jet in inclusive Z/γ^* production at the LHC as obtained by `MC@NLO` (red), `PYTHIA` (blue) and `SHERPA` (black). The dashed (dotted) curve corresponds to the prediction of `SHERPA` when matrix elements for up to two (three) additional partons are used.

5.5 W-pair production at the Fermilab Tevatron

After having validated that the new event generator SHERPA performs well for the cases of e^+e^-–annihilations into jets, and the production of single vector bosons at the Fermilab Tevatron and the CERN LHC in the previous sections, the merging algorithm is now further tested at the case of W-pair production.

Studying the production of W-pairs at collider experiments offers a great possibility for tests of the gauge sector of the Standard Model, that has been extensively investigated by the LEP2 collaborations [162–166]. Tests in this channel are quite sensitive, because there is a destructive interference of two contributions: a t-channel contribution, where both W bosons couple to incoming fermions, and a s-channel contribution, where the W bosons emerge through a triple gauge coupling, either γW^+W^- or ZW^+W^-. New physics beyond the Standard Model could easily manifest itself, either through new particles propagating in the s-channel, like, for instance, a Z' particle in L-R symmetric models [167–170], or through anomalous triple gauge couplings, which could be loop-induced, mediated by heavy virtual particles running in the loop. In [171–173] the most general form of an effective Lagrangian for such interactions has been developed and discussed. Such tests of anomalous triple gauge couplings have been performed both at LEP2 [174–177] and at Tevatron, Run I [178–181] and at Run II [182]. Both scenarios could clearly modify the total cross section or, at least, lead to different distributions of the final state particles. In addition, W-pairs, eventually in addition with jets, represent a background to a number of relevant other processes, such as the production of top quarks, the production of a Higgs boson with a mass above roughly 135 GeV, or the production of supersymmetric particles, such as charginos or neutralinos [183, 184].

Accordingly, there are a number of calculations and programs dealing with this process. At next-to-leading order in the strong coupling constant, W-pair production has been calculated by [185–187]. In addition, a number of programs have been made available, allowing the user to implement own cuts etc.. First of all, there are fixed-order calculations. At leading order (LO), i.e. at tree-level, they are usually performed through automated tools, like for instance MadGraph/MadEvent [61,62] or AMEGIC++ [23]. At NLO, the program MCFM [188] provides cross sections and distributions for this process. Apart from such fixed-order calculations, multi-purpose event generators such as PYTHIA [76, 82] proved to be extremely successful in describing global features of such processes, like, for instance, the transverse momenta or rapidity distributions of the bosons. On the other hand MC@NLO, can be used also to describe the production of electroweak bosons pairs [11].

In the following this series of studies of the merging algorithm as presented in Sec. 4.2 will be continued with investigation of W-pair production at the Fermilab Tevatron, Run II, where both W bosons decay leptonically, i.e. $p\bar{p} \to W^+W^- + X \to e^+\mu^-\nu_e\bar{\nu}_\mu + X$. Again the procedure is kept very similar to previous sections. After some consistency checks of the merging algorithm in Sec. 5.5.2, results obtained with SHERPA will be confronted with those provided by MCFM, cf. Sec. 5.5.3. Then, in Sec. 5.5.4 some exemplary results of SHERPA are compared with those obtained from other event generators, in particular with PYTHIA and MC@NLO.

5.5.1 Input parameters and phase-space cuts

For all analyses, the PDF set CTEQ6L has been used, and α_S has been chosen according to the corresponding value of this PDF, namely $\alpha_S = 0.118$. If not stated otherwise, jets or initial partons are restricted to the light flavour sector, namely g, u, d, s, c, and b. All flavours are taken to be massless.

SM input parameters

The SM parameters are given in the G_μ scheme:

$$\begin{aligned} &M_W = 80.419\ \text{GeV}\,, \quad \Gamma_W = 2.06\ \text{GeV}, \\ &M_Z = 91.188\ \text{GeV}\,, \quad \Gamma_Z = 2.49\ \text{GeV}, \\ &G_\mu = 1.16639 \times 10^{-5}\ \text{GeV}^{-2}, \\ &\sin^2\theta_W = 1 - m_W^2/m_Z^2, \\ &\alpha_s = 0.118. \end{aligned} \tag{5.12}$$

The electromagnetic coupling is derived from the Fermi constant G_μ according to

$$\alpha_{\text{em}} = \frac{\sqrt{2}\, G_\mu\, M_W^2\, \sin^2\theta_W}{\pi}\,. \tag{5.13}$$

The constant widths of the electroweak gauge bosons are introduced through the fixed-width scheme. CKM mixing of the quark generations is neglected.

Cuts and jet criteria

For all jet analysis the Run II $k_\perp$-clustering algorithm defined in [154] has been used. The additional parameter of this jet algorithm is a pseudo-cone size D, whose value has been chosen to $D = 0.7$. In addition jets have to fulfil the following cuts on pseudo-rapidity and transverse momentum,

$$p_T^{\text{jet}} > 15\ \text{GeV}, \quad |\eta^{\text{jet}}| < 2.0. \tag{5.14}$$

For charged leptons the cuts applied are:

$$p_T^{\text{lepton}} > 20\ \text{GeV}, \quad |\eta^{\text{lepton}}| < 1.0\,. \tag{5.15}$$

No cut on missing transverse momentum has been applied.
The final selection criteria correspond to the separation of the leptons,

$$\Delta R_{lj} > 0.4\ \text{GeV}, \quad \Delta R_{ll} > 0.2. \tag{5.16}$$

5.5.2 Consistency checks

The study of W-pair production is started with the presentation of some sanity checks of the merging algorithm. Therefore, again, the dependence on the resolution scale Q_{cut} and the highest multiplicity $n_{\max}$, as well as the sensitivity to changes of the renormalisation scale μ_R and the factorisation scale μ_F is investigated.

All distributions shown in this section are inclusive results at the hadron level, where restrictive jet and lepton cuts have been applied, as given above, in Sec. 5.5.1. In all cases, the distributions are normalised to the total cross section as delivered by the merging algorithm.

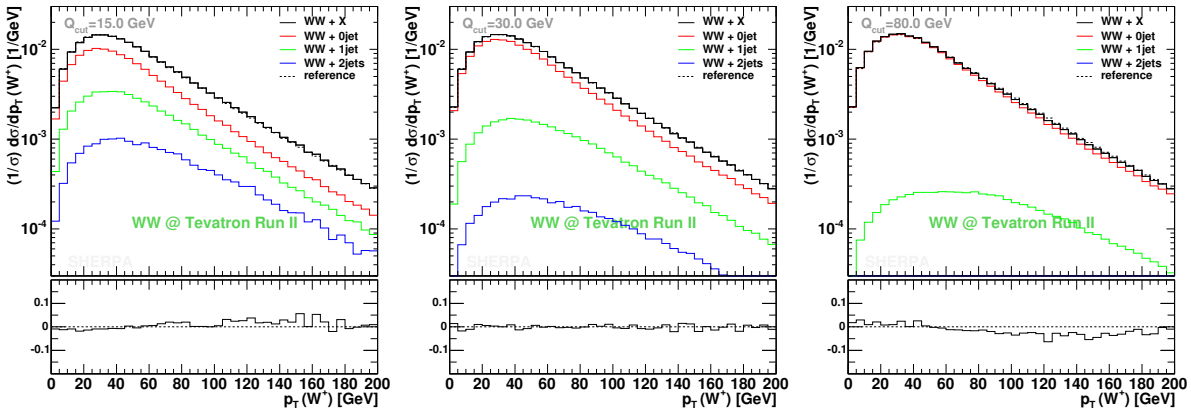

Figure 5.44: The p_T distribution of the W^+ boson and its dependence on Q_{cut}, chosen to be 15, 30 and 80 GeV (from left to right). The black solid line shows the SHERPA prediction obtained with $n_{\max} = 2$, the black dashed one is the reference obtained as the mean of different Q_{cut} runs (for details, see text) and the coloured lines indicate the different multiplicity contributions.

Varying the jet resolution cut Q_{cut}

First of all, the impact of varying the jet resolution cut is studied. SHERPA results have been obtained with an inclusive 2-jet production sample. In all figures the black solid line represents the total inclusive result as obtained by SHERPA for the respective resolution cut Q_{cut}. The reference curve drawn as a black dashed line has been obtained as the mean of five different runs, where the resolution cut has been gradually increased, $Q_{\text{cut}} = 10, 15, 30, 50$ and 80 GeV. The coloured curves give, as usual, the contributions stemming from the different matrix element final-state multiplicities. Results are shown for three different resolution cuts, namely $Q_{\text{cut}} = 15, 30$ and 80 GeV. First. it should be noted that the change of the rate predicted by the merging procedure under Q_{cut} variation has been found to be very small, by varying the separation cut between 10 and 80 GeV, the deviation of the rate amounts to 2.4% only.

As a first observable, the p_T distribution of the W^+ boson, is considered in Fig. 5.44. Obviously, the distributions become slightly softer for increasing cuts. However, this observable is very stable under the variation of Q_{cut} with maximal deviations on the 5% level only. In Fig. 5.45 the transverse momentum spectrum of the W^+W^- system is depicted. Here, deviations show up, but they do not amount to more than 20%. Thus, the QCD radiation pattern depends only mildly on Q_{cut}, which has been varied by nearly one order of magnitude.

As already seen in the previous sections, differential jet rates most accurately probe the merging algorithm, since they most suitably reflect the interplay of the matrix elements and the parton shower in describing QCD radiation below and above the jet resolution cut. Results obtained with the Run II $k_\perp$-algorithm using $D = 1$ are shown for the $1 \to 0$, $2 \to 1$ and $3 \to 2$ transition in the left, middle and right panels of Fig. 5.46, respectively. The value for the internal cut increases from $Q_{\text{cut}} = 15$ GeV to $Q_{\text{cut}} = 80$ GeV. Compared with the p_T^{WW} spectra, similar characteristics of deviations from the reference curve appear. However, here, they are moderately larger reaching up to 30%. Especially for the two smaller

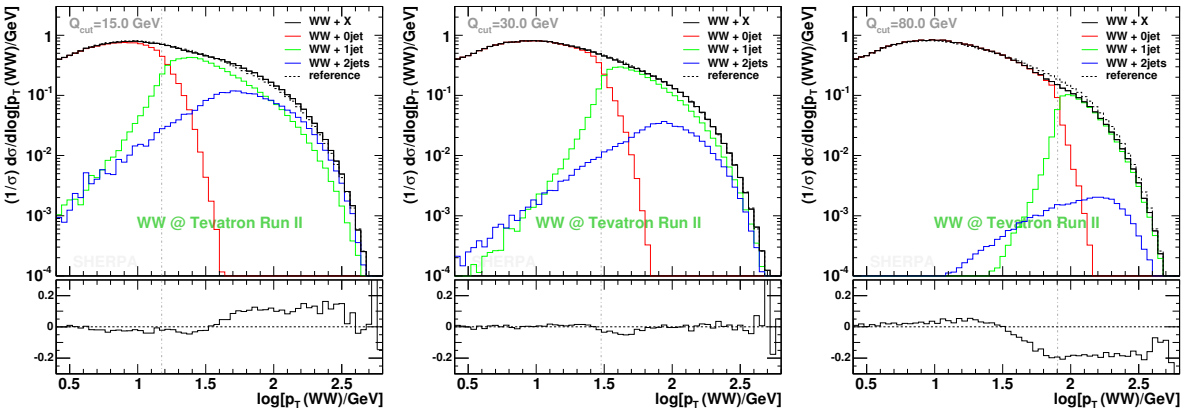

Figure 5.45: The p_T distribution of the W^+W^- system and its dependence on the cut variation. The cut has been chosen as $Q_{\text{cut}} = 15$, 30 and 80 GeV (from left to right). The black solid line shows the SHERPA prediction obtained with $n_{\max} = 2$, the black dashed one is the reference obtained as the mean of different Q_{cut} runs (for details, see text) and the coloured lines indicate the different multiplicity contributions. The actual Q_{cut} value is indicated through a vertical dashed-dotted line.

separation cuts small dips around the cut are visible, which are due to a mismatch of matrix element and parton shower kinematics. In general, the deviations are largest for $Q_{\text{cut}} = 80$ GeV, reflecting the failure of the parton shower in filling the hard p_T emission phase space appropriately.

Taken together, the discrepancies found are on the 20% level. This is very moderate, since the merging algorithm guarantees Q_{cut} independence on the leading logarithmic accuracy only. The residual dependence of the results on Q_{cut} may be exploited to tune the perturbative part of the Monte Carlo event generator.

Varying the maximal jet number $n_{\max}$

The approach of varying the maximal jet number can be exploited for further scrutinising the merging procedure. In all cases considered here, Q_{cut} has been fixed to $Q_{\text{cut}} = 15$ GeV. This maximises the impact of higher order matrix elements. In spite of this, for very inclusive observables, the rates differ very mildly, the change is less than 2%.

In Fig. 5.47, once more the transverse momentum distribution of the W^+ gauge boson is presented, illustrating the impact of varying the highest multiplicity, i.e. $n_{\max}$. Apparently, the distribution becomes only slightly harder when changing from the $n_{\max} = 1$ to the $n_{\max} = 2$ prediction. In contrast, $n_{\max} = 0$ leads visibly to a softer distribution, which is connected to the fact that the parton shower alone does not produce a sizable amount of hard QCD radiation. However, there are a number of observables, which turned out to be rather stable under the variation of $n_{\max}$, such as the pseudo-rapidity spectra of the W^+ boson, the positron and muon or correlations between the leptons, e.g. the $\Delta\phi$ or ΔR distribution. In these cases, deviations turn out to be smaller than 5% in total, when considering the change between the pure shower and the inclusive 2-jet production performance of SHERPA. Even the pseudo-rapidity spectra of the resolved jets are rather unaffected. In contrast, two more observables are presented showing a sizeable (40%) or even strong ($\approx 100\%$) dependence on

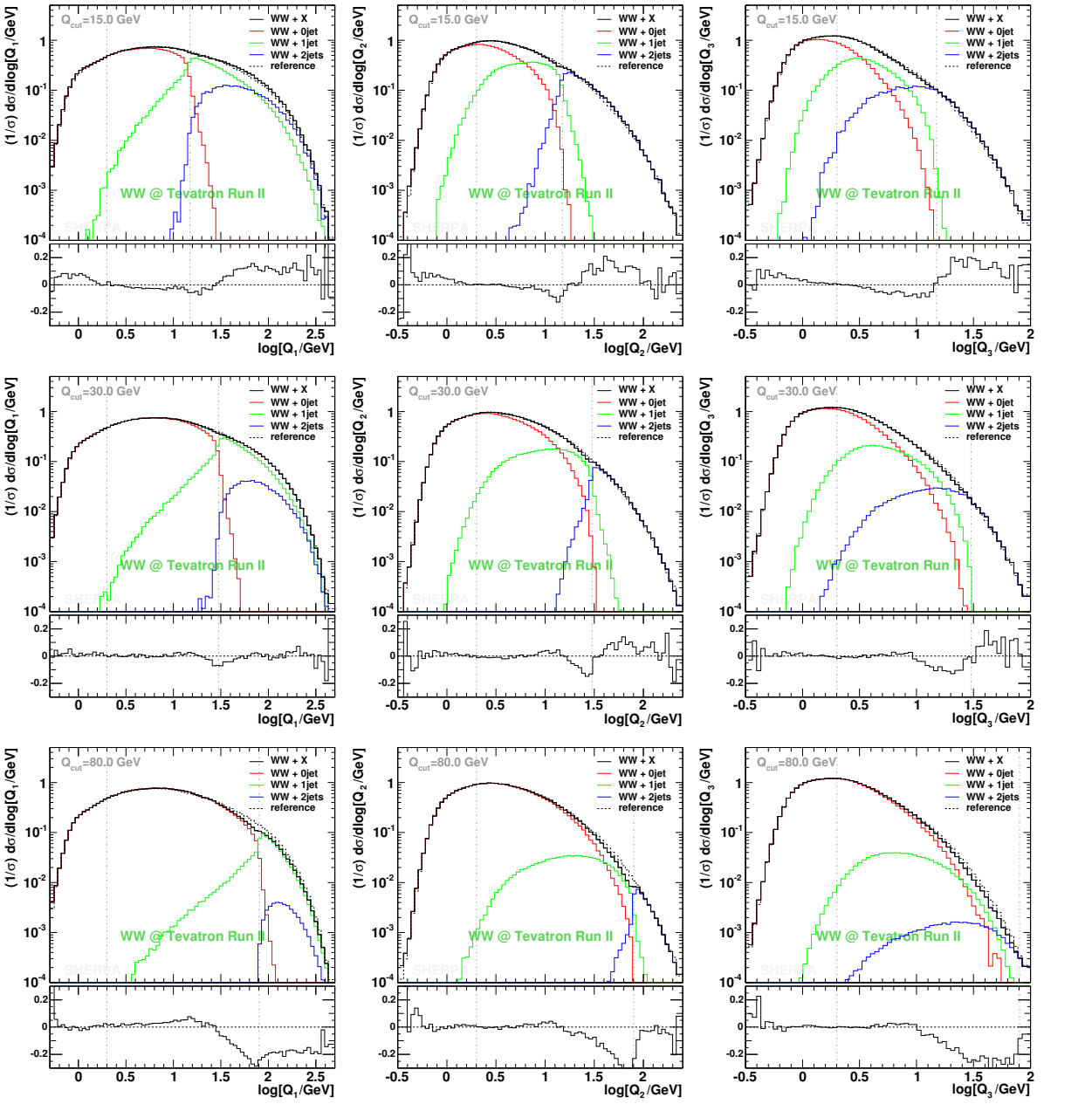

Figure 5.46: Differential $1 \to 0$ jet-rate Q_1, $2 \to 1$ jet-rate Q_2 and $3 \to 2$ jet-rate Q_3 (left to right) shown on a logarithmic scale for the SHERPA $n_{\max} = 2$ configuration. The cut has been chosen to be 15, 30 and 80 GeV (from top to bottom). The black solid line shows the total result, the black dashed one is the reference obtained as the mean of different Q_{cut} runs (for details, see text) and the coloured lines indicate the different multiplicity contributions. The vertical dashed dotted line indicates the separation cut position.

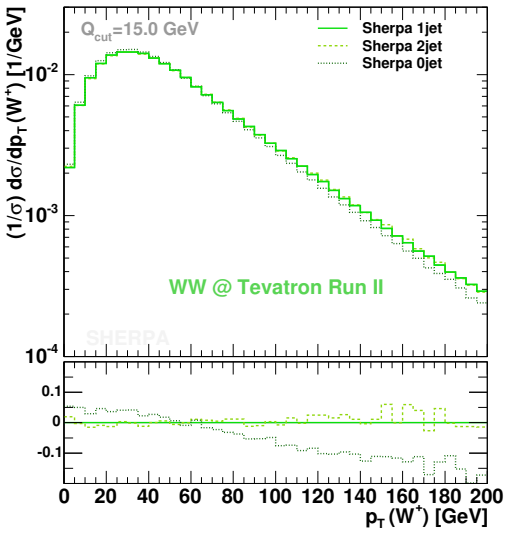

Figure 5.47: The p_T distribution of the W^+ boson and its dependence on the variation of the maximal jet number. The separation cut has been chosen to be 15 GeV. The green solid line shows the SHERPA prediction obtained with $n_{\max} = 1$, the lighter dashed one stands for the prediction where $n_{\max} = 2$ and the darker dotted curve pictures the pure shower performance of SHERPA starting off with the LO matrix element. The lower part of the plot shows the normalised differences with respect to the $n_{\max} = 1$ case.

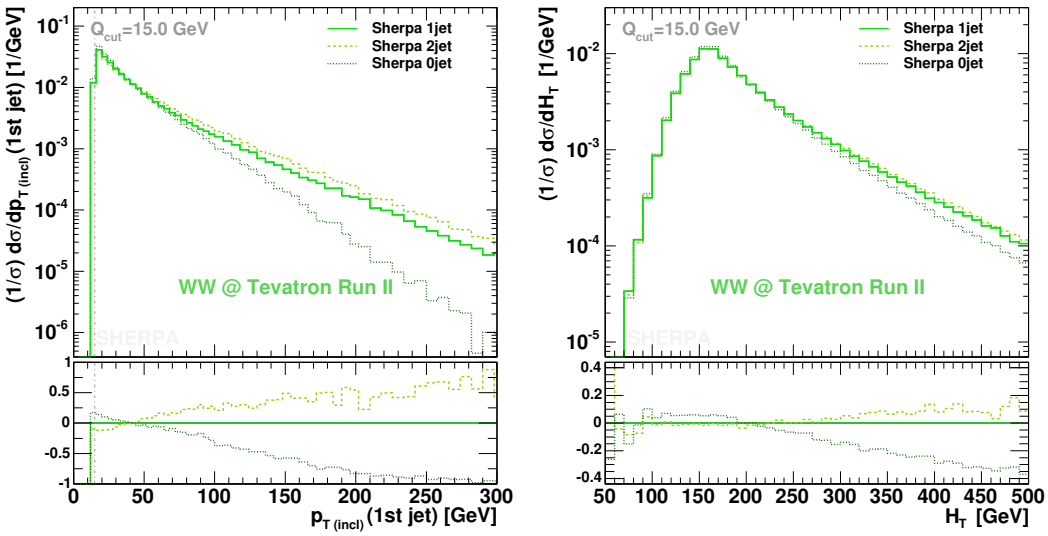

Figure 5.48: SHERPA predictions of the inclusive p_T of the hardest jet (left) and the H_T distribution (right) in dependence on the variation of the maximal jet number. The jet resolution cut has been taken to be 15 GeV. The green solid line shows the result of the $n_{\max} = 1$ run, the brighter dashed one stands for the $n_{\max} = 2$ run and the darker dotted curve depicts the pure shower performance. The lower part of the plot shows the normalised differences with respect to the $n_{\max} = 1$ case.

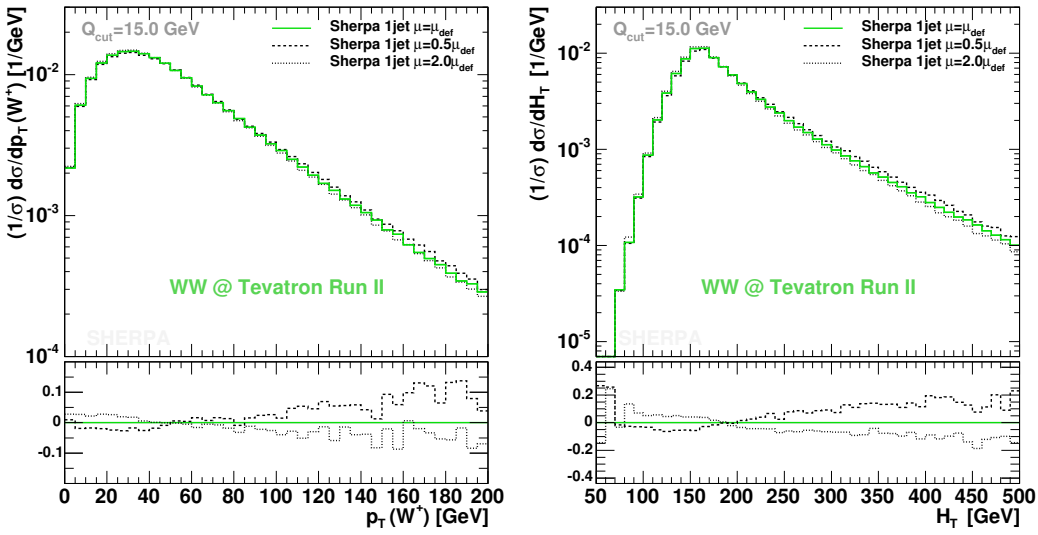

Figure 5.49: The p_T distribution of the W^+ boson (left panel) and the H_T distribution (right panel) in dependence on scale variations. All predictions stem from SHERPA with $n_{\max} = 1$ and $Q_{\text{cut}} = 15$ GeV. The green solid line shows the prediction obtained with the default scale choices for the merging procedure. For the black dashed and the black dotted curves all scales in the coupling constants and PDFs have been multiplied by 0.5 and 2.0, respectively.

the variation of the maximal jet number, namely the H_T distribution and the inclusive p_T spectrum of the hardest jet exhibited in Fig. 5.48. In both observables, predictions become harder with the increase of $n_{\max}$.

Effects of renormalisation and factorisation scale variations

In the following the impact of renormalisation and factorisation scale variations is discussed. For this study, SHERPA samples are produced with $n_{\max} = 1$ and $Q_{\text{cut}} = 15$ GeV. In all figures the green solid line represents SHERPA's default scale choices, whereas the black dashed and the black dotted curve show the outcome for scale multiplications by 0.5 and 2.0, respectively. Again, the change of the LO rate as provided by the merging algorithm is considered first. The rate is remarkably stable, varying with respect to the default only by 4.2%.

The transverse momentum distribution of the W^+ boson is investigated in the left part of Fig. 5.49. Scale variations distort the shape, shifting it towards harder (softer) p_T for smaller (larger) scales. The distortions reach up to 10%. A similar behaviour is also found for the p_T spectrum of the positron. The effect is even more pronounced in the H_T distribution, see the right part of Fig. 5.49. There the variations go up to 20%. Roughly the same deviations appear in the transverse momentum distribution of the diboson system, depicted in Fig. 5.50.

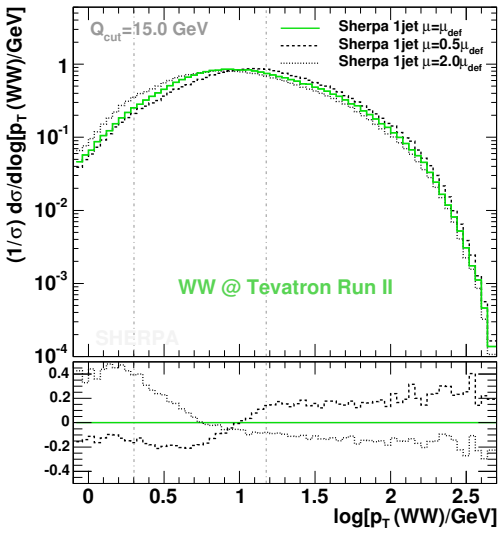

Figure 5.50: The p_T distribution of the W-pair and its dependence on the variation of μ_R and μ_F. Fixing $n_{\max} = 1$ and $Q_{\text{cut}} = 15$ GeV, the green solid line shows the prediction under default scale choices. For the black dashed and the black dotted curves all scales in the coupling constants and PDFs have been multiplied by 0.5 and 2.0, respectively.

5.5.3 SHERPA vs. NLO results

In this section, the focus shifts from internal sanity checks to comparisons with a NLO calculation. For this, once more the MCFM program [188] has been used. In both, MCFM and SHERPA the CKM matrix has been taken diagonal, and no b-quarks are considered in the partonic initial state of the hard process. If not stated otherwise, in MCFM the renormalisation and factorisation scale have been chosen as $\mu_R = \mu_F = M_W$, according to the choice made in [188]. In the following the results of MCFM are confronted with those of SHERPA obtained at the parton shower level, in order to have an inclusive prediction.

Consider first the H_T distribution, depicted in Fig. 5.51. Clearly, higher order corrections affect the H_T shape. This is due to two reasons. First of all, the additional QCD radiation may manifest itself as jet(s), thus leading to other hard objects contributing to H_T. In addition, even if they do not produce a jet, the additional partons form a system against which the W-pair may recoil. Quantitatively, the inclusion of NLO results in a shift of the H_T distribution at harder values by up to 20%; in SHERPA this trend is amplified by roughly the same amount. These differences between MCFM and SHERPA, however, are due to the fact that in MCFM all scales have been fixed to $\mu = M_W$, whereas in SHERPA the scales are dynamically set.

The impact of scale variations on the same observable are quantified in Fig. 5.52. This time, however, the SHERPA result with $n_{\max} = 1$ is compared to NLO results obtained from MCFM with scale choices in the range $\mu_R = \mu_F = \{1 \ldots 4\} \cdot M_W$ and with a LO result taken at $\mu_R = \mu_F = 2M_W$. Obviously, the smaller choice of scale results in the MCFM result to be closer to the one of SHERPA. To underline this, in Fig. 5.53, H_T is depicted, this time for exclusive W-pair production. There, the real part of the NLO correction in MCFM is

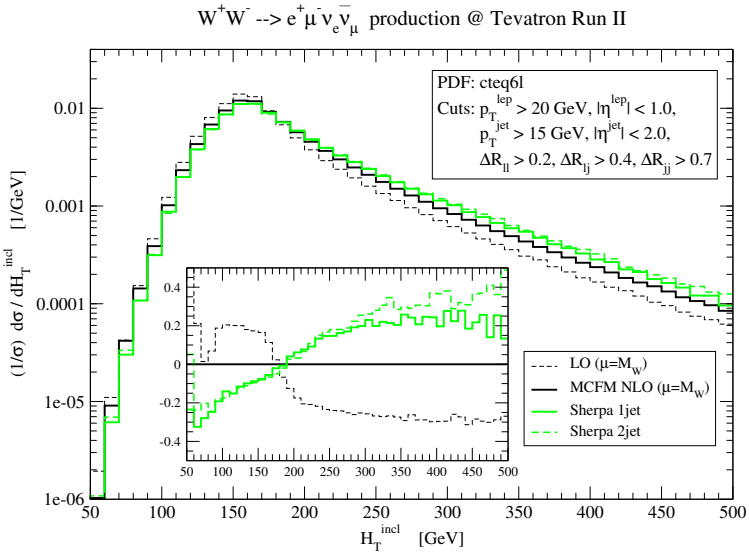

Figure 5.51: Normalised H_T distribution. SHERPA results are shown for $n_{\max} = 1$ (green solid line) and $n_{\max} = 2$ (green dashed line) and compared to the QCD NLO result of MCFM in the "inclusive mode" (black solid line). The LO result with the same scale choice is depicted as a black dashed line.

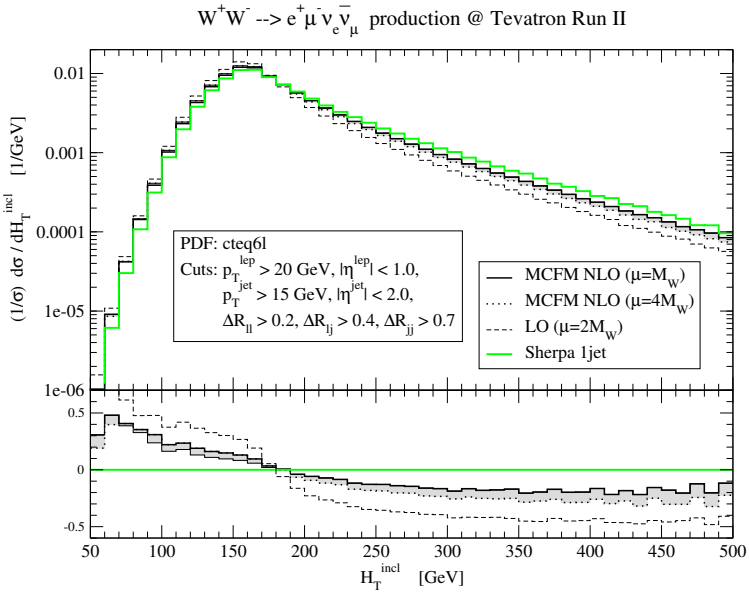

Figure 5.52: Normalised inclusive H_T distribution. Here, both the factorisation and renormalisation scale of the NLO calculation have been varied in the range $\mu_{\text{ren}} = \mu_{\text{fac}} = \{1 \ldots 4\} \cdot M_W$ (shaded area). These MCFM results are compared with the leading order result at $\mu_{\text{ren}} = \mu_{\text{fac}} = 2M_W$ (dashed line) and with the result of SHERPA with $n_{\max} = 1$.

constrained such that it does not produce an extra jet, and in SHERPA the matrix element with zero jets only is considered. In addition, the parton shower attached to this matrix

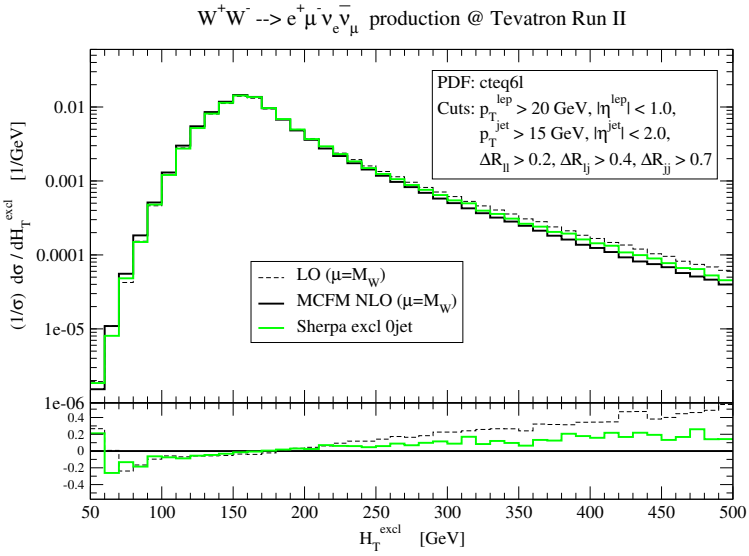

Figure 5.53: Normalised exclusive H_T distribution. The SHERPA result (green solid line) is obtained with $n_{\max} = 0$ and a parton shower that is constrained not to produce any extra jets. This result is compared with the MCFM result at NLO (black solid line) and with a LO result (black dashed line). The latter two are taken for the default scale choices.

element is now forced not to produce any jet at all. In this case, the higher order corrections lead to a slightly softer H_T distribution compared to the leading order case, and the results of MCFM and SHERPA are in good agreement.

The effect of radiation is best observed in the p_T distribution of the W-pair, depicted in Fig. 5.54. Clearly, without any radiation, the p_T of the W-pair is exactly zero, and only the emission of partons gives the boson system something to recoil against. In the NLO MCFM calculation, however, the spectrum therefore is described at LO, in this particular case taken at $\mu_R = \mu_F = M_W$. In contrast, in the SHERPA result a variable scale choice is applied, which may explain the differences found. Contrasting this with the parton shower approach, it is clear that parton emission through the shower alone is not sufficient to generate sizable p_T of the W-pair in the hard region. For this, the corresponding matrix element has to be employed, leading to very good agreement in the high-p_T tail of the distribution.

The slightly different radiation patterns in the two aproaches have some minor effect on the distribution of the W bosons, take as examples the p_T distribution of the W^+ and of the e^+, displayed in Figs. 5.55 and 5.56, and the η distribution of the W^+ depicted in Fig. 5.57. Such differences also manifest themselves in correlations of the two leptons produced in the decays of both W bosons. For instance, in the $\Delta R_{e\mu}$ distribution, cf. 5.58, higher order effects tend to change the shape by roughly 10%. The interesting observation here is that this change is seemingly not related to the p_T of the W-pair system. This can be seen from the fact that the NLO results of MCFM and SHERPA results for $n_{rmmax} = 1$ *and* $n_{rmmax} = 2$ are in nearly perfect agreement with each other. This gives rise to the assumption that it the change w.r.t. the LO result is due to some altered spin structure in the matrix element.

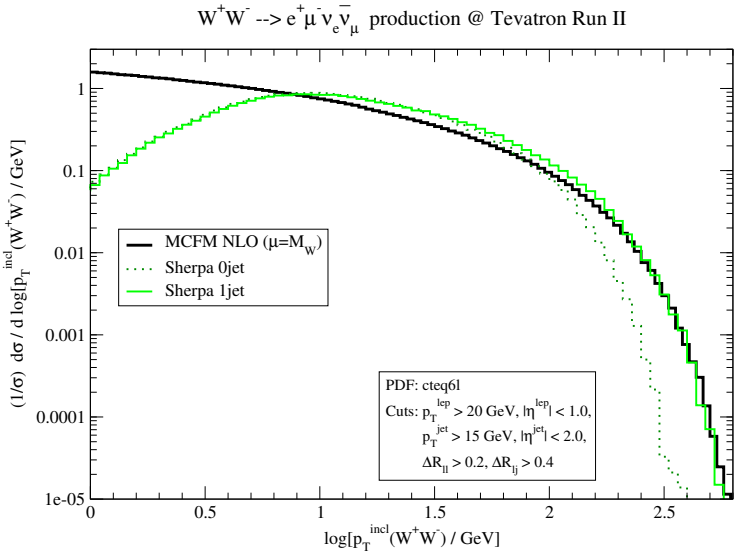

Figure 5.54: Normalised p_T distribution of the W-pair. The `MCFM` result (black) is contrasted with results from `SHERPA`, both for $n_{\max} = 0$ (green dotted) and for $n_{\max} = 1$ (green solid).

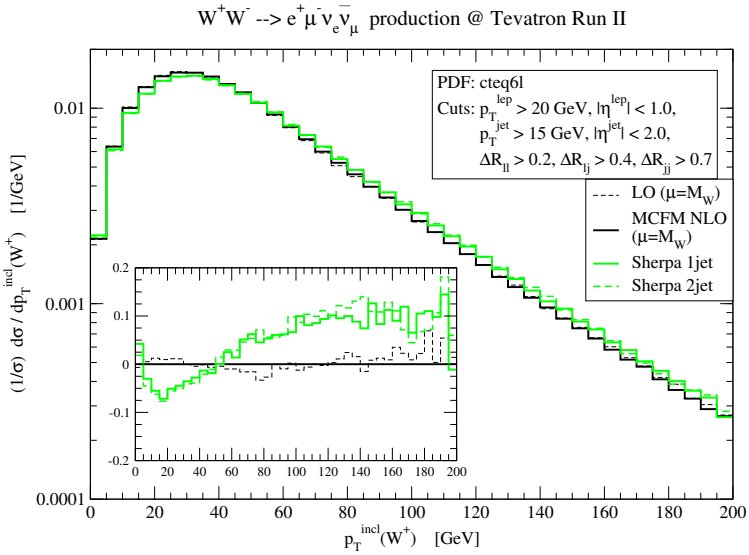

Figure 5.55: Normalised inclusive transverse momentum distribution of the W^+ boson. The results of `SHERPA` for $n_{\max} = 1$ (green solid line) and for $n_{\max} = 2$ (green dashed line) are compared with the QCD NLO result obtained by `MCFM` (black solid line) and with a LO result (black dashed line). For the latter two, the scales are again fixed according to the default choice, i.e. $\mu_R = \mu_F = M_W$.

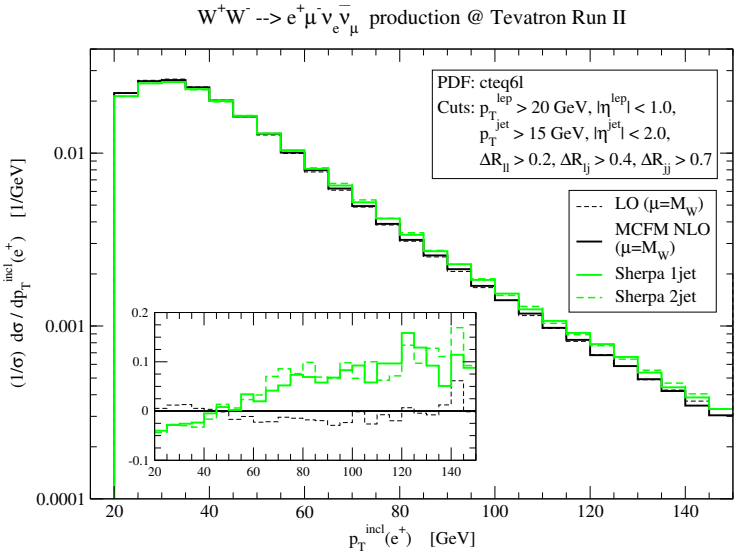

Figure 5.56: Normalised inclusive transverse momentum distribution of the e^+ produced in the decay of the W^+. The results of SHERPA for $n_{\max} = 1$ (green solid line) and for $n_{\max} = 2$ (green dashed line) are confronted with the QCD NLO result obtained by MCFM (black solid line) and with a LO result (black dashed line). For the latter two, the scales are again fixed according to the default choice, i.e. $\mu_R = \mu_F = M_W$.

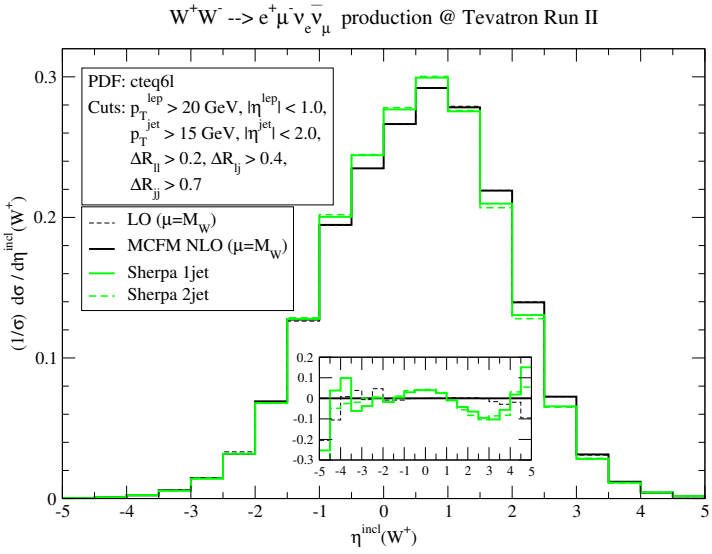

Figure 5.57: Normalised inclusive η distribution of the W^+ boson. The SHERPA results for $n_{\max} = 1$ (green solid line) and $n_{\max} = 2$ (green dashed line) are confronted with those of MCFM (solid black line) and with a LO result (dashed black line). Again, in the latter two the scales are chosen as $\mu_R = \mu_F = M_W$.

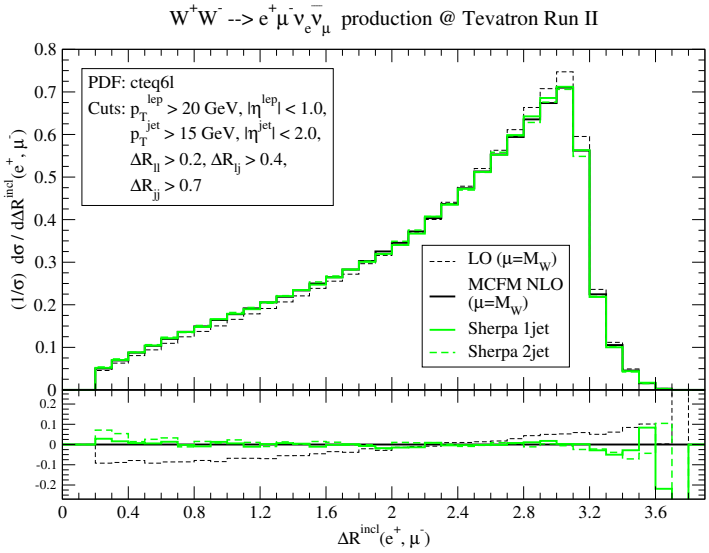

Figure 5.58: Normalised inclusive ΔR distribution between the two charged leptons emerging from the W decays. `SHERPA` results for $n_{\max} = 1$ (green solid line) and $n_{\max} = 2$ (green dashedline) are compared to those predicted by `MCFM` (black solid line). The LO result with the same scale choice, is shown as a black dashed line.

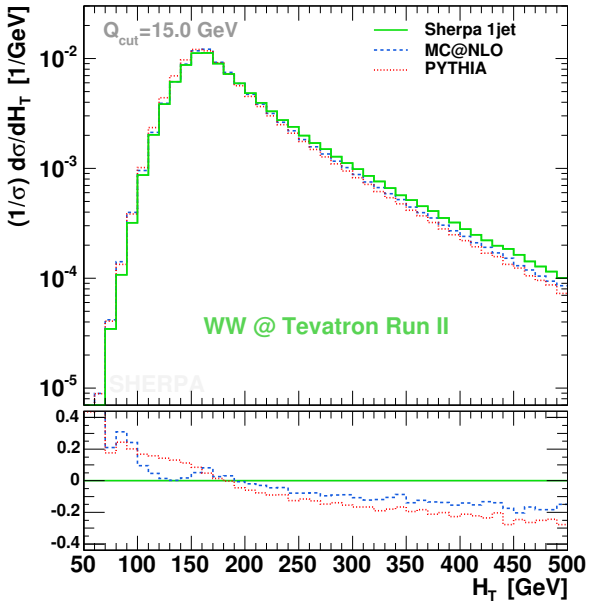

Figure 5.59: Normalised inclusive H_T distribution obtained from PYTHIA (red dotted line), MC@NLO (blue dashed line) and SHERPA (green solid line). For the generation of the SHERPA sample, $n_{\max} = 1$ and $Q_{\text{cut}} = 15$ GeV have been chosen.

5.5.4 SHERPA vs. MC@NLO and PYTHIA

In this section, the focus shifts now to a comparison of SHERPA with other hadron-level event generators, in particular PYTHIA and MC@NLO.

Comparison of the QCD activity

As before, the starting point will be the discussion of the radiation activity predicted by the various codes. As seen before, the H_T distribution allows some first global statements. In Fig. 5.59, results for this observable obtained from PYTHIA, MC@NLO, and SHERPA are displayed. Apparently, the former two codes agree nicely with each other. However, SHERPA predicts a slightly harder spectrum, with relative deviations of up to 20%.

Closer inspection of the reason for the differences in the H_T spectrum reveals that the agreement of PYTHIA and MC@NLO is presumably a little bit coincidental. A first hint into that direction can be read off Fig. 5.60, where the p_T spectrum of the W-pair is displayed. Apparently, in the region of low p_T (up to 80 GeV), the results of MC@NLO and SHERPA are in fairly good agreement, and sizeable differences larger than 10% appear only for $p_T \gtrsim 100$ GeV. In contrast, the PYTHIA result for this observable has a significant peak at low p_T and dies off rapidly.

Fig. 5.61 depicts the norm of the scalar difference of the transverse momenta of the W^+ and W^- gauge boson, $|p_T^{W^+} - p_T^{W^-}|$. This observable is sensitive to higher order effects, since at LO it merely has a delta peak at $p_T = 0$ GeV. Again, the hardest prediction is delivered by SHERPA with $n_{\max} = 1$, results from MC@NLO, PYTHIA, and the pure shower performance of SHERPA are increasingly softer. For $|\Delta p_T| > 60$ GeV, this observable seems to depend

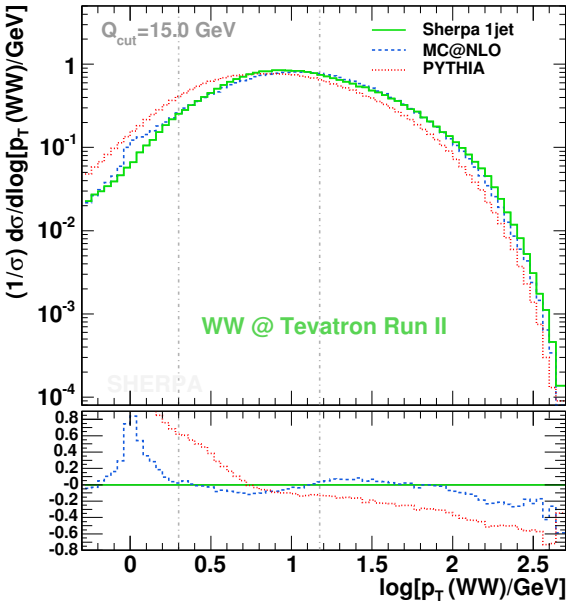

Figure 5.60: Normalised inclusive p_T distribution of the W^+W^- system. Results from PYTHIA (red dotted line), MC@NLO (blue dashed line) and SHERPA (green solid line) are compared. For the generation of the latter, $n_{\max} = 1$ and $Q_{\text{cut}} = 15$ GeV have been chosen.

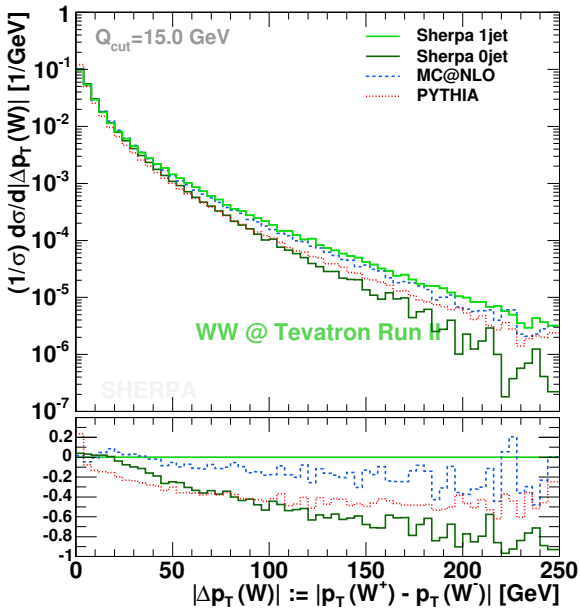

Figure 5.61: Difference of the scalar transverse momenta of the two W bosons $|p_T^{W^+} - p_T^{W^-}|$. The predictions compared are: SHERPA inclusive 1jet production at $Q_{\text{cut}} = 15$ GeV drawn as a green solid line, SHERPA's pure shower performance shown as a dark-green line, MC@NLO depicted as a blue dashed line and PYTHIA given as a red dotted curve.

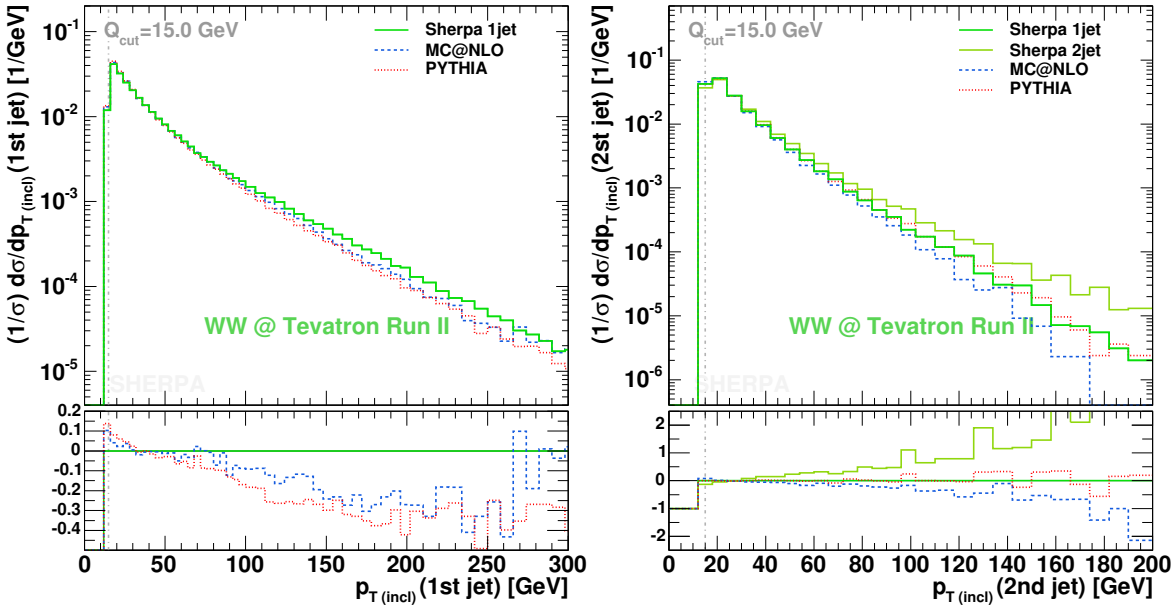

Figure 5.62: Transverse momentum distributions of the associated jets. In the left panel, the p_T of the hardest jet is depicted, whereas in the right panel the second hardest jet is displayed. Again, results from PYTHIA are given by the red dotted line, MC@NLO results are represented as a blue dashed line and SHERPA results are the green solid line(s). For the generation of the latter, $n_{\max} = 1$ and $Q_{\text{cut}} = 15$ GeV have been chosen. The black solid line in the lower panel corresponds to the SHERPA result obtained with $n_{\max} = 2$.

more on the quality of the modelling of the hardest emission, which is intrinsically better described by MC@NLO and by SHERPA with $n_{\max} = 1$. The fact that the PYTHIA shower performs better than the pure SHERPA shower for high p_T differences can be traced back to the starting scale of the shower evolution, which is either $s_{p\bar{p}}$ (PYTHIA) or s_{WW} (SHERPA).

Taken together, these findings hint that the three codes differ in their modelling of the QCD activity. In fact, considering the p_T distributions of the hardest two jets in Fig. 5.62, sizable differences appear. In the left part of this figure, the transverse momentum spectrum of the hardest jet is depicted. Surprisingly, although MC@NLO contains a matrix element for the emission of an extra jet, its p_T distribution is considerably softer (by up to 40%) than the result of SHERPA generated with $n_{\max} = 1$, i.e. with matrix elements for up to one extra jet. This trend is greatly amplified when going to the spectrum of the second hardest jet. There, differences of the order of a factor 2 between SHERPA and MC@NLO show up for $p_T \approx 150$ GeV, and there is a clear difference in the shape of both results. The surprise in this figure is the fact that PYTHIA and SHERPA with $n_{\max} = 1$ seem to agree on the p_T distribution of the second jet, although they were different for the hardest jet. At that point it should be noted that the second jet in both cases, PYTHIA and SHERPA with $n_{\max} = 1$, is produced by the parton shower only, giving the considerably larger shower scale of PYTHIA the opportunity to compensate to some extent for the deficiencies in filling the phase space of hard emissions intrinsic to parton showers. However, in the very moment, SHERPA events are generated with appropriate matrix elements, i.e. with $n_{\max} = 2$, large differences appear, i.e. almost a factor two for $p_T \approx 100$ GeV.

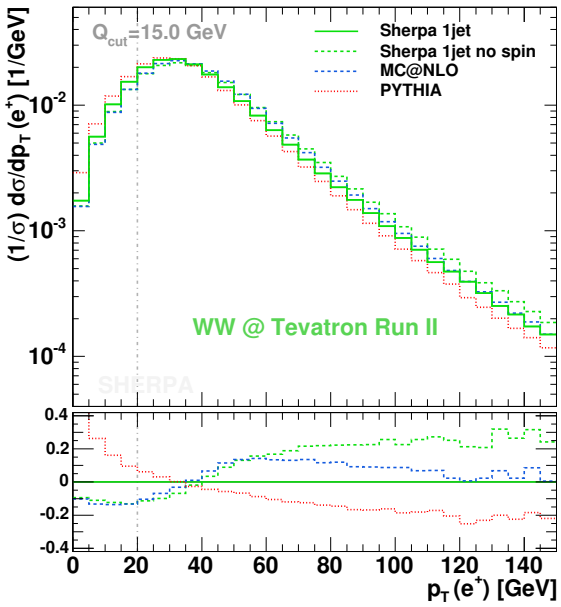

Figure 5.63: Normalised p_T spectrum of the positron. Results of PYTHIA (red dotted line) and SHERPA (light green solid line) including spin correlations are confronted with those obtained from MC@NLO (blue dashed line) and with results from SHERPA, where spin correlations have been switched off (dark green solid line).

Comparison of lepton observables

Finally, the leptons in the final state as described by the three event generators PYTHIA, MC@NLO and SHERPA will be investigated. There, some significant differences appear between SHERPA and PYTHIA on the one hand, and MC@NLO on the other hand. These differences are due to the fact that at the moment spin correlations of the W decay products are not implemented in MC@NLO[3]. The impact of the lack of spin correlations already becomes visible in one-particle observables, such as the p_T or the η spectrum of the positron produced in the W^+ decay. This is shown in Figs. 5.63 and 5.64, where in order to quantify the impact of spin correlation effects without any bias due to cuts the results have been obtained with the analysis being free of lepton and jet cuts. To validate that the effects, reaching up to 40%, are indeed due to the lack of spin correlations, SHERPA samples have been prepared, where these correlations are artificially switched off.

First, the transverse momentum distribution of the e^+ is considered. Confronting the two methods with each other, which correctly respect spin correlations, a pattern similar to the one found in the SHERPA MCFM comparison, cf. Sec. 5.5.3, Fig. 5.56, emerges. Due to the inclusion of higher order tree-level matrix elements, the SHERPA $n_{\max} = 1$ setup produces a considerably harder spectrum than PYTHIA. In contrast, the distributions with no spin correlations both result in a harder high-p_T tail. They agree quite well up to $p_T = 60$ GeV, hence this coincidence may be assigned to the lack of spin correlations in the gauge boson decays. Above that region, the MC@NLO spectrum becomes softer with respect to the SHERPA prediction with spin correlations switched off.

[3]This situation is currently being cured by the MC@NLO authors who prepare a new version of their code including spin correlations [155].

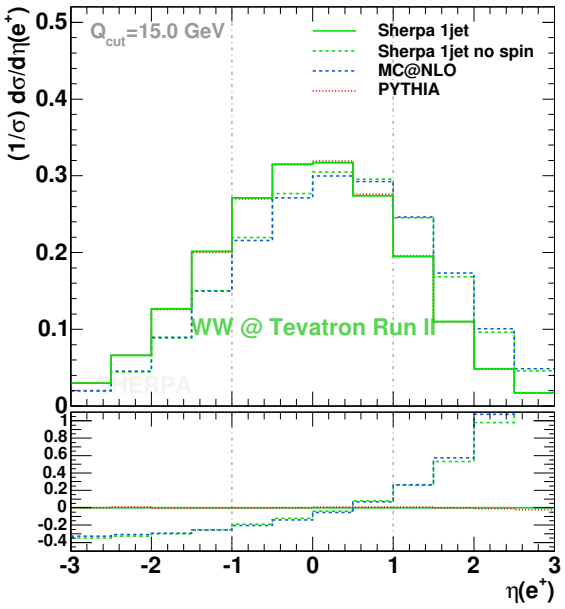

Figure 5.64: Normalised η spectrum of the positron. Results of PYTHIA (red dotted line) and SHERPA (light green solid line) including spin correlations are compared with those obtained from MC@NLO (blue dashed line) and with results from SHERPA, where spin correlations have been switched off (dark green solid line).

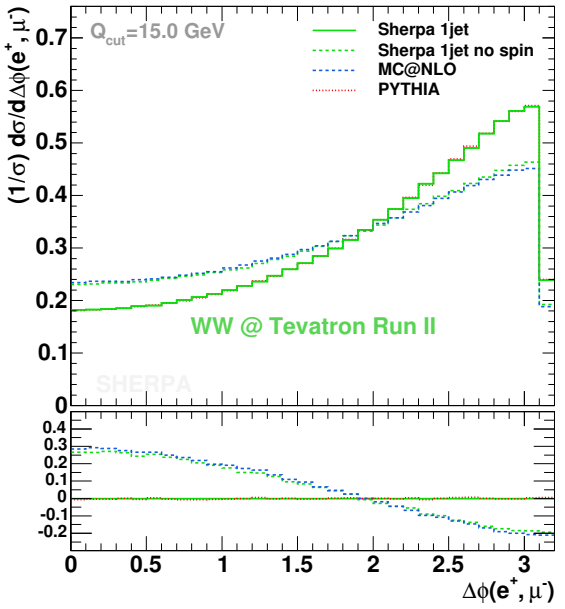

Figure 5.65: Normalised $\Delta\phi_{e\mu}$ distribution. Results of PYTHIA (red dotted line) and SHERPA (light green solid line) including spin correlations are compared with those obtained from MC@NLO (blue dashed line) and with results from SHERPA, where spin correlations have been switched off (dark green solid line).

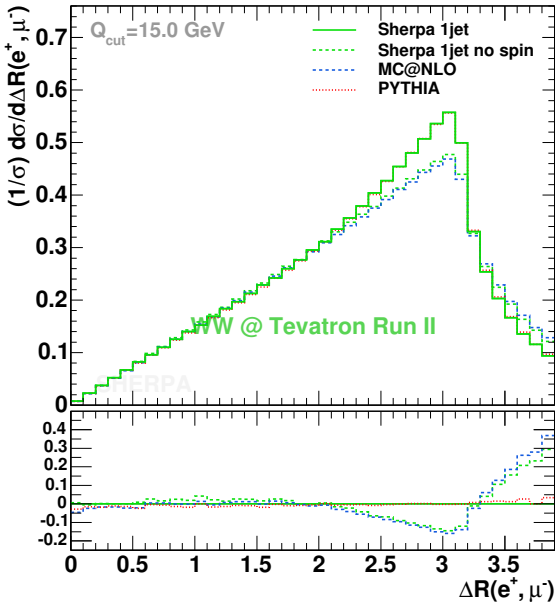

Figure 5.66: Normalised $\Delta R_{e\mu}$ distribution. Results of PYTHIA (red dotted line) and SHERPA (light green solid line) including spin correlations are compared with those obtained from MC@NLO (blue dashed line) and with results from SHERPA, where spin correlations have been switched off (dark green solid line).

In contrast, the η distribution of the e^+, the results of PYTHIA and SHERPA with spin correlations on the one hand and of MC@NLO and of SHERPA without spin correlations on the other hand show perfect agreement.

This is equally true for observables based on two particle correlations. As two illustrative examples take the $\Delta\phi$ and the ΔR distribution of the e^+ and the μ^- produced in the decay of the two W bosons. Again, the corresponding spectra, exhibited in Figs. 5.65 and 5.66, differ significantly in shape depending on whether spin correlations are taken into account or not.

To complete this discussion of the impact of spin correlation effects, a few example plots will be shown, where the superposition of spin correlations (or their absence) together with cuts may possibly lead to misinterpretations. It is clear that jet and lepton cuts strongly affect the event sample. Here, the cuts are mainly on the η and p_T of the leptons, such that the corresponding distributions drive alterations to secondary observables. An example is the pseudo-rapidity distribution of the W^+ boson. Without the application of cuts one starts off distributions that agree on a $< 10\%$ level. This is severely changed by the introduction of the cuts, see the rightmost panel of Fig. 5.67. In contrast to the aforementioned two-particle correlations, here the predictions without spin correlations are well separated from the other ones only after the application of the cuts. As a last example, consider the transverse momentum distribution of the W^+ boson. Both types of predictions stemming from the analysis without (left panel) and with cuts (middle panel) are pictured in Fig. 5.67. The inclusion of cuts seems to bring MC@NLO and SHERPA including the full correlations into good agreement, but this clearly happened accidentally.

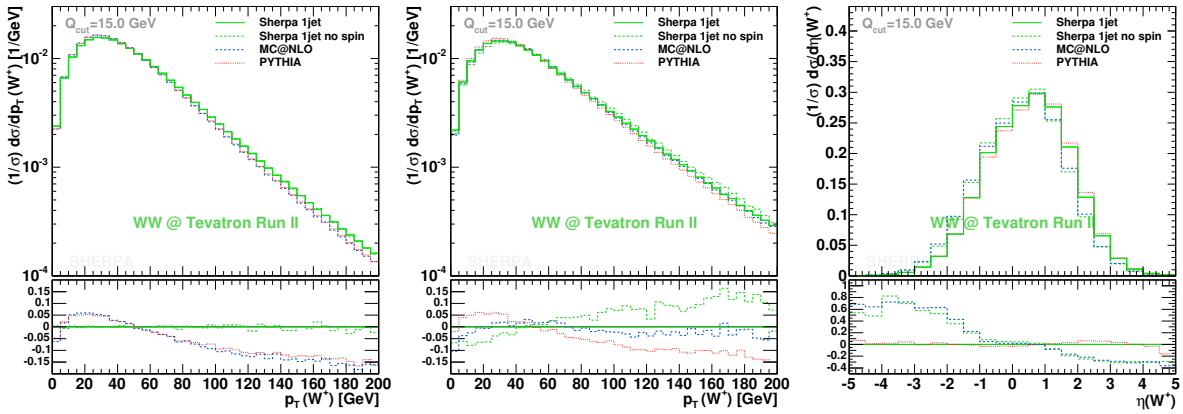

Figure 5.67: Distributions showing significant alterations after the application of lepton and jet cuts. Strong alterations appear in cases where the spin correlations of the W boson decays are not respected. In the left panel the p_T spectrum of the W^+ using an analysis free of cuts is depicted. The same observable is shown in the middle panel, but now for the case of lepton and jet cuts being applied. The right panel exhibits the η distribution of the W^+ under the influence of cuts. The predictions compared are: SHERPA inclusive 1jet production at $Q_{\text{cut}} = 15$ GeV drawn as a green solid line, SHERPA as before but no correlations in the boson decays shown as a dark-green line, MC@NLO depicted as a blue dashed line and PYTHIA given as a red dotted line.

5.6 Summary

In this chapter, the merging procedure as implemented in the event generator SHERPA has been successfully tested for various physics scenarios both at e^+e^-–colliders and at hadron colliders.

Starting with a comparison with LEP1 data, SHERPA performed very well in describing these high precision data. In particular, the description of 4-jet angles often provides a challenge to existing Monte Carlo event generators. After merging matrix elements with up to 5 jets with the parton shower an excellent agreement of Monte Carlo results and data could be reached. A test of the energy extrapolation abilities of SHERPA is provided by LEP2 data. There, the agreement with data collected at 189 GeV is again very convincing.

At hadron colliders, SHERPA predictions have been generated for the production of single electroweak gauge bosons at the Tevatron and the LHC, and for the production of leptonically decaying W-pairs at the Tevatron. The results have been compared with the results from other programs and, if available, with data. The merging procedure turned out to yield stable results over a wide range of internal parameters, rendering it a predictive way of incorporating the full information available in tree-level matrix elements into multi-purpose event generators, as anticipated. In addition, when comparing the results obtained from SHERPA with those of a full next-to-leading order calculation, it turned out that the results of SHERPA reproduce the essential features in the NLO shapes. However, it should be stressed here that the total normalisation of the cross sections is still at leading order accuracy only in SHERPA. Nevertheless, the fact that SHERPA seems to reproduce the NLO shapes of the observables, the NLO rates can be recovered by simply multiplying with a constant K-factor.

When comparing the results of SHERPA with those of other event generators, some differences appear. Especially for observables sensitive to the correct treatment of multi-particle final states these differences become significant, in the case of the LHC, ranging up to orders of magnitude. This is due to the huge phase space available for emission of extra jets. This finding necessitates the usage of multi-jet matrix elements for realistic analyses. In addition, the impact of spin correlations has been quantified for the production of W-pairs. In the observables considered there, it reaches 20-50%, for some observables it turned out to be even larger than the impact of higher order corrections.

6 Summary

In this thesis, the new C++-based multi-purpose event generator SHERPA has been further extended, such that it is suitable now for the simulation of physics at present and future hadron colliders. In view of the start of the LHC in the near future and in anticipation of its tremendous challenge in terms of precise understanding of signals and backgrounds for new physics beyond the Standard Model, the construction of new advanced and versatile simulation tools is of paramount importance for the field of particle physics phenomenology. In this respect, the development of SHERPA marks the advent of a new generation of such tools, meant to replace older programs. This is also reflected by the fact that it is the first of the new tools that start being actually used for experimental analyses.

To reach this state, a number of issues have been dealt with during this thesis. First of all, the performance of SHERPA's internal matrix element generator AMEGIC++ has been improved. Matrix element generators such as AMEGIC++ are a central building block of any modern event generator; they deliver the cross sections and distributions for the signal or background processes at the core of each event. By providing algorithms for the symbolic optimisation of the helicity expressions, the efficiency of the program could be improved substantially. Thus, this program was put into the position to describe final states with up to six particles in electron-positron annihilations or in hadron induced reactions. Of course, the individual algorithms and the complete code has passed an extensive testing procedure; in this thesis some exemplary results has been presented. They all illustrate the correctness of the improvements and extensions of AMEGIC++ and the abilities of this program.

Apart from the production of high-energetic particles, that are well-separated in phase space and can thus be treated with exact, quantum-mechanically correct perturbative matrix elements, also soft and collinear quanta emerge. For their treatment, a different technique has to be employed, the parton shower approach. This approach uses an expansion around the logarithmically enhanced soft and collinear region of particle production to disentangle the complex pattern of multiple secondary radiation and to reduce it to a Markov-chain of individual particle emissions, correctly taking into account the leading logarithms. In this thesis the program APACIC++, which so far has been able to perform the parton shower evolution in the final state of particle reactions, has been extended to deal also with parton emission in the initial state. This step enabled SHERPA to realistically describe hadron induced high-energy reactions. During this extension, APACIC++ experienced a complete re-write, necessitating further detailed tests of its correctness in describing both initial and final state radiation. During this validation, both against analytical calculations and data, APACIC++ proved to be perfectly capable of describing a plethora of observables sensitive to the soft and collinear regions of QCD radiation. It thus forms the link to the soft regime of strong interactions which can be described by phenomenological models only.

In order to use the information of multi-jet matrix elements inside an event generator, they have to be merged with the parton shower responsible for the modelling of QCD radia-

tion of secondary particles, similar to bremsstrahlung. This radiation of secondary partons is organised in terms of leading logarithms associated to each single emission. The parton shower which organises the simulation of this process is exact to all orders in the leading logarithms, therefore there is some potential double counting of logarithmic contributions from both matrix elements and the parton shower. To handle them, a new algorithm has been implemented and further extended, which correctly merges the matrix elements and the parton shower at leading logarithmic accuracy. This algorithm has been validated in a number of different processes; the results obtained with it are in surprising agreement with data and with other, analytic higher-order calculations. At this point it should be stressed that this algorithm is capable of reproducing non-trivial effects on the shapes of observables that are sensitive to next-to-leading order corrections in perturbative QCD. This allows, for the first time, to multiply SHERPA results with a flat, constant K-factor, such that non-trivial predictions accurate to next-to-leading order precision in the rate can be made. This clearly renders SHERPA a unique tool for the simulation of multi-jet events, which constitute one of the major backgrounds for experiments at Tevatron and the LHC.

Therefore, during this thesis, SHERPA has been extended such that it is now perfectly capable of simulating realistic events not only at electron-positron colliders but also at experiments with protons or anti-protons in the initial state. Thus, SHERPA seems well positioned, for tackling the new challenges provided by upcoming experiments at the LHC.

Appendix A Observables

A.1 Definitions of event shapes

The global properties of hadronic events may be characterised by a set of observables, usually called event shape observables. In this thesis, the following shape observables have been considered:

- Thrust T :
  The thrust axis $\boldsymbol{n}_T$ maximises the following quantity

  $$T = \max_{\boldsymbol{n}_T} \left(\frac{\sum_i |\boldsymbol{p}_i \cdot \boldsymbol{n}_T|}{\sum_i |\boldsymbol{p}_i|} \right) , \tag{A.1}$$

  where the sum extends over all final-state particles in the event. The thrust T tends to 1 for events that have two thin back-to-back jets ("pencil-like" event), and it tends towards 1/2 for perfectly isotropic events.

- Thrust Major T_{Major} :
  The thrust major vector $\boldsymbol{n}_{\text{Major}}$ is defined in the same way as the thrust vector, but with the additional condition that $\boldsymbol{n}_{\text{Major}}$ must lie in the plane perpendicular to $\boldsymbol{n}_T$:

  $$T_{\text{Major}} = \max_{\boldsymbol{n}_{\text{Major}} \perp \boldsymbol{n}_T} \left(\frac{\sum_i |\boldsymbol{p}_i \cdot \boldsymbol{n}_{\text{Major}}|}{\sum_i |\boldsymbol{p}_i|} \right) . \tag{A.2}$$

- Thrust Minor T_{Minor} :
  The minor axis is perpendicular to both the thrust axis and the major axis, $\boldsymbol{n}_{\text{Minor}} = \boldsymbol{n}_T \times \boldsymbol{n}_{\text{Major}}$. The value of thrust minor is then given by

  $$T_{\text{Minor}} = \frac{\sum_i |\boldsymbol{p}_i \cdot \boldsymbol{n}_{\text{Minor}}|}{\sum_i |\boldsymbol{p}_i|} . \tag{A.3}$$

- Oblateness O :
  The oblateness is defined as the difference between thrust major T_{Major} and thrust minor T_{Minor} :

  $$O = T_{\text{Major}} - T_{\text{Minor}} \tag{A.4}$$

- C-parameter C :
  The C-parameter is derived from the eigenvalues of the linearised momentum tensor $\Theta^{\alpha\beta}$, defined through

  $$\Theta^{\alpha\beta} = \frac{1}{\sum_i |\boldsymbol{p}_i|} \sum_i \frac{p_i^\alpha p_i^\beta}{|\boldsymbol{p}_i|} , \ \alpha, \beta = \{x, y, z\} . \tag{A.5}$$

The three eigenvalues λ_i of this tensor define C with

$$C = 3\,(\lambda_1\lambda_2 + \lambda_2\lambda_3 + \lambda_1\lambda_3)\,. \tag{A.6}$$

- D-parameter D :
  The D-parameter is also calculated from the eigenvalues of the linearised momentum tensor $\Theta^{\alpha\beta}$, cf. Eq. A.5. It is defined as

$$D = 27\,\lambda_1\lambda_2\lambda_3\,. \tag{A.7}$$

- Sphericity S :
  The sphericity is derived from the eigenvalues μ_i of the quadratic momentum tensor,

$$M^{\alpha\beta} = \frac{\sum_i p_i^\alpha p_i^\beta}{\sum_i |\boldsymbol{p}_i|^2}\,,\ \alpha,\beta = \{x,y,z\}\,. \tag{A.8}$$

  The eigenvalues are ordered according to $\mu_1 \geq \mu_2 \geq \mu_3$, then the sphericity is given by

$$S = \frac{3}{2}(\mu_2 + \mu_3)\,. \tag{A.9}$$

- Aplanarity A :
  The aplanarity is calculated from the third eigenvalue of the quadratic momentum tensor,

$$S = \frac{3}{2}\mu_3\,. \tag{A.10}$$

- Planarity P :
  The planarity is the difference between the second and the third eigenvalues of the quadratic momentum tensor,

$$P = \mu_2 - \mu_3\,. \tag{A.11}$$

- Wide Jet Broadening B_W :
  A plane through the origin and perpendicular to the thrust axis $\boldsymbol{n}_T$ divides the event into two hemispheres, H_1 and H_2. Then the broadening B_i of particles in transverse momentum with respect to the thrust axis is calculated for each hemisphere,

$$B_i = \frac{\sum_{k\in H_i} |\boldsymbol{p}_k \times \boldsymbol{n}_T|}{2\sum_j |\boldsymbol{p}_j|}\,,\ i = \{1,2\}\,, \tag{A.12}$$

  where j runs over all final-state particles in the event. The wide jet broadening is the larger of the two hemisphere broadenings,

$$B_W = \max(B_1, B_2) \tag{A.13}$$

- Narrow Jet Broadening B_N :
  The narrow jet broadening is the smaller of the two hemisphere broadenings,

$$B_N = \min(B_1, B_2) \tag{A.14}$$

- Total Jet Broadening B_T :
  The total jet broadening is the sum of the wide and the narrow jet broadening,

$$B_T = B_W + B_N \tag{A.15}$$

- Jet Broadening Difference B_D :
  The jet broadening difference is the difference of the wide and the narrow jet broadening,

$$B_D = B_W - B_N \tag{A.16}$$

- Heavy Jet Mass M_H :
  Similar to the definition of hemisphere broadening, each event is divided into two hemispheres, H_1 and H_2 by a plane perpendicular to the thrust axis. Then in each hemisphere, the invariant masses are defined by

$$M_i = \frac{1}{E_{vis}^2}\left(\sum_{k\in H_i} p_k\right)^2 , \; i = \{1,2\}\,, \tag{A.17}$$

  where E_{vis} is the total visible energy in the event. The larger of the two hemisphere masses is called the heavy jet mass,

$$M_H = \max(M_1, M_2)\,. \tag{A.18}$$

- Light Jet Mass M_L :
  On the other hand, the smaller of the two hemisphere masses is called light jet mass,

$$M_L = \min(M_1, M_2)\,. \tag{A.19}$$

- The jet mass difference is the difference between the heavy jet mass M_H and the light jet mass M_L,

$$M_D = M_H - M_L\,. \tag{A.20}$$

A.2 Topological structure of four-jet events

The topological structure of four-jet events is often investigated by the determination of four-jet angles. Therefore, the four-momenta of the jets in four-jet events are ordered by their energies, $E_1 \leq E_2 \leq E_3 \leq E_4$. Then, the following angles can be defined.

- The Bengtsson-Zerwas angle [118] is defined as the angle between the plane of the two high energy jets and the plane of the two low energy jets,

$$\cos\chi_{\mathrm{BZ}} = \frac{(\boldsymbol{p}_1 \times \boldsymbol{p}_2)\cdot(\boldsymbol{p}_3 \times \boldsymbol{p}_4)}{|\boldsymbol{p}_1 \times \boldsymbol{p}_2||\boldsymbol{p}_3 \times \boldsymbol{p}_4|}\,. \tag{A.21}$$

- The modified Nachtmann-Reiter angle [119] is the angle between the two difference vectors $(\boldsymbol{p}_1 - \boldsymbol{p}_2)$ and $(\boldsymbol{p}_3 - \boldsymbol{p}_4)$,

$$\cos\theta^*_{\mathrm{NR}} = \frac{(\boldsymbol{p}_1 - \boldsymbol{p}_2)\cdot(\boldsymbol{p}_3 - \boldsymbol{p}_4)}{|\boldsymbol{p}_1 - \boldsymbol{p}_2||\boldsymbol{p}_3 - \boldsymbol{p}_4|}\,. \tag{A.22}$$

- The Körner–Schierholz–Willrodt angle [129] is the mean value of the angle between the planes defined by jet 1 and jet 3, and jet 2 and jet 4, and the angle between the planes defined by jet 1 and jet 4, and jet 2 and jet 3,

$$\phi_{\mathrm{KSW}} = \left[\arccos\left(\frac{(\boldsymbol{p}_1 \times \boldsymbol{p}_3)\cdot(\boldsymbol{p}_2 \times \boldsymbol{p}_4)}{|\boldsymbol{p}_1 \times \boldsymbol{p}_3||\boldsymbol{p}_2 \times \boldsymbol{p}_4|}\right) + \arccos\left(\frac{(\boldsymbol{p}_1 \times \boldsymbol{p}_4)\cdot(\boldsymbol{p}_2 \times \boldsymbol{p}_3)}{|\boldsymbol{p}_1 \times \boldsymbol{p}_4||\boldsymbol{p}_2 \times \boldsymbol{p}_3|}\right)\right]\,. \tag{A.23}$$

- The angle α_{34} [130] is the angle between the two low energy jets,

$$\cos\alpha_{34} = \frac{\boldsymbol{p}_3 \cdot \boldsymbol{p}_4}{|\boldsymbol{p}_3||\boldsymbol{p}_4|} \tag{A.24}$$

Appendix B Parton shower details

B.1 Splitting kinematics

In the following, different possible definitions of the argument z of the splitting functions are considered. The aim is to justify the choice made in the implementation of the initial and final state shower, cf. Sec. 3.1, by showing that these definitions agree with the definition as light-cone momentum fraction in the limit of small virtualities.

B.1.1 Kinematics of the final state shower

Final state shower kinematics in terms of the light-cone momentum fraction α

Consider a time-like splitting of a massive parton with momentum p into two massless partons with momenta p_1 and p_2 as depicted in Fig. B.1. Using Sudakov notation the mother momentum can be decomposed as

$$\begin{aligned} p &= (p^+, p^-, \mathbf{0}) \\ &= (E + |\boldsymbol{p}|, E - |\boldsymbol{p}|, \mathbf{0}) \end{aligned} \tag{B.1}$$

fulfilling the relation

$$p^2 = p^+ p^- = t \; . \tag{B.2}$$

Consequently, the daughter momenta can be expressed in terms of $\pm$-components of the mother momentum, introducing α_i and β_i as corresponding light-cone momentum factions,

$$\begin{aligned} p_1 &= (p_1^+, p_1^-, \boldsymbol{k}_\perp) & p_2 &= (p_2^+, p_2^-, -\boldsymbol{k}_\perp) \\ &= (\alpha_1 p^+, \beta_1 p^-, \boldsymbol{k}_\perp) \; , & &= (\alpha_2 p^+, \beta_2 p^-, -\boldsymbol{k}_\perp) \; . \end{aligned} \tag{B.3}$$

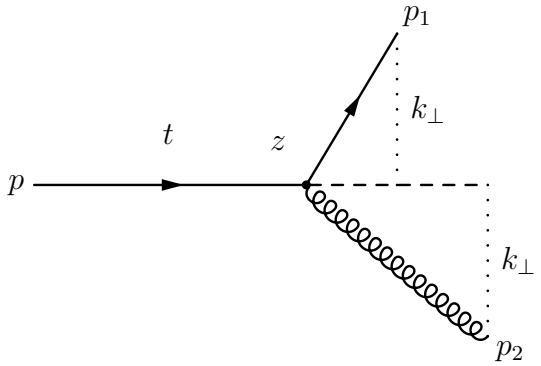

Figure B.1: Kinematics in a time-like parton splitting process.

Four momentum conservation translates into the conditions

$$\alpha_1 + \alpha_2 = 1 \,, \qquad \beta_1 + \beta_2 = 1 \,. \tag{B.4}$$

Employing the on-shell conditions for the daughter momenta p_1 and p_2,

$$\begin{aligned} {p_1}^2 &= p_1^+ p_1^- - {\boldsymbol{k}_\perp}^2 \\ &= \alpha_1 \beta_1 p^+ p^- - {\boldsymbol{k}_\perp}^2 = 0 \,, \end{aligned} \tag{B.5}$$

and

$$\begin{aligned} {p_2}^2 &= p_2^+ p_2^- - {\boldsymbol{k}_\perp}^2 \\ &= \alpha_2 \beta_2 p^+ p^- - {\boldsymbol{k}_\perp}^2 = 0 \,, \end{aligned} \tag{B.6}$$

the transverse momentum ${\boldsymbol{k}_\perp}^2$ can be expressed in terms of α_1 and t, leading to

$${\boldsymbol{k}_\perp}^2 = \alpha_1 \beta_1 t \,, \tag{B.7}$$

$$\begin{aligned} {\boldsymbol{k}_\perp}^2 &= \alpha_2 \beta_2 t \\ &= (1 - \alpha_1)(1 - \beta_1) t \\ &= (1 - \alpha_1)\Big(1 - \frac{{\boldsymbol{k}_\perp}^2}{\alpha_1 t}\Big) t \\ &= (1 - \alpha_1)\, t - \frac{1 - \alpha_1}{\alpha_1} {\boldsymbol{k}_\perp}^2 \,. \end{aligned} \tag{B.8}$$

Hence, their transverse momentum reads

$${\boldsymbol{k}_\perp}^2 = \alpha_1 (1 - \alpha_1)\, t \,. \tag{B.9}$$

This result can easily be extended to the case where p_1 and p_2 are massive, by taking into account that the on-shell condition now reads ${p_1}^2 = t_1$ and ${p_2}^2 = t_2$ in Eqs. (B.5) and (B.6). This leads to the well-known expression

$${\boldsymbol{k}_\perp}^2 = \alpha_1 (1 - \alpha_1)\, t - (1 - \alpha_1) t_1 - \alpha_1 t_2 \,. \tag{B.10}$$

Note that this result does not contain any approximation.

Final state shower kinematics in terms of the energy fraction z

Consider now the time-like splitting depicted in Fig. B.1 in the context of the final state shower. The mother parton is massive with a virtuality of $p^2 = t$, whereas the daughters are assumed to be massless. The argument of the splitting function is interpreted as energy fraction,

$$z = \frac{E_1}{E} \,. \tag{B.11}$$

The momenta obviously fulfil four-momentum conservation

$$E = E_1 + E_2 \,, \tag{B.12}$$

$$\boldsymbol{p} = \boldsymbol{p}_1 + \boldsymbol{p}_2 \,. \tag{B.13}$$

Putting momentum $\boldsymbol{p}$ on the z-axis enables the explicit determination of p_{z1} and $\boldsymbol{k}_\perp$. Starting with

$$\begin{aligned} p_2^2 &= (p - p_1)^2 = 0 \\ &= t - 2[EE_1 - p_z p_{z1}] \end{aligned} \tag{B.14}$$

the z-component of momentum p_1 is found to be

$$p_{z1} = \frac{2EE_1 - t}{2p_z} \,, \tag{B.15}$$

where p_z equals $|\boldsymbol{p}|$. Hence, the transverse momentum $\boldsymbol{k}_\perp$ can be easily determined using the energy-momentum relation

$$\begin{aligned} {\boldsymbol{k}_\perp}^2 &= {E_1}^2 - p_{z1}^2 \\ &= \frac{4tE_1E_2 - t^2}{4\boldsymbol{p}^2} \\ &= \frac{t(4E_1E_2 - t)}{4(E^2 - t)} \,. \end{aligned} \tag{B.16}$$

Inserting the definition of z as energy fraction, i.e. identifying $E_1 = zE$ and $E_2 = (1-z)E$ results in

$$\begin{aligned} {\boldsymbol{k}_\perp}^2 &= \frac{t(4E^2 z(1-z) - t)}{4(E^2 - t)} \\ &= z(1-z)t - \left(z - \tfrac{1}{2}\right)^2 \frac{t}{E^2 - t} \,. \end{aligned} \tag{B.17}$$

In the limit that $t \ll E^2$ this result coincides with the $p_\perp$ definition using the light-cone momentum fraction α_1, cf. Eq. (B.9). In case, the the daughter momenta have the virtualities t_1 and t_2, a similar expression can be achieved. It reads

$${\boldsymbol{k}_\perp}^2 = \frac{4E^2\big[z(1-z)t - zt_2 - (1-z)t_1\big] - \lambda^2(t, t_1, t_2)}{4(E^2 - t)} \tag{B.18}$$

where

$$\lambda^2(t, t_1, t_2) = (t - t_2 - t_1)^2 - 4t_1t_2 \,. \tag{B.19}$$

B.1.2 Kinematics of the initial state shower

Initial state shower kinematics in terms of the light-cone momentum fraction α

Here, a splitting of a massless parton with momentum p into two daughter partons with momenta p_1 and p_2 is considered. Parton p_1 is assumed to be one of the initiators of the hard subprocess, having a space-like virtuality t_1. Parton p is resolved from the incoming hadron, whereas parton p_2 is to be radiated off. The situation is schematically pictured in Fig. B.2.
When the momentum p is taken to be parallel to the z-axis, only the +-component of its light-cone momentum contributes. Therefore, it can conveniently be used in a basis for the

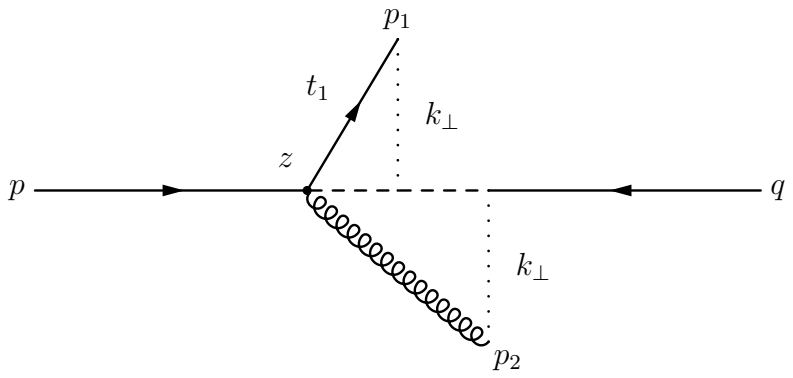

Figure B.2: Kinematics in a space-like parton splitting process.

decomposition into light-cone momenta. In addition, another light-like momentum q is defined, pointing into the direction opposite to p, which consequently exhibits a $-$-component only. The third basis vector $k_\perp$ is space-like, containing only a transverse momentum

$$\begin{aligned} p &= (p^+, 0, \mathbf{0}) \,, \\ q &= (0, q^-, \mathbf{0}) \,, \\ k_\perp &= (0, 0, \boldsymbol{k}_\perp) \,. \end{aligned} \tag{B.20}$$

The aim is to express the transverse momentum $\boldsymbol{k}_\perp$ in terms of the light-cone momentum fraction α and the virtuality t_1 of parton p_1. Using the decomposition

$$\begin{aligned} p_1 &= \alpha p + \beta q + k_\perp \,, \\ p_2 &= (1-\alpha) p - \beta q - k_\perp \,, \end{aligned} \tag{B.21}$$

of the momenta p_1 and p_2 into light-cone momenta p and q and using the on-shell conditions

$$p_1{}^2 = \alpha\beta\, pq - \boldsymbol{k}_\perp{}^2 = t_1 \,, \tag{B.22}$$

$$p_2{}^2 = -(1-\alpha)\beta\, pq - \boldsymbol{k}_\perp{}^2 = 0 \,, \tag{B.23}$$

a relation between α and β is obtained:

$$\beta = \frac{t_1 + \boldsymbol{k}_\perp{}^2}{\alpha\, pq} \,. \tag{B.24}$$

Hence, the transverse momentum is given by

$$\boldsymbol{k}_\perp{}^2 = -(1-\alpha)\, t_1 \,. \tag{B.25}$$

Note that the dependence on the momentum q cancels. Furthermore, the result agrees with Eq. (B.10), assuming that $t = t_2 = 0$.

Initial state shower kinematics in terms of the squared c.m. energy fraction z

In the initial state shower the argument of the splitting function z is interpreted as

$$z = \frac{(p+q)^2}{(p_1+q)^2} \tag{B.26}$$

with p_1 and q being the momenta of the initiators of the hard interaction, and p being the momenta of the mother of the splitting $p \to p_1 + p_2$, as depicted in Fig. B.2. This definition of z has the advantage of being boost invariant, on the other hand it has the drawback that the interpretation now depends on the partner momentum q, which is frame-dependent. For the determination of the transverse momentum it is convenient to examine the splitting process in the c.m. frame of p and q, where both momenta are parallel to the z-axis, and to assume that all considered momenta apart from p_1 are massless. With the definitions

$$s' = (p_1 + q)^2 \qquad\qquad s = \frac{s'}{z} = (p + q)^2 \tag{B.27}$$

the energies of partons p and q are found to be

$$E_p = E_q = \frac{\sqrt{s}}{2} \tag{B.28}$$

Starting from

$$t_1 = {p_1}^2 \tag{B.29}$$

and using ${p_1}^2 = (p - p_2)^2$ yields

$$\begin{aligned} t &= -2pp_2 \\ &= -2E(E_2 - p_{z2}) \end{aligned} \tag{B.30}$$

Similarly,

$$\begin{aligned} s' &= (p_1 + q)^2 \\ &= t_1 + 2p_1 q \\ &= t_1 + 2(E_1 + p_{z1})E \; . \end{aligned} \tag{B.31}$$

Using four-momentum conservation yields

$$\begin{aligned} E_1 + E_2 &= E \; , \\ p_{z1} + p_{z2} &= |\boldsymbol{p}| = E \; , \end{aligned} \tag{B.32}$$

Eqs. (B.30) and (B.31) can be used to explicitly determine the energy and the z-component of the partons p_1 momentum:

$$E_1 = \frac{s'}{4E} \; , \qquad\qquad p_{z1} = \frac{s' - 2t_1}{4E} \; . \tag{B.33}$$

Hence the transverse momentum reads

$$\begin{aligned} p_\perp^2 &= E_1^2 - p_{z1}^2 - t_1 \\ &= \frac{s'^2 - (s' - 2t_1)^2}{4s'} z - t_1 \\ &= -t_1(1 - z) - \frac{t_1^2}{s} \end{aligned} \tag{B.34}$$

Note that in the limit $t \ll s'$ this result agrees with Eq. (B.25).

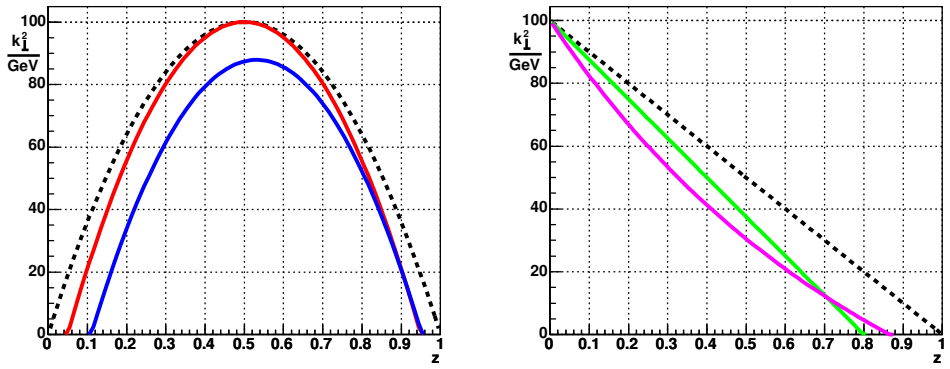

Figure B.3: Comparison of different $\boldsymbol{k}_\perp$ definitions.

In the case that all involved partons are massive, i.e. $p^2 = t$, ${p_1}^2 = t_1$, ${p_2}^2 = t_2$ and $q^2 = t_q$, the expression for the transverse momentum looks rather complicated. Here only the result is given,

$$\begin{aligned} p_\perp^2 = \frac{1}{4\boldsymbol{p}^2}\Big\{ & \left[-t_1\big(s+(t-t_q)\big) - tt_q\right](1-z) \\ & \left[-t_2\big(s-(t+t_q)\big) - t^2\right] z \\ & + ts\, z(1-z) \; - \left[t_1(t_1-t_2-2t) - t_2 t_q\right] \\ & - \frac{t_2(t-t_q)(t_1-t_q) + t_2^2 t_q)}{s}\Big\} \end{aligned} \tag{B.35}$$

with

$$\boldsymbol{p}^2 = \frac{(s-t-t_q)^2 - 4tt_q}{4s}\,. \tag{B.36}$$

In the limit that all virtualities $t, t_1, t_2, t_q \ll s$ Eq. (B.10) is again recovered.

B.2 The DGLAP evolution equation

In this section, the DGLAP evolution equation will be motivated and its connection with the Sudakov form factor will be discussed. To start with, consider the change of a parton distribution $f(x,t)$, where the resolution scale t is increased to $t+\delta t$. In this change, there is a loss and and a gain term. The latter is given by

$$\delta f_{\text{in}}(x,t) = \frac{\delta t}{t}\int_x^1 dx' dz \frac{\alpha_S}{2\pi} P(z) f(x',t)\delta(x-zx') \tag{B.37}$$

$$= \frac{\delta t}{t}\int_x^1 \frac{dz}{z}\frac{\alpha_S}{2\pi} P(z) f(x/z,t) \tag{B.38}$$

whereas the former term reads

$$\delta f_{\text{out}}(x,t) = \frac{\delta t}{t}\int_0^x dx' dz \frac{\alpha_S}{2\pi} P(z) f(x,t) \tag{B.39}$$

$$= \frac{\delta t}{t}\int_0^x dz \frac{\alpha_S}{2\pi} P(z) f(x,t) \tag{B.40}$$

Consequently, the evolution is governed by the DGLAP evolution equation

$$\frac{\partial}{\partial t} f(x,t) = \frac{1}{t}\int \frac{dz}{z}\frac{\alpha_S}{2\pi} P(z) f(x/z,t) - \frac{1}{t}\int dz \frac{\alpha_S}{2\pi} P(z) f(x,t) \tag{B.41}$$

Using the definition of the Sudakov form factor

$$\Delta(t) = \exp\left\{ -\int_{t_0}^{t_1} \frac{\mathrm{d}t}{t}\int \sum_{b,c} \mathrm{d}z \frac{\alpha_S(p_\perp)}{2\pi} P_{a\to bc}(z) \right\} , \tag{B.42}$$

the second term in the evolution equation can be rewritten, leading to

$$\frac{\partial}{\partial t} f(x,t) = \frac{1}{t}\int \frac{dz}{z}\frac{\alpha_S}{2\pi} P(z) f(x/z,t) + \frac{f(x,t)}{\Delta(t)}\frac{\partial}{\partial t}\Delta(t) \tag{B.43}$$

and finally to

$$\frac{\partial}{\partial t}\left(\frac{f(t,x)}{\Delta(t)}\right) = \frac{1}{t}\frac{1}{\Delta(t)}\int \frac{dz}{z}\frac{\alpha_S}{2\pi} P(z) f(x/z,t) \tag{B.44}$$

This equation can be integrated in the domain $[t_0 \dots t]$. Using the property $\Delta(t_0,t_0) = 1$ from the definition above, the result can be identified as the integral form of the DGLAP evolution equation. It is specially suited for the use in a Monte Carlo program.

The interpretation of the Sudakov form factor can be read off the integral form of the DGLAP evolution equation

$$f_a(x,t) = \Delta_a(t_0,t)\, f_a(x,t_0) + \int_{t_0}^{t} \frac{\mathrm{d}t'}{t'}\, \frac{\Delta_a(t_0,t)}{\Delta_a(t_0,t')}\, \frac{\alpha_s(t')}{2\pi} \sum_{b,c} \int_x^1 \frac{\mathrm{d}z}{z}\, P_{b\to ac}(z)\, f_b\left(\frac{x}{z},t'\right) \tag{B.45}$$

for the structure function $f_a(x,t)$. In this form, the evolution equation has a rather simple interpretation: The first term on the right hand side gives the contribution from paths in the x-t space that do not branch between the cutoff scale t_0 and the factorisation scale t, while the second term describes the contribution from one branching, which occurs at the scale t', where $t_0 \le t' \le t$. Due to the interpretation of the first term as being related with no branchings between two scales, the Sudakov form factor is interpreted as a no-branching probability. Its occurrence in the second term describing a splitting at some scale in addition exhibits how from ratios of Sudakov form factors the scales for the next branching can be determined.

Appendix C NLL jet rates

In this appendix, the discussion of section 4.1 is extended to the case of four-quark production, and the case of five-jet final states.

C.1 The differential four-quark rate

Starting with Eq. (4.4), the differential jet rate for the production of four quarks can be derived, reading

$$\begin{aligned}\frac{dR_4^{4q}(Q,Q_0)}{dq\,dq'} &= 2\left[\Delta_q(Q,Q_0)\right]^2\,\Gamma_q(q,Q)\,\Delta_g(q,Q_0)\,\Gamma_f(q')\,\Delta_f(q',Q_0)\\ &= \Gamma_q(q,Q)\,\Gamma_f(q')\,F_{q\bar{q}q\bar{q}}(Q,Q_0;q,q')\end{aligned} \tag{C.1}$$

C.2 The differential five-jet rate

The resummed differential and total jet rates for three- and four-jets have been stated explicitly in Sec. 4.1. Here the five-jet rate is considered, reading

$$
\begin{aligned}
R_5(Q,Q_0) = [\Delta_q(Q,Q_0)]^2 \Bigg\{ & \frac{4}{3} \int_{Q_0}^{Q} dq\, \Gamma_q(q,Q) \Delta_g(q,Q_0) \\
& \times \Bigg[\int_{Q_0}^{Q} dq\, \Gamma_q(q,Q) \Delta_g(q,Q_0) \int_{Q_0}^{Q} dq'\, \Gamma_q(q',Q) \Delta_g(q',Q_0) \\
& + 3 \int_{Q_0}^{Q} dq\, \Gamma_q(q,Q) \Delta_g(q,Q_0) \int_{Q_0}^{q} dq'\, \Gamma_g(q',q) \Delta_g(q',Q_0) \\
& + 3 \int_{Q_0}^{Q} dq\, \Gamma_q(q,Q) \Delta_g(q,Q_0) \int_{Q_0}^{q} dq'\, \Gamma_f(q') \Delta_f(q',Q_0) \Bigg] \\
& + \int_{Q_0}^{Q} dq\, \Gamma_q(q,Q) \Delta_g(q,Q_0) \\
& \times \Bigg[\int_{Q_0}^{q} dq'\, \Gamma_g(q',q) \Delta_g(q',Q_0) \int_{Q_0}^{q} dq''\, \Gamma_g(q'',q) \Delta_g(q'',Q_0) \\
& + 2 \int_{Q_0}^{q} dq'\, \Gamma_g(q',q) \Delta_g(q',Q_0) \int_{Q_0}^{q'} dq''\, \Gamma_g(q'',q') \Delta_g(q'',Q_0) \\
& + 4 \int_{Q_0}^{q} dq'\, \Gamma_g(q',q) \Delta_g(q',Q_0) \int_{Q_0}^{q'} dq''\, \Gamma_f(q'') \Delta_f(q'',Q_0) \\
& + 2 \int_{Q_0}^{q} dq'\, \Gamma_f(q') \Delta_f(q',Q_0) \\
& \times \int_{Q_0}^{q'} dq''\, [2\Gamma_q(q'',q') - \Gamma_g(q'',q') + \Gamma_g(q'',q)] \Delta_g(q'',Q_0) \Bigg] \Bigg\} .
\end{aligned}
\tag{C.2}
$$

In the following explicit expressions for the different parts of the five-jet rate are given.

The Abelian part of the $q\bar{q}3g$ final state reads

$$\begin{aligned}\frac{dR_5^A(Q,Q_0)}{dq\,dq'\,dq''} &= \frac{4}{3}\,\left[\Delta_q(Q,Q_0)\right]^2\,\Gamma_q(q,Q)\,\Delta_g(q,Q_0)\,\Gamma_q(q',Q)\,\Delta_g(q',Q_0)\\ &\quad\times\,\Gamma_q(q'',Q)\,\Delta_g(q'',Q_0)\\ &= \frac{4}{3}\,\Gamma_q(q,Q)\,\Gamma_q(q',Q)\,\Gamma_q(q'',Q)\,F_{q\bar{q}ggg}(Q,Q_0;q,q',q'')\,. \end{aligned}\tag{C.3}$$

The mixed non-Abelian and Abelian part is obtained through

$$\begin{aligned}\frac{dR_5^{A+NA}(Q,Q_0)}{dq\,dq'\,dq''} &= 4\,\left[\Delta_q(Q,Q_0)\right]^2\,\Gamma_q(q,Q)\,\Delta_g(q,Q_0)\,\Gamma_q(q',Q)\,\Delta_g(q',Q_0)\\ &\quad\times\,\Gamma_g(q'',q')\,\Delta_g(q'',Q_0)\\ &= 4\,\Gamma_q(q,Q)\,\Gamma_q(q',Q)\,\Gamma_g(q'',q')\,F_{q\bar{q}ggg}(Q,Q_0;q,q',q'')\,. \end{aligned}\tag{C.4}$$

The totally non-Abelian part of the differential five-jet rate with a $q\bar{q}3g$ final state can be divided into

$$\begin{aligned}\frac{dR_5^{NA1}(Q,Q_0)}{dq\,dq'\,dq''} &= \left[\Delta_q(Q,Q_0)\right]^2\,\Gamma_q(q,Q)\,\Delta_g(q,Q_0)\,\Gamma_g(q',q)\,\Delta_g(q',Q_0)\\ &\quad\times\,\Gamma_g(q'',q)\,\Delta_g(q'',Q_0)\\ &= \Gamma_q(q,Q)\,\Gamma_g(q',q)\,\Gamma_g(q'',q)\,F_{q\bar{q}ggg}(Q,Q_0;q,q',q'') \end{aligned}\tag{C.5}$$

and

$$\begin{aligned}\frac{dR_5^{NA2}(Q,Q_0)}{dq\,dq'\,dq''} &= 2\,\left[\Delta_q(Q,Q_0)\right]^2\,\Gamma_q(q,Q)\,\Delta_g(q,Q_0)\,\Gamma_g(q',q)\,\Delta_g(q',Q_0)\\ &\quad\times\,\Gamma_g(q'',q')\,\Delta_g(q'',Q_0)\\ &= 2\,\Gamma_q(q,Q)\,\Gamma_g(q',q)\,\Gamma_g(q'',q')\,F_{q\bar{q}ggg}(Q,Q_0;q,q',q'')\,. \end{aligned}\tag{C.6}$$

Again it can be observed that all parts can be divided into a number of integrated splitting functions and a unique factor:

$$F_{q\bar{q}ggg}(Q,Q_0;q,q',q'') = \left[\Delta_q(Q,Q_0)\right]^2\,\Delta_g(q,Q_0)\,\Delta_g(q',Q_0)\,.\tag{C.7}$$

The same considerations can be applied to the differential five-jet rate with a $q\bar{q}q\bar{q}g$ final state. The Abelian part is then

$$\begin{aligned}\frac{dR_5^{A-4qg}(Q,Q_0)}{dq\,dq'\,dq''} &= 4\,\left[\Delta_q(Q,Q_0)\right]^2\,\Gamma_q(q,Q)\,\Delta_g(q,Q_0)\,\Gamma_q(q',Q)\,\Delta_g(q',Q_0)\\ &\quad\times\,\Gamma_f(q'')\,\Delta_f(q'',Q_0)\\ &= 4\,\Gamma_q(q,Q)\,\Gamma_q(q',Q)\,\Gamma_f(q'')\,F_{q\bar{q}q\bar{q}g}(Q,Q_0;q,q',q'')\,, \end{aligned}\tag{C.8}$$

the first non-Abelian part results in

$$\begin{aligned}\frac{dR_5^{NA1-4qg}(Q,Q_0)}{dq\,dq'\,dq''} &= 4\,\left[\Delta_q(Q,Q_0)\right]^2\,\Gamma_q(q,Q)\,\Delta_g(q,Q_0)\,\Gamma_g(q',q)\,\Delta_g(q',Q_0)\\ &\quad\times\,\Gamma_f(q'')\,\Delta_f(q'',Q_0)\\ &= 4\,\Gamma_q(q,Q)\,\Gamma_g(q',q)\,\Gamma_f(q'')\,F_{q\bar{q}q\bar{q}g}(Q,Q_0;q,q',q'') \end{aligned}\tag{C.9}$$

and the second non-Abelian part is

$$\begin{aligned}\frac{dR_5^{NA2-4qg}(Q,Q_0)}{dq\,dq'\,dq''} &= 2\,\left[\Delta_q(Q,Q_0)\right]^2\,\Gamma_q(q,Q)\,\Delta_g(q,Q_0)\,\Gamma_f(q')\,\Delta_f(q',Q_0)\\ &\times\,\left[2\,\Gamma_q(q'',q') - \Gamma_g(q'',q') + \Gamma_g(q'',q)\right]\,\Delta_g(q'',Q_0)\\ &= 2\,\Gamma_q(q,Q)\,\Gamma_f(q')\,\left[2\,\Gamma_q(q'',q') - \Gamma_g(q'',q') + \Gamma_g(q'',q)\right]\\ &\times\,F_{q\bar{q}q\bar{q}g}(Q,Q_0;q,q',q'')\,. \end{aligned} \tag{C.10}$$

As before, a unique factor can be extracted:

$$F_{q\bar{q}q\bar{q}g}(Q,Q_0;q,q',q'') = \left[\Delta_q(Q,Q_0)\right]^2\,\Delta_g(q,Q_0)\,\Delta_g(q',Q_0)\,. \tag{C.11}$$

To summarise: All differential rates can be divided into a part with a sequence of integrated splitting functions (depending on the chosen Feynman diagram) and a unique factor which depends on the final state particles only.

Appendix D Brief program documentation

In this appendix the implementation of the algorithms described in the previous chapters is discussed.

D.1 The parton shower module APACIC++

`APACIC++` is the module responsible for parton showers inside the `SHERPA` framework. Therefore, basic physics tools, like e.g. four-momentum, PDFs, particle definitions, and the jet algorithm, are provided through the overall framework. Furthermore, a number of features related to the jet-veto are closely connected to the implementation of the merging procedure in `SHERPA`. Nevertheless, `APACIC++` could be employed by the framework of a different event generator, provided the basic physics tools are made available.

D.1.1 Implementation

This section focuses on the basic strategies according to which the formalism discussed in the section 3.1, is implemented in `APACIC++`. A detailed reference to all individual classes can be found in the subsequent sections.

The basic unit for the realisation of the parton shower in terms of a computer program is the individual branching of a single parton. Connecting such branchings automatically leads to the Markov structure of the full emission pattern. In other words, the task of a parton shower program is to fill and to connect such individual branchings. It is the strength of an object-oriented programming language like `C++` that it is well suited to map the underlying physical pictures onto program code by using an appropriate class structure.

Representation of the parton shower

Following the reasoning above, the basic structure representing a single branching is a `Knot`, reflecting the $a \to bc$ binary decay structure inherent to the parton shower. A `Knot` carries information on the incoming particle a, encoded in the class `Particle`, and on the `Knot`, where it originates from. When it is filled, i.e. when the decay is specified, it also yields the two offsprings and their respective decay `Knots`. In addition, a number of other quantities are stored in a `Knot`, namely

- the scale t_a,
- the energy splitting parameter z,

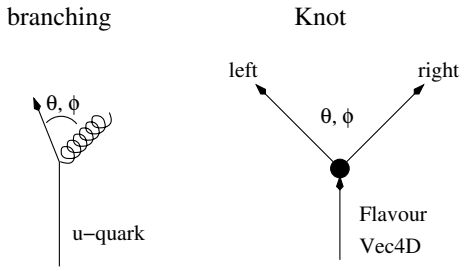

Figure D.1: The basic building blocks of shower emission are binary branchings, represented by `Knot`s.

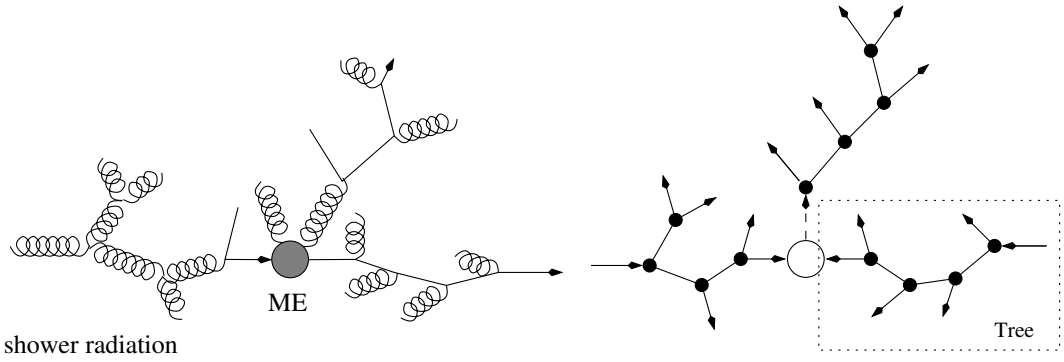

Figure D.2: Sketch of the mapping between radiation processes and the corresponding classes. The full radiation pattern is identified as a chain of $1 \to 2$ processes, a Markov chain, which translates into the class `Tree`. A `Tree` in turn is realised as a list of linked `Knot`s. The shower evolution of an event is represented by three `Tree`s, one for the final state shower, and two for the initial state shower.

- the squared energy, E_a^2,
- and its minimal virtuality $t_a^{(0)}$,
- the respective opening angle in the approximation of Eqs. (3.13, 3.27) θ_{bc},
- the azimuthal angle ϕ,
- and the Bjorken-x of the particle x_a (if needed).

These `Knot`s are then linked in terms of a (binary) Markov chain, represented in the class `Tree`. Each `Tree` contains a pointer to its first `Knot`, the root `Knot`[1]. Starting from this root `Knot`, all other `Knot`s are then accessible by successively following the pointer inside the `Knot`s, thereby spanning the full `Tree` structure. Each event consist of three `Tree`s, as indicated in Fig. D.2; one `Tree` gives rise to the complete final state shower, eventually with a dummy particle as root `Knot`. The other two `Tree`s represent the initial state showers from both sides, therefore they have one of the two particles entering the hardest subprocess as their respective root `Knot`. Since the full parton shower evolution is represented by these

[1]Since a parton shower history is reconstructed in the merging procedure, this root `Knot` may reflect the already fully defined splitting of an internal line of some matrix element.

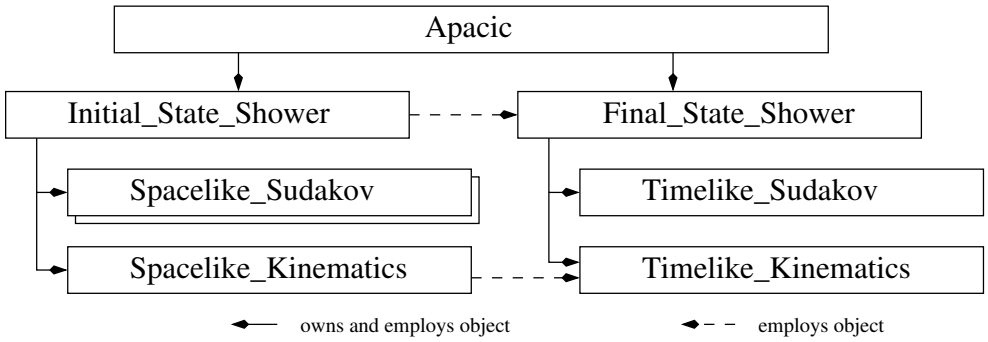

Figure D.3: Relation of the main classes of APACIC++.

Trees, they provide routines to create and delete individual Knots, or to boost and rotate the full structure. The latter option is relevant for the transparent implementation of the initial state parton shower.

Filling the Trees

The Trees are now to be filled by the corresponding parton shower. In APACIC++, two classes are responsible for this, namely the Final_State_Shower and the Initial_State_Shower, who have access to one or two Trees, respectively. Since the latter, the Initial_State_Shower, produces particles that may undergo a time-like shower evolution, it also has a pointer to the former, the Final_State_Shower. Apart from switches steering the specific way the shower works [2], however, both showers need information from Sudakov form factors and they have to construct the respective time-like or space-like kinematics. These necessities are encoded in corresponding classes, named Timelike_Sudakov or Spacelike_Sudakov, and Timelike_Kinematics or Spacelike_Kinematics. It is clear that the Spacelike_Kinematics must use methods from its time-like counterpart, hence it has a pointer to Timelike_Kinematics. Since the two Kinematics-classes are responsible for jet vetoes, they have a pointer to a Jet_Finder class made available through the SHERPA framework and some flags steering its proper usage. An overview over the basic relations between the main classes of APACIC++ is depicted in Fig. D.3.

In contrast to the Kinematics classes, the two Sudakov classes are a bit more intricate. Since most of their actions are related to the selection of splitting functions and their usage, both are derived from the class Splitting_Group, and contain a Splitting_Group for each flavour, the shower can handle. splitting functions $P_{a\to bc}(z)$ for all branchings allowed for a certain incoming particle a. As an example, consider the case of a gluon. It may undergo either a $g \to gg$ or a $g \to q\bar{q}$ branching, each of which is represented by its corresponding Splitting_Function. Consequently, the class Splitting_Group responsible for the gluon branching contains one Splitting_Function for the gluon final state and one for each quark flavour. Any individual Splitting_Function incorporates information like its incoming and outgoing flavours, an estimate for its integral over z, and methods to extract z distributed according to $P_{a\to bc}(z)$. In addition, Splitting_Groups allow to select a splitting mode and the corresponding flavours.

[2] There are some options for specific questions made available in APACIC++, that go beyond the standard settings discussed above.

The two Sudakov classes construct all such Splitting_Groups for physical branchings. When a parton, encoded in Knot is to be split, the respective Sudakov form factor implementation selects the physically relevant Splitting_Group, i.e. the one with the flavour of the parton as incoming or outgoing particle, and uses its estimated z integral to select a corresponding t [3]. Then vetos are applied, either in the procedure of the hit-or-miss method used in the Sudakov classes, or in the framework of the merging procedure to reject unwanted jets to be produced in the parton shower. The latter test is performed with the help of the corresponding Kinematics class. It should be noted that the Spacelike_Sudakov classes contain a PDF due to the backward evolution described above; in view of the possibility to have two different beam particles with different PDFs the class Initial_State_Shower has two of them.

This section gives a brief summary of the tasks each class in APACIC++ is responsible for. Where needed, some details on specific implementation issues are presented that should, in principle, enable the interested user to implement and test some of his or her own ideas. As stated above, in Sec. D.1.1, APACIC++ represents the evolving parton shower in terms of binary Trees, consisting of doubly linked Knots. Each of them represents one individual parton splitting. APACIC++ steers the shower evolution in the initial and final through two different classes, Initial_State_Shower and Final_State_Shower, respectively. These shower classes fill the Knots through corresponding Sudakov form factors, encoded in Timelike_Sudakov and Spacelike_Sudakov, where the latter carries a link to the appropriate PDF. Therefore, there are two instances of Spacelike_Sudakov with potentially different PDF in the Initial_State_Shower. For convenience, both Sudakov classes are derived from the class Splitting_Group; as such, they contain all relevant Splitting_Functions. However, both showers reconstruct the branching kinematics of each splitting from quantities like the scale t and the energy splitting parameter z. This is achieved in the two classes Timelike_Kinematics and Spacelike_Kinematics, respectively.

D.1.2 The interface with SHERPA

The class Apacic

This class defines the general interface to the shower package APACIC++. The parton shower evolution for a set of given partons is performed along the following steps:

- The parton shower of each event is started after setting appropriate initial conditions, taken from the merging with the matrix element. These initial conditions - basically starting scales t and maximal angles for the coherent shower evolution - are brought directly into the Trees by filling the pseudo parton shower history of the matrix elements into corresponding Knots. Pointers to the Trees needed for this operation are extracted from the showers and handed to the outside world through the methods FinTree() and IniTrees().

- By calling PerformShowers(), the corresponding methods in the class Final_State_Shower and in the class Initial_State_Shower are triggered to perform the shower evolution. All necessary boosts at the beginning and at the end of the shower[4] are

[3] Other information needed for this selection, like the start scale t_{start} and the maximally allowed angle θ_{crit} are obtained from the Knot.

[4] For instance, the final state shower is always performed in the rest frame of the particles starting it.

carried out in here. The methods `SetJetvetoPt2()` and `SetFactorisationScale()` are used to pass settings relevant for the parton shower piece of the merging into the showers. The check of whether a jet was lost during shower evolution is performed through `Final_State_Shower::ExtraJetCheck()`.

- The final result of the shower evolution can be transfered to the `SHERPA` frame work with the help of `ExtractPartons()`.

D.1.3 Running the showers

The class `Final_State_Shower`

This is the central class of the final state shower implementation. It controls the sequence of evolution steps[5]. For the individual shower evolution of a single parton the class `Timelike_Sudakov` is employed. Branching kinematics are constructed after the evolution has finished, using the class `Timelike_Kinematics`. It is also responsible for some kinematics checks during the shower evolution and for the jet veto.

The final state shower evolution of a given jet ensemble is performed by `PerformShower()`, while the method `FirstTimelikeFromSpacelike()` is called for the final state (time-like) shower of a parton emitted during the initial state (space-like) shower evolution.

The different methods of the class `Final_State_Shower` are responsible for the following tasks:

- The method `PerformShower()` initiates the final state shower on a given tree, i.e. starting from its root `Knot`. This is done in `InitializeJets()`, the kinematics are constructed afterwards utilising `TimelikeKinematics::DoKinematics()`.

- `InitializeJets()` initialises the jet system emerging from a given (dummy) mother knot. The algorithm is performed recursively along the following steps:

  1. If one or both of the two daughters are allowed to decay, the mother `Knot` is filled accordingly and the parton system produced by the decaying daughter(s) must be further evolved. These tasks are achieved by `FillBranch()` and `EvolveJet()`, respectively.
  2. If any the two daughters can not decay (internal lines of a ME), `InitializeJets()` is called again, with the daughter in question taking the role of the mother knot.

- To fill a branch, its splitting scale t and energy splitting variable z have to be determined. In `APACIC++`, this is realised through `FillBranch()`. There, a mother with parameters $\{t_a,\, z_a\}$ for a decay $a \to bc$ into two already specified massless daughters serves as input for the determination of their $\{t_i,\, z_i\}$ $(i = b,\, c)$.

  Step by step one of the daughters is chosen to obtain a new trial virtuality $\bar{t}_i$ according to Eq. (3.2), realised by `Timelike_Sudakov::Dice()`. In each step, the last $\bar{t}_i$ serves as starting condition for the determination of the new one. Only if the system of both daughters passes the kinematic constraints, this sequence of alternating reduction

[5]Note that the class `Final_State_Shower` is also utilised for the (time-like) evolution of any parton emitted off the initial state shower.

of the $\bar{t}_i$ is interrupted and they are accepted. Then, the mothers energy splitting variable z_a must be modified according to Eqs. (3.15, 3.33) implemented in `Timelike_Kinematics::Shuffle()` to compensate for the gain in virtuality of the daughters.

- `EvolveJet()` evolves a given parton system, consisting of a mother knot with two daughters. The algorithm works recursively: Both daughters may branch further, therefore `FillBranch()` is called first to determine both virtualities within the given kinematical constraints. In case neither of the daughters branches, the algorithm stops at once. Otherwise, `EvolveJet()` is called for the corresponding daughter(s).

- `FirstTimelikeFromSpacelike()` in contrast tries to initialise a new jet system emerging from a time-like particle emitted by a space-like shower. If, starting from the virtuality t_a of the space-like branch $b \to ac$, the `Timelike_Sudakov::Dice()` yields a suitable virtuality $t_c > t_0$ respecting the constraint Eq. (3.24), daughters are initialised and the jet is evolved by `EvolveJet()`.

- After the shower is completed, colours are set through the method `SetAllColours()` according to the algorithm described above. Then, the method `ExtractPartons()` extracts the partons (instances of the class `Particle` of the full framework) from the outgoing `Knot`s of the `Tree` and fills them into the event record.

The class `Initial_State_Shower`

The class `Initial_State_Shower` governs the space-like shower evolution. Starting with the particles entering the hard $2 \to 2$ piece of the process, a backward shower is performed with the help of the classes `Spacelike_Sudakov` (two objects, one for each beam) and `Spacelike_Kinematics`. For the treatment of time-like parton emissions the control is transfered to the class `Final_State_Shower`. The `Initial_State_Shower` object contains the following methods:

- `PerformShower()` is called in order to start the space-like shower evolution. Information one the matrix element kinematics is given in form of two partially filled trees, corresponding to the evolution of the left and the right incoming parton, respectively. Similar to the final state case, the shower is initiated by employing `InitializeSystem()`. After the evolution has finished some consistency checks are done, and the shower history is transfered back into the laboratory frame.

- `InitializeSystem()` determines the initial system for the shower evolution. The algorithm starts with calling `FillBranch()` for each of the given matrix element partons in order to obtain the virtuality t_i and energy fraction z_i of the first splittings. Then, the off-shell momenta are constructed with the help of `Spacelike_Kinematics::InitKinematics()`.

- Additional branchings are appended by `EvolveSystem()`. This methods performs the evolution of a given system of two space-like partons, by recursively appending additional branchings. In each step a system consisting two partons of different incoming beams. The shower evolution is performed backward, i.e. from the hard interaction towards the beam particle. The parton with larger virtuality is supposed to be closer to the hard interaction and is selected for the next evolution step. There, the virtuality t

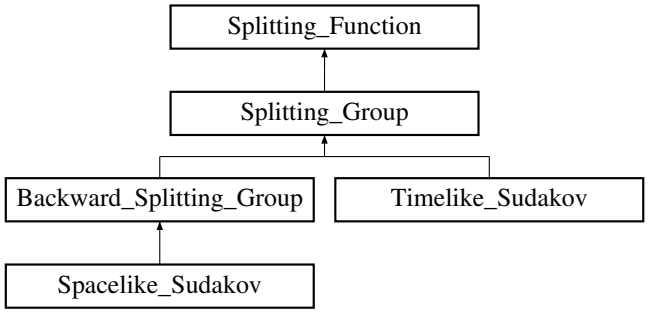

Figure D.4: class hierarchy

and energy fraction z is fixed by consecutive calls of `FillBranch()`, `CalculateMaxT()`, and `FirstTimelikeFromSpacelike()`. After each step, the four-momenta of the participating partons are evaluated with `DoKinematics()`, leading to a new system of two space-like partons.

- After the shower evolution is finished, the created parton set can be accessed by calling `ExtractPartons()`. It fills all final state particles connected to the two incoming `Trees` into the event record.

- Two configuration methods need to be mentioned, which are of special importance in the context of merging ME and PS, namely `SetJetvetoPt2()` and `SetFactorisationScale()`. In order to guarantee a clean separation between, the jet-veto is imposed on any trial emission inside the shower. Usually, the $p_\perp$ for any trial radiation is restricted by the jet resolution scale $p_\perp^{\text{cut}}$. For the matrix element with the highest multiplicity of jets, the separation cut is dynamically fixed by the smallest transverse momentum present in the hard interaction, owing to the fact that shower is not supposed to produce radiation harder than any QCD radiation present in the matrix element. In full analogy, merging ME and PS involves evaluating the PDFs at a specific factorisation scale μ_F. The dependence on the μ_F is to be cancelled by a corresponding PDF evaluation during the first parton emission in the initial state shower. The factorisation scale μ_F does not necessary coincide with the jet-veto scale mentioned above $p_\perp^{\text{cut}}$. For instance for (leptonically decaying) W bosons produced in hadronic collisions, there is no jet-veto applied, but of course μ_F is not vanishing. In fact, in this example case, the factorisation scale is identified with the hard c.m energy $\sqrt{s'}$.

D.1.4 Splitting functions & Sudakov form factors

The class `Splitting_Function`

The class `Splitting_Function` is purely virtual. It defines a common interface to the splitting functions $P_{a\to bc}(z)$. Among others, this class and its specific instantiations include methods to

- access its flavours (`GetFlA()`, `GetFlB()`, and `GetFlC()`)

- to determine z according to an approximative distribution (`GetZ()`), and its integral in a given region (`CrudeInt()`),
- a correction weight (`GetWeight()`), and the exact functional form of the splitting function through its `operator()`)
- and some methods to manage `Splitting_Groups`.

All implemented splitting functions are derived from this class, cf. Tab. D.5. This abstraction renders the inclusion of further splitting functions an easy task.

The class `Splitting_Group`

The class `Splitting_Group` is a container derived from the abstract class `Splitting_Function`. It contains all splitting functions of a given flavour, either in the forward splitting or for backward splitting as a `Backward_Splitting_Group` object. It is thus responsible for the determination of a branching for one specific flavour. The integration routine therefore returns the sum of the integrals of all single `Splitting_Functions`. After the integration the routine `SelectOne()` can be called to choose one splitting mode out of the available options according to the integrals. All subsequent calls to flavour access methods, dice routines or the weight calculation then correspond to the selected branching. Note that the `Splitting_Group` is also the base of any Sudakov form factor determination, as depicted in Fig. D.4.

The classes `Timelike_Sudakov` and `Spacelike_Sudakov`

Both Sudakov classes are derived from the corresponding `Splitting_Group`. Of course, in the space-like case, the mother class is the `Backward_Splitting_Group`. Following their names, the classes `Timelike_Sudakov` and `Spacelike_Sudakov` govern the time-like and space-like shower evolution, respectively. The latter one must be supplemented with a link to a PDF implementation, realised in `SHERPA` through an object derived from an abstract `PDF_Base`. However, both Sudakov classes store appropriate `Splitting_Groups` for every flavour taking part in the shower. In both classes, the method `Dice()` is responsible for the determination of virtualities (`ProduceT()`), daughter flavours, and energy fractions. The algorithm chosen is the hit-or-miss method, and both classes thus contain various veto methods implementing cuts and correction weights. To exemplify this, both classes have a method `CplVeto()` incorporating the correction weight $\alpha_s(Q)/\alpha_s(Q_{\min})$. Especially for the incorporation of issues related with coupling constants, both have a link to the class `Sudakov_Tools`.

D.1.5 Kinematics

The classes `Timelike_Kinematics` and `Spacelike_Kinematics`

Kinematics are implemented in two classes, `Timelike_Kinematics` and `Spacelike_Kinematics` for the determination of the kinematics in the final and initial state showers, respectively. They include

- checks whether a branching is kinematically possible (`KinCheck()`),

QED splitting functions	
`Fermion_To_Fermion_Photon`	$P_{f\to f\gamma}(z)$ cf. Eq. (D.1)
`Photon_Fermion_Fermion`	$P_{\gamma\to f\bar{f}}(z)$ cf. Eq. (D.2)
QCD splitting functions	
`Quark_To_Quark_Gluon`	$P_{q\to qg}(z)$ cf. Eq. (D.3)
`Gluon_To_Quark_Quark`	$P_{g\to q\bar{q}}(z)$ cf. Eq. (D.4)
`Gluon_To_Gluon_Gluon`	$P_{g\to gg}(z)$ cf. Eq. (D.5)
SUSY QCD splitting functions	
`Gluino_To_Gluino_Gluon`	$P_{\tilde{g}\to\tilde{g}g}(z)$ cf. Eq. (D.9)
`Gluon_To_Gluino_Gluino`	$P_{g\to\tilde{g}\tilde{g}}(z)$ cf. Eq. (D.10)
`SQuark_To_SQuark_Gluon`	$P_{\tilde{q}\to\tilde{q}g}(z)$ cf. Eq. (D.11)
`Gluon_To_SQuark_SQuark`	$P_{g\to\tilde{q}\bar{\tilde{q}}}(z)$ cf. Eq. (D.12)

Figure D.5: A summary of implemented splitting functions and their `class` names in `SHERPA`.

- a check whether an emission yields a jet that must be vetoed in the merging procedure (`JetVeto()`), and
- a method to construct kinematics (`DoKinematics()`).

In addition, `Timelike_Kinematics` provides a method to redefine the energy splitting z according to Eqs. (3.15, 3.33) (`Shuffle()`), and `Spacelike_Kinematics` has a method to determine the maximal kinematically allowed t for the initialisation of a final state shower off an initial state splitting (`CalculateMaxT()`), cf. Eq. (3.24)

D.1.6 Basic structures

The classes `Tree` and `Knot`

`Tree`s are used as representations of parton shower histories in terms of interconnected binary splittings. It provides the basic structure and all necessary routines to handle operations, like boosts, on the whole or parts of a tree. Three trees form a complete parton shower history: Two trees correspond to the initial state shower evolution of the right and the left incoming particle, respectively, and the other tree holds information of the final state shower of the outgoing particles, cf. Sec. D.1.1.

The `Knot`s are the basic elements forming a binary `Tree`. They store all properties of a single branching, like flavour, momentum, virtuality, energy component, etc..

D.1.7 Altarelli–Parisi splitting functions

In this section all splitting functions, relevant for the shower evolution of `APACIC++` are listed, cf. [189, 190]. The splitting functions are obtained after averaging over the azimuthal angle. The mass terms in each case are parametrised by the variable $\mu_{ij}^2 = (m_i^2 + m_j^2)/[(p_i + p_j)^2 - m_{(ij)}^2]$. The expressions for splittings with the decay products exchanged fulfil the obvious symmetry relation $P_{a\to bc}(z) = P_{a\to cb}(1-z)$.

Fermions and photons:

$$P_{f\to f\gamma}(z;\mu^2_{f\gamma}) = e_f^2\ \left[\frac{1+z^2}{1-z} - 2\mu^2_{f\gamma}\right]\ , \tag{D.1}$$

$$P_{\gamma\to f\bar{f}}(z;\mu^2_{f\bar{f}}) = e_f^2\ \left[z^2+(1-z)^2+\mu^2_{f\bar{f}}\right]\ . \tag{D.2}$$

Quarks and gluons:

$$P_{q\to qg}(z;\mu^2_{qg}) = C_F\ \left[\frac{1+z^2}{1-z} - 2\mu^2_{qg}\right]\ , \tag{D.3}$$

$$P_{g\to q\bar{q}}(z;\mu^2_{q\bar{q}}) = T_R\ \left[z^2+(1-z)^2+\mu^2_{q\bar{q}}\right]\ , \tag{D.4}$$

$$P_{g\to gg}(z) = C_A\ \left[\frac{z}{1-z} + \frac{1-z}{z} + z(1-z)\right]\ . \tag{D.5}$$

In the massless limit ($\mu \to 0$), these splitting functions reduce to the well-known form

$$P_{qq}(z) = C_F\,\frac{1+z^2}{1-z}\ , \tag{D.6}$$

$$P_{gq}(z) = T_R\ \left[z^2+(1-z)^2\right]\ , \tag{D.7}$$

$$P_{gg}(z) = C_A\ \left[\frac{z}{1-z} + \frac{1-z}{z} + z(1-z)\right]\ . \tag{D.8}$$

Gluinos and gluons:

$$P_{\tilde{g}\to\tilde{g}g}(z;\mu^2_{\tilde{g}g}) = C_A\ \left[\frac{1+z^2}{1-z} - 2\mu^2_{\tilde{g}g}\right]\ , \tag{D.9}$$

$$P_{g\to\tilde{g}\tilde{g}}(z;\mu^2_{\tilde{g}\tilde{g}}) = C_A\ \left[z^2+(1-z)^2+\mu^2_{\tilde{g}\tilde{g}}\right]\ . \tag{D.10}$$

Squarks and gluons:

$$P_{\tilde{q}\to\tilde{q}g}(z;\mu^2_{\tilde{q}g}) = C_F\ \left[\frac{2z}{1-z} - 2\mu^2_{\tilde{q}g}\right]\ , \tag{D.11}$$

$$P_{g\to\tilde{q}\bar{\tilde{q}}}(z;\mu^2_{\tilde{q}\bar{\tilde{q}}}) = T_R\,\frac{1}{2}\left[2z(1-z) - \mu^2_{\tilde{q}\bar{\tilde{q}}}\right]\ . \tag{D.12}$$

D.2 The merging module

The module, in which the merging algorithm is implemented, is an integral part of the SHERPA framework. It is situated inside the main module SHERPA, and it employs SHERPAs basic physics tools, e.g., four-momenta, parton distribution functions, and jet algorithms. Of course, in its present form it has many connections to specific features of SHERPAs matrix element generator AMEGIC++ and its parton shower module APACIC++. An extension to other matrix element generators or parton showers, however, is straightforward.
This section gives a brief overview over the classes responsible for the merging and their specific tasks within the algorithm. Where needed, details on specific implementation issues are presented that should, in principle, enable the interested user to implement and test some of his or her own ideas.

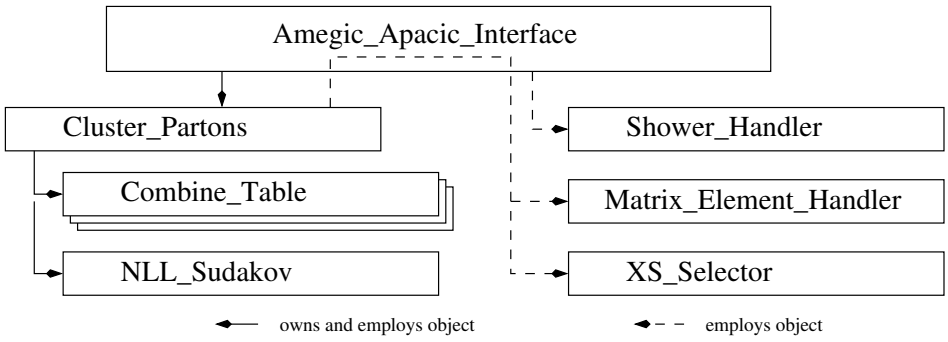

Figure D.6: Ownership of the main classes responsible for the merging of ME and PS.

D.2.1 Implementation

The basic algorithmic steps underlying the realisation of the merging algorithm in SHERPA can be summarised in the following way:

1. First of all, the pseudo parton shower history is reconstructed. To simplify the presentation, the focus here is on the implementation of the original approach only. Modifications to the extension described above can be found in the detailed description of the individual classes.

   - Take all Feynman diagrams with a binary tree structure, i.e. those that contain vertices with three legs only. For a given $2 \to n$ process the resulting structure will have $n + 2$ external particles. In AMEGIC++, this doubly linked binary tree structure is represented through the class Point, each Point contains pointers to its predecessor and offsprings. In the merging procedure the Points of each Feynman diagram that correspond to an external particle are translated into a Leg. The merging is performed in terms of the Legs, which ensures that the underlying Feynman diagram structure is not modified through the algorithms[6].
   - Test all pairs of external particles, i.e. Legs. In the original version of the merging algorithm, for each allowed pair the relative transverse momentum according to the $k_\perp$-algorithm is calculated. Pairings which do not correspond to a junction in the Feynman diagrams, are discarded. Each allowed pairing is stored in a table, conveniently represented as a class Combine_Table, together with the list of diagrams where it occurs and with the $k_\perp$ value. Each Combine_Table has pointers to the previous one and its successor, i.e. to a Combine_Table with one Leg more, and to another one, with one Leg less.
   - In this Combine_Table the pairing with the smallest $k_\perp$ is selected. Their common predecessor is obtained from the first Feynman diagram(s) - in the original approach, the flavour of it is an unique choice anyhow. Its four-momentum is the

[6]Of course, any other matrix element generator with an internal representation of Feynman diagrams through doubly linked binary trees can easily be treated in the same way. If such a binary tree structure does not exist, it must be provided.

sum of the two momenta of its offsprings, taken together this fully defines the intermediate particle, i.e. the corresponding `Leg`. It replaces the two offsprings and it is used for the next round of clustering, operating on a duly reduced number of `Leg`s. All diagrams that did not contain the selected splitting are discarded in the further procedure.

- The procedure terminates as soon as a splitting results in a structure with four external legs, i.e. a $2 \to 2$ process.

2. The Sudakov weight for the selected configuration is evaluated.

   - The starting point is the core $2 \to 2$ process. Its hard scale Q_h is defined though the colour structure; in case there are different competing colour structures the winner is selected according to the relative weights. The details of this are implemented in an extra module of `SHERPA`, basically a library of $2 \to 2$ processes called EXTRA_XS. It incorporates the processes as realisations of an abstract base class, `XS_Base`, the relevant one is chosen through an `XS_Selector`.

     In addition, the $2 \to 2$ process determines the scale for the coupling weight, $Q_{\rm QCD}$. Then, however, this core process may result in a factor of

     $$[\alpha_S(Q_{\rm QCD})/\alpha_S(Q_{\rm cut})]^m \ , \tag{D.13}$$

     where m is the number of strong interactions in the core process. In most cases, these two scales are identical, exceptions are, for instance, the process $e^+e^- \to q\bar{q}$, which for sure has no strong interaction, and therefore no scale $Q_{\rm QCD}$, cf. Sec. 4.2. At that point, each `Leg` is associated with a value $Q_1 = Q_h$

   - The previous `Combine_Table` "unclusters" one of the particles and yields the corresponding nodal $k_\perp$ measure, Q_2. If the decay of this particle proceeds through the strong interaction, the weight is multiplied by

     $$[\alpha_S(Q_2)/\alpha_S(Q_{\rm cut})] \ . \tag{D.14}$$

     If the decaying particle a is strongly interacting, a Sudakov weight is attached, namely

     $$[\Delta_a(Q_1, Q_{\rm cut})/\Delta_a(Q_2, Q_{\rm cut})] \ , \tag{D.15}$$

     where Q_1 is the nodal value of the previous iteration step for this particle, i.e. the $k_\perp$ measure associated to the vertex, where it stems from. Then, for the two offsprings produced in the decay, their production scale is identified as $Q_1 = Q_2$.

   - If no previous `Combine_Table` exists, there is no decaying particle left, and all `Leg`s are external. Then, each `Leg` with strong quantum numbers results in a factor

     $$\Delta_a(Q_1, Q_{\rm cut}) \tag{D.16}$$

     attached to the Sudakov weight.

3. If the event is accepted after the Sudakov weight, the parton shower has to be attached. For this, the binary tree structure of the `Point`s is translated to the `Tree` structure of `APACIC++`. `APACIC++`, however, does not order its shower in terms of transverse momenta. Instead it employs an ordering by virtuality. Therefore, for each particle, the virtual mass of its production vertex is identified and used as the starting scale of the parton shower evolution. Again, this is easily accomplished by just following the `Combine_Table`, starting from the core process[7].

D.2.2 Steering

The class `Amegic_Apacic_Interface`

is the central interface class, steering the various steps of the merging procedure. It is derived from the abstract class `Perturbative_Interface`. Each `Perturbative_Interface` owns pointers to a `Shower_Handler` and to a `Matrix_Element_Handler`, which provide access to the internal structure of the parton shower and to the matrix elements, respectively. In principle, other shower algorithms or another matrix element treatment can easily be connected to the `SHERPA` framework - from `SHERPA`s point of view merely the two handler classes (the `Shower_Handler` and the `Matrix_Element_Handler`) would have to be suitably extended, and a corresponding interface of the type `ME_PS_Interface` would have to be constructed.
The `Amegic_Apacic_Interface` is used through consecutive calls to the following methods.

- `DefineInitialConditions()`
  performs all steps necessary in order to construct a pseudo parton shower history and its corresponding weight, to accept or reject this configuration, and, eventually, to initialise the parton shower. In particular for the first task, it heavily relies on the helper class `Cluster_Partons`, presented below. Depending on the success of the procedure, the integer return value of this method is "0", "1" or "3" indicating a rejected event, an accepted event, or a rejected event after the *lose-jet-veto*, respectively.

  `DefineInitialConditions()` executes the following steps:

  1. Cluster the matrix element configuration to a $2 \to 2$ core process by calling `ClusterConfiguration()`.
  2. Determine the starting scale and colour connections of this core process with the help of an `XS_Base` from the EXTRA_XS library. The corresponding process is selected through a call of `Cluster_Partons::GetXS()`.
  3. Evaluate the NLL Sudakov weight used for reweighting the ME kinematics through `Cluster_Partons::CalculateWeight()`. Accept or reject the configuration accordingly.
  4. If accepted initialise the parton shower evolution by employing `Cluster_Partons::FillTrees()`.

- `ClusterConfiguration()`
  is used to obtain a pseudo parton shower history. The clustering actually is achieved in

[7] Any other parton shower algorithm can be used in a similar fashion, even when it is operating in terms of dipoles.

the helper class, through the method `Cluster_Partons::ClusterConfiguration()`. This method merely forms an intelligent wrapper around it, and it prepares merging `Blob`s of the type "ME PS Interface". These `Blob`s are used to translate the on-shell partons from the matrix element into the off-shell partons experiencing the parton shower. Therefore they are filled after the parton shower evolution. The latter is triggered by

- `PerformShowers()`,
  which calls the appropriate routine in the `Shower_Hander`. The jet-veto scale and the renormalisation scale, which have been determined in the merging procedure before[8], are handed over to the parton shower, also through the `Shower_Hander`. If the shower evolution was successful,

- `FillBlobs()`
  inserts the prepared and filled "ME PS Interface" and the shower `Blob`s into the event record.

Apart from `ClusterConfiguration()`, which is obsolete for instance for $2 \to 2$ processes, these general methods have to be provided by any realisation of a `Perturbative_Interface`.

The class `Cluster_Partons`

is the class central to the implementation of the merging algorithm. It has three main routines, and a number of helper methods, which will be discussed in the following:

- `ClusterConfiguration()`
  is the method that clusters a given $2 \to n$ process until a $2 \to 2$ core process remains. In so doing, it creates a history of successive emissions, each of which is associated with a specific emission scale, the nodal value of the respective clustering. The algorithm for the clustering implemented here proceeds as follows:

  1. All possible Feynman graphs are iterated over. In `AMEGIC++`, a diagram consists of a doubly linked tree of `Point`s. They represent vertices, whereas the links are the propagating particles. Also, the external particles of each diagram are represented as `Point`s, but with all but one of the links empty. The number of diagrams and these `Point` structures themselves are accessible through the methods `Matrix_Element_Handler::NumberOfDiagrams()` and `Matrix_Element_Handler::GetDiagram()`, respectively. However, the external particles of each diagram, both incoming and outgoing are translated into `Leg`s, on which the actual clustering is performed without disturbing the `Point`s underneath.
  2. These first `Leg`s and their four-momenta are stored in a `Combine_Table`. Ultimately, it is this class, which, step by step, clusters two particles, i.e. `Leg`s into an intermediate particle, i.e. `Leg`. Its four-momentum in due course will be given by the appropriate combination of the two incident particles. As a result of this particular step, a new `Combine_Table` emerges with the number of `Leg`s diminished by one, which is linked to the previous one.

[8] Remember, they may change because of, e.g., the highest multiplicity treatment described in Sec. 4.2.

Having thus filled the first `Combine_Table` through its method `FillTable`, the list of all emerging `Combine_Table`s is constructed by calling `CalcJet()` of the fist one.

- `GetXS()`
  identifies the hard $2 \to 2$ core process. In particular, it determines the colour structure of it, and the relevant hard scale(s). The preferred way to carry out this task is to employ an internal library of analytical $2 \to 2$ processes provided by the module EXTRA_XS. An implemented cross section calculator can be obtained by `XS_Selector::GetXS()`, selecting the process in question through the flavours of its external particles. The cross section calculator is realised as an `XS_Base`, and it has suitable routines available for selecting colour connections (`XS_Base::SetColours()`) and for retrieving a renormalisation scale (`XS_Base::Scale()`).

  An alternative solution exists for those processes which are not implemented yet but for which the colour connections are unambiguously defined. This is actually always the case if the number of strongly interacting particle involved is smaller than four. Then, the colour connections are explicitely constructed, using the routine `Cluster_Partons::SetColours()`. In this case the hard scale reads

$$Q^2_{\rm hard} = \begin{cases} p_\perp^2 + p_3^2 + p_4^2 & \text{if initial and final state are colour connected, and} \\ (p_1+p_2)^2 & \text{if there is no colour connection between initial and final state,} \end{cases} \tag{D.17}$$

  with p_1/p_2 and p_3/p_4 denoting the four-momenta of the incoming and outgoing particles, respectively. In case there are 3 coloured particles involved in the hard process, a scale for the evaluation of the strong coupling has to be determined too, which is identified with the transverse momentum $p_\perp$ of the outgoing coloured particle.

- `CalculateWeight()`
  follows the previously obtained history and calculates from it the corresponding Sudakov weight according to the merging prescription described above. For this, the nodal values Q_i determined before in `ClusterConfiguration()` are employed. The start scale for the Sudakov weight Q_h and the scale $Q_{\rm QCD}$ for possible α_S factors have been prepared by `GetXS()`/`SetColours()`, see above.

  The construction of the weight starts with the core $2 \to 2$ process. Hence, the first part of the weight is given by a factor $(\alpha_S(Q_{\rm QCD})/\alpha_S(Q_{\rm cut}))^m$, with m specifying the number of strong couplings involved in the hard process. The clustering is followed backward through the sequence of `Combine_Table`s, adding a factor

$$w = \frac{\Delta(Q_i, Q_{\rm cut})}{\Delta(Q_j, Q_{\rm cut})} \frac{\alpha_S(Q_j)}{\alpha_S(Q_{\rm cut})}\,, \tag{D.18}$$

  for each internal line constructed during the backward clustering. The Sudakov form factors $\Delta(Q_i, Q_{\rm cut})$ are provided by the method `Delta()` of the class `NLL_Sudakov`. The algorithm ends with a factor as $\Delta(Q_i, Q_{\rm cut})$ for any dangling coloured particle,

with possible another coupling weight in case of the extended merging algorithm (see Sec. 4.2)[9].

- `FillTrees()`
  translates the pseudo parton shower history into the `Tree` structures, which `APACIC++` uses to represent the parton shower. This history includes the starting scales of the shower evolution of each parton and possible constraints on shower emissions such as, e.g., opening angles determined from colour connections of the partons. The `Knot`s forming the `Tree` are taken from the pseudo parton shower through `Point2Knot()`, the mutual relations are constructed through `EstablishRelations()`.

- `EstablishRelations()`
  builds a tree by creating mutual links between a given set of three `Knot`s. At each step, the actual `Tree` represents a partially performed shower. For the mutual relations, three cases are distinguished

  1. two incoming partons from the hard $2 \to 2$ process:
     the energy fractions x_1 and x_2 are filled from the information in the `Combine_Table`.
  2. two outgoing partons from a common mother:
     The two final state particles are initialised using `Final_State_Shower::EstablishRelations()`. There, the more energetic parton is initialised with the angle and virtuality of the mother, the less energetic parton is initialised with angle and virtuality of the current branch.
  3. one incoming parton, its mother and its sister:
     The incoming parton, its mother and its sister are initialised using `Initial_State_Shower::SetColours()`. Note, angle conditions inside the shower are fixed only during shower evolution. The starting scale of the shower is given by the virtual mass of the mother due to `APACIC++`s shower evolution in terms of virtualities.

- `DetermineColourAngles()`
  determines the maximum angle between colour connected partons of a hard $2 \to 2$ process. These angles are used in the explicit angular vetoes of the parton shower.

  For initial state particles the colour angle is determined in the lab frame after a boost along the z-axis, whereas starting angles for the final state system are determined in its c.m. frame. The starting angles are stored in the variable *"thcrit"* of each knot.

A number of simple access methods make the result of the clustering process available to the interface class `Amegic_Apacic_Interface`.

- `Weight()` returns the weight calculated in `CalculateWeight()`.
- `Scale()` returns the hardest scale (of the core process) as determined in `SetColours()`.
- `AsScale()` returns the scale associated with the strong coupling in the core process as determined in `SetColours()`.

[9]Note that the treatment of matrix element events with a maximal number of outgoing particles is slightly modified, however, the general algorithm remains the same.

- `Flav()` provides the flavours of the core $2 \to 2$ process.
- `Momentum()` returns the momenta of the core $2 \to 2$ process.

D.2.3 Clustering

The class `Combine_Table`

provides the structure for storing histories of successive clusterings. The structure fills itself recursively, with the only input being the Feynman diagrams of the process under consideration and the four-momenta of the current event.
Each `Combine_Table` consists of a list of possible clusterings (particles i, j and the flavour of the resulting intermediate particle) and the $k_\perp$ values and Feynman diagrams associated with them. These informations are realised through the classes `Combine_Key` and `Combine_Data`, see below. In addition, a number of methods allows a `Combine_Table` to create these data and to construct the sequence of `Combine_Table`s representing the clustering history:

- `FillTable()`
  has two tasks to fulfil. First of all, a set of given `Leg`s, i.e. particles, are filled into the table. Then, all pairs of them are checked whether they can be clustered. A clustering is possible only, if it occurs in a corresponding Feynman diagram, which disables unphysical parton histories. This check is performed through the method `Combinable()`, see below.

- `CalcJet()`
  evaluates the $k_\perp$ distance of all allowed parton pairs (i,j) created by `FillTable()` with the `Jet_Finder`. After that, a pair to be clustered is selected according to the merging prescription, and a new `Combine_Table` is constructed, where the number of `Leg`s is reduced by one. Consequently, after each clustering step, the set of Feynman diagrams is pruned, to include only those where the selected combination is possible. The four-momentum of the new (joined) `Leg` is given by the corresponding combination of the two individual four momenta. The algorithm continues recursively with corresponding calls to `FillTable()` and `CalcJet()` until only a $2 \to 2$ process remains.

- `CalcPropagator()`
  performs all basic calculations for the determination of cluster probability for a given pair (i,j). This usually includes the evaluation of the $k_\perp$ measure, and the invariant mass s_{ij}. In case of the extended clustering algorithm, an estimate for the branching probability is also computed, which includes the couplings of that branching process, as well as the corresponding propagator. The couplings are available in the Feynman diagrams provided by `AMEGIC++`.

- `Combinable`
  determines whether two particles, i.e. `Leg`s can be clustered. To this end, the two `Point`s related to the `Leg`s are checked whether they have a common third `Point`, i.e. vertex, linked to them.

To exemplify the description above, consider the representation of a `Combine_Table` below.

$i\&j$	y_{ij}	*graphs*	*down* link to the next table
0&2	0.0810366	2,3,4,5,8	
0&4	0.0691623	6,7	→ `Combine_Table` 2
1&3	0.0844243	0,1,6,7,8	
1&4	0.293399	4,5	
2&4	0.111385	0,1	
3&4	0.215127	2,3	

For each combination (i,j) a $k_\perp$ measure y_{ij} and a list of contributing Feynman *graphs* is stored. For the winner combination a *down* link to a subsequent `Combine_Table` is provided. In addition the `Combine_Table` contains a list of four-momenta of the current configuration, and a matrix of all dangling legs (one row for each graph), as well as a reference to the winner combination (i,j), and an *up*-link to the table with one combination less performed. In case the extended merging algorithm is applied, the `Combine_Table` also has to include further information needed for the winner determination: the virtuality of the resulting propagator s_{ij}, the estimate of the propagator *prop*, and the *coupling* of the corresponding vertices.

The class `Leg`

represents a particle dangling from a Feynman diagram. It stores all information of a `AMEGIC::Point` and an extra "anti"-flag.
Since `AMEGIC::Point` is the basic component of a Feynman graph representation in `AMEGIC++`, it can be conveniently used in the clustering process to determine possible combinations and resulting propagators. The additional *anti*-flag helps to keep track of charge conjugations during the clustering process. In order to access all information of a `Point` more easily the `operator->` is overloaded. [10]

The class `Combine_Key`

is one of the basic elements for the creation of a `Combine_Table`. It includes the numbers of combinable legs (i and j) and the flavour of the resulting propagator. It is used as a key in a fast access map in `Combine_Table` in order to access the information placed in a `Combine_Data` object.

The class `Combine_Data`

is the basic element for the determination of clustering when using a `Combine_Table`. It includes the distance of two legs i and j according to a $k_\perp$ measure (y_{ij}), a list of numbers of graphs where this combination is possible (*graphs*) and a link to the new table where those legs have been combined (*down*).
In case the extended merging algorithm is active, additional information is included, namely: the virtuality of the resulting propagator s_{ij}, the estimate of the propagator *prop*, and the *coupling* of the corresponding vertices.

[10] The overloaded `operator->` can sometimes lead to confusion, especially the *anti* flag can not be accessed via this operator in case a pointer to a leg is used. In this case the `operator*` together with the dot has to be used. So always think `Leg` as a synonym for `Point*`.

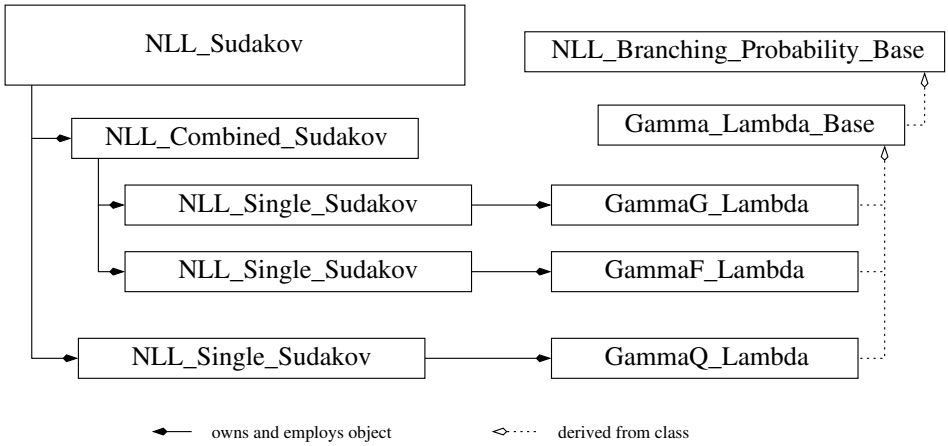

Figure D.7: Ownership and inheritance diagram of the main classes related to the numerical evaluation of NLL Sudakov form factors. The sketch corresponds to the status after the initialisation via `NLL_Sudakov::PrepareMap()`.

D.2.4 Weighting

The class `NLL_Sudakov`

provides the numerical values for the Sudakov form factors used in the merging procedure of parton shower and matrix elements. Consequently, the main routine is `Delta(const ATOOLS::Flavour &)`, which returns the Sudakov form factor for a given flavour. A corresponding table of Sudakov form factor objects for all possible flavours is created by respective calls to `PrepareMap()` or `PrepareMassiveMap()`.
In the following a short description of the individual methods of this class is given.

- `Delta (const ATOOLS::Flavour &)`
  is the main access method to NLL Sudakov form factors. It returns the appropriate NLL Sudakov form factor (in form of a `NLL_Sudakov_Base` object) for any given flavour. For not strongly interacting particles a reference to a `NLL_Dummy_Sudakov` object is provided.

  For instance, a typical call to determine the numerical value of the gluon Sudakov form factor at a scale Q with a jet resolution scale Q_0 would look like

  ```
  double  dg = sud.Delta(Flavour(kf::gluon))(Q,Q0);
  ```

- `PrepareMap()`
  initialises a map with all massless Sudakov form factors needed in the Standard Model. In so doing, a Sudakov form factor (cf. `NLL_Single_Sudakov` and `NLL_Combined_Sudakov`) is initialised for each strongly interacting flavour (d-, u-, s-, c-, b-quark or anti-quark, and gluon) and put into a map for fast access. For the sake of completeness, a `NLL_Dummy_Sudakov` (always one) is added to the map, which will be returned for any

flavour without a dedicated Sudakov form factor[11]. The default massless integrated splitting functions used for the evaluation of the Sudakov form factors are `GammaQ_Lambda`, `GammaG_Lambda`, and `GammaF_Lambda`.

- `PrepareMassiveMap()`
  initialises a map with all massive Sudakov form factors. This method is very similar to `PrepareMap()`. However, using the massive version of Sudakov form factors necessitates the initialisation of a `NLL_Single_Sudakov` for each flavour ($d-$, $u-$, $s-$, $c-$, $b-$quark) individually being now distinguishable by their mass (cf. [111, 191]). The default massive integrated splitting functions used are `GammaQ_Lambda_Massive`, `GammaG_Lambda_Massive`, and `GammaF_Lambda_Massive`. An overview of the implemented branching probabilities is given in Tab. D.8.

The class `NLL_Sudakov_Base`

is a pure virtual base class, providing an interface to any Sudakov form factor like object.

The class `NLL_Single_Sudakov`

provides the Sudakov form factor for a single given integrated splitting function.

The class `NLL_Combined_Sudakov`

provides the Sudakov form factor for a sum of integrated splitting functions.

The class `NLL_Dummy_Sudakov`

is a simple example of an Sudakov returning always one. It can be used for only weakly interacting flavours.

The class `NLL_Branching_Probability_Base`

represents a prototype for a branching probability (integrated splitting function), which can be used in the evaluation of Sudakov form factors (cf. class `NLL_Sudakov`). All realisations are derived from this class. A list of available branching probabilities can be found in Tab. D.8. In general single integrated splitting functions have the form

$$\Gamma(Q,q) = \int_{z-(q/Q)}^{z+(q/Q)} dz \frac{\alpha_S(q)}{\pi} P(z)\,,$$

where α_S is the (running) strong coupling and $P(z)$ is the splitting kernel.

The class provides methods to access the branching probability $\Gamma(Q,q)$ through `Gamma(`q`,`Q`)` as well as the value of the integrated branching probability

$$-\log(\Delta(Q,Q_0)) = \int_{Q_0}^{Q} dq\, \Gamma(Q,q)\,.$$

[11] In order to keep track of all Sudakov objects inserted into the map, a list of unique `NLL_Sudakov_Base` objects is maintained. It is used for proper destruction at the end of a run. This double book-keeping allows the usage of the same Sudakov object for all quark flavours, since (massless) QCD is flavour blind.

`Gamma_AlphaS` and `Gamma_Lambda`

$$\Gamma_q(Q,q) = \frac{2C_F}{\pi}\frac{\alpha_{\rm S}(q)}{q}\left(\log\frac{Q}{q} - \frac{3}{4}\right)$$
$$\Gamma_g(Q,q) = \frac{2C_A}{\pi}\frac{\alpha_{\rm S}(q)}{q}\left(\log\frac{Q}{q} - \frac{11}{12}\right)$$
$$\Gamma_f^{n_f}(q) = n_f\frac{2T_R}{3\pi}\frac{\alpha_{\rm S}(q)}{q}$$

`GammaQ_Lambda`

$$\int_{Q_0}^{Q} dq\Gamma_q(Q,q) = \frac{2C_F}{\beta_0}\left\{\log\frac{Q_0}{Q} + \left(\xi_1 - \frac{3}{4}\right)\log\left|\frac{\xi_1}{\xi_0}\right|\right\}$$

`GammaG_Lambda`

$$\int_{Q_0}^{Q} dq\Gamma_q(Q,q) = \frac{2C_A}{\beta_0}\left\{\log\frac{Q_0}{Q} + \left(\xi_1 - \frac{11}{12}\right)\log\left|\frac{\xi_1}{\xi_0}\right|\right\}$$

`GammaF_Lambda`

$$\int_{Q_0}^{Q} dq\Gamma_f(q) = n_f\frac{T_R}{3\beta_0}\log\left|\frac{\xi_1}{\xi_0}\right|$$

`GammaQ_AlphaS`

$$\int_{Q_0}^{Q} dq\Gamma_q(Q,q) = \frac{2C_F}{\beta_0}\left\{\log\frac{Q_0}{Q} + 2\left[\log\frac{Q}{\mu} - \frac{3}{4} + \frac{2\pi}{\beta_0\alpha_{\rm S}(\mu)}\right]\log\frac{1+\eta_1}{1-\eta_0}\right\}$$

`GammaG_AlphaS`

$$\int_{Q_0}^{Q} dq\Gamma_g(Q,q) = \frac{2C_A}{\beta_0}\left\{\log\frac{Q_0}{Q} + 2\left[\log\frac{Q}{\mu} - \frac{11}{12} + \frac{2\pi}{\beta_0\alpha_{\rm S}(\mu)}\right]\log\frac{1+\eta_1}{1-\eta_0}\right\}$$

`GammaF_AlphaS`

$$\int_{Q_0}^{Q} dq\Gamma_f(q) = \frac{2n_f}{3\beta_0}\log\frac{1+\eta_1}{1+\eta_0}$$

`Gamma_Lambda_Massive`

$$\Gamma_Q(Q,q,m) = \Gamma_q(Q,q) + \frac{C_F}{\pi}\frac{\alpha_{\rm S}(q)}{q}\left[\frac{1}{2} - \frac{q}{m}\arctan\left(\frac{m}{q}\right) - \frac{2m^2-q^2}{2m^2}\log\left(\frac{m^2+q^2}{q^2}\right)\right]$$
$$\Gamma_F(q,m) = \frac{T_R}{\pi}\frac{\alpha_{\rm S}(q)}{q}\frac{q^2}{q^2+m^2}\left[1 - \frac{1}{3}\frac{q^2}{q^2+m^2}\right]$$

`GammaQ_Lambda_Massive`,
`GammaG_Lambda_Massive`, and
`GammaF_Lambda_Massive` use numerical integration.

$$\alpha_{\rm S}^{\mu}(Q) = \frac{\alpha_{\rm S}(\mu)}{1 - \frac{\beta_0}{4\pi}\frac{\alpha_{\rm S}(\mu)}{\log(\mu^2/Q^2)}} \qquad \eta_0 = \frac{\beta_0\alpha_{\rm S}(\mu)}{4\pi}\log\left(\frac{Q_0^2}{\mu^2}\right) \qquad \eta_1 = \frac{\beta_0\alpha_{\rm S}(\mu)}{4\pi}\log\left(\frac{Q^2}{\mu^2}\right)$$
$$\alpha_{\rm S}^{\Lambda}(Q) = \frac{2\pi}{\beta_0\log(Q/\Lambda)} \qquad \xi_0 = \log\frac{Q_0}{\Lambda} \qquad \xi_1 = \log\frac{Q}{\Lambda}$$

Figure D.8: Available implementations of NLL branching probabilities.

The latter is accessible through `IntGamma(`Q_0`,`Q`)`, which is used as the basis of Sudakov form factors.

5 Publication list

Journals and eprints

1. F. Krauss and A. Schälicke,
   Implementing the ME+PS merging algorithm,
   hep-ph/0503281.

2. F. Krauss, A. Schälicke, S. Schumann, and G. Soff,
   Simulating W/Z + jets production at the CERN LHC,
   hep-ph/0503280.

3. F. Krauss, A. Schälicke, and G. Soff,
   APACIC++ 2.0: A PArton Cascade In C++,
   hep-ph/0503087.

4. F. Krauss, A. Schälicke, S. Schumann, and G. Soff,
   Simulating W/Z+jets production at the Fermilab Tevatron,
   Phys. Rev. **D70** (2004), 114009, [arXiv:hep-ph/0409106].

5. T. Gleisberg, F. Krauss, C. G. Papadopoulos, A. Schälicke and S. Schumann,
   Cross sections for multi-particle final states at a linear collider,
   Eur. Phys. J. C **34** (2004) 173 [arXiv:hep-ph/0311273].

6. T. Gleisberg, S. Höche, F. Krauss, A. Schälicke, S. Schumann and J. C. Winter,
   SHERPA 1.alpha, a proof-of-concept version,
   JHEP **0402** (2004) 056 [arXiv:hep-ph/0311263].

7. T. Gleisberg, F. Krauss, K. T. Matchev, A. Schälicke, S. Schumann and G. Soff,
   Helicity formalism for spin-2 particles,
   JHEP **0309** (2003) 001 [arXiv:hep-ph/0306182].

8. A. Schälicke, F. Krauss, R. Kuhn and G. Soff,
   Implementing initial state radiation for lepton induced processes in AMEGIC++,
   JHEP **0212** (2002) 013 [arXiv:hep-ph/0203259].

Conference reports

1. T. Gleisberg, S. Höche, F. Krauss, A. Schälicke, S. Schumann, G. Soff, J. Winter,
   Predictions for multi-particle final states with SHERPA,
   to appear in Czech. J. Phys., arXiv:hep-ph/0409122.

2. T. Gleisberg, S. Höche, F. Krauss, A. Schälicke, S. Schumann, J. Winter and G. Soff, *Towards a fragmentation model for Sherpa*,
to appear in Proccedings to the International Conference on Linear Colliders (LCWS 04), Paris 2004, arXiv:hep-ph/0408245.

3. T. Gleisberg, S. Höche, F. Krauss, A. Schälicke, S. Schumann, J. Winter and G. Soff, *New tools for automatic cross section calculation*,
to appear in Proccedings to International Workshop on Deep Inelastic Scattering, Strbske Pleso, 2004, arXiv:hep-ph/0407366.

4. T. Gleisberg, S. Höche, F. Krauss, A. Schälicke, S. Schumann, J. Winter and G. Soff, *Monte Carlo models at the LHC*,
to appear in Proccedings to International Workshop on Deep Inelastic Scattering, Strbske Pleso, 2004, arXiv:hep-ph/0407365.

5. A. Schälicke, T. Gleisberg, S. Höche, S. Schumann, J. Winter, F. Krauss and G. Soff, *Event generator for particle production in high-energy collisions*,
Prog. Part. Nucl. Phys. **53** (2004) 329 [arXiv:hep-ph/0311270].

6. R. Kuhn, A. Schälicke, F. Krauss and G. Soff,
Parton showers and multijet events,
Fundamental and Applied Aspects of Modern Physics, World Scientific, 2000, ISBN 981-02-4589-0, arXiv:hep-ph/0012025.

Bibliography

[1] T. Gleisberg et al., *SHERPA 1.alpha, a proof-of-concept version*, JHEP **02** (2004), 056.

[2] T. Sjöstrand et al., *High-energy-physics event generation with PYTHIA 6.1*, Comput. Phys. Commun. **135** (2001), 238–259.

[3] G. Corcella et al., *HERWIG 6: An event generator for hadron emission reactions with interfering gluons (including supersymmetric processes)*, JHEP **01** (2001), 010.

[4] M. Mangano, *Monte Carlo tools for the LHC*, Seminar, TH Division, CERN, Nov 6 2002.

[5] L. Lönnblad, *Development strategies for PYTHIA version 7*, Comput. Phys. Commun. **118** (1999), 213–228.

[6] S. Gieseke, A. Ribon, M. H. Seymour, P. Stephens, and B. R. Webber, *Herwig++ 1.0: An event generator for e+ e- annihilation*, JHEP **02** (2004), 005.

[7] S. Moretti, K. Odagiri, P. Richardson, M. H. Seymour, and B. R. Webber, *Implementation of supersymmetric processes in the HERWIG event generator*, JHEP **04** (2002), 028.

[8] T. Sjöstrand and P. Z. Skands, *Baryon number violation and string topologies*, Nucl. Phys. **B659** (2003), 243.

[9] L. Lönnblad, http://www.thep.lu.se/ThePEG/.

[10] L. Lönnblad, *CLHEP: A project for designing a C++ class library for high-energy physics*, Comput. Phys. Commun. **84** (1994), 307–316.

[11] S. Frixione and B. R. Webber, *Matching NLO QCD computations and parton shower simulations*, JHEP **06** (2002), 029.

[12] S. Frixione, P. Nason, and B. R. Webber, *Matching NLO QCD and parton showers in heavy flavour production*, JHEP **08** (2003), 007.

[13] S. Frixione and B. R. Webber, *The MC@NLO 2.3 event generator*, (2004), hep-ph/0402116.

[14] S. Catani, F. Krauss, R. Kuhn, and B. R. Webber, *QCD matrix elements + parton showers*, JHEP **11** (2001), 063.

[15] F. Krauss, *Matrix elements and parton showers in hadronic interactions*, JHEP **08** (2002), 015.

[16] L. Lönnblad, *Correcting the colour-dipole cascade model with fixed order matrix elements*, JHEP **05** (2002), 046.

[17] S. Catani, Yu. L. Dokshitzer, M. Olsson, G. Turnock, and B. R. Webber, *New clustering algorithm for multi - jet cross-sections in e+ e- annihilation*, Phys. Lett. **B269** (1991), 432–438.

[18] S. Catani, Yu. L. Dokshitzer, and B. R. Webber, *The K-perpendicular clustering algorithm for jets in deep inelastic scattering and hadron collisions*, Phys. Lett. **B285** (1992), 291–299.

[19] S. Catani, Yu. L. Dokshitzer, M. H. Seymour, and B. R. Webber, *Longitudinally invariant K(t) clustering algorithms for hadron hadron collisions*, Nucl. Phys. **B406** (1993), 187–224.

[20] F. Krauss, A. Schälicke, and G. Soff, *APACIC++ 2.0: A PArton Cascade In C++*, (2005), hep-ph/0503087.

[21] F. Krauss, A. Schälicke, S. Schumann, and G. Soff, *Simulating W/Z + jets production at the Tevatron*, Phys. Rev. **D70** (2004), 114009.

[22] F. Krauss, A. Schälicke, S. Schumann, and G. Soff, *Simulating W/Z + jets production at the CERN LHC*, hep-ph/0503280.

[23] F. Krauss, R. Kuhn, and G. Soff, *AMEGIC++ 1.0: A matrix element generator in C++*, JHEP **02** (2002), 044.

[24] A. Schälicke, F. Krauss, R. Kuhn, and G. Soff, *Implementing initial state radiation for lepton induced processes in AMEGIC++*, JHEP **12** (2002), 013.

[25] T. Gleisberg et al., *Helicity formalism for spin-2 particles*, JHEP **09** (2003), 001.

[26] R. Kuhn, F. Krauss, B. Ivanyi, and G. Soff, *APACIC++ 1.0: A parton cascade in C++*, Comput. Phys. Commun. **134** (2001), 223–266.

[27] A. F. Zarnecki, *CompAZ: Parametrization of the photon collider luminosity spectra*, Acta Phys. Polon. **B34** (2003), 2741–2758.

[28] A. D. Martin, R. G. Roberts, W. J. Stirling, and R. S. Thorne, *Parton distributions and the LHC: W and Z production*, Eur. Phys. J. **C14** (2000), 133–145.

[29] J. Pumplin et al., *New generation of parton distributions with uncertainties from global QCD analysis*, JHEP **07** (2002), 012.

[30] M. Gluck, E. Reya, and A. Vogt, *Photonic parton distributions beyond the leading order: Heavy quark and dilepton production at e p colliders*, Phys. Lett. **B285** (1992), 285–290.

[31] *LHAPDF version 3*, see the homepage: http://durpdg.dur.ac.uk/lhapdf/.

[32] H. E. Haber and G. L. Kane, *The search for supersymmetry: Probing physics beyond the standard model*, Phys. Rept. **117** (1985), 75.

[33] N. Arkani-Hamed, S. Dimopoulos, and G. R. Dvali, *The hierarchy problem and new dimensions at a millimeter*, Phys. Lett. **B429** (1998), 263–272.

[34] R. Kleiss and W. J. Stirling, *Spinor techniques for calculating p anti-p → W+- / Z0 + jets*, Nucl. Phys. **B262** (1985), 235–262.

[35] A. Ballestrero, E. Maina, and S. Moretti, *Heavy quarks and leptons at e+ e- colliders*, Nucl. Phys. **B415** (1994), 265–292.

[36] T. Gleisberg, F. Krauss, C. G. Papadopoulos, A. Schälicke, and S. Schumann, *Cross sections for multi-particle final states at a linear collider*, Eur. Phys. J. **C34** (2004), 173–180.

[37] T. Gleisberg et al., *Predictions for multi-particle final states with SHERPA*, (2004), in proceedings to the Conference on Physics at LHC, Vienna, Austria, 13-17 Jul 2004, hep-ph/0409122.

[38] T. Gleisberg et al., *New tools for automatic cross section calculation*, (2004), Talk given at 12th International Workshop on Deep Inelastic Scattering (DIS 2004), Strbske Pleso, Slovakia, 14-18 Apr 2004. Published in *Strbske Pleso 2004, Deep inelastic scattering* 959-962, hep-ph/0407366.

[39] R. Kleiss and R. Pittau, *Weight optimization in multichannel Monte Carlo*, Comput. Phys. Commun. **83** (1994), 141–146.

[40] F. A. Berends, R. Pittau, and R. Kleiss, *All electroweak four fermion processes in electron - positron collisions*, Nucl. Phys. **B424** (1994), 308–342.

[41] R. Kleiss, W. J. Stirling, and S. D. Ellis, *A new Monte Carlo treatment of multiparticle phase space at high-energies*, Comput. Phys. Commun. **40** (1986), 359.

[42] P. D. Draggiotis, A. van Hameren, and R. Kleiss, *SARGE: An algorithm for generating QCD antennas*, Phys. Lett. **B483** (2000), 124–130.

[43] S. Höche, *Sherpa underlying events vs. Tevatron data*, HERA - LHC workshop, DESY Hamburg, March 21 2005.

[44] T. Sjöstrand and M. van Zijl, *A multiple interaction model for the event structure in hadron collisions*, Phys. Rev. **D36** (1987), 2019.

[45] J. Winter, F. Krauss, and G. Soff, *A modified cluster-hadronization model*, Eur. Phys. J. **C36** (2004), 381–395.

[46] T. Gleisberg et al., *Towards a fragmentation model for Sherpa*, (2004), in proceedings to the International Conference on Linear Colliders (LCWS 04), Paris, France, 19-24 Apr 2004, hep-ph/0408245.

[47] Peter Richardson, *Spin correlations in Monte Carlo simulations*, JHEP **11** (2001), 029.

[48] S. Dittmaier and M. Roth, *Lusifer: A lucid approach to six fermion production*, Nucl. Phys. **B642** (2002), 307–343.

[49] K. Kolodziej, *eett6f v. 1.0: A program for top quark pair production and decay into 6 fermions at linear colliders*, Comput. Phys. Commun. **151** (2003), 339–353.

[50] F. Gangemi, G. Montagna, M. Moretti, O. Nicrosini, and F. Piccinini, *Six-fermion production and Higgs boson physics at future e+ e- colliders*, Eur. Phys. J. **C9** (1999), 31–41.

[51] F. Gangemi, G. Montagna, M. Moretti, O. Nicrosini, and F. Piccinini, *Top-quark physics in six-quark final states at the next linear collider*, Nucl. Phys. **B559** (1999), 3–16.

[52] F. Gangemi, *Anomalous quartic couplings in six-fermion processes at the linear collider*, (2000), hep-ph/0002142.

[53] Borut Paul Kersevan and Elzbieta Richter-Was, *The Monte Carlo event generator AcerMC version 2.0 with interfaces to PYTHIA 6.2 and HERWIG 6.5*, (2004), hep-ph/0405247.

[54] M. L. Mangano, M. Moretti, F. Piccinini, R. Pittau, and A. D. Polosa, *ALPGEN, a generator for hard multiparton processes in hadronic collisions*, JHEP **07** (2003), 001.

[55] A. Pukhov et al., *CompHEP: A package for evaluation of feynman diagrams and integration over multi-particle phase space. user's manual for version 33*, (1999), Preprint INP MSU 98-41/542, hep-ph/9908288.

[56] T. Ishikawa et al., *Grace manual: Automatic generation of tree amplitudes in standard models: Version 1.0*, KEK-92-19.

[57] *Proc. VII International Workshop on Advanced Computing and Analysis Techniques in Physics Research (ACAT 2000)*, P. C. Bhat and M. Kasemann, AIP Conference Proceedings **583** (2001) 214.

[58] C. G. Papadopoulos, *PHEGAS: A phase space generator for automatic cross-section computation*, Comput. Phys. Commun. **137** (2001), 247–254.

[59] M. Moretti, T. Ohl, and J. Reuter, *O'mega: An optimizing matrix element generator*, (2001), hep-ph/0102195.

[60] W. Kilian, *WHIZARD 1.0: A generic Monte-Carlo integration and event generation package for multi-particle processes. manual*, LC-TOOL-2001-039.

[61] T. Stelzer and W. F. Long, *Automatic generation of tree level helicity amplitudes*, Comput. Phys. Commun. **81** (1994), 357–371.

[62] F. Maltoni and T. Stelzer, *Madevent: Automatic event generation with madgraph*, JHEP **02** (2003), 027.

[63] H. Murayama, I. Watanabe, and K. Hagiwara, *HELAS: HELicity Amplitude Subroutines for feynman diagram evaluations*, KEK-91-11.

[64] E. Byckling and K. Kajantie, *N-particle phase space in terms of invariant momentum transfers*, Nucl. Phys. **B9** (1969), 568–576.

[65] G. Peter Lepage, *A new algorithm for adaptive multidimensional integration*, J. Comput. Phys. **27** (1978), 192.

[66] F. Caravaglios and M. Moretti, *An algorithm to compute born scattering amplitudes without feynman graphs*, Phys. Lett. **B358** (1995), 332–338.

[67] F. Caravaglios and M. Moretti, *e^+ e^- into 4 fermions + γ with ALPHA*, Z. Phys. **C74** (1997), 291–296.

[68] A. Kanaki and C. G. Papadopoulos, *HELAC: A package to compute electroweak helicity amplitudes*, Comput. Phys. Commun. **132** (2000), 306–315.

[69] A. Kanaki and C. G. Papadopoulos, *HELAC-PHEGAS: Automatic computation of helicity amplitudes and cross sections*, (2000), hep-ph/0012004.

[70] T. Ohl, *Vegas revisited: Adaptive Monte Carlo integration beyond factorization*, Comput. Phys. Commun. **120** (1999), 13–19.

[71] A. Denner, H. Eck, O. Hahn, and J. Kublbeck, *Feynman rules for fermion number violating interactions*, Nucl. Phys. **B387** (1992), 467–484.

[72] M. W. Grunewald et al., *Four-fermion production in electron positron collisions*, (2000), hep-ph/0005309.

[73] J. A. Aguilar-Saavedra et al., *TESLA technical design report part III: Physics at an e^+e^- linear collider*, (2001), hep-ph/0106315.

[74] S. Dittmaier, *Theoretical tools for a future e+ e- linear collider*, (2003), hep-ph/0308079.

[75] G. Klämke and K. Mönig, *Studies on chargino production and decay at a photon collider*, (2005), hep-ph/0503191.

[76] T. Sjöstrand, L. Lönnblad, S. Mrenna, and P. Skands, *PYTHIA 6.3 physics and manual*, (2003), hep-ph/0308153.

[77] G. Corcella et al., *HERWIG 6.5 release note*, (2002), hep-ph/0210213.

[78] L. Lönnblad, *ARIADNE version 4: A program for simulation of QCD cascades implementing the color dipole model*, Comput. Phys. Commun. **71** (1992), 15–31.

[79] L. Lönnblad, *Combining matrix elements and the dipole cascade model*, Acta Phys. Polon. **B33** (2002), 3171–3176.

[80] S. Mrenna and P. Richardson, *Matching matrix elements and parton showers with HERWIG and PYTHIA*, JHEP **05** (2004), 040.

[81] M. L. Mangano, M. Moretti, and R. Pittau, *Multijet matrix elements and shower evolution in hadronic collisions: W b anti-b + (n)jets as a case study*, Nucl. Phys. **B632** (2002), 343–362.

[82] T. Sjöstrand, *High-energy physics event generation with PYTHIA 5.7 and jetset 7.4*, Comput. Phys. Commun. **82** (1994), 74–90.

[83] T. Sjöstrand, L. Lönnblad, and S. Mrenna, *PYTHIA 6.2: Physics and manual*, (2001), hep-ph/0108264.

[84] T. Sjöstrand and P. Z. Skands, *Transverse-momentum-ordered showers and interleaved multiple interactions*, Eur. Phys. J. **C39** (2005), 129–154.

[85] S. Gieseke, P. Stephens, and B. Webber, *New formalism for QCD parton showers*, JHEP **12** (2003), 045.

[86] Yu. L. Dokshitzer, *Calculation of the structure functions for deep inelastic scattering and e+ e- annihilation by perturbation theory in quantum chromodynamics*, Sov. Phys. JETP **46** (1977), 641–653.

[87] V. N. Gribov and L. N. Lipatov, *Deep inelastic e p scattering in perturbation theory*, Yad. Fiz. **15** (1972), 781–807, [Sov. J. Nucl. Phys. **15** (1972), 438].

[88] L. N. Lipatov, *The parton model and perturbation theory*, Sov. J. Nucl. Phys. **20** (1975), 94–102.

[89] G. Altarelli and G. Parisi, *Asymptotic freedom in parton language*, Nucl. Phys. **B126** (1977), 298.

[90] T. Sjöstrand, *A model for initial state parton showers*, Phys. Lett. **B157** (1985), 321.

[91] G. Marchesini and B. R. Webber, *Monte Carlo simulation of general hard processes with coherent QCD radiation*, Nucl. Phys. **B310** (1988), 461.

[92] S. Jadach, *Non-Markovian Monte Carlo algorithm for QCD evolution*, talk given at the HERA-LHC workshop, Oct. 2004, CERN, http://home.cern.ch/jadach/public/cern_oct04.pdf.

[93] A. H. Mueller, *On the multiplicity of hadrons in QCD jets*, Phys. Lett. **B104** (1981), 161–164.

[94] B. I. Ermolaev and V. S. Fadin, *Log - log asymptotic form of exclusive cross-sections in quantum chromodynamics*, JETP Lett. **33** (1981), 269–272, [Pisma Zh. Eksp. Teor. Fiz. **33** (1981) 285].

[95] Yu. L. Dokshitzer, V. S. Fadin, and V. A. Khoze, *Coherent effects in the perturbative QCD parton jets*, Phys. Lett. **B115** (1982), 242–246.

[96] G. Marchesini and B. R. Webber, *Simulation of QCD jets including soft gluon interference*, Nucl. Phys. **B238** (1984), 1.

[97] S. Gieseke, *Uncertainties of Sudakov form factors*, JHEP **01** (2005), 058.

[98] X. Artru and G. Mennessier, *String model and multiproduction*, Nucl. Phys. **B70** (1974), 93–115.

[99] X. Artru, *Classical string phenomenology. 1. how strings work*, Phys. Rept. **97** (1983), 147.

[100] M. G. Bowler, *e+ e- production of heavy quarks in the string model*, Zeit. Phys. **C11** (1981), 169.

[101] Bo Andersson, G. Gustafson, and B. Soderberg, *A general model for jet fragmentation*, Z. Phys. **C20** (1983), 317.

[102] T. Sjöstrand, *Jet fragmentation of nearby partons*, Nucl. Phys. **B248** (1984), 469.

[103] Bo Andersson, *The lund model*, Cambridge University Press, 1997, Camb. Monogr. Part. Phys. Nucl. Phys. Cosmol., Volume 7.

[104] Ya. I. Azimov, Yu. L. Dokshitzer, V. A. Khoze, and S. I. Troian, *The string effect and QCD coherence*, Phys. Lett. **B165** (1985), 147–150.

[105] T. D. Gottschalk, *A realistic model for e+ e- annihilation including parton bremsstrahlung effects*, Nucl. Phys. **B214** (1983), 201.

[106] B. R. Webber, *A QCD model for jet fragmentation including soft gluon interference*, Nucl. Phys. **B238** (1984), 492.

[107] B. R. Webber, *Monte Carlo simulation of hard hadronic processes*, Ann. Rev. Nucl. Part. Sci. **36** (1986), 253.

[108] R. D. Field and R. P. Feynman, *A parametrization of the properties of quark jets*, Nucl. Phys. **B136** (1978), 1.

[109] D. Amati and G. Veneziano, *Preconfinement as a property of perturbative QCD*, Phys. Lett. **B83** (1979), 87.

[110] F. Krauss and A. Schälicke, *Implementing the ME+PS merging algorithm*, hep-ph/0503281.

[111] F. Krauss and G. Rodrigo, *Resummed jet rates for e+ e- annihilation into massive quarks*, Phys. Lett. **B576** (2003), 135–142.

[112] P. Abreu et al., *m(b) at M(Z)*, Phys. Lett. **B418** (1998), 430–442.

[113] G. Rodrigo, A. Santamaria, and M. S. Bilenky, *Do the quark masses run? extracting m-bar(b)(m(z)) from LEP data*, Phys. Rev. Lett. **79** (1997), 193–196.

[114] P. Abreu et al., *Tuning and test of fragmentation models based on identified particles and precision event shape data*, Z. Phys. **C73** (1996), 11–60.

[115] K. Hamacher and M. Weierstall, *The next round of hadronic generator tuning heavily based on identified particle data*, (1995), hep-ex/9511011.

[116] U. Flagmeyer, *Multijet-Produktion in der e^+e^--Annihilation von $\sqrt{s} = 89$ GeV bis 207 GeV*, Ph.D. thesis, Fachbereich Physik, Bergische Universität Wuppertal, 2001 [WUB-DIS 2001-4].

[117] H. Hoeth, *Messung der Vierjet–Winkelverteilungen und Bestimmung der QCD–Farbfaktoren mit Hilfe des Apacic++–Generators*, diploma thesis, Fachbereich Physik, Bergische Universität Wuppertal, 2003 [WUD 03-11].

[118] M. Bengtsson and P. M. Zerwas, *Four jet events in e+ e- annihilation: Testing the three gluon vertex*, Phys. Lett. **B208** (1988), 306.

[119] O. Nachtmann and A. Reiter, *A test for the gluon selfcoupling in the reactions e+ e- → four jets and Z0 → four jets*, Z. Phys. **C16** (1982), 45.

[120] P. D. Acton et al., *A study of charged particle multiplicities in hadronic decays of the Z0*, Z. Phys. **C53** (1992), 539–554.

[121] S. Eidelman et al., *Review of particle physics*, Phys. Lett. **B592** (2004), 1.

[122] P. Pfeifenschneider et al., *QCD analyses and determinations of alpha(s) in e+ e- annihilation at energies between 35-GeV and 189-GeV*, Eur. Phys. J. **C17** (2000), 19–51.

[123] T. Affolder et al., *The transverse momentum and total cross section of e+ e- pairs in the z boson region from p anti-p collisions at s**(1/2) = 1.8-TeV*, Phys. Rev. Lett. **84** (2000), 845–850.

[124] T. Gleisberg, S. Höche, F. Krauss, A. Schälicke, S. Schumann, and J. Winter, *Studying W^+W^- production at the Fermilab Tevatron*, in preparation.

[125] G. Hesketh, *W and Z (plus jets) cross sections at 1.96-TeV*, (2004), see also Andrea Messina, in preparation., hep-ex/0405067.

[126] R. Hamberg, W. L. van Neerven, and T. Matsuura, *A complete calculation of the order alpha-s**2 correction to the Drell-Yan K factor*, Nucl. Phys. **B359** (1991), 343–405, [Erratum-ibid. B **644** (2002) 403].

[127] R. V. Harlander and W. B. Kilgore, *Next-to-next-to-leading order Higgs production at hadron colliders*, Phys. Rev. Lett. **88** (2002), 201801.

[128] J. Abdallah et al., *A study of the energy evolution of event shape distributions and their means with the DELPHI detector at LEP*, Eur. Phys. J. **C29** (2003), 285–312.

[129] J. G. Körner, G. Schierholz, and J. Willrodt, *QCD predictions for four jet final states in e+ e- annihilation. 2. angular correlations as a test of the triple gluon coupling*, Nucl. Phys. **B185** (1981), 365.

[130] P. Abreu et al., *Experimental study of the triple gluon vertex*, Phys. Lett. **B255** (1991), 466–476.

[131] S. Abachi et al., *W and Z boson production in p anti-p collisions at s**(1/2) = 1.8-TeV*, Phys. Rev. Lett. **75** (1995), 1456–1461.

[132] T. Affolder et al., *Measurement of the W boson mass with the collider detector at fermilab*, Phys. Rev. **D64** (2001), 052001.

[133] V. M. Abazov et al., *Improved W boson mass measurement with the D0 detector*, Phys. Rev. **D66** (2002), 012001.

[134] V. M. Abazov et al., *Combination of CDF and D0 results on W boson mass and width*, (2003), hep-ex/0311039.

[135] C. Albajar et al., *Measurement of the ratio R = sigma(w) Br (W) → mu neutrino) / sigma(Z) Br (Z → mu mu) and gamma(W) total at the CERN proton - anti-proton collider*, Phys. Lett. **B253** (1991), 503–510.

[136] J. Alitti et al., *A measurement of the W and Z production cross-sections and a determination of gamma (W) at the CERN anti-p p collider*, Phys. Lett. **B276** (1992), 365–374.

[137] F. Abe et al., *A measurement of the ratio sigma x b (p anti-p → W → e neutrino) / sigma x b (p anti-p → Z0 → e e) in p anti-p collisions at s**(1/2) = 1800-GeV*, Phys. Rev. **D52** (1995), 2624–2655.

[138] B. Abbott et al., *Extraction of the width of the W boson from measurements of sigma(p anti-p → W + X) x B(W → e nu) and sigma(p anti-p → Z + X) x B(Z → e e) and their ratio*, Phys. Rev. **D61** (2000), 072001.

[139] T. Affolder et al., *Direct measurement of the W boson width in p anti-p collisions at s**(1/2) = 1.8-TeV*, Phys. Rev. Lett. **85** (2000), 3347–3352.

[140] V. M. Abazov et al., *A direct measurement of W boson decay width*, Phys. Rev. **D66** (2002), 032008.

[141] G. Altarelli, R. K. Ellis, and G. Martinelli, *Large perturbative corrections to the Drell-Yan process in QCD*, Nucl. Phys. **B157** (1979), 461.

[142] J. Kubar-Andre and F. E. Paige, *Gluon corrections to the Drell-Yan model*, Phys. Rev. **D19** (1979), 221.

[143] K. Harada, T. Kaneko, and N. Sakai, *Hadronic lepton pair production beyond the leading order in perturbative QCD*, Nucl. Phys. **B155** (1979), 169, [Erratum-ibid. B **165** (1980) 545].

[144] J. Abad and B. Humpert, *Perturbative QCD corrections in Drell-Yan processes*, Phys. Lett. **B80** (1979), 286.

[145] B. Humpert and W. L. Van Neerven, *On the nonleading q anti-q and q g contributions in drell- yan processes*, Phys. Lett. **B85** (1979), 293–296.

[146] C. Anastasiou, L. Dixon, K. Melnikov, and F. Petriello, *High-precision QCD at hadron colliders: Electroweak gauge boson rapidity distributions at NNLO*, Phys. Rev. **D69** (2004), 094008.

[147] C. Balazs and C. P. Yuan, *Soft gluon effects on lepton pairs at hadron colliders*, Phys. Rev. **D56** (1997), 5558–5583.

[148] F. A. Berends, H. Kuijf, B. Tausk, and W. T. Giele, *On the production of a W and jets at hadron colliders*, Nucl. Phys. **B357** (1991), 32–64.

[149] J. Campbell and R. K. Ellis, *Next-to-leading order corrections to W + 2jet and Z + 2jet production at hadron colliders*, Phys. Rev. **D65** (2002), 113007.

[150] J. Campbell, R. K. Ellis, and D. L. Rainwater, *Next-to-leading order QCD predictions for $W + 2jet$ and $Z + 2jet$ production at the CERN LHC*, Phys. Rev. **D68** (2003), 094021.

[151] G. Miu and T. Sjöstrand, *W production in an improved parton shower approach*, Phys. Lett. **B449** (1999), 313–320.

[152] M. H. Seymour, *Matrix element corrections to parton shower algorithms*, Comp. Phys. Commun. **90** (1995), 95–101.

[153] G. Corcella and M. H. Seymour, *Initial state radiation in simulations of vector boson production at hadron colliders*, Nucl. Phys. **B565** (2000), 227–244.

[154] G. C. Blazey et al., *Run II jet physics*, (2000), hep-ex/0005012.

[155] S. Frixione, private communication.

[156] B. Abbott et al., *Differential cross section for W boson production as a function of transverse momentum in p anti-p collisions at s**(1/2) = 1.8-TeV*, Phys. Lett. **B513** (2001), 292–300.

[157] *Detector and physics performance technical design report, vol. 2*, CERN, Geneva, 1999, CERN-LHCC-99-015; ATLAS-TDR-15.

[158] S. Haywood et al., *Electroweak physics*, (1999), hep-ph/0003275.

[159] Valery A. Khoze, Alan D. Martin, R. Orava, and M. G. Ryskin, *Luminosity monitors at the LHC*, Eur. Phys. J. **C19** (2001), 313–322.

[160] M. Dittmar, F. Pauss, and D. Zurcher, *Towards a precise parton luminosity determination at the CERN LHC*, Phys. Rev. **D56** (1997), 7284–7290.

[161] W. T. Giele and S. A. Keller, *Hard scattering based luminosity measurement at hadron colliders*, (2001), hep-ph/0104053.

[162] LEP & SLD collaborations, *A combination of preliminary electroweak measurements and constraints on the standard model*, (2003), hep-ex/0312023.

[163] R. Barate et al., *Measurement of W pair production in e+ e- collisions at 189-GeV*, Phys. Lett. **B484** (2000), 205–217.

[164] G. Abbiendi et al., *W+ W- production cross section and W branching fractions in e+ e- collisions at 189-GeV*, Phys. Lett. **B493** (2000), 249–265.

[165] J. Abdallah et al., *Measurement of the W pair production cross-section and W branching ratios in e+ e- collisions at s**(1/2) = 161-GeV to 209-GeV*, Eur. Phys. J. **C34** (2004), 127–144.

[166] P. Achard et al., *Measurement of the cross section of W-boson pair production at LEP*, Phys. Lett. **B600** (2004), 22–40.

[167] Jogesh C. Pati and Abdus Salam, *Lepton number as the fourth color*, Phys. Rev. **D10** (1974), 275–289.

[168] Rabindra N. Mohapatra and Jogesh C. Pati, *Left-right gauge symmetry and an 'iso-conjugate' model of CP violation*, Phys. Rev. **D11** (1975), 566–571.

[169] Rabindra N. Mohapatra and Goran Senjanovic, *Neutrino masses and mixings in gauge models with spontaneous parity violation*, Phys. Rev. **D23** (1981), 165.

[170] E. Eichten, I. Hinchliffe, Kenneth D. Lane, and C. Quigg, *Super Collider Physics*, Rev. Mod. Phys. **56** (1984), 579–707, [Addendum-ibid. **58** (1986) 1065].

[171] K. J. F. Gaemers and G. J. Gounaris, *Polarization amplitudes for e+ e- → W+ W- and e+ e- → Z Z*, Zeit. Phys. **C1** (1979), 259.

[172] K. Hagiwara, R. D. Peccei, D. Zeppenfeld, and K. Hikasa, *Probing the weak boson sector in e+ e- → W+ W-*, Nucl. Phys. **B282** (1987), 253.

[173] Mikhail S. Bilenky, J. L. Kneur, F. M. Renard, and D. Schildknecht, *Trilinear couplings among the electroweak vector bosons and their determination at LEP-200*, Nucl. Phys. **B409** (1993), 22–68.

[174] P. Abreu et al., *Measurements of the trilinear gauge boson couplings W W V (V = gamma, Z) in e+ e- collisions at 183-GeV*, Phys. Lett. **B459** (1999), 382–396.

[175] A. Heister et al., *Measurement of triple gauge boson couplings at LEP energies up to 189-GeV*, Eur. Phys. J. **C21** (2001), 423–441.

[176] G. Abbiendi et al., *Measurement of charged current triple gauge boson couplings using W pairs at LEP*, Eur. Phys. J. **C33** (2004), 463–476.

[177] P. Achard et al., *Measurement of triple gauge boson couplings of the W boson at LEP*, Phys. Lett. **B586** (2004), 151–166.

[178] F. Abe et al., *Limits on W W Z and W W gamma couplings from W W and W Z production in p anti-p collisions at s**(1/2) = 1.8-TeV*, Phys. Rev. Lett. **75** (1995), 1017–1022.

[179] S. Abachi et al., *Studies of gauge boson pair production and trilinear couplings*, Phys. Rev. **D56** (1997), 6742–6778.

[180] B. Abbott et al., *Limits on anomalous W W gamma and W W Z couplings*, Phys. Rev. **D58** (1998), 031102.

[181] B. Abbott et al., *Limits on W W gamma and W W Z couplings from W boson pair production*, Phys. Rev. **D58** (1998), 051101.

[182] D. Acosta et al., *Measurement of the W+ W- production cross section in p anti-p collisions at s**(1/2) = 1.96-TeV using dilepton events*, (2005), hep-ex/0501050.

[183] B. Abbott et al., *Experimental search for chargino and neutralino production via gauge-mediated supersymmetry breaking models*, Phys. Rev. Lett. **80** (1998), 442–447.

[184] F. Abe et al., *Search for chargino neutralino associated production at the Fermilab Tevatron Collider*, Phys. Rev. Lett. **80** (1998), 5275–5280.

[185] J. Ohnemus, *An order alpha-s calculation of hadronic W- W+ production*, Phys. Rev. **D44** (1991), 1403–1414.

[186] Stefano Frixione, *A next-to-leading order calculation of the cross-section for the production of W+ W- pairs in hadronic collisions*, Nucl. Phys. **B410** (1993), 280–324.

[187] J. Ohnemus, *Hadronic Z Z, W- W+, and W+- Z production with qcd corrections and leptonic decays*, Phys. Rev. **D50** (1994), 1931–1945.

[188] J. M. Campbell and R. K. Ellis, *An update on vector boson pair production at hadron colliders*, Phys. Rev. **D60** (1999), 113006.

[189] S. Catani, S. Dittmaier, and Z. Trocsanyi, *One-loop singular behaviour of QCD and SUSY QCD amplitudes with massive partons*, Phys. Lett. **B500** (2001), 149–160.

[190] W. Beenakker, R. Hopker, M. Spira, and P. M. Zerwas, *Squark and gluino production at hadron colliders*, Nucl. Phys. **B492** (1997), 51–103.

[191] G. Rodrigo, M. S. Bilenky, and A. Santamaria, *Quark-mass effects for jet production in e+ e- collisions at the next-to-leading order: Results and applications*, Nucl. Phys. **B554** (1999), 257–297.

Acknowledgements

I mourn the death of my supervisor, Prof. Gerhard Soff, he was not only a supporting teacher but also a trusted friend.

I am especially grateful to Dr. Frank Krauss for his continuous support. His encouragement was essential for the final success of this thesis.

Further, I am deeply indebted to Stefan Höche, Tanju Gleisberg, Steffen Schumann and Jan-Christopher Winter for fruitful collaboration on `SHERPA`, many stimulating physics discussions and, in particular, for their patient tests of `APACIC++` and the merging routines.

I also want to thank Prof. Bryan Webber for providing me the opportunity to stay one year at the Cavendish Laboratory (Cambridge), as well as Michelangelo Mangano, as the organiser of the MC4LHC workshop at CERN in the summer 2003. Both periods have largely helped me to broaden my knowledge of high-energy physics phenomenology.

I owe a lot to the secretaries G. Latus, G. Schädlich and U. Wächtler, who often helped to solve non-physics problems that came up during the work on my thesis.

I also want to thank Dr. Günter Plunien, Dr. Ralf Schützhold, Thomas Laubrich, Gernot Schaller, Caroline Semmling and all my other colleagues at the group "Theory of hadrons and nuclei" and the whole Institute for Theoretical Physics at Dresden University of Technology. They all have contributed to a pleasant working atmosphere.

Thanks are due to Prof. Ketzmerick and Prof. Schmidt for their support after the premature death of my supervisor.

I am grateful to our experimentalist colleagues K. Hamacher and H. Hoeth for many helpful discussions and for the patient tuning of our parton shower.

Thanks are due to my friends. Our time together has been a continual source of entertainment and diversion.

Finally, I thank my family, especially my girlfriend, Andrea, for their love and support. Without them I would never have got so far at all.

Versicherung

Hiermit versichere ich, dass ich die vorliegende Arbeit ohne unzulässige Hilfe Dritter und ohne Benutzung anderer als der angegebenen Hilfsmittel angefertigt habe; die aus fremden Quellen direkt oder indirekt übernommenen Gedanken sind als solche kenntlich gemacht. Die Arbeit wurde bisher weder im Inland noch im Ausland in gleicher oder ähnlicher Form einer anderen Prüfungsbehörde vorgelegt.

Die vorliegende Arbeit wurde am Institut für Theoretische Physik der Technischen Universität Dresden unter wissenschaftlicher Betreuung von Herrn Prof. Dr. Gerhard Soff und Herrn Dr. Frank Krauss angefertig.

Es haben keinen früheren erfolglosen Promotionsverfahren stattgefunden.

Hiermit erkenne ich die Promotionsordnung der Fakultät Mathematik und Naturwissenschaften der Technischen Universität vom 20. März 2000 an.

Dresden, den 30.03.2005 Andreas Schälicke